SCIENCE OF CLIMATE CHANGE

Volume 4.1
2024

https://scienceofclimatechange.org

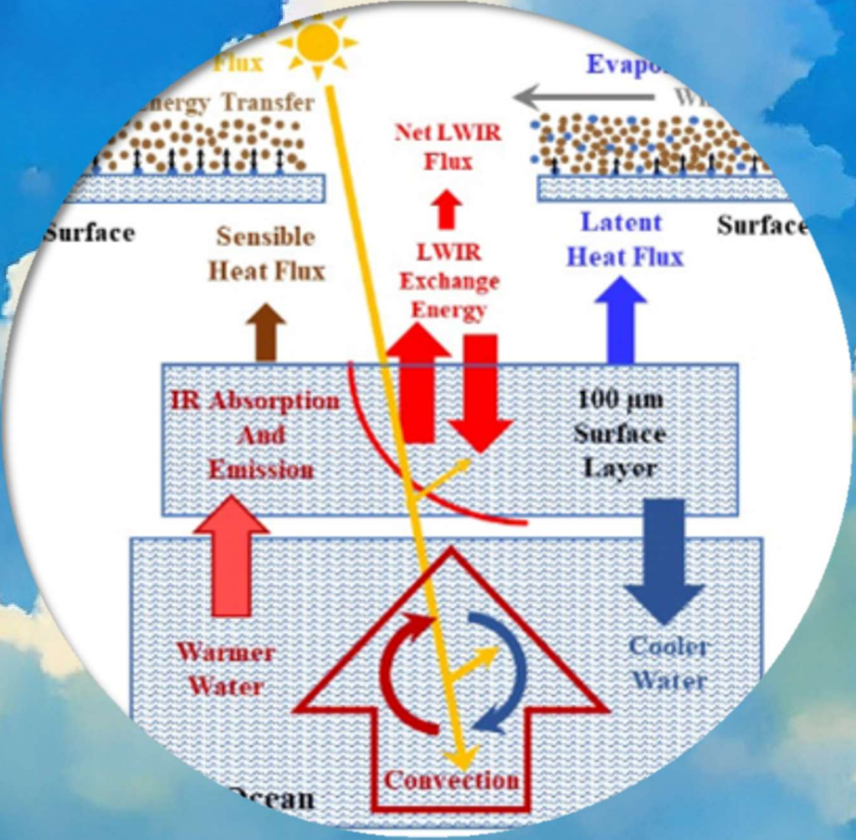

SCC
Published by: Klimarealistene (Org.no.995314592)

ISSN2703-9080(print)   ISNN2703-9072(online)

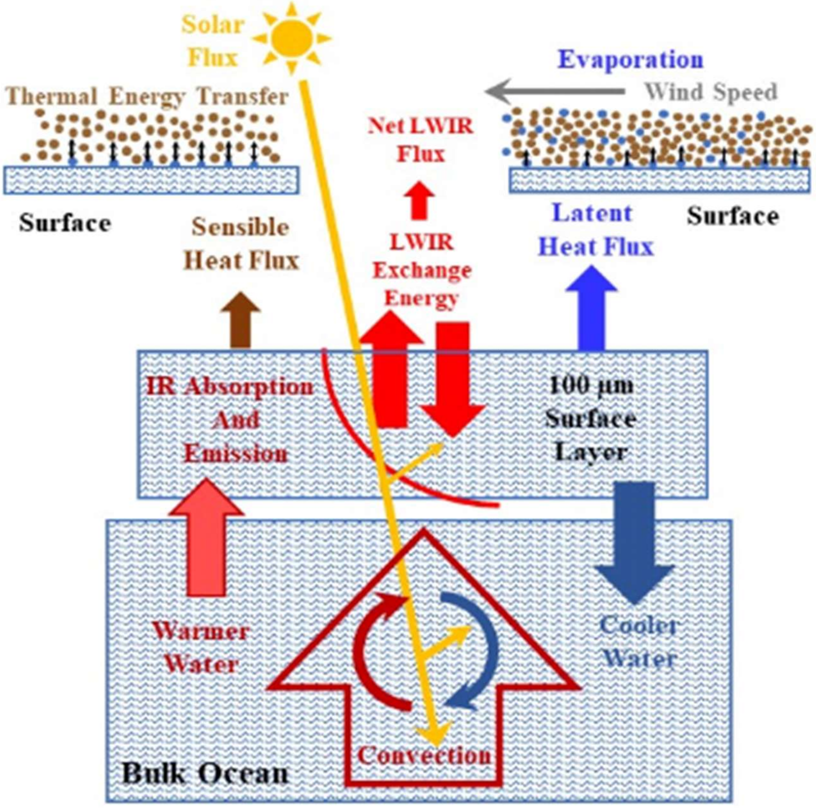

Figure 27: Ocean cooling (schematic): heat is removed from the surface by wind driven evapo ration (latent heat flux) and the sensible heat flux. The net LWIR cooling flux removes heat from the first 100 micron layer. The cooler water produced by these three processes is combined in the surface layer, sinks and cools the bulk ocean below.

From the review article of Roy Clark: *A Nobel Prize for Climate Model Errors.* Page 31

SCIENCE OF CLIMATE CHANGE

Volume 4.1

June 2024

ISSN 2703 9072

Published by: Klimarealistene (Org. no. 995 314 592)
Vollsveien 109, 1358 Jar, Norway

Table of Content

Review Article

Articles

Comment

Preface

The Journal Science of Climate Change is a non-profit venture, hosted and supported by the Norwegian Klimarealistene (KR – Climate Realists). Also, other climate organizations and their members support the journal with qualified publications or their engagement as guest editors and reviewers.

The objective of this journal was and is, to publish – different to many other journals – also peer reviewed scientific contributions, which contradict the often very unilateral climate hypotheses of the IPCC and thus, to open the view to alternative interpretations of climate change.

In 2021 SCC started in the classical format publishing two volumes. Since 2022 it is operating as Open Access Journal with very moderate publication fees, with a new layout and new website. In 2022 three volumes and in 2023 five volumes could be published, consisting of research and review articles, of essays, discussion papers, conference summaries and book reviews.

Within less than three years SCC could develop to an internationally recognized Journal of Climate Sciences presenting alternative views for a much broader discussion and understanding of climate phenomena. This success is essentially due to the dedicated engagement of the previous Chief Editors, in the founding phase, *Geir Hasnes*, and from October 2022 to December 2023 by Prof. Jan Erik Solheim, strongly supported by Dr. Stein Bergsmark.

The Scientific Board of Klimarealistene and the Editorial Board of SCC would like to thank them all for their unprecedented engagement, the good cooperation within the board and their further advice.

The new Editorial Board tries to continue the previous successful work and at the same time to gain further experts on the wide field of climate sciences, who can strengthen the editorial work and who are well known representatives of their countries and/or organizations. This should also contribute to a closer exchange and cooperation between different scientists and nations.

Ole Henrik Ellestad	Hermann Harde
(KR's Scientific Board)	(SCC's Editorial Board)

Editorial

Volume 4 is planned to appear in two issues. This first issue contains a longer review paper of Roy Clark, who explains in detail, why the Royal Swedish Academy of Sciences, who awarded part of the 2021 Nobel Prize for Physics to Syukuro Manabe, failed to recognize that the climate models used to justify the award, were invalid.

Antero Ollila analyses in an article about the record temperatures in the summer months of 2023 that the temperature increase, different to the IPCC's interpretation, cannot be explained exclusively by anthropogenic climate drivers. The hypothesis of this study is to show that the main climate driver at least over this period has been the Absorbed Shortwave Radiation (ASR) as measured within the CERES (Clouds and the Earth's Radiant Energy System) satellite radiation program.

Ian McHaughton presents a detailed compilation of temperature records from seven Australian Capital Cities, seven Australian towns and five global cities/regions, to test the relationship between the observed temperatures and the atmospheric CO_2 concentration. None of the graphs showed any visible correlation between exponentially increasing concentrations of CO_2 and increasing temperatures.

Finally, this issue contains a Comment from Anthony Sadar, who discusses the impact of temperature inversions on the climate. He reports about own review and analysis of more than 21,000 observations over 30 years, which revealed the amount and strength of surface inversions and their trends over the decades.

We hope that the above contributions will stimulate our readers to a further critical discussion of climate science, and we wish interesting reading.

Hermann Harde
(Editor-in-chief)

A digital version of this volume can be found here: https://doi.org/10.53234/scc202407/19

Review Article

OPEN ACCESS

Klimarealistene
Vollsveien 109
1358 Jar
Norway
ISSN: 2703-9072

Correspondence:
roy.clark@ventura-photonics.com

Vol. 4.1 (2024)
pp. 1-73

A Nobel Prize for Climate Model Errors

Roy Clark

Ventura Photonics,
Thousand Oaks, CA, USA

Abstract

When the Royal Swedish Academy of Sciences awarded part of the 2021 Nobel Prize for Physics to Syukuro Manabe they failed to recognize that the climate models used to justify the award were invalid. When the CO_2 concentration was increased in the 1967 model developed by Manabe and Wetherald it created warming as a mathematical artifact of the simplistic steady state energy transfer assumptions that they used. The initial temperature increase was then amplified by a second artifact, the assumption of a fixed relative humidity distribution that created a water vapor feedback. When the CO_2 concentration was doubled from 300 to 600 parts per million (ppm), the 1967 model predicted an increase in equilibrium surface temperature of 2.9 °C for clear sky conditions. The equilibrium temperature increase produced by a CO_2 doubling later became known as the equilibrium climate sensitivity (ECS). The algorithms used in the 1967 model were incorporated into their 1975 global circulation model (GCM). This also had an ECS of 2.9 °C. The steady state assumption provided the foundation for the concept of radiative forcing. The water vapor feedback became part of a set of feedbacks that were used to adjust the radiative forcings. The ECS produced by the 1967 model artifacts provided a benchmark for the temperature increases to be expected in future climate models. The invalid concepts of radiative forcings, feedbacks and climate sensitivity were accepted by the UN Intergovernmental Panel on Climate Change (IPCC) and have been used in all six of the IPCC Climate Assessment Reports. A thermal engineering analysis of the interactive, time dependent surface energy transfer processes that determine the surface temperature demonstrates that it is impossible for the observed increase in atmospheric CO_2 concentration since 1800 to have caused any unequivocal change in surface temperature.

Keywords: Anthropogenic Forcing; Climate Model; Climate Sensitivity; Extreme Weather; Global Mean Temperature Record; Mission Creep; Nobel Prize; Radiative Forcing; Slab Ocean; Syukuro Manabe; Thermal Equilibrium; Time Dependent Energy Transfer; Time Integration; Water Vapor Feedback.

Submitted 2024-02-05, Accepted 2024-03-02. https://doi.org/10.53234/SCC202404/17

1. Introduction

The invalid concepts of radiative forcing, feedbacks and climate sensitivity used by the UN Intergovernmental Panel on Climate Change (IPCC) can be traced back to Table 5 of the climate modeling paper published by Manabe and Wetherald (1967). Here they claimed that a doubling of the CO_2 concentration from 300 to 600 ppm would produce an increase in the equilibrium surface temperature of the earth of 2.9 °C for clear sky conditions. A closer examination reveals that this number was largely a mathematical artifact produced by using a highly simplified one dimensional radiative convective (1-D RC) computer model. Manabe and Wetherald (M&W) failed to correct the obvious simplification errors in this paper and spent the next eight years incorporating the 1967 model algorithms into every unit cell of a highly simplified global circulation model (GCM), Manabe and Wetherald (1975). They also failed to understand that the errors associated with the numerical solution of large numbers of coupled non-linear equations used in a GCM could grow over time and seriously compromise the predictive capabilities of such a model. These issues were described by Lorenz (1963).

As funding was reduced for space exploration and later for nuclear programs, there was mission creep at various US government agencies. The steady state air column was copied by other modeling groups seeking an alternate source of funding, notably the planetary atmospheres group at NASA, Hansen et al (2000). In 1976, the NASA Goddard group copied the 1967 M&W model and created warming artifacts for ten other molecules including methane (CH_4) and nitrous oxide (N_2O), Wang et al (1976). Later, Hansen et al (1981) added a simple two layer slab ocean to the 1967 model. They ignored the wind driven evaporation at the ocean surface and assumed, incorrectly, that the ocean could be heated by a small increase in the downward long wave IR (LWIR) flux at the surface, Clark and Rörsch (2023). The slab ocean was a flat ocean without wind or waves. Hansen et al then tuned this model to simulate a global temperature record from 1880 to 1980 using a combination of increased CO_2 concentration, changes in volcanic aerosol levels and variations in the solar flux. The 1981 Hansen et al paper is one of the earliest examples of the use of a contrived set of radiative perturbations, later called radiative forcings, to tune an equilibrium climate model to match the global average temperature record.

Hansen et al also ignored the obvious 1940 peak in their global temperature record. They assumed that recent warming was caused by the increase in CO_2 concentration. In reality, there can be no CO_2 signal in the global temperature record. The observed warming may be explained as a combination of four factors. First, the dominant term, especially in the early record, is ocean oscillations, mainly the contribution from the Atlantic Multidecadal Oscillation (AMO), Akasofu (2010). Second, there are urban heat islands related to population growth that were not part of the earlier record. Third, the mix of urban and rural weather stations used to create the global record has changed. Fourth, there are so called 'homogenization' adjustments that have been made to the raw temperature data. These include the infilling of missing data and adjustments to correct for bias related to changes in weather station location and instrumentation. It has been estimated that half of the warming in the global record has been created by such adjustments. This has been considered in more detail for example by Andrews (2001a; 2017b; and 2017c), D'Aleo and Watts (2010), Berger and Sherrington (2022) and O'Neill et al (2022).

As funding for nuclear programs was reduced, mission creep spread to the Atomic Energy Commission that became part of the US Department of Energy (DOE) in 1977. An extensive report of the work on CO_2 at DOE was published in 1985 (Riches and Koomanoff, 1985; MacCracken and Luther 1985a; 1985b). The issue was how to detect the CO_2 signal in the surface air temperature record. This work gradually evolved into the Climate Model Intercomparison Project (CMIP) that became the major source of climate model results used by the IPCC. Later, in the Third Climate Assessment Report published by the UN Intergovernmental Panel on Climate change (IPCC, 2001) the radiative forcings were split into anthropogenic and natural contributions. This approach was used to claim that increases in atmospheric greenhouse gas concentrations could cause an increase in the frequency and intensity of extreme weather events.

Manabe and his group failed to recognize and correct the errors in their early climate models. They provided the foundation for the radiative forcings, feedbacks and climate sensitivities still used in the climate models today, IPCC (2021).

Section 2 gives a general description of the early development of the equilibrium models. Section 3 provides a more detailed technical analysis of selected models. Section 4 explains the energy transfer processes that determine the surface temperature and the simplification errors introduced by the climate models. Section 5 considers climate change over time including the influence of ocean oscillations and the limitations of a global mean temperature.

2. The Early Development of the Equilibrium Climate Models

Starting in the early 1960s, Manabe's group at the US Weather Bureau began the development of a GCM for climate prediction. This work is described in four main papers, Manabe and Möller (1961), Manabe and Strickler, (1964), Manabe and Wetherald, (1967) and Manabe and Wetherald (1975). For convenience these are abbreviated as MM61, MS64, MW67 and MW75. The first step was to develop a radiative transfer model that could simulate the atmospheric temperature profile. MM61 started with a one dimensional (1-D) radiative equilibrium model. MS64 was a 1-D radiative convective (1-D RC) model with a fixed absolute humidity profile. MW67 added a fixed relative humidity profile to MS64 and MW75 was a 'highly simplified' GCM that incorporated the MW67 algorithms into each unit cell of the larger model.

2.1 The 1967 Manabe and Wetherald Model

The set of assumptions used in the MW67 steady state air column model were clearly stated on the second page of the paper:

1) *At the top of the atmosphere, the net incoming solar radiation should be equal to the net outgoing long wave radiation.*
2) *No temperature discontinuity should exist.*
3) *Free and forced convection and mixing by the large scale eddies prevent the lapse rate from exceeding a critical lapse rate equal to 6.5 °C km^{-1}.*
4) *Whenever the lapse rate is subcritical, the condition of local radiative equilibrium is satisfied.*
5) *The heat capacity of the earth's surface is zero.*
6) *The atmosphere maintains the given vertical distribution of relative humidity (new requirement).*

The questions that M&W set out to answer were:

1) *How long does it take to reach a state of* ***thermal equilibrium*** *when the atmosphere maintains a realistic distribution of relative humidity that is invariant with time?*
2) *What is the influence of various factors such as the solar constant, cloudiness, surface albedo and the distributions of various atmospheric absorbers on the* ***equilibrium temperature*** *of the atmosphere with a realistic distribution of relative humidity?*
3) *What is the* ***equilibrium temperature*** *of the earth's surface corresponding to realistic values of these factors?*

The MW67 model was a mathematical platform for the development of radiative transfer and related algorithms that could be incorporated into a larger global circulation model. Given the limited spectral data that were available to M&W in 1967, the radiative transfer algorithms were quite reasonable. However, a single radiative transfer analysis only provides a snapshot of the atmospheric LWIR flux and the rates of heating and cooling for the temperature and species profiles specified in the calculation. There were two distinct temperature artifacts in the MW67 calculations. First, the steady state assumption required that the model warm up when the CO_2 concentration was increased so that the flux balance was restored at the top of the model atmosphere. Second, the fixed relative humidity assumption created a water vapor feedback that amplified the initial CO_2 warming. In addition, the time integration algorithm assumed that the small temperature changes calculated at each integration step could accumulate over time.

M&W did not consider the effects of molecular collisions and turbulence in the troposphere. Here, the additional photon energy absorbed by the increase in CO_2 concentration is transferred to the local air parcel as heat. This is then dissipated by wideband LWIR emission that maintains the flux balance at TOA. They also neglected the diurnal temperature and humidity variations related to the solar heating of the surface. These energy transfer processes are discussed in more detail in Section 4.

The equilibrium or steady state climate model was introduced by Arrhenius (1896), A96. He started with a uniform air volume at a single temperature. He also used a fixed average solar flux, a partially reflective blackbody surface with zero heat capacity and imposed an exact flux balance at the top of the model atmosphere (TOMA). When the CO_2 concentration is increased, there is a small increase in the LWIR flux to the surface and a similar decrease in the LWIR emission to space within the spectral region of the CO_2 emission bands. Arrhenius simply increased the surface temperature to restore the flux balance at TOMA. However, in the real atmosphere, any surface temperature changes that might be produced by a change in the atmospheric CO_2 concentration are too small to detect in the normal daily and seasonal temperature variations at the surface and in the adjacent turbulent boundary layer, Clark and Rörsch (2023).

M&W copied the main features of the Arrhenius model and added a 9 or 18 layer radiative transfer algorithm. Three molecules were included in the radiative transfer analysis: carbon dioxide, CO_2, water vapor, H_2O and ozone, O_3. Both LWIR absorption/emission and shorter wavelength solar absorption were calculated. The model was illuminated by a 24-hour average solar flux. The surface was a partially reflective blackbody with zero heat capacity. The magnitude of the lapse rate (vertical tropospheric temperature profile) was constrained so that it did not exceed 6.5 °C per kilometer. The relative humidity (RH) profile for the air layers was also fixed. The temperatures of the surface and air layers were adjusted iteratively until the model reached a steady state in which the temperatures were stable and the LWIR flux emitted at TOMA matched the net incoming solar flux. As various model parameters, such as the solar intensity and the surface reflectivity were varied, the steady state temperature profile was similar to an average of measured values. This was sufficient for M&W to claim that this model could simulate an equilibrium temperature of the earth. However, such a temperature is just a mathematical construct, Essex et al (2007). There is no steady state air column in the real atmosphere and both turbulent moist convection and subsurface thermal storage have to be included in the time dependent surface energy transfer analysis. Under clear sky conditions, almost all of the downward LWIR flux from the lower troposphere to the surface originates from within the first 2 km layer. (At an altitude of 2 km, the pressure is approximately 800 mbar). Almost half of this flux comes from within the first 100 m layer (Clark, 2013a; 2013b; Clark and Rörsch, 2023).

M&W extended the normal radiative transfer calculation of the LWIR flux to include the rate of cooling (or heating) at each level in their model. The net LWIR flux at each level was divided by the heat capacity to give the cooling (or heating) rate. This was multiplied by the time step, usually set to 8 hours, to derive the change in temperature for each air layer. These small temperature changes were then added to the start temperatures and the iteration procedure was repeated for the next step. The MW67 model required about a year of iteration time (time step multiplied by the number of iterations) to reach steady state (see Fig. 4c). For a CO_2 doubling from 280 to 560 ppm, modern radiative transfer calculations for low to mid latitudes give an initial decrease in the tropospheric cooling rate of up to +0.08 K per day, Iacono et al (2008). This is approximately +0.027 K per 8-hour time step (see Fig. 21c). These iterative temperature steps decrease as the model integration proceeds. In the real atmosphere, such small temperature changes cannot accumulate in the normal daily and seasonal temperature cycles.

The fixed RH assumption now added a water vapor feedback that amplified the initial CO_2 warming artifact. Relative humidity is defined as a fraction of the saturated water vapor pressure. As the temperature increases, the saturated water vapor pressure also increases. This produced an increase in the water vapor pressure in the air layers in MW67 even though the RH distribution was fixed. The resulting increases in LWIR flux related to the water vapor concentration amplified the temperature needed to reach the imposed steady state condition in MW67. This water vapor feedback led to the 2.9 K (or °C) model result. For a fixed absolute humidity, the corresponding model temperature rise was 1.36 K. In the real atmosphere near the surface there is no fixed RH, Clark and Rörsch (2023). At fixed absolute humidity, the changes in temperature over the diurnal cycle change the RH. In addition, evaporation changes the absolute humidity (see Fig. 34). Local conditions also change day by day as different weather systems pass through (see Fig. 36).

M&W failed to understand and correct their own errors and went on to incorporate the algorithms from MW67 into every unit cell of the 'highly simplified' MW75 GCM. When the atmospheric CO_2 concentration was doubled in MW75 the average increase in surface temperature was 2.93 °C. This should be compared to the 2.36 °C increase for average cloudiness conditions in MW67. This provided an invalid warming benchmark for the climate models developed by other groups. The 1979 Charney Report claimed an increase in temperature of 3 ±1.5 °C for a doubling of the CO_2 concentration, Charney et al (1979). In addition to model simplifications, there was another calculation issue that was introduced in MW75. A GCM requires the solution to large numbers of coupled nonlinear equations. Such solutions are unstable and the climate GCMs have limited predictive capabilities over the time scales used in climate studies (Lorenz, 1973; 1963). These issues were minimized in MW75 because the model was run to a steady state condition over a 2-year model time period for CO_2 concentrations of 300 and 600 ppm.

2.2 Mission Creep at NASA

Outside events now intervened. Mission creep at NASA started when funding was reduced significantly as the Apollo (moon landing) program ended in 1972. Those modeling planetary atmospheres at NASA were told to switch to earth studies, Hansen et al (2000). Melodramatic claims about climate change related to runaway greenhouse effects or air pollution were used to justify the extension of their radiative transfer studies to the earth's atmosphere. They did not conduct any independent model validation and started to use the steady state air column approach.

During the 1970s there was a global cooling scare related to the cooling phase of the Atlantic Multi-decadal Oscillation (AMO) that was coupled to the weather station record (Akasofu, 2010; Douglas, 1975). Ocean cooling was not part of the climate change narrative, so Rasool and Schneider (1971) claimed that an increase in aerosol concentration could over-ride any CO_2 induced warming and produce atmospheric cooling. If this continued, then it could trigger an Ice Age. This was based on the results from a 1-D steady state climate model. At the time, both authors were with NASA Goddard.

Ramanathan (1975) at NASA Langley then claimed a greenhouse effect or a warming for an increase in the atmospheric concentration of chlorofluorocarbons (CFCs). When the atmospheric CFC concentration was increased in his 1-D model, there was a decrease in LWIR flux at TOMA. It was claimed that this perturbed the climate equilibrium state and produced an increase in surface temperature. Later, this was recognized as the first use of radiative forcing, Ramaswamy et al (2019). The effects of molecular line broadening and surface temperature variations were not considered (see Section 4.1). In 1976, a group at NASA Goddard including Hansen, extended the MW67 1-D RC model to include another 8 minor species, N_2O, CH_4, NH_3, HNO_3, C_2H_4, SO_2, CH_3Cl and CCl_4. They also included the CFCs analyzed by Ramanathan and the original molecules, CO_2, H_2O and O_3 from MW67, Wang et al (1976), H76.

The slab ocean, the step CO_2 doubling and the calculation of a global mean temperature record were added to the 1-D RC model calculations by Hansen et al, (1981), H81. They began by tuning their model so that a CO_2 doubling from 300 to 600 ppm produced an increase in temperature of 2.8 °C. Then they introduced a slab ocean model with a mixed ocean layer 100 m thick and a thermocline layer below this. The surface energy transfer was ignored and only the time delays related to the increase in heat capacity were considered. The penetration depth of the LWIR flux into the oceans is less than 100 micron, Hale and Querry (1973). Here it is fully coupled to the wind driven evaporation or latent heat flux. The large wind driven variations in the latent heat flux overwhelm any possible heating effects produced by the increase in LWIR flux related to a CO_2 doubling, Clark and Rörsch (2023). The slab ocean was a flat ocean without wind or waves.

The H81 model was then used to calculate changes in surface temperature using a variety of forcing agents including greenhouse gases, clouds and aerosols. This was an extension of the work started in H76. The step CO_2 doubling was then introduced. The CO_2 concentration was first doubled in the 1-D RC model from 300 to 600 ppm. This produces a small decrease in the upward LWIR flux emitted to space at TOA and a small increase in the downward LWIR flux to the surface. After a few months, the H81 model stratosphere cooled by ~5 °C and the decrease in

LWIR flux at TOA was 3.8 W m^{-2}. The energy gained was used to warm the oceans. Years later, the surface temperature increased by 2.8 °C. Of this, 1.2 °C was produced by the increase in CO_2 concentration and the rest was from feedbacks. In reality, all of this is too small to detect in the normal daily and seasonal temperature variations near the surface and cannot accumulate over time. At present the annual increase in the average CO_2 concentration is near 2.4 ppm and the change in flux is 0.034 W m^{-2} per year, Harde (2017). At low pressures and temperatures in the stratosphere, there is increased cooling, but any flux changes here are small and do not propagate to the surface because of molecular line broadening at lower altitudes.

Available weather station and related data were combined and averaged into a global mean temperature record. The obvious large peak near 1940 created by the warming phase of the AMO was ignored, AMO (2022). The H81 model was 'tuned' to simulate the global temperature record. A combination of increased CO_2, solar variation and volcanic aerosols was used to fit the climate model output to the temperature record. The H81 paper is one of the earliest examples of the use of a contrived set of radiative perturbations, later called radiative forcings to tune an equilibrium climate model to match the global average temperature record.

A global average temperature is not a good measure of climate. Temperature is an intensive thermodynamic property. The temperature sum of two independent thermodynamic systems is simply a number, so is the average. A global average temperature is a mathematical construct that has no physical meaning. The temperature anomaly obtained by subtracting the mean from a time series of global temperatures is just a number series. This is discussed in detail by Essex et al (2007). Climate and climate change should be analyzed using a zonal climate approach based on the Koppen Geiger or similar classification, Kottek et al (2006). This is considered in more detail in Section 5.

Later, Hansen et al (1984), H84, applied electronic feedback theory to equilibrium climate modeling. The concept of radiative forcing was accepted by the UN Intergovernmental Panel on climate Change (IPCC) and has been used in all of the IPCC climate assessment reports, Ramaswamy (2019). None of the work at NASA was challenged by Manabe's group. They accepted the flat ocean model and calculated an ocean warming of 3.2 K in a mixed ocean layer produced by a 4x increase in CO_2 concentration (Manabe and Stouffer 1979; 1980).

2.3 The Growth of the Climate Models

As computer technology improved, the climate models became more complex, but the equilibrium climate assumption was still there, hidden in the unit cells of the GCMs. A global average planetary energy balance was used instead of the exact flux balance at TOMA in a 1-D model. However, the initial decrease in LWIR flux at TOA produced by an increase in greenhouse gas concentration still changed the energy balance of the earth, Knutti and Hegerl (2008). A greenhouse gas radiative forcing could still heat the oceans. More forcing agents were added to the climate models and the changes over time were adapted so that the global average temperature record generated by the models matched the one derived from the weather station data. Both are just number series that contain almost no information on climate change. More feedback mechanisms were also added so that the models could be tuned to give any desired result. Effective radiative forcings were introduced by Hansen et al (2005). These just added additional tuning to the climate models. The models were compared to each other using the equilibrium climate sensitivity (ECS) to a CO_2 doubling as a benchmark. The MW67 model had an ECS of 2.9 °C for clear sky conditions. The H81 model was tuned to an ECS of 2.8 °C. For the Sixth IPCC Climate Assessment, AR6 (2021), the ECS range for models in the sixth phase of the Climate Model Intercomparison Project (CMIP6) ensemble is from 1.8 to 5.6 °C, Zelinka et al (2020).

As funding for nuclear programs was reduced, mission creep spread to the Atomic Energy Commission that became part of the US Department of Energy (DOE) in 1977. An important part of the DOE climate research program has been model intercomparison. The Program for Climate Model Diagnosis and Intercomparison (PCMDI) was established at Lawrence Livermore National Laboratory (LLNL) in 1990. One of the early intercomparison efforts was the Atmospheric Model

Intercomparison Project (AMIP), Gates (1992). The Coupled Model Intercomparison Program (CMIP) started in 1996, Meehl et al (1997). Various phases of this program have been a major source of the climate model results used by the IPCC. The CMIP3 model results were used for the Fourth IPCC Climate Assessment Report, AR4, (IPCC, 2007: Meehl et al, 2007). The CMIP5 results were used for the Fifth IPCC Climate Assessment Report, AR5 (IPCC, 2013; Taylor et al, 2012) and the CMIP6 results were used for the Sixth IPCC Climate Assessment Report, AR6, (IPCC, 2021; Stouffer et al, 2017; Hausfather, 2019).

There was a significant change in the climate modeling approach that started with the Third IPCC Climate Assessment Report, TAR (2001). The time series of radiative forcings used to simulate the global mean temperature record was split into natural and anthropogenic forcings. The climate models were then rerun to create a separate natural baseline and an anthropogenic contribution to the global mean temperature. A vague statistical argument using changes to the normal distribution ('bell' or Gaussian curve) of temperature was then used to claim that the increase in temperature caused by anthropogenic forcings would cause an increase in the frequency and intensity of extreme weather events (see Section 3.5). This extreme weather argument has been incorporated into all of the later IPCC Climate Assessment Reports (see Figs. 14d through 14g and Sections 3.5 and 3.6).

3. Equilibrium Climate Models: A More Detailed Analysis

3.1 The 1967 Manabe and Wetherald Model (MW67)

The data from tables 4 and 5 of Manabe and Wetherald's 1967 paper, MW67, are shown in Figs. 1a and 1b. The increase in surface temperature for a CO_2 doubling from 300 to 600 ppm is claimed to be 2.9 K (°C) for clear sky conditions for a fixed RH distribution. The temperatures and the temperature changes for a CO_2 doubling from 300 to 600 ppm are circled in red.

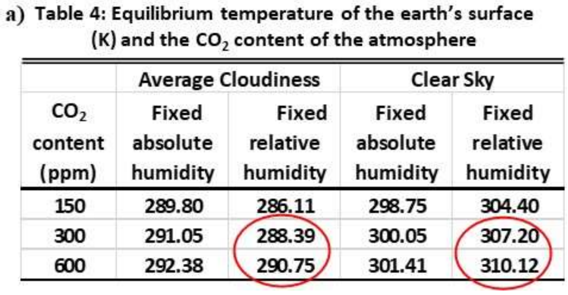

a) Table 4: Equilibrium temperature of the earth's surface (K) and the CO_2 content of the atmosphere

	Average Cloudiness		Clear Sky	
CO_2 content (ppm)	Fixed absolute humidity	Fixed relative humidity	Fixed absolute humidity	Fixed relative humidity
150	289.80	286.11	298.75	304.40
300	291.05	288.39	300.05	307.20
600	292.38	290.75	301.41	310.12

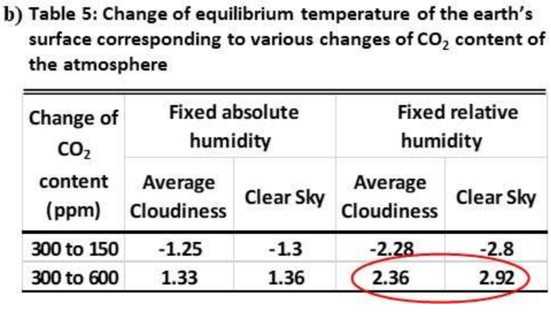

b) Table 5: Change of equilibrium temperature of the earth's surface corresponding to various changes of CO_2 content of the atmosphere

Change of CO_2 content (ppm)	Fixed absolute humidity		Fixed relative humidity	
	Average Cloudiness	Clear Sky	Average Cloudiness	Clear Sky
300 to 150	-1.25	-1.3	-2.28	-2.8
300 to 600	1.33	1.36	2.36	2.92

Figure 1: Tables 4 and 5 adapted from MW67 showing the temperatures and temperature changes produced by doubling the CO_2 concentration from 300 to 600 ppm.

The basic steady state assumptions used by M&W were the same as those used by Arrhenius in 1896. These included a fixed, average solar flux and a partially reflective blackbody surface with zero heat capacity. The effects of advection, evaporation, subsurface thermal storage and ocean transport were ignored. The Arrhenius model is illustrated in Fig. 2. (Modern symbols for Stefan's constant, σ, and the surface emissivity, ε, are used). Because of the simplifications introduced, the surface temperature depends only on the surface emissivity ε and the air column LWIR absorption β (A96, Eqn. 3). The results obtained by Arrhenius for the average annual temperature changes vs. latitude for relative CO_2 concentrations of 0.67, 1.5, 2.0, 2.5 and 3.0 are shown in Fig. 3.

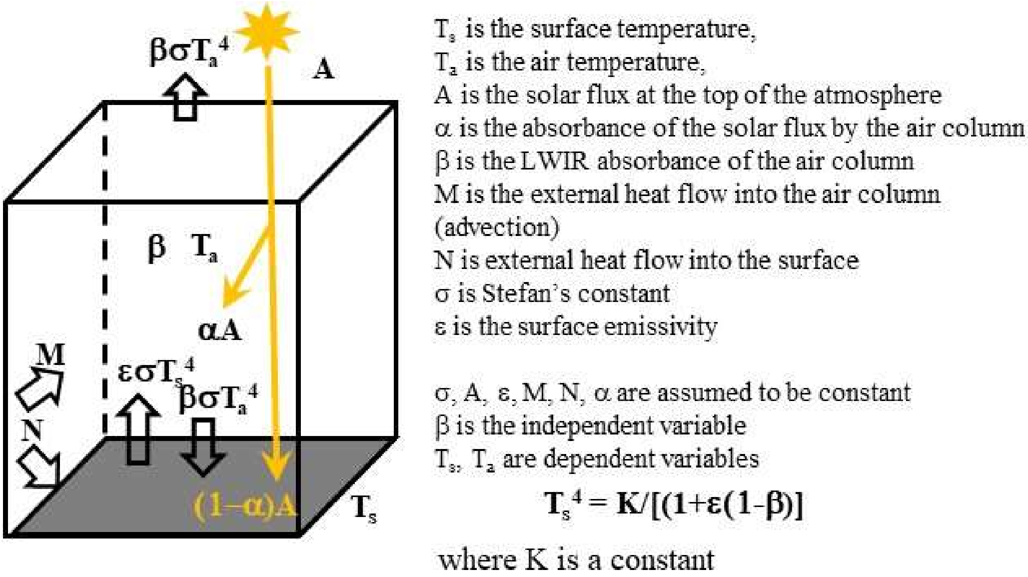

T_s is the surface temperature,
T_a is the air temperature,
A is the solar flux at the top of the atmosphere
α is the absorbance of the solar flux by the air column
β is the LWIR absorbance of the air column
M is the external heat flow into the air column (advection)
N is external heat flow into the surface
σ is Stefan's constant
ε is the surface emissivity

σ, A, ε, M, N, α are assumed to be constant
β is the independent variable
T_s, T_a are dependent variables

$$T_s^4 = K/[(1+\varepsilon(1-\beta)]$$

where K is a constant

Figure 2: The 1896 Arrhenius steady state model.

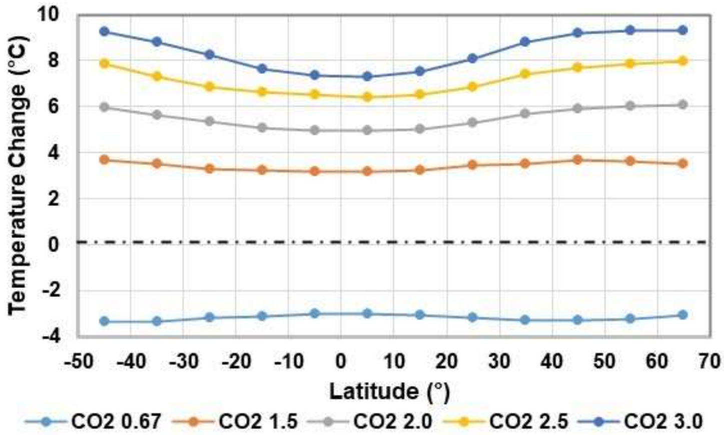

Figure 3: Annual average temperature changes vs. latitude for selected CO_2 concentrations from Arrhenius, 1896, Table VII.

The MW67 model configuration for 9 layers is illustrated in Fig. 4a. The incident solar flux at TOA for a given model run was fixed. The default was 2 Langley per minute (~1395 W m^{-2}). This was converted to a 24 hour average value (see MS64, pp. 367-368). The Langley (Ly) is an older unit of heat per unit area, 1 Ly = one calorie or 4.186 Joules per square centimeter. The surface was a partially reflective blackbody with zero heat capacity. The outline of the time marching or integration procedure is shown in Fig. 4b (MW67, fig.2). Starting from the top right box, the radiative transfer calculation was used to determine the changes in temperature for each layer during the model time step. This was usually 8 hours. The temperature changes were then added to the temperatures at the start of the step. If necessary, the model was forced to maintain the lapse rate at 6.5 K km^{-1}. The water vapor concentration was then adjusted for the new temperatures. The iteration was repeated until the model reached a steady state where the temperatures were stable and the LWIR flux at TOMA matched the net solar flux. The MW67 model required approximately one year of iteration time (step time multiplied the number of steps) to reach a steady state as shown in Fig. 4c (data from MW67, fig. 6). The computational time was much less.

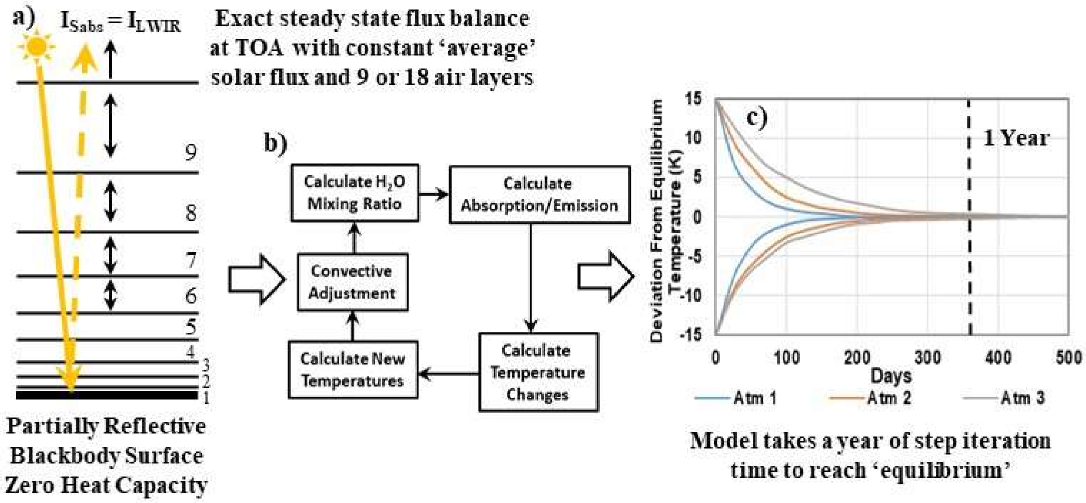

Figure 4: a) The MW67 model configuration (9 air layers shown) with a fixed average solar flux and a partially reflective blackbody surface with zero heat capacity. b) Outline of the 'time marching procedure' used to drive the MW67 model to a steady state condition where the net solar flux equals the LWIR flux at the top of the model atmosphere and the air layer temperatures are stable. c) The time required for the model to reach a steady state.

The tropospheric RH distribution used in MW67 was derived in part from the latitude-height summer and winter averages shown in Fig. 5a (data from MW67, fig, 1). The derived RH profile, h, is shown in Fig. 5b (data from MW67, fig. 3). The linear function for h vs. altitude is given in the text box. The default value for the surface RH, h*, is 0.77 (77%). The surface pressure is set to 1000 mbar. At low pressures in the stratosphere, the H_2O mixing ratio is set to a fixed value of 3 x 10^{-6} gm gm^{-1} air (grams of water vapor per gram of air). The vertical distributions of radiative convective temperature for h* values of 0.2, 0.6 and 1.0 (20%, 60% and 100%) are shown in Fig. 5c (data from MW67, fig. 11). The equilibrium surface temperature increases from approximately 280 to 300 K as h* increases from 0.2 to 1.0. Under clear sky conditions, almost all of the downward LWIR flux to the surface originates from within the first 2 km layer above the surface (see Fig. 19c, below). An altitude of 2 km is close to the 800 mbar level. Approximately half of this flux comes from the first 100 m layer closest to the surface. The 2 km or 800 mbar level is indicated by the blue dashed line in Fig. 5.

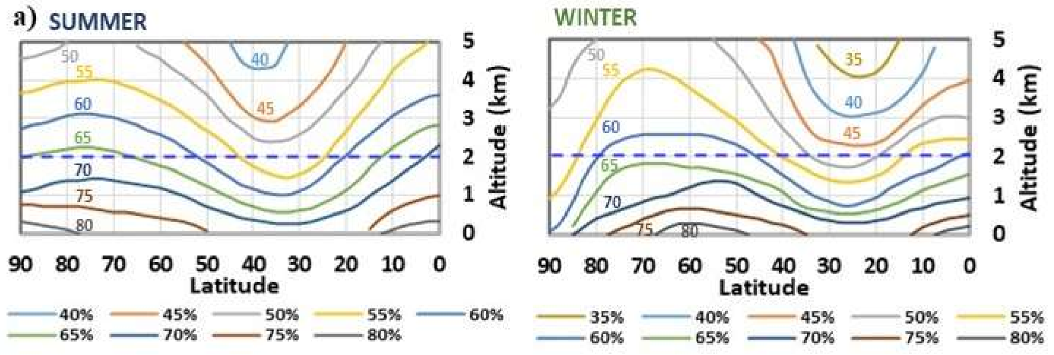

Fig. 1. Latitude-height distribution of relative humidity for both summer and winter (Telegadas and London, 1953)

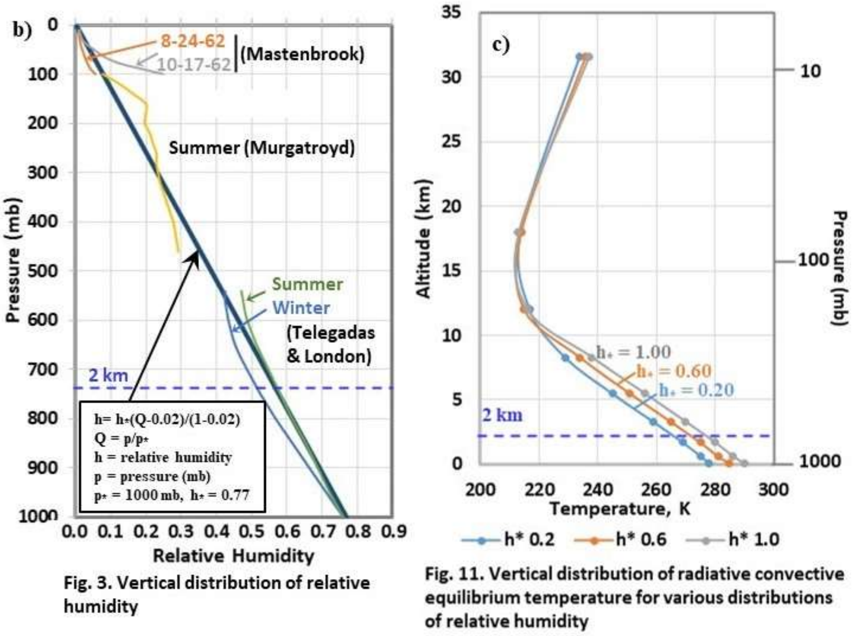

Fig. 3. Vertical distribution of relative humidity

Fig. 11. Vertical distribution of radiative convective equilibrium temperature for various distributions of relative humidity

Figure 5: *a) The latitude-height distributions of relative humidity up to 5 km used to determine the fixed RH distribution for MW67, b) the relative humidity profile used by MW67 and c) the vertical distribution of radiative convective temperature for surface RH (h_*) values of 0.2, 0.6 and 1.0 (20%, 60% and 100% RH). Almost all of the downward LWIR flux from the lower troposphere to the surface originates from within the 2 km layer indicated by the dashed blue line.*

Fig. 6a (data from MW67, fig. 8) shows the steady state temperature profiles for selected values of the solar constant. The table, inset gives the values for the solar constant in Langley per minute and in W m^{-2} and the corresponding equilibrium surface temperatures (K). Fig. 6b (data from MW67, fig. 19) shows the steady state temperature profiles for selected values of the surface albedo. The table, inset gives the values for the albedo and the corresponding equilibrium surface temperature. The results shown in Figs. 5 and 6 were accepted by M&W as sufficient to validate their equilibrium or steady state model.

Fig. 7 (data from MW67, fig. 16) shows the effect of doubling and halving the atmospheric CO_2 concentration in the MW67 model from 300 ppm. In the troposphere, an increase in CO_2 concentration from 300 to 600 ppm produces a slight increase in equilibrium temperature and a decrease to 150 ppm produces a slight decrease. At higher levels in the stratosphere, with lower pressures and temperatures, an increase in the CO_2 concentration produces a decrease in temperature. However, the downward LWIR flux from the stratosphere is absorbed by the wider molecular lines in the troposphere (see Fig. 19) and does not influence the surface temperature. In the real atmosphere there is no equilibrium and the changes in the rates of cooling have to be considered, not the changes in temperature. At low and mid latitudes, the total tropospheric LWIR cooling rate is between -2.0 and -2.5 K per day, Feldman et al (2008). A doubling of the CO_2 concentration from 300 to 600 ppm produces a decrease in the rate of cooling or a slight warming of up to +0.08 K per day (see Fig. 21), Iacono et al (2008). This is simply too small to measure in the normal daily temperature changes in the lower troposphere and cannot accumulate over time. M&W applied their time integration procedure in MW67 without any consideration of the errors involved. The fixed RH assumption amplified the initial CO_2 induced warming produced by their model. This amplification or water vapor feedback was a secondary effect in the model. The fixed RH assumption was made so that the atmospheric temperature profiles generated by MW67 were a better match to the average of the measured data compared to steady state model results obtained using a fixed absolute humidity as described in MS64.

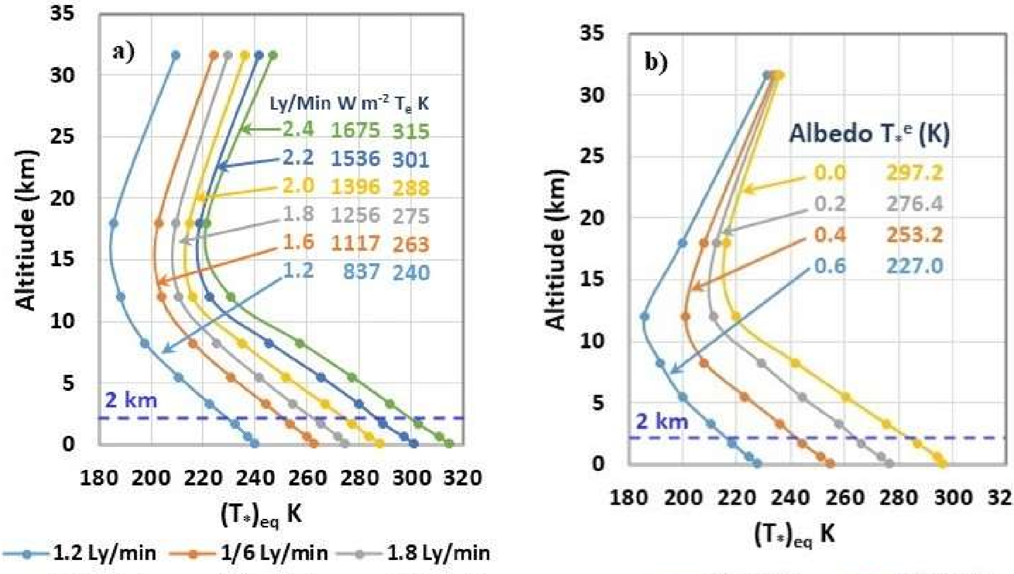

Fig. 8. Vertical Distribution of radiative convective equilibrium temperature of the atmosphere with a given distribution of relative humidity for various values of the solar constant.

Fig. 19. Vertical distributions of radiative convection equilibrium for various values of the surface albedo

Figure 6: a) Steady state temperature profiles for selected values of the solar flux. The table, inset, gives the values of the solar flux in Ly min^{-1} *and W m*$^{-2}$ *and the equilibrium surface temperatures. b) steady state temperature profiles for selected surface albedos. The table, inset gives the values of the albedo and the corresponding equilibrium surface temperatures. The 2 km level is indicated. Under clear sky conditions, almost all of the downward LWIR flux to the surface originates from within this 2 km layer.*

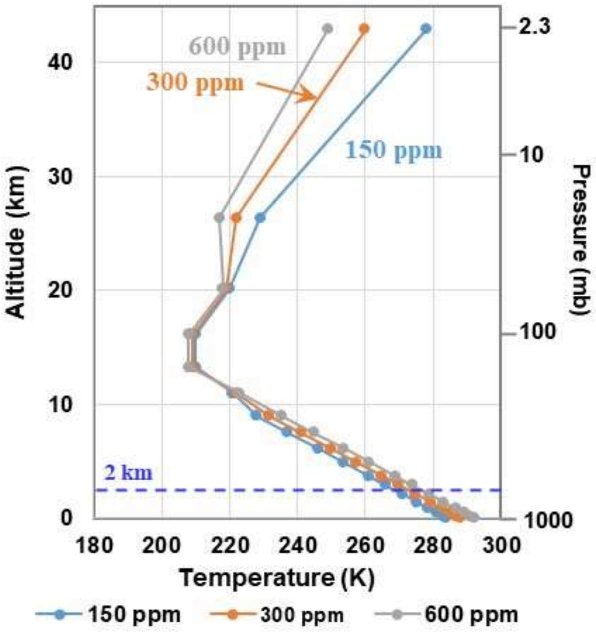

Fig. 16. Vertical distribution of temperature in radiative convective equilibrium for various values of the CO_2 content.

Figure 7: *The equilibrium temperature profiles calculated by the MW67 model for atmospheric* CO_2 *concentrations of 150, 300 and 600 ppm.*

3.2 The 1975 Manabe and Wetherald Model (MW75)

M&W spent the next eight years incorporating the algorithms used in the MW67 model into every unit cell of a ‘highly simplified’ global circulation climate model (MW75). They used the same time integration procedure and the model still required a year of model integration time to reach a steady state. This is shown in Fig. 8 (data from MW67, figs. 5 and 3). When the atmospheric CO_2 concentration was doubled from 300 to 600 ppm in MW75, the average increase in surface temperature was 2.93 °C. This should be compared to the 2.36 °C increase for average cloudiness conditions in MW67.

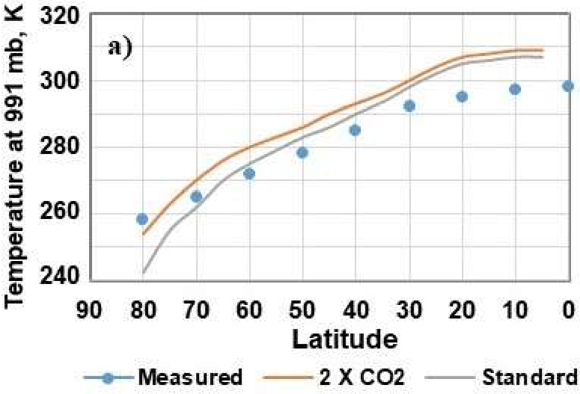

Fig. 5. Zonal mean temperature at the lowest prognostic level (i.e.~991 mb). Dots indicate the observed distribution of zonal mean surface air temperature (Oort and Rasmusson, 1977)

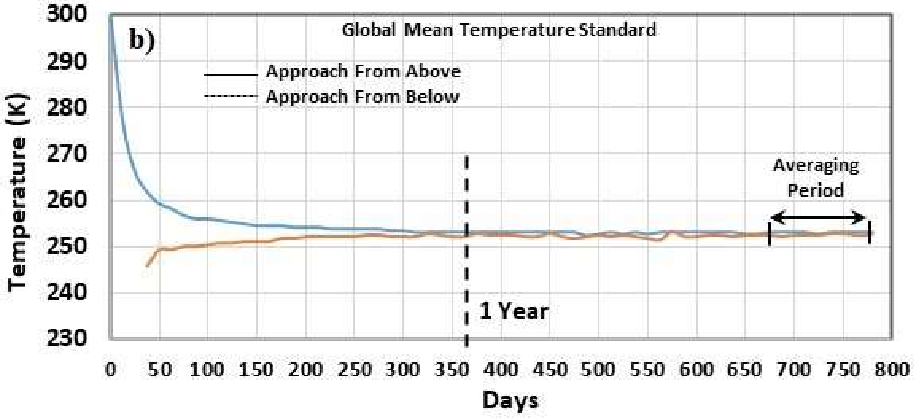

Fig. 3. Time variation of (mass-weighted) mean temperature for the entire period of the two standard runs.

Figure 8: *a) The warming generated by a CO_2 doubling in MW75 and b) the time to reach model equilibrium.*

3.3 Mission Creep: Climate Modeling at NASA

The planetary atmospheres group at NASA started to transition to the analysis of the earth’s climate as the Apollo (moon landing) program ended in 1972 (Hansen, 2000; Rasool and Schneider, 1971; Wang and Domoto 1974; Ramanathan, 1975). In 1976 they added 10 minor species to the MW67 model, Wang et al (1976), H76. Their results are summarized in Fig. 9, from H76, table 3. Separate calculations were run for fixed cloud top temperature and fixed cloud top altitude. All of the temperature changes were created by the MW67 model assumptions.

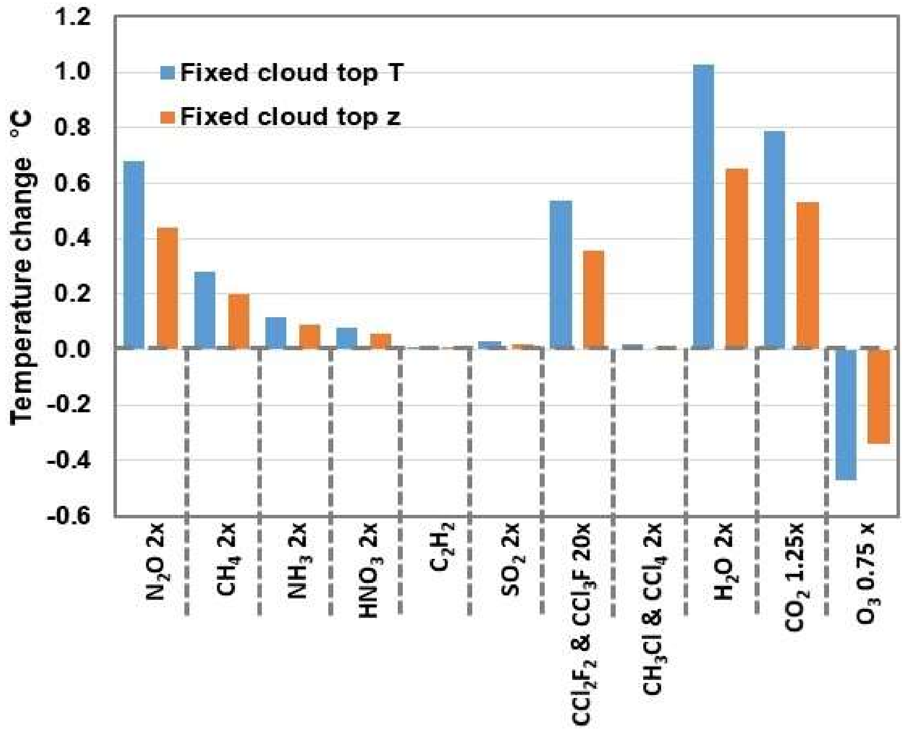

Figure 9: Calculated changes in equilibrium surface temperature obtained by using the H76 1-D RC model with changes in species concentration as shown. Separate calculations were run for fixed cloud top temperature and fixed cloud top altitude (data from H76, Table 3).

Later, in H81 Hansen et al (1981) added a slab ocean model, the step CO_2 doubling and the calculation of a global mean temperature record to the MW67 model calculations. First, they tuned their model so that a doubling of the CO_2 concentration from 300 to 600 ppm produced an increase in equilibrium surface temperature of 2.8 °C. This is shown in Fig. 10a (H81, table1). Model configuration number 4 was selected. Next, they added a two layer slab ocean to the MW67 model. This added heat capacity and a time delay, but the surface energy transfer, particularly the wind driven evaporation or latent heat flux was ignored. This was a flat ocean model without wind or waves. The calculated increase in temperature produced by increasing the CO_2 concentration in H81 for various slab ocean configurations is shown in Fig. 10b (data from H81, fig. 1). The equilibrium temperature changes produced by various radiative perturbations were then considered as shown in Fig. 10c (data from H81, fig. 2). This was a continuation of H76 that included cooling from clouds and aerosols as well as warming from greenhouse gases. Next, the step CO_2 doubling was introduced. These are the flux and temperature changes produced by the H81 model when the CO_2 concentration is first doubled from 300 to 600 ppm and the model is then allowed to return to a steady state. This is shown in Fig. 10d (data from H81, fig. 4). The global temperature record used in H81 is shown in Fig. 10e (adapted from H81 fig. 3). The increase in CO_2 concentration, Keeling (2023) has been added for reference. The 1940 peak produced by the warming phase of the AMO is indicated. The authors of H81 now claimed that they could simulate this global temperature record using a combination of warming from an increase in atmospheric CO_2 concentration, changes in solar flux and cooling produced by volcanic aerosols. This is shown in Fig. 10f (adapted from H81, figure 5). The 1940 AMO peak in Fig. 10f is indicated with a red asterisk.

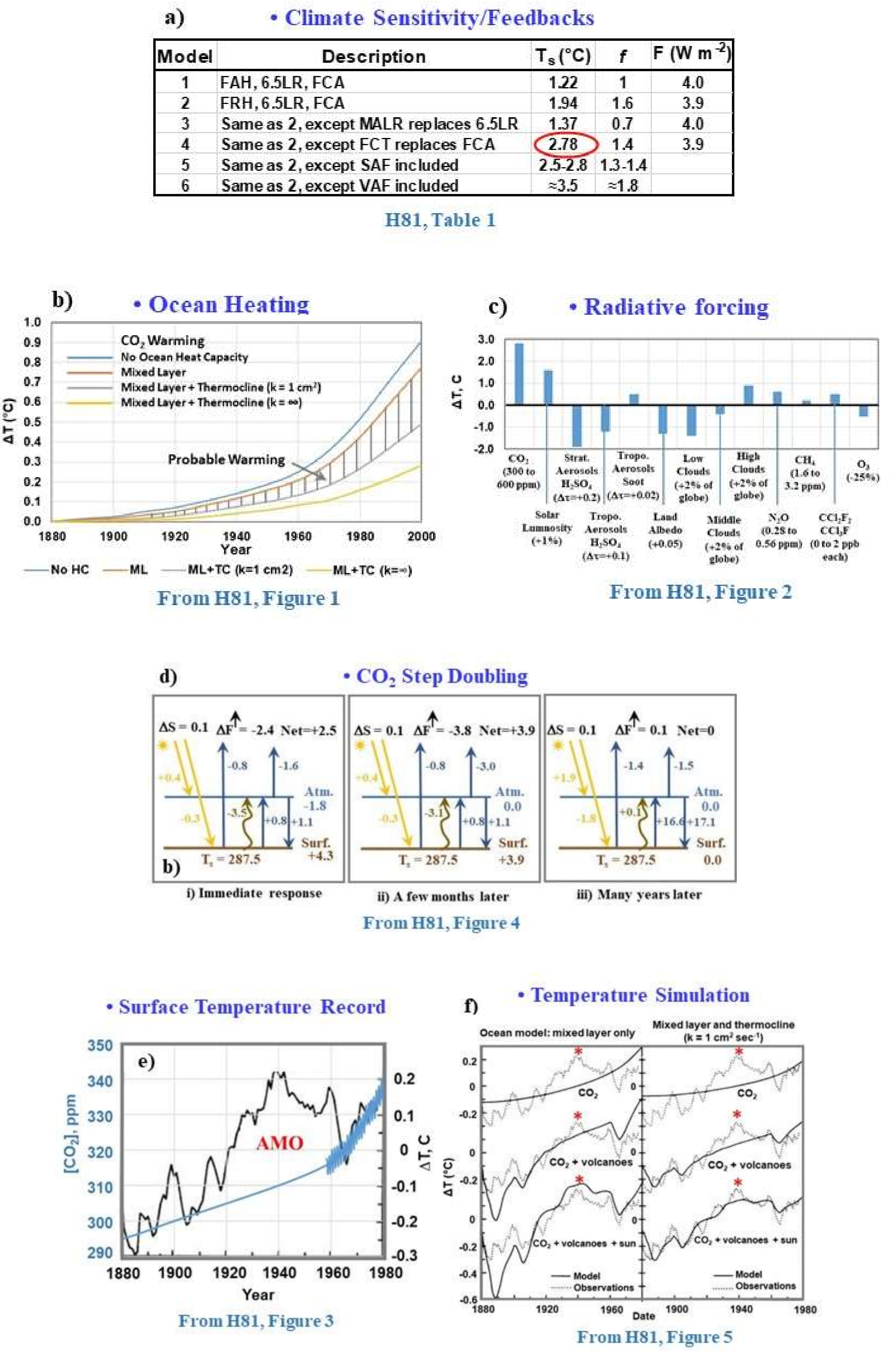

a) • Climate Sensitivity/Feedbacks

Model	Description	T_s(°C)	*f*	F (W m^{-2})
1	FAH, 6.5LR, FCA	1.22	1	4.0
2	FRH, 6.5LR, FCA	1.94	1.6	3.9
3	Same as 2, except MALR replaces 6.5LR	1.37	0.7	4.0
4	Same as 2, except FCT replaces FCA	2.78	1.4	3.9
5	Same as 2, except SAF included	2.5-2.8	1.3-1.4	
6	Same as 2, except VAF included	≈3.5	≈1.8	

H81, Table 1

From H81, Figure 1

From H81, Figure 2

From H81, Figure 4

From H81, Figure 3

From H81, Figure 5

Figure 10: *The foundation of the pseudoscience of radiative forcings, feedbacks and climate sensitivity established by H81. The 1940 AMO peak in the global mean temperature record from e) is indicated by an asterisk in f).*

The radiative perturbations used in H81 were later called radiative forcings. They have been used to explain climate change in all of the IPCC Climate Assessment Reports (Ramaswamy, 2019). None of the work at NASA was challenged by Manabe's group. They accepted the slab ocean model and calculated the ocean heating in a mixed ocean layer produced by a 4x increase in CO_2 concentration using a simplified GCM, Manabe and Stouffer (1979; 1980). They obtained an increase in ocean temperature of 3.2 °C. This is illustrated in Fig. 11 (data from Manabe and Stouffer, 1980, fig. 6).

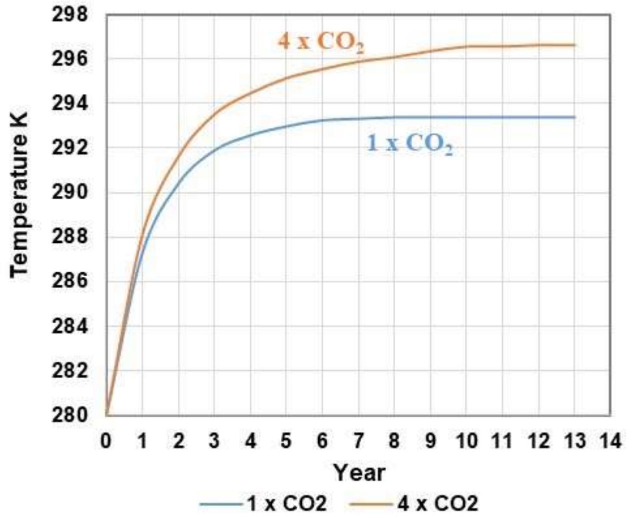

Fig. 6. Time variation of the global mean water temperature of the mixed layer ocean from 1 x CO_2 and 4 x CO_2 experiments. A 1 year running mean operator is applied to both curves

Figure 11: Ocean warming produced by a 4x increase in CO_2 concentration. (Data from fig. 6, Manabe and Stouffer, 1980).

The climate models use radiative transfer algorithms to calculate rates of LWIR cooling and solar heating that are integrated over time to determine the changes in temperature in the model. The calculation of the LWIR rates of cooling was discussed by various authors including Plass (1956a) for CO_2 only, Manabe and Strickler (1964), Stone and Manabe (1968) and Ackerman (1979). Most of this work was focused on the total LWIR cooling rate. More recent work by Feldman et al (2008) for a tropical model atmosphere gives a tropospheric cooling rate between -2.0 and -2.5 °C per day (see Fig. 21a). Ackerman provided both total cooling rates for mid latitude summer conditions and the change in cooling rates produced by a doubling of the CO_2 concentration from 300 to 600 ppm. The total cooling rates are shown in Fig. 12a (data from Ackerman, fig. 3a). They are similar to those published by Feldman et al. The 800 mbar level at approximately 2 km is indicated by the blue dotted line. Almost all of the downward LWIR flux from the lower troposphere to the surface originates from below this 2 km level. The maximum change in tropospheric cooling rate for a doubling of the CO_2 concentration from 300 to 600 ppm is near +0.08 °C per day. This is shown in Fig. 12b and on a larger scale in the inset, Fig. 12c (data from Ackerman, fig. 3b). The changes in tropospheric cooling rates are similar to those given by Iacono et al (2008) (see Fig. 21c). These are too small to detect in the normal diurnal and seasonal variations of the surface and near surface boundary layer temperatures. At a lapse rate of -6.5 °C km^{-1}, an increase in temperature of +0.08 °C is produced by a decrease in altitude near 12 meters. This is equivalent to riding an elevator down 4 floors.

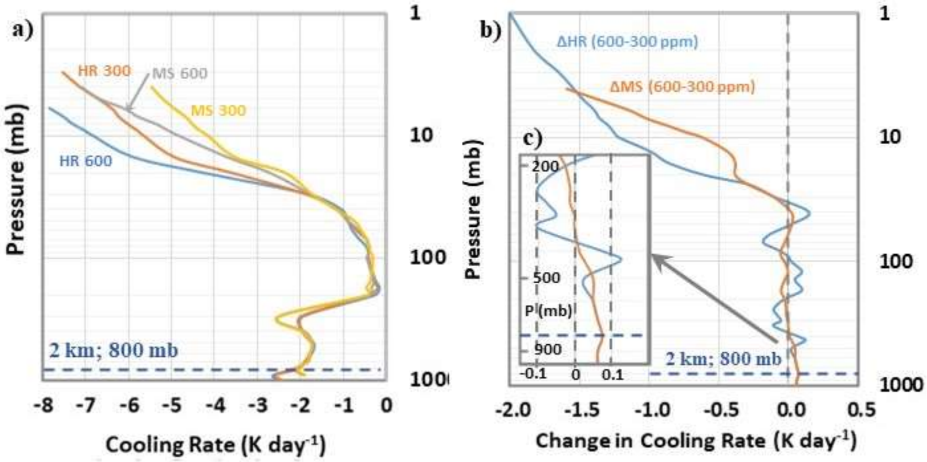

Fig. 3(a) Heating rate profiles computed with HR and MS codes for CO_2 concentrations of 300 ppm and 600 ppm using mid latitude summer profiles.

Fig. 3(b) Difference between heating rate profiles for computed CO_2 concentration of 300 ppm and 600 ppm for HR code and MS code

Figure 12: a) LWIR cooling rates for atmospheric CO_2 concentrations of 300 and 600 ppm, b) the change in these cooling rates produced by the doubling of the CO_2 concentration from 300 to 600 ppm and c) change in tropospheric cooling rates on an enlarged scale. Data from Ackerman (1979).

In H84, Hansen et al (1984) applied electronic feedback theory to climate modeling and the concept of climate sensitivity. They assumed that the amplification created by the fixed relative humidity assumption introduced in MW67 was real. Other feedbacks related to cloud cover and snow/ice extent were also included. When the flux balance at TOA was perturbed by a CO_2 doubling or a 2% increase in solar flux, their GCM would respond and restore the flux balance at TOA by adjusting the surface and air temperatures. The feedbacks altered the temperature response needed to achieve this energy balance. They also assumed that the planetary average LWIR flux emitted to space defined an effective emission temperature. In reality, there is no global average temperature, nor is there an effective emission temperature, Essex et al (2007). This is discussed in more detail in Section 5.3.

3.4 From 1-D RC Models to Coupled GCMs

As computer technology improved, the 1-D RC model was replaced by larger atmospheric GCMs and later by coupled atmosphere-ocean GCMs. The exact flux balance at TOMA in the 1-D models was replaced by an average planetary flux balance. However, the fundamental equilibrium assumption, that an increase in greenhouse gas forcings perturbed the planetary energy balance did not change, Knutti and Hegerl (2008). The surface temperature had to warm to restore the planetary flux balance. Furthermore, the initial change in LWIR flux was still amplified by a water vapor feedback. In addition, the ocean was warmed by the increase in downward CO_2 LWIR flux to the surface.

In 1979 there were only two modeling groups that provided GCM data for the Charney Report (1979). By 1995, 18 coupled climate models were available from seven different countries, Meehl et al (1997). In 2019 there were 49 modeling groups with approximately 100 different models involved in CMIP6 generating data to be incorporated into the Sixth IPCC Climate Assessment, Hausfather (2019). All of these models used the same basic approach established by MW67 and H81.

The radiative forcings, the climate model simulation of the global mean temperature record and the equilibrium climate sensitivities (ECS) published in each of the IPCC Climate Assessment Reports are shown in Figs. 13, 14 and 15 (IPCC, 2021; 2013; 2007; 2001; 1995; 1990). The simulation from H81 (fig. 5) is also shown in Fig. 14a. The 1940 AMO peak in the global mean temperature record is indicated by a red asterisk. The ECSs vary from approximately 2 to 5 °C and are indicators of the differences in the model parameters such as feedbacks that are used to tune the models to match the global mean temperature record. The IPCC uses FAR, SAR and TAR to denote the First, Second and Third Assessment Reports, then changed to AR4, AR5 and AR6 for the later reports. AR1, AR2 and AR3 labels are also included on Figs A14, A15 and A16. The ocean oscillations such as the AMO are produced by a natural imbalance between the solar heating and the wind driven cooling within the ocean gyre circulation.

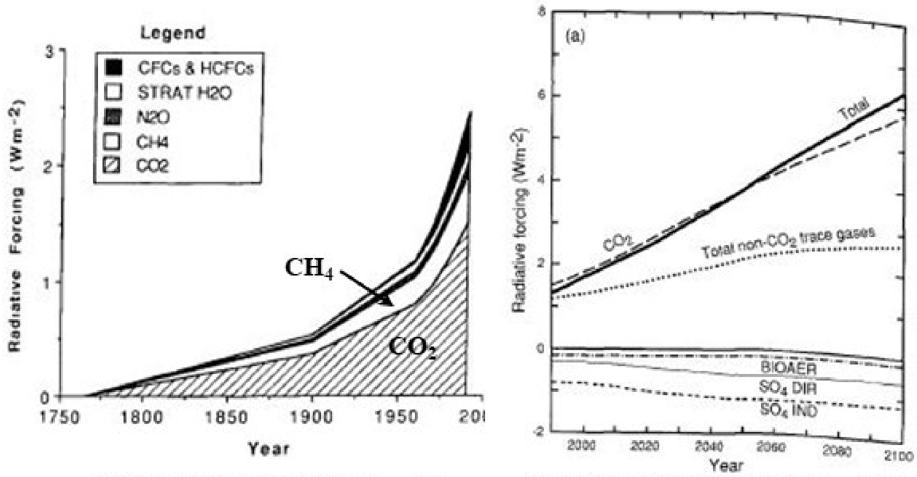

a) FAR (AR1) 1990 Fig. 2.2

b) SAR (AR2) 1995 Fig 6.19a

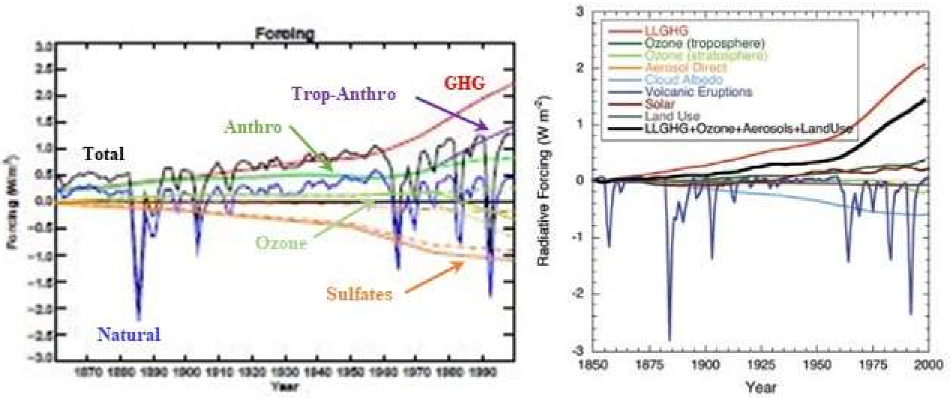

c) TAR (AR3) Tett et al, 2000, fig. 1

d) AR4 2007 Fig 2.23

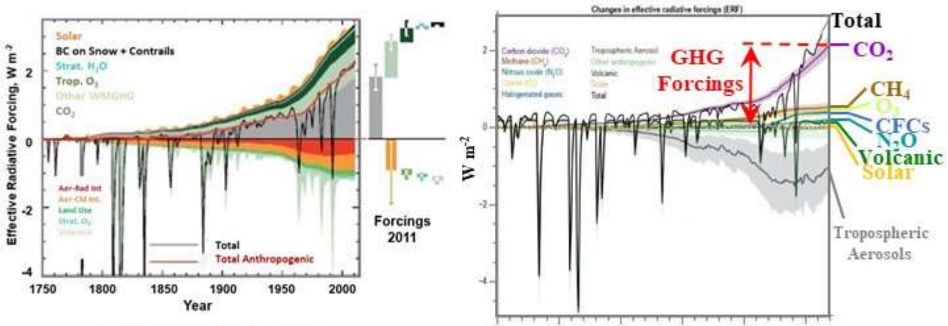

e) AR5 2013 Fig 8.18

f) AR6 2021 Fig 2.10

Figure 13: The time series of the radiative forcings (W m^{-2}) from the six IPCC climate assessment reports. For the Third AR, the source is Tett et al (2000). This is given as one of the sources of TAR Figure 12.7.

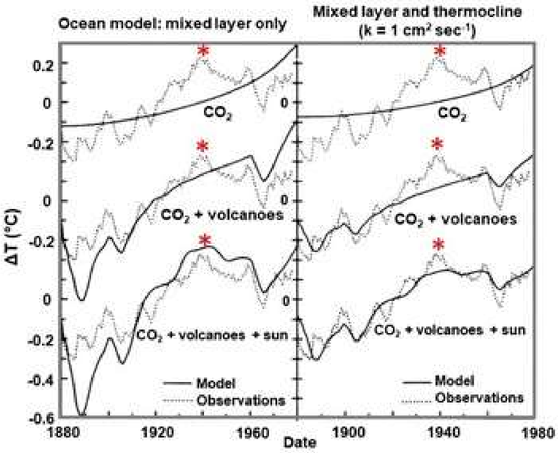

a) H81, Fig. 5 (1981)

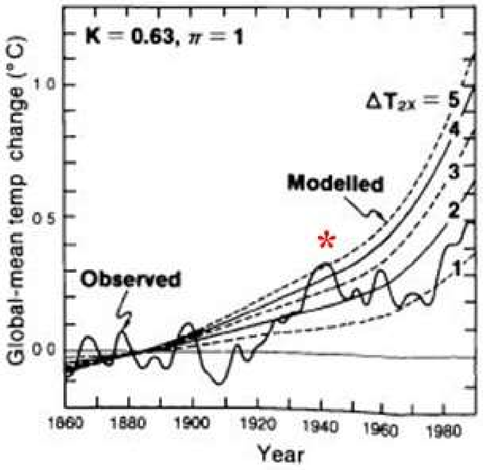

b) FAR (AR1) Fig 8.1, Panel 1 (1990)

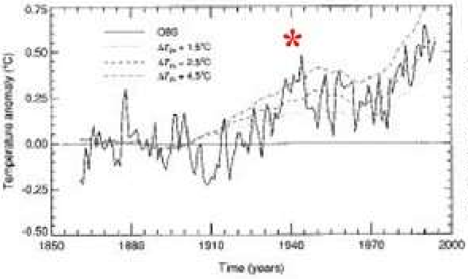

c) SAR (AR2) Fig 8.6c (1995)

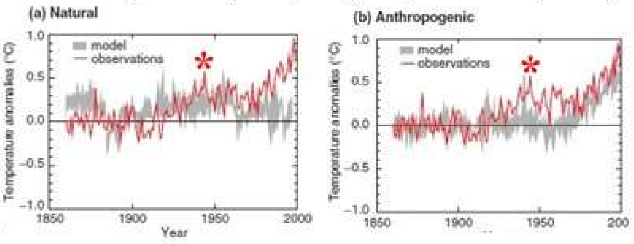

d) TAR (AR3) Fig 4, SPM (2001)

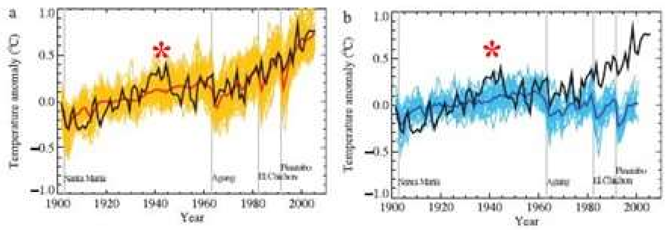

e) AR4 Fig 9.5 (2007)

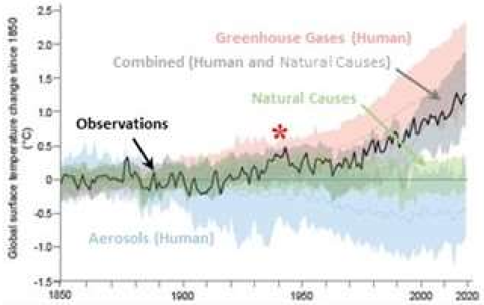

g) AR6 FAQ 3.1 Fig. 1 (2021)

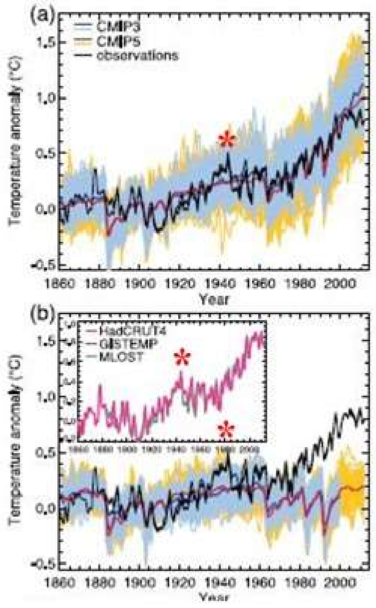

f) AR5 Fig. 10.1 (2013)

Figure 14: *Climate model simulations of the global mean temperature record from H81 to AR6. Starting with the TAR in 2001, the radiative forcings were split into natural and anthropogenic causes with separate contributions to the global mean temperature record. The 1940 AMO peak is indicated with a red asterisk.*

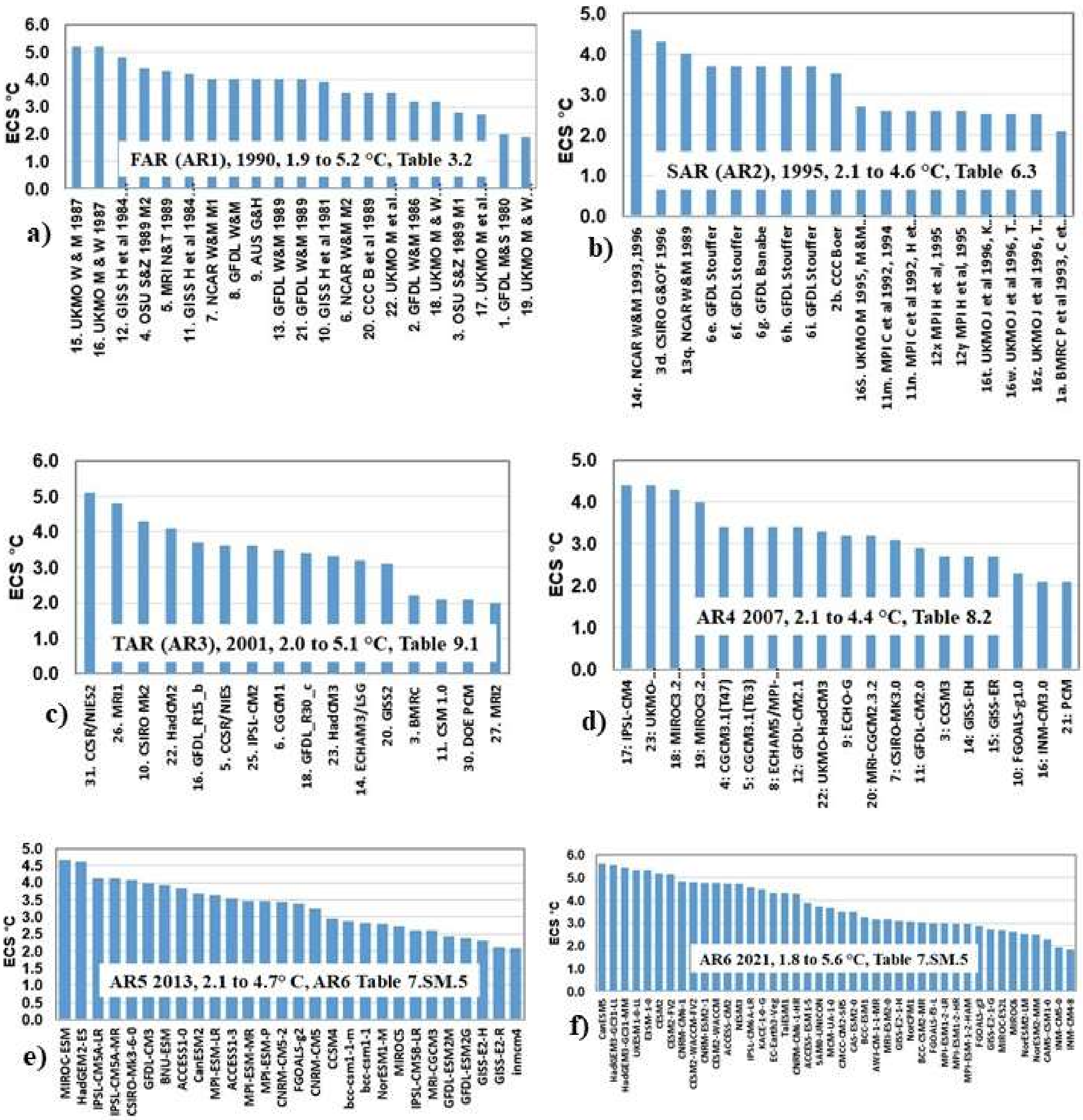

Figure 15: The equilibrium climate sensitivities (ECS) for various climate models from the six IPCC reports. The sources are indicated in the figures.

3.5 Anthropogenic Radiative Forcing and Extreme Weather Attribution

Starting with the Third IPCC Climate Assessment Report (2001), the time series of radiative forcings was split into 'natural' and 'anthropogenic' forcings as shown in Fig. 16a, Tett et al (2000). Three different climate model configurations were used. The first was a natural baseline, run using just the solar and volcanic forcings agents. The second was the anthropogenic contribution, run with a combination of well mixed greenhouse gases, changes in stratospheric and tropospheric ozone and the direct and indirect effects of sulfate aerosols. The third was a combined run with both sets of forcings. The results for these model configurations are shown in Figs 16b, 16c and 16d. The statistical argument used to link an increase in anthropogenic forcings to an increase in the intensity and frequency of extreme weather events shown in Fig. 16e. It is based on changes in the mean and variance of the normal distribution of temperature. Little has changed since 2001. A good example is the annual supplement to the Bulletin of the American Meteorological Society 'Explaining Extreme Events of [Year] from a Climate Perspective', Herring et al (2022). The series has been published annually since 2012. The BAMS publication guidelines state:

> *Each paper will start with a 30 word capsule summary that includes, if possible, how anthropogenic climate change contributed to the magnitude and/or likelihood of the event.*

The CMIP5 and CMIP6 model ensembles and other climate models have been used without question to explain the observed extreme weather events for the year of interest. Natural climate changes related, for example to ocean oscillations and blocking high pressure systems have to be ‘enhanced’ by radiative forcings. The same approach using natural and anthropogenic forcings was used in the Sixth IPCC Climate Assessment Report (2021) as shown in Fig. 17.

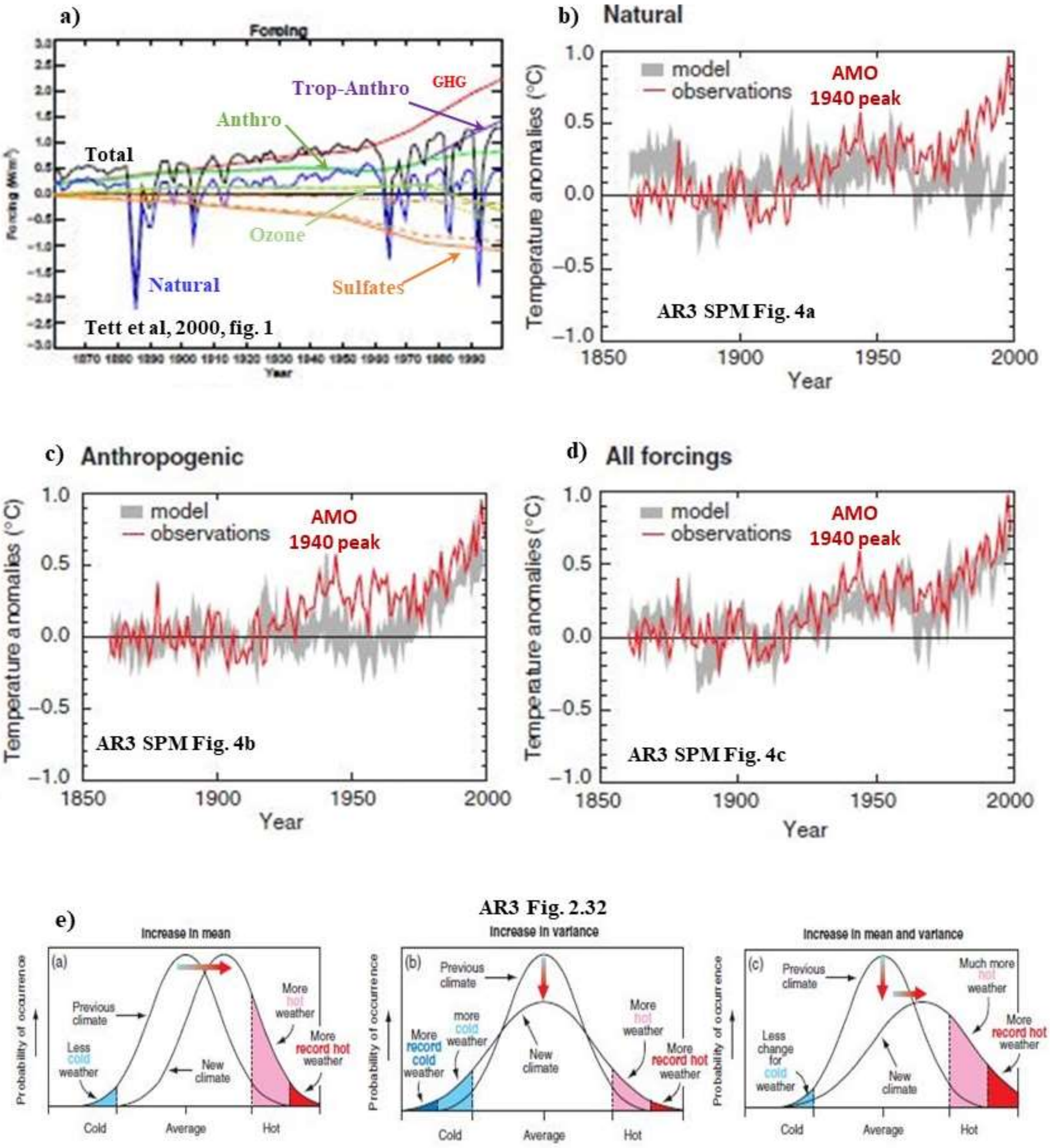

Figure 16: The radiative forcings used by the climate models to simulate the global mean temperature record shown in a) are separated into natural and anthropogenic sources. The climate models are rerun using the natural forcings to establish a ‘natural’ baseline b) and the anthropogenic forcings c) to show the ‘human caused’ warming. A vague statistical argument e) is used to claim that the anthropogenic warming caused an increase in the frequency and intensity of ‘extreme weather events’.

3.6 Radiative Forcings, Feedbacks and Climate Sensitivity in AR6

The introduction to Chapter 7 of the Working Group 1 Report in the latest UN Intergovernmental Panel on Climate Change (IPCC), Climate Assessment, AR6, WG1 (2021) ‘*The Earth’s energy budget, climate feedbacks, and climate sensitivity*’ starts:

> *This chapter assesses the present state of knowledge of Earth's energy budget, that is, the main flows of energy into and out of the Earth system, and how these energy flows govern the climate response to a radiative forcing. Changes in atmospheric composition and land use, like those caused by anthropogenic greenhouse gas emissions and emissions of aerosols and their precursors, affect climate through perturbations to Earth's top-of-atmosphere energy budget. The effective radiative forcings (ERFs) quantify these perturbations, including any consequent adjustment to the climate system (but excluding surface temperature response). How the climate system responds to a given forcing is determined by climate feedbacks associated with physical, biogeophysical and biogeochemical processes. These feedback processes are assessed, as are useful measures of global climate response, namely equilibrium climate sensitivity (ECS) and the transient climate response (TCR).*

The time series of the radiative forcings used in the AR6 CMIP6 models and the related temperature changes are shown in Figs. 17a and 17b. The comparison to the global temperature record is shown in Fig. 17c. The attribution to human causes obtained by dividing the radiative forcings into 'natural' and 'human causes' is shown in Fig. 17d. The real causes of the observed temperature changes are shown in Fig. 17e. They are a combination of ocean temperature changes, urban heat island effects, changes to the rural/urban mix in the weather station averages and various 'adjustments' used to 'homogenize' the temperature data. It has been estimated that half of the warming in the 'global record' has been created by such adjustments. See for example, Andrews (2001a; 2017b; and 2017c), D'Aleo and Watts (2010), Berger and Sherrington (2022) and O'Neill et al (2022). The dominant terms in the ocean temperature contribution are the AMO (2022) and a linear temperature recovery from the Little Ice Age (LIA), Akasofu (2010). Further details are given in Section 4.5 (see Figs. 38 and 40). The climate models are simply 'tuned' to match the global temperature record. The 'tuned' models are then used to simulate the increase in global average temperature produced by a doubling of the CO_2 concentration. This gives the climate sensitivities shown in Fig. 17f (repeated from Fig. 15f).

There has been an extensive discussion in the literature over the magnitude of the climate sensitivity and the related feedbacks. (Lewis and Curry, 2018; Monckton, 2008; Soden and Held, 2006; Terando et al, 2020; Zelinka et al, 2020). These issues may be resolved by examining the time dependent energy transfer processes that contribute to the surface temperature. Climate energy transfer will now be considered in more detail in Section 4.

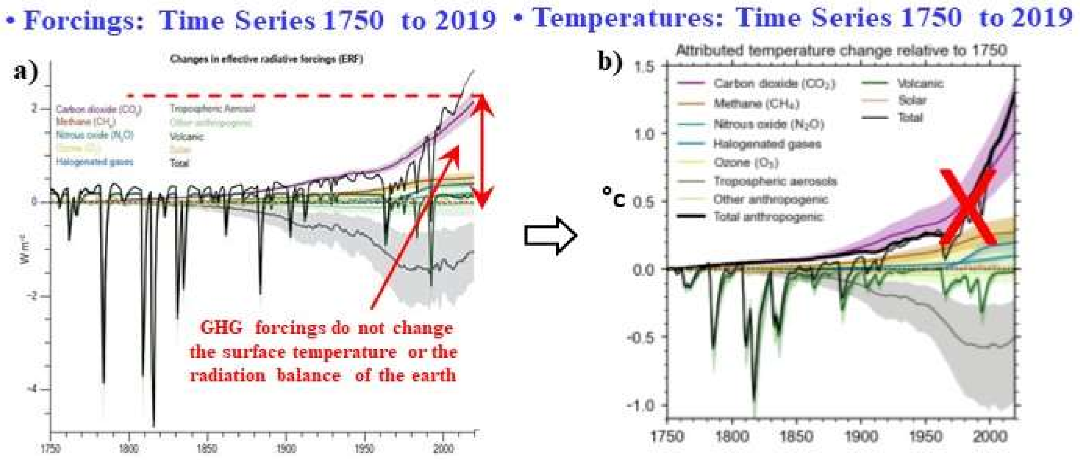

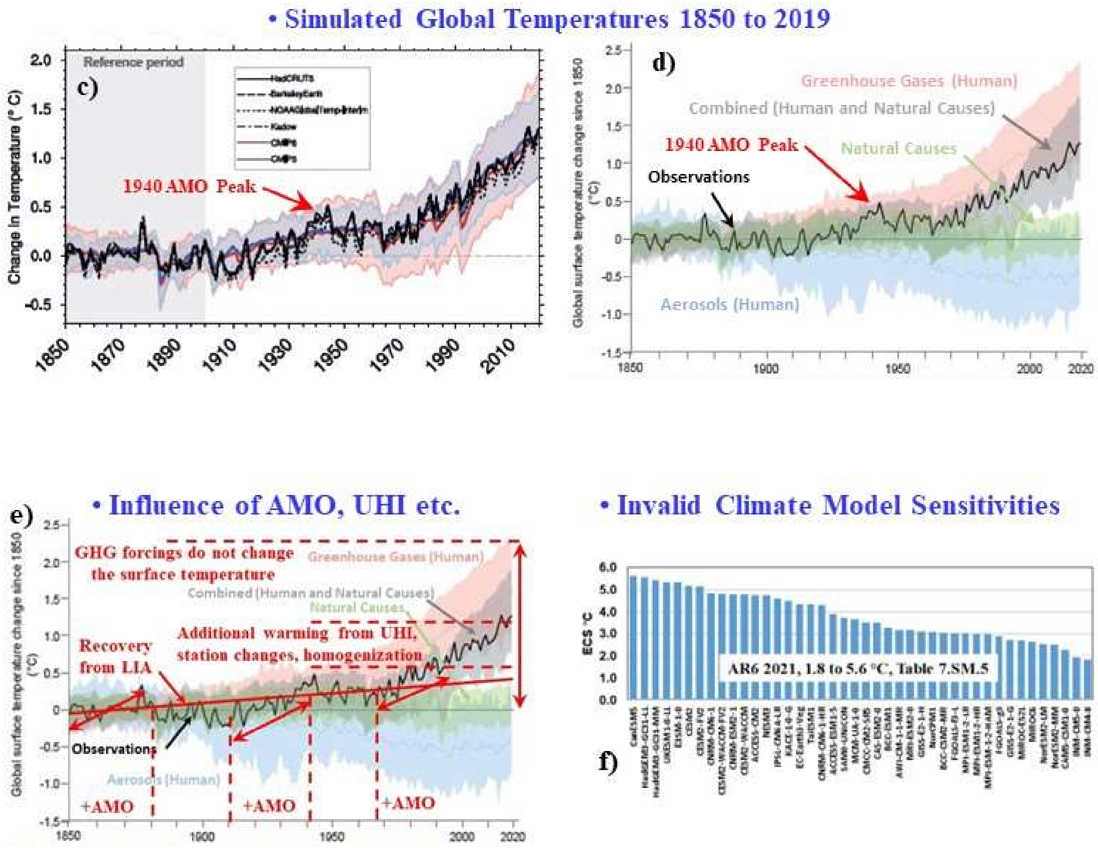

Figure 17: *The attribution process from the CMIP6 model ensemble used in AR6. a) time dependence of the radiative forcings and b) time dependence of the temperature changes derived from a), c) 'tuned' temperature record using a set of radiative forcings to simulate the global mean temperature record, d) separate sets of forcings are used to calculate 'human' and 'natural' temperature records, e) the contributions of the AMO, UHI etc. to the global mean climate record, f) the invalid equilibrium climate sensitivity (ECS) estimated from the CMIP6 models (IPCC AR6, WG1, figures 2.10, 7.8, 3.4b and FAQ 3.1 Fig. 1, ECS data from Table 7.SM.5)*

4. Climate Energy Transfer

Since 1800, the atmospheric concentration of CO_2 has increased by approximately 140 ppm, from 280 to 420 ppm, Keeling (2023). This has produced a decrease near 2 W m^{-2} in the LWIR flux emitted to space at TOA within the spectral range of the CO_2 emission bands. There has also been a similar increase in the downward LWIR flux from the lower troposphere to the surface, Harde (2017). For a CO_2 doubling from 280 to 560 ppm, the decrease in the outgoing longwave radiation (OLR) is estimated to be 3.7 W m^{-2}, IPCC (2013). At present, the average annual increase in CO_2 concentration is near 2.4 ppm. This produces an increase in the downward LWIR flux to the surface of approximately 0.034 W m^{-2} per year. The changes in CO_2 concentration are shown in Fig. 18a and the changes in total flux are shown in Fig. 18b. More detailed calculations of the change in flux at TOA produced by increases in the atmospheric concentration of H_2O, CO_2, O_3, N_2O and CH_4 have been provided by Wijngaarden and Happer (2022).

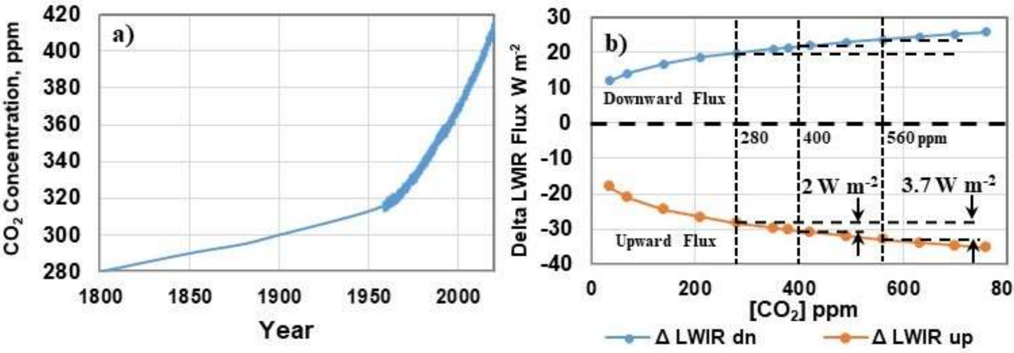

Figure 18: a) The measured increase in atmospheric CO_2 concentration from 1800 (Keeling curve) and b) calculated changes in atmospheric LWIR flux produced by an increase in atmospheric CO_2 concentration from 0 to 760 ppm. Data from table 1, Harde (2017).

In a non-equilibrium system, a change in flux produces a change in the rate of heating or cooling of a thermal reservoir. A change in temperature has to be determined by taking the change in heat content or enthalpy of the thermal reservoir of interest over a given time period and dividing this by the local heat capacity, Clark (2013a; 2013b). In addition to the LWIR flux, the solar heating, the evapotranspiration (moist convection) and the subsurface thermal transport are all coupled to the surface thermal reservoir and must be included in the analysis of the surface temperature. There may also be significant daily and seasonal time delays or phase shifts between the peak solar flux and the temperature response, Clark (2023). The energy transfer processes at the land-air and ocean-air interfaces are different and have to be considered separately.

Convection is also a mass transport process that is coupled to the gravitational field and the rotation of the earth. These interactions result in the formation of the Hadley, Ferrell and polar cell convective structure, the trade winds and the ocean gyre circulation. This is the source of the earth's weather patterns. In the troposphere, vertical motion changes the temperature of an air parcel by air compression/expansion (see Section 4.6). This process is fully coupled to the air parcel cooling produced by the net LWIR emission.

The IPCC assumes that the decrease in LWIR flux at TOA produced by an increase in atmospheric greenhouse gas concentration changes the energy balance of the earth and that the surface temperature increases until the energy balance at TOA is restored. In addition, it is assumed that the initial increase in temperature produces an increase in water vapor concentration that the amplifies the temperature response. Other effects, such as an increase in aerosol concentration may increase the solar flux reflected back to space and produce surface cooling. Changes in flux at TOA are called radiative forcings, Ramaswamy et al (2019). An elaborate scheme of forcings and feedbacks is used in the coupled atmosphere-ocean climate models to simulate climate change. This approach is illustrated above in Figs. 13 and 14. However, when the time dependent energy transfer processes that determine the surface temperature are considered, a very different picture emerges. This has been discussed in detail by Clark and Rörsch (2023). There are five parts to this analysis.

1) The LWIR flux in the atmosphere consists of many thousands of overlapping molecular lines. The line intensity depends on the molecular concentration and the temperature. The linewidth is influenced by molecular collisions. The lines are wider and more intense at lower altitudes. Almost all of the downward greenhouse gas LWIR flux from the atmosphere to the surface is emitted from within the lowest 2 km layer of the troposphere. When the atmospheric greenhouse gas concentration is increased, any additional heat released into the troposphere is decoupled from the surface by a combination of molecular line broadening and turbulent convection.

2) There is no thermal equilibrium or steady state, so a change in flux has to be interpreted as a change in the rate of cooling (or heating) of a set of coupled thermal reservoirs. In the troposphere, at low to mid latitudes, a doubling of the CO_2 concentration from 300 to 600 ppm produces a

maximum decrease in the LWIR cooling rate, or a slight warming of +0.08 °C per day. When this is combined with the normal daily and seasonal variations in surface temperature, any temperature increases from a CO_2 doubling are too small to detect.

3) Over the oceans, the penetration depth of the LWIR radiation is less than 100 micron (0.004 inches). The wind driven evaporation removes water molecules from the surface. The net LWIR cooling flux and the latent heat flux are combined in a thin surface layer. The cooler water produced in this layer sinks and is replaced by warmer water from the bulk ocean below. Within the ±30° latitude bands, the annual average long term latent heat flux is at least 100 W m^{-2}. The average annual increase in atmospheric CO_2 concentration is currently near 2.4 ppm per year. This produces a decrease in the net LWIR cooling flux of approximately 0.034 W m^{-2} yr^{-1}. This is too small to have any measurable effect on ocean temperatures.

4) Over land, almost all of the absorbed solar flux is dissipated within the same diurnal cycle in which it is received. Heat is removed from the surface by convection during the day when the surface is warmer than the air layer above. There is a convection transition temperature each evening when the convection stops and the surface continues to cool more slowly by net LWIR emission. This transition temperature is reset each day by the local weather system passing through. A decrease in net LWIR cooling flux of approximately 0.034 W m^{-2} yr^{-1} is too small to produce a detectable change in surface temperature variation associated with this transition temperature.

5) The IPCC claims that a series of radiative forcings can be used to explain the observed global mean temperature record. Consideration of the time dependent energy transfer processes that determine the surface temperature and the averaging process used to determine the global temperature record provide an alternative explanation. The well-known quasi-periodic oscillations in ocean surface temperature are coupled to the land based weather station record by weather systems that form over the oceans and move over land. This coupling is produced by changes to the convection transition temperature in the diurnal temperature cycle. In addition, urban heat island effects have increased as urban areas have grown in size. Changes to the mix of urban and rural weather stations used to determine the global average temperature have also added bias to the record. The process of homogenization used to adjust the raw temperature data may also add warming.

These areas will now be considered in more detail.

4.1 Radiative Forcing by Greenhouse Gases does not Change the Radiation Balance of the Earth

When the atmospheric concentration of a greenhouse gas is increased, there is a decrease in the LWIR flux emitted to space at TOA, within the spectral region of the absorption/emission band specific to each greenhouse gas considered, Wijngaarden and Happer (2022). A change in flux at TOA is considered to be a radiative forcing that changes the radiation balance of the earth (see Section 3.6). Other radiative forcings, such as changes in aerosol concentration may increase the reflected solar flux at TOA and produce cooling. It is then assumed that the surface temperature adjusts to restore the flux balance at TOA, Knutti and Hegerl (2008). The IPCC also assumes that there is a linear relationship between the radiative forcing ΔF and the surface temperature response ΔT (IPCC, 2021; Ramaswamy, 2019). The change flux at TOA, ΔN is given by:

$$\Delta N = \Delta F + \alpha\Delta T \qquad (1)$$

Here α is a net feedback parameter. The initial forcing, ΔF is reduced by the surface temperature response.

The concept of radiative forcing by greenhouse gases was first introduced by Ramanathan, (1975) for a 1-D RC steady state model. It is a mathematical construct based on conservation of energy applied to an equilibrium average climate state. The secondary energy transfer processes that occur after the initial photon absorption by the greenhouse gas molecules were not considered. The excited molecular vibration-rotation states formed by IR photon absorption are rapidly quenched by molecular collisions and the photon energy is transferred to the local air parcel as heat. The small amount of additional heat released at each level in the troposphere is then dissipated by a combination of wideband LWIR emission and local turbulence. The downward transfer of energy by LWIR emission is limited by the increase in linewidth with decreasing altitude. The initial wavelength specific decrease in LWIR flux at TOA is converted to wideband LWIR emission back to space at TOA. Any change to the energy balance of the earth is insignificant.

The atmospheric LWIR flux consists of IR emission and absorption from many overlapping lines (Clark and Rörsch, 2023; Wijngaarden and Happer, 2022). Each line is a specific transition between two molecular rotation-vibration states. The lines are broadened by molecular collisions. The collision frequency in the troposphere is $>10^9$. The increase in linewidth associated with the decrease in excited state lifetime by molecular collisions is a consequence of the Heisenberg Uncertainty Principle applied to energy and time, Messiah (1999). Near the surface within the main absorption emission bands, the lines overlap and merge into a quasi-continuum. At higher altitudes, these lines become narrower as the temperature and pressure decrease. Some of the upward LWIR flux can pass through the gaps between these narrower lines above and continue to space without additional absorption/emission. The downward flux is absorbed by the wider lines below. This is illustrated schematically in Fig. 19a for a single line and in Fig. 19b for a group of lines in the 590 to 600 cm^{-1} region. Almost all of the downward LWIR flux that reaches the surface originates from within the first 2 km layer of the troposphere. Approximately half of this downward flux originates from the first 100 m layer. This is shown in Fig. 19c.

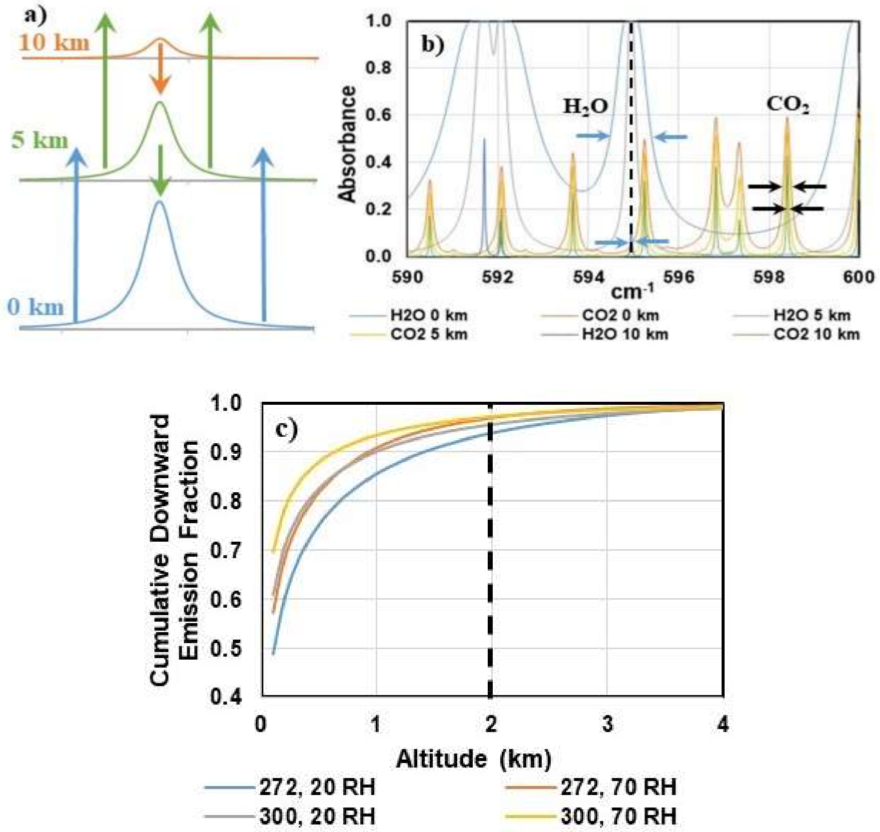

Figure 19: a) Transition from absorption-emission to free photon flux as the linewidth decreases with altitude. Single H_2O line near 231 cm^{-1}. b) Linewidths for H_2O and CO_2 lines in the 590 to 600 cm^{-1} spectral region for altitudes of 0, 5 and 10 km. c) Cumulative fraction of the downward flux at the surface vs. altitude for surface temperatures of 272 and 300 K, each with 20 and 70% relative humidity (RH). Almost all of the downward flux reaching the surface originates from within the first 2 km layer. Approximately half originates from within the first 100 m layer above the surface.

Fig. 20a illustrates the energy transfer processes for an air parcel in the troposphere (within the plane parallel atmosphere approximation). The air parcel is emitting LWIR radiation upwards and downwards at the local air temperature. It is also absorbing part of the upward LWIR flux from below and the downward LWIR flux from above. There may also be some direct heating produced by the absorption of near IR (NIR) solar radiation by the water vapor overtone bands. The air parcel is also in a turbulent convective flow field. Vertical motion changes the temperature of the air parcel at the local lapse rate. As the air parcel cools during convective ascent, internal molecular energy is converted to gravitational potential energy. Fig. 20b illustrates the dissipation of the radiative forcing in the troposphere produced by an increase in the atmospheric CO_2 concentration. The small amount of additional heat that is produced by increased absorption at each level is initially coupled to the local air parcel. It is dissipated and radiated back to space at TOA as wideband LWIR emission, mainly by the water bands.

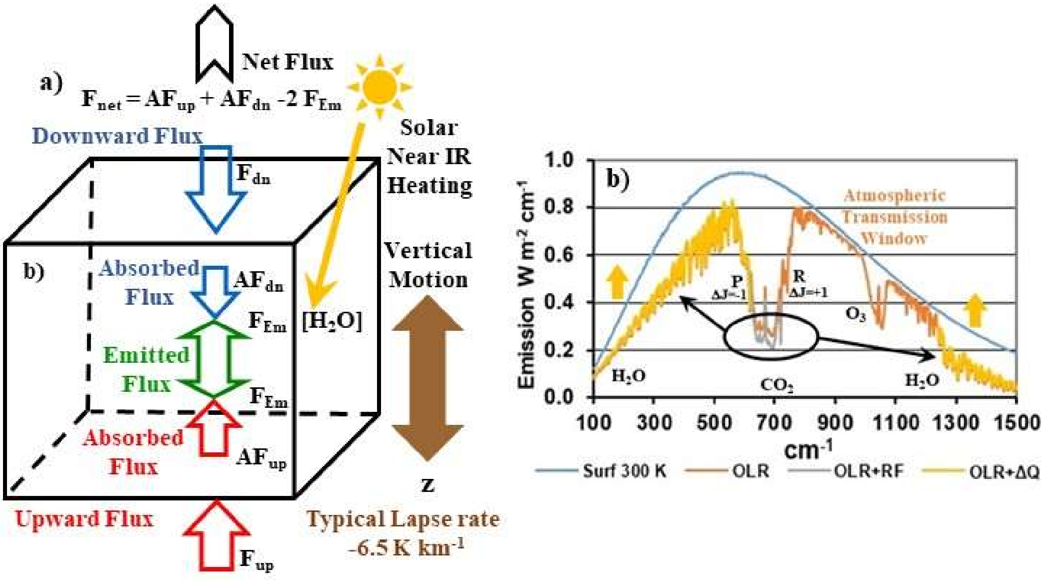

Figure 20: *a) The energy transfer processes for a local tropospheric air parcel (in a plane-parallel atmosphere) and b) the dissipation of the absorbed heat from a 'CO_2 doubling' by the normal tropospheric energy transfer processes (schematic). The wavelength specific increase in absorption in the CO_2 P and R bands is dissipated as small changes in broadband LWIR emission and gravitational potential energy.*

4.2 The LWIR Cooling Rate and the LWIR Surface Exchange Energy

When the atmospheric concentration of a greenhouse gas is increased, the decrease in LWIR flux at TOA is produced by small changes in emission at many different levels in the atmosphere. The emission from each level is modified by the absorption and emission of the levels above. In order to understand the atmospheric heating effects of a CO_2 doubling, the change in net LWIR flux has to be calculated at each level in the atmosphere and converted to a change in the rate of cooling by dividing by the heat capacity of the local air parcel. The total (10 to 3250 cm^{-1}) and spectral band average LWIR cooling rates for a tropical atmosphere are shown in Fig. 21a, Feldman et al (2008). The LWIR cooling rate for most of the troposphere at low latitudes is in the range 2 to 2.5 K per day.

The change in the rate of LWIR cooling in the atmosphere at mid latitudes produced by a doubling of the CO_2 concentration is shown in Fig. 21b, Iacono et al. (2008). In the stratosphere, there is a maximum change in the cooling rate of -3 K per day at an altitude of approximately 50 km with a pressure near 1 mbar and a temperature near 270 K. Because of the low pressure, the heat capacity of the air is also low, about 1.2 J m^{-3} K^{-1}. Therefore, the change in local net LWIR flux needed to produce a cooling rate of -3 K per day is approximately 40 μW m^{-3}. In addition, this cooling is decoupled from lower altitudes by molecular line broadening (see Fig. 19). Fig. 21c shows change in cooling rate for the troposphere on an enlarged scale. Here, the maximum change is +0.08 K per day at an altitude of 2 km. The required change in net LWIR flux is approximately 900 µW m^{-3}. At a lapse rate of -6.5 K km^{-1}, a daily change in temperature of +0.08 K requires a decrease in altitude of 12 meters. This is equivalent to riding an elevator down four floors. Similar results were obtained by Ackerman (1979), (see Fig 12).

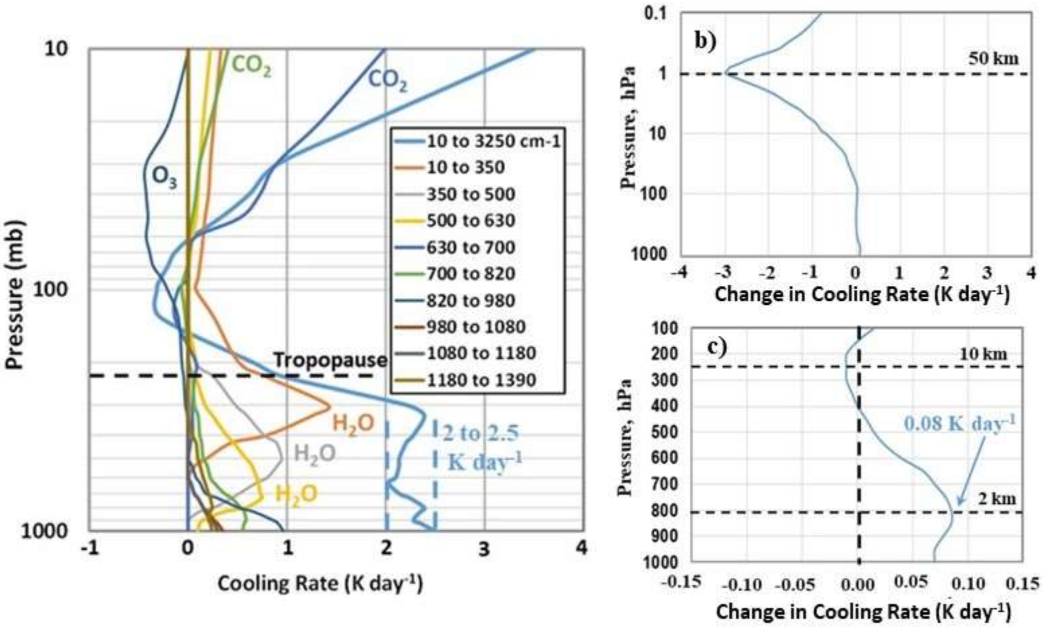

Figure 21: a) Total (10 to 3250 cm^{-1}) and band-averaged IR cooling rate profiles for the Tropical Model Atmosphere on a log-pressure scale, b) the change in atmospheric cooling rates produced by a CO_2 doubling from 287 to 574 ppm at mid latitude and c) the change in tropospheric cooling rates from b) on an enlarged scale.

Fig. 22 shows the vertical velocity profile up to 2 km altitude in the turbulent surface boundary layer. This is from Doppler heterodyne LIDAR measurements recorded over 10 hours at the École Polytechnique, south of Paris, July 10th 2005, Gibert et al (2007). The change in vertical velocity is ±2 m s^{-1}. For a vertical velocity of 1 m s^{-1} and a lapse rate of -6.5 K km^{-1}, an air parcel will cool by 6.5 K in 1000 seconds or about 17 minutes as it ascends to an altitude of 1 km. The short term cooling rate is -0.4 K per minute. This is much larger than any changes in the cooling rate produced by a CO_2 doubling as shown in Fig. 21c. Here the maximum decrease in the cooling rate is +0.08 K per day. In signal processing terms, the noise produced by the normal temperature variations in the surface boundary layer is sufficiently large that any temperature signal related to a CO_2 doubling is well below the detection limit. The increase in CO_2 concentration from 1880 to the present is near 140 ppm. In this case, the decrease in the LWIR cooling rate is near +0.04 K per day, which is also well below the detection limit.

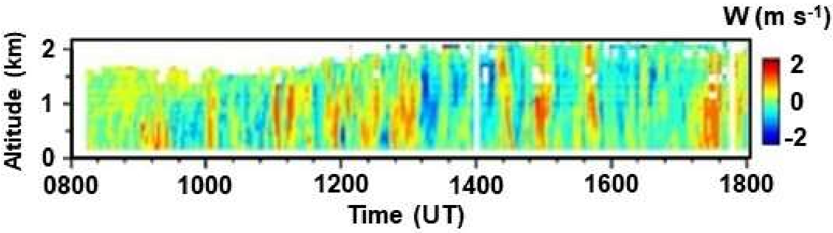

Figure 22: *Vertical velocity profile in the turbulent boundary layer recorded over 10 hours at the École Polytechnique, south of Paris, July 10th, 2005, using Doppler heterodyne LIDAR. Data adapted from Gibert (2007), fig.6.*

The basic assumption of a perturbation by a radiative forcing as introduced by Ramanathan (1975) is invalid.

> *The implications of Eq. 3 for the global climate can be examined by invoking the global energy balance condition which states that on a global average the incoming net solar radiation should be in balance with F [the net LWIR flux emitted to space]. Since the net incoming solar radiation would not change with the addition of chlorofluorocarbons, the energy balance condition implies that F has to be the same for the perturbed and the unperturbed atmosphere.* Ramamathan, 1975

He simply accepted the invalid equilibrium climate assumption and did not conduct any detailed energy transfer analysis. The heat released by the initial greenhouse gas radiative forcing or decrease in LWIR flux at TOA is radiated back to space at TOA as wideband LWIR emission (see Fig. 20b). There is no significant change to the energy balance of the earth. Any tropospheric heating effects are too small to be detected in the turbulent boundary layer near the surface. There is no accumulation of heat over time.

The downward LWIR flux from the lower troposphere to the surface establishes a partial LWIR exchange energy with the upward LWIR flux emitted by the surface. When the surface and surface air layer are at similar temperatures, within the main tropospheric absorption emission bands, IR photons are exchanged without any significant transfer of thermal energy. The net LWIR cooling flux (upward minus downward LWIR flux) at the surface is limited to the emission into the LWIR atmospheric transmission window. This net LWIR flux is insufficient to dissipate the absorbed solar insolation. The surface warms up so that the excess solar heat is removed by moist convection. This drives the tropospheric heat engine. The net cooling flux changes with temperature, humidity and cloud cover. In particular, clouds are close to blackbody emitters. The downward LWIR flux from the cloud base ‘fills in’ the atmospheric LWIR transmission window. This is illustrated in Fig. 23. When the surface is warmer than the air layer above, the excess upward LWIR flux emitted by the surface outside of the LWIR transmission window is absorbed in the lower troposphere and can increase the convection, Clark and Rörsch (2023). The ocean-air and the land-air interfaces have different energy transfer properties and have to be analyzed separately.

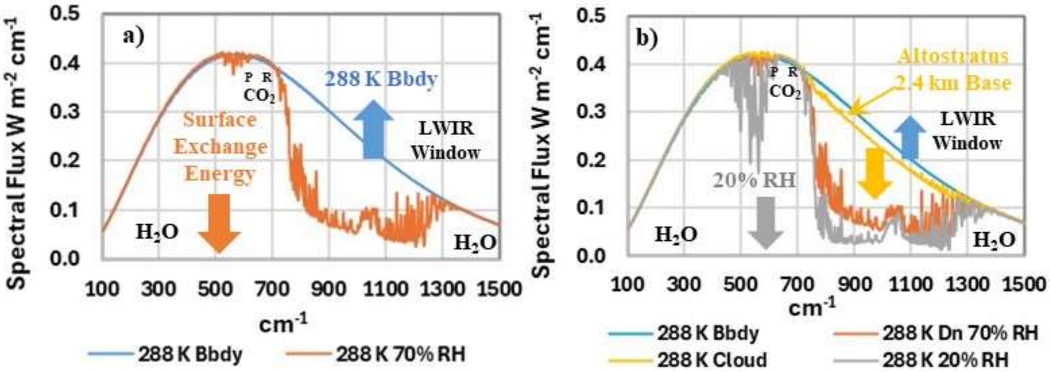

Figure 23: The surface exchange energy for surface and air temperatures of 288 K. a) Blackbody surface emission and downward LWIR flux for a relative humidity of 70% and CO_2 concentration of 400 ppm. The H_2O and CO_2 bands are indicated. b) Same as a) with the downward emission for 20% RH and for altostratus cloud cover with a 2.5 km cloud base added. MODTRAN calculations, 100 to 1500 cm^{-1} spectral range, 2 cm^{-1} spectral resolution, MODTRAN, (2024).

4.3 The Effect of an Increase in Atmospheric CO_2 Concentration on Ocean Surface Temperatures

Over the oceans, the surface is almost transparent to the solar flux. Approximately half is absorbed within the first meter layer and 90% is absorbed within the upper 10 m layer. The diurnal temperature rise is small and the bulk ocean temperature increases until the water vapor pressure is sufficient for the excess solar heat to be removed by wind driven evaporation. During the summer, at latitudes outside of the tropics, the solar heating exceeds the surface cooling. The lower sub-surface layers are not coupled to the surface by convective mixing and a stable thermal gradient is established. During the winter, the surface cooling exceeds the solar heating and the surface temperatures cool and establish a uniform temperature layer down to 100 m or lower depths. The monthly temperature profiles for 2018 from 2.5 to 200 m depth for a 5° x 1° strip (longitude x latitude) centered at 30° N, 20° W in the N. Atlantic Ocean are shown in Fig. 24, Clark and Rörsch (2023). The data are from the Argo Marine Atlas (2021). In summer, the ocean surface layers to a depth of 30 m reach a temperature of 24 °C. In winter the temperatures decrease to 19 °C to a depth of 100 m. The surface temperature phase shift or time delay between the peak solar flux and the peak ocean temperatures response is approximately 10 weeks. At 60 m depth it is 18 weeks. The phase shifts or time delays are clear evidence of a non-equilibrium thermal response, Clark (2023). At higher latitudes, the ocean temperature profiles follow a similar pattern to that shown in Fig. 24, with lower temperatures. The amount of heat stored and released over a year may easily reach 1000 MJ m^{-2} for a 1 m^2 water column extending down to 100 m depth. There is no requirement for an exact flux balance between the solar heating and surface cooling of the oceans.

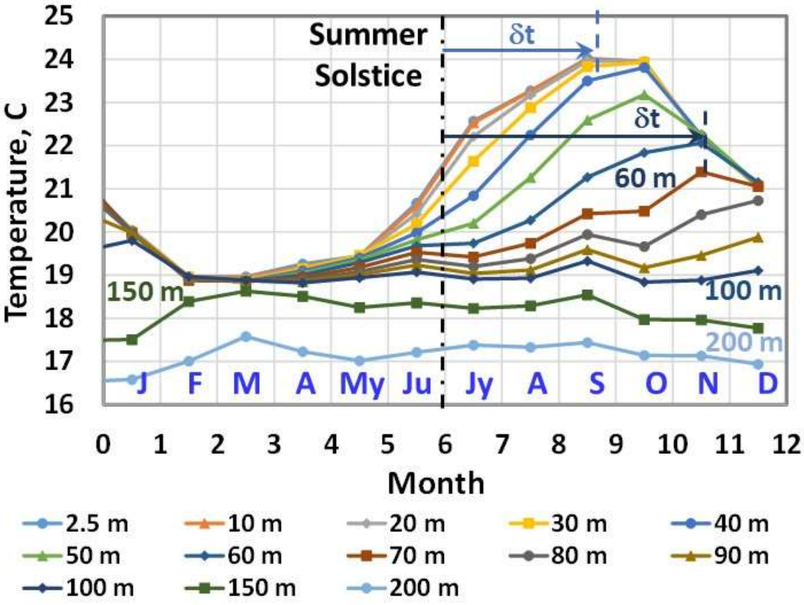

Figure 24: Monthly ocean temperatures at 30° N, 20° W and 2.5 to 200 m depth from 2018 Argo float data.

Long term (1958-2006) zonal latitude band averages of the air and surface temperatures, the latent heat and sensible heat flux, the wind speed and the absolute humidity are shown in Figs. 25a through 25f, adapted from Yu et al (2008). The penetration depth of the LWIR flux into the ocean surface is less than 100 micron (0.004 inches), Hale and Querry (1973). This is illustrated in Figure 26. The net LWIR cooling flux removes heat from this surface layer. The wind driven evaporation or latent heat flux is the removal of water molecules from the surface. The sensible heat flux is the transfer of thermal energy from the water surface to the air layer above. The cooler water produced by these three processes is mixed within a thin surface layer and then sinks. It is replaced by warmer water from below. This allows the evaporation to continue at night. The surface cooling processes are illustrated schematically in Fig. 27. There is a surface or skin layer that is cooler than the bulk ocean underneath. This establishes a thermal gradient close to the surface that enables the heat removed by the surface cooling to be replaced by thermal conduction from the warmer water layer below. The cooler skin layer has to be included in the determination of ocean surface temperatures using remote sensing techniques, Donlon et al (2002), Gentemann et al (2004).

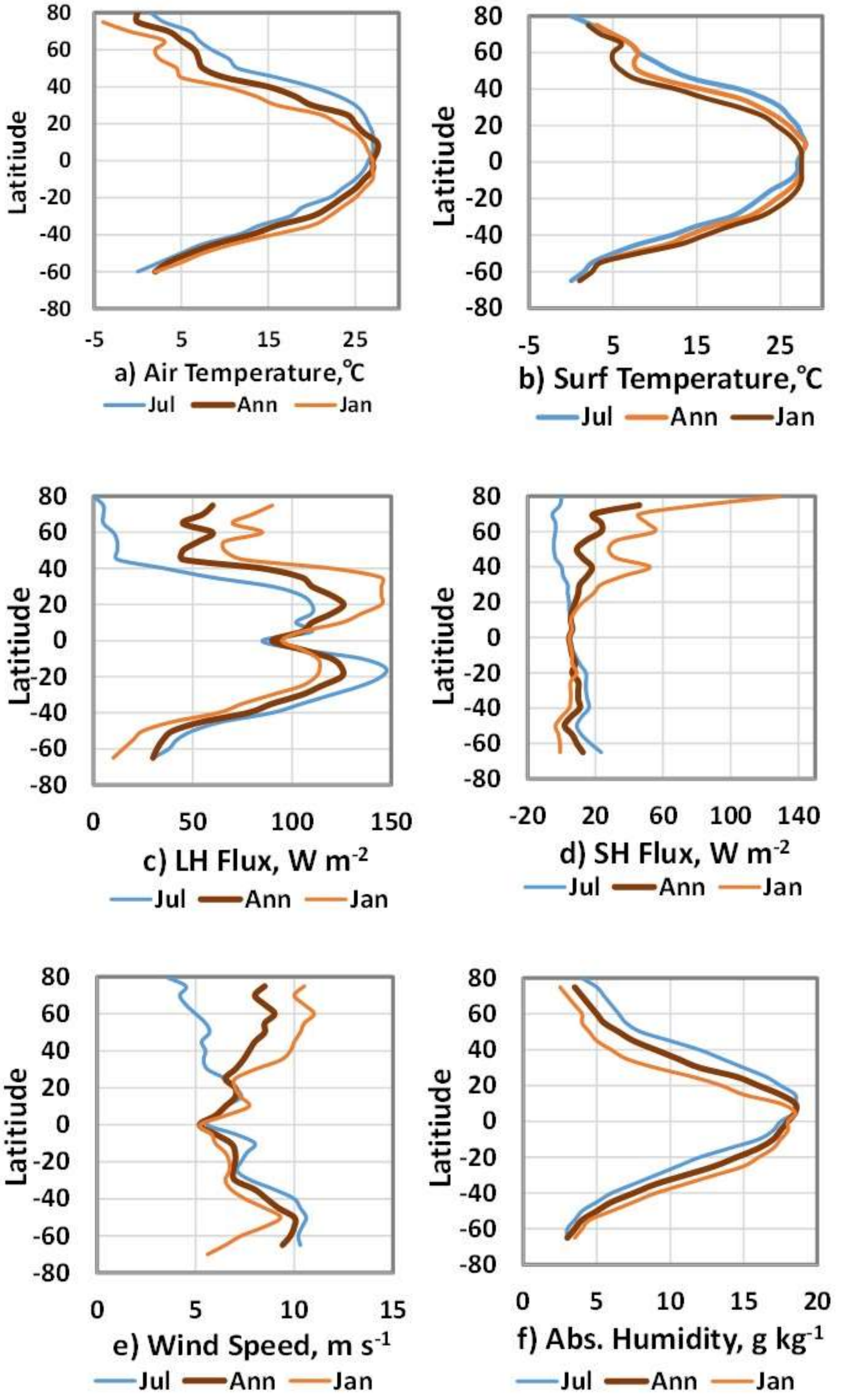

Figure 25: Long term latitude band averages of air and surface temperatures, latent heat flux, sensible heat flux, wind speed and absolute humidity. Annual averages and the values for July and January are shown. Adapted from Yu et al (2008).

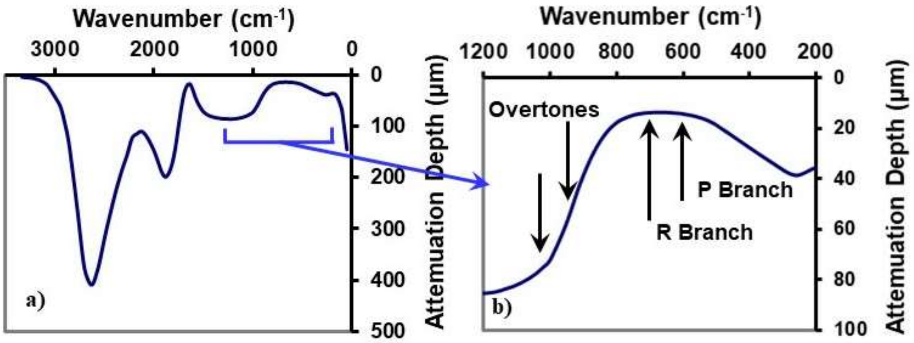

Figure 26: The penetration depth (99% absorption) of the LWIR flux into water a) below 3300 cm^{-1} and b) 1200 to 200 cm^{-1}. The locations of the main CO_2 absorption bands and the overtones are indicated.

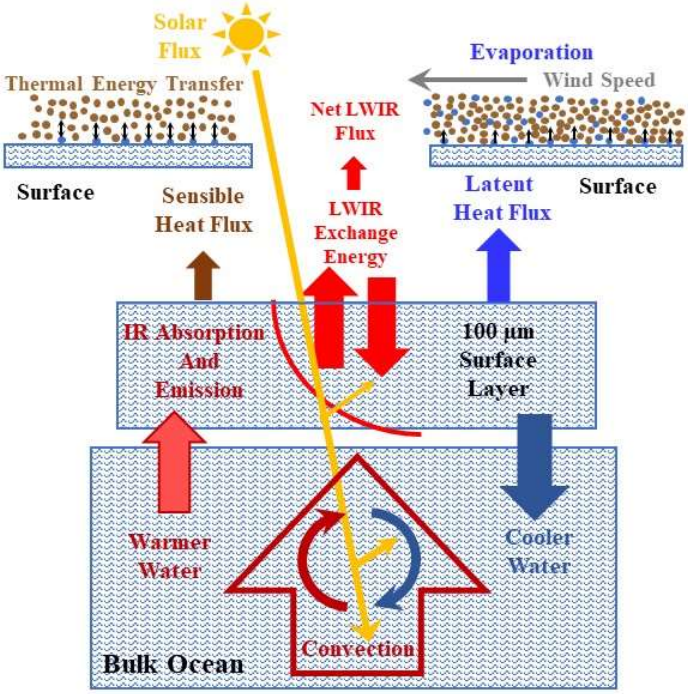

Figure 27: Ocean cooling (schematic): heat is removed from the surface by wind driven evaporation (latent heat flux) and the sensible heat flux. The net LWIR cooling flux removes heat from the first 100 micron layer. The cooler water produced by these three processes is combined in the surface layer, sinks and cools the bulk ocean below.

Ocean energy transfer involves the interaction between two very different thermal reservoirs. There is a large solar heated reservoir that may extend to over 100 m in depth. However, the initial cooling is limited to a thin surface reservoir that is less than 1 mm thick. Heat is also transported by ocean currents within the ocean gyre circulation (see Fig. 51). There are short term fluctuations in the LWIR flux and latent heat flux that do not produce a significant change in surface temperature. In signal processing terms, this is noise. There are also longer term changes in the surface cooling that produce variations in ocean surface temperature over different time scales. Increases in winter wind speed at higher latitudes enhance both the sensible and latent heat fluxes. Changes in wind speed over periods of a few years lead to quasi-periodic variations in tropical ocean temperatures including the El Niño Southern Oscillation (ENSO) and the Indian Ocean Dipole (IOD). There are also changes in wind speed over decadal time scales that are related to the AMO and the Pacific Decadal Oscillation (PDO). Ocean oscillations are considered in more detail in Sections 4.5 and 5.2.

Using the available hourly data for 2006 to 2024 from the TRITON buoy located at 170° W, 0° N (on the equator), the long term averages of the latent heat flux and the net LWIR flux are 105 ±39 W m^{-2} and 53 ±15 W m^{-2} (1σ standard deviation), TRITON (2024). There are large blocks of missing data. Approximately 40,400 hourly data points were recorded over 154,000 hours. This is a capture rate near 26%. These latent heat and LWIR fluxes give a combined surface cooling rate of 158 ±42 W m^{-2}. The main source of fluctuations or noise in the LWIR flux is the change in the downward LWIR flux produced by variations in cloud cover (see Fig. 23). For the latent heat flux, it is changes in the wind speed. Fig. 28a shows the 10 minute average RH (%) recorded for the first 6 months of 2016. Fig. 28b shows the hourly average wind speed and Fig. 28c shows the hourly average net LWIR flux and latent heat flux for the same time period.

The sensitivity of the latent heat flux to the wind speed may be estimated using the long term zonal averages of the latent heat flux and the wind speed from Figs. 25c and 25e. This is shown in Fig. 29. Within the ±30° latitude bands this sensitivity is at least 15 W m^{-2} for a change in wind speed of 1 m s^{-1}. Here, a 2 W m^{-2} decrease in net LWIR cooling flux is dissipated by an increase in wind speed near 13 m s^{-1}. For comparison, the long term 1σ variation in wind speed along the equator, recorded by the TRITON buoy network is near 2 m s^{-1}, Clark and Rörsch (2023).

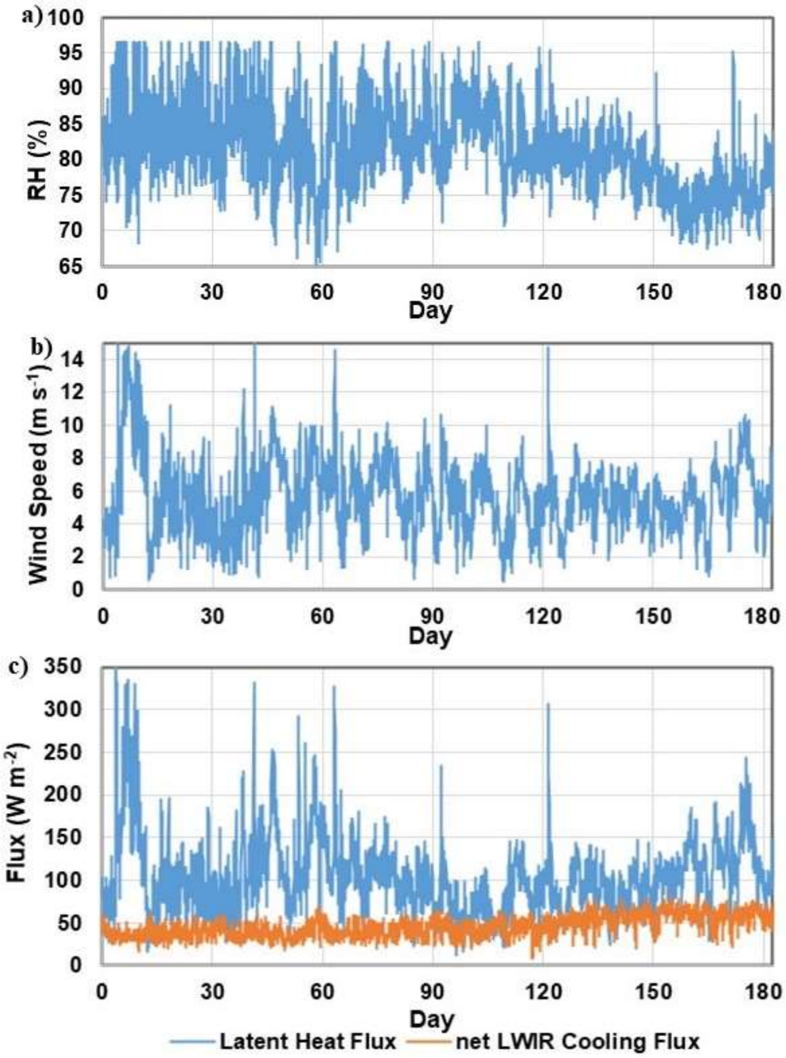

Figure 28: Short term average data recorded for the first six months of 2016 by the TRITON buoy at 170° W, 0° N (equator): a) 10-minute average relative humidity, b) 1-hour average wind speed and c) 1-hour average latent heat and net LWIR fluxes.

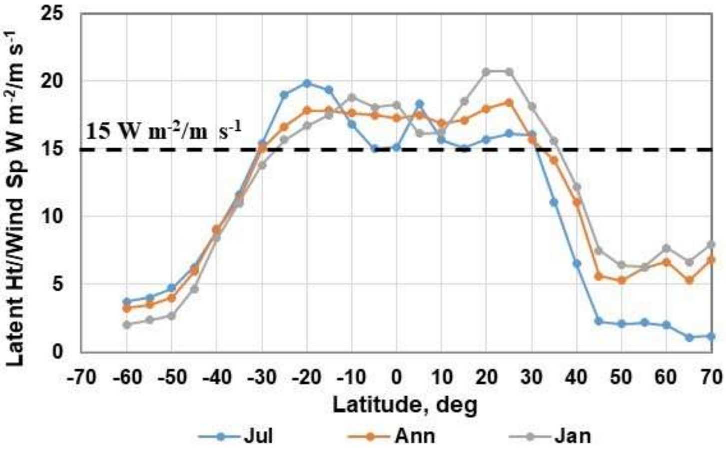

Figure 29: The sensitivity of the ocean latent heat flux to the wind speed. Based on data from Yu et al (2008).

The immediate cause of the ENSO is a change in the energy balance at the ocean surface between the solar heating and wind driven evaporation produced by a change in wind speed. The 2016 ENSO peak was produced by a decrease in wind speed of approximately 2 m s^{-1} over a period of 6 months. The corresponding decrease in latent heat flux was near 30 W m^{-2} and the temperature increase of 2.5 °C extended to a depth of at least 75 m. The related increase in ocean heat content was approximately 800 MJ m^{-2} for a 1 x 1 x 75 m water column. Over a six month period, the cumulative increase in downward LWIR flux to the surface produced by the increase in CO_2 concentration was near 0.26 MJ m^{-2}. The change in ocean heat content was approximately 3000 times larger than the cumulative increase in the downward LWIR flux from CO_2 (see Section 5.2 for further details).

Over large areas of the oceans, the sensible heat flux is less than 10 W m^{-2}. However, there is a significant increase in winter sensible heat flux at higher N. latitudes as shown in Fig. 25d. This is produced by an increase in winter wind speed as shown in Fig. 25e. The latent heat flux also increases. Part of the increase in winter cooling flux is produced by seasonal storms that increase the cold air flow from N. America across the warm water flow associated with the Gulf Stream. Within the area bounded by 30° to 42° N and 70° to 50° W, the long term (1947-2007) daily average sensible and latent heat fluxes are shown in Fig. 30, adapted from Shaman et al (2010). The summer to winter increases in the sensible and latent heat fluxes are 70 and 140 W m^{-2}.

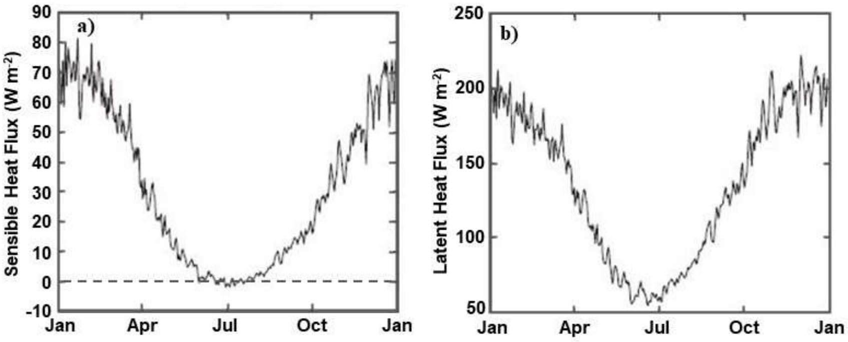

Figure 30: Long term (1947-2007) daily average sensible heat flux (a) and latent heat flux (b) for the area bounded by 30° to 42° N and 70° to 50° W that includes part of the Gulf stream off the coast of N. America.

The variation in the annual mean evaporation rate for the global ice free oceans from 1958 to 2005 is shown in Fig. 31, adapted from Yu, (2007). There was an increase in evaporation rate of 11 cm per year from 103 cm per year in 1977 to a peak of 114 cm per year in 2003. This is an increase in average latent heat flux of approximately 8.5 W m^{-2}. For reference, a latent heat flux of 2 W m^{-2} corresponds to an evaporation rate of 2.6 cm year^{-1}. The increase in evaporation is attributed to an increase in winter wind speed in both hemispheres.

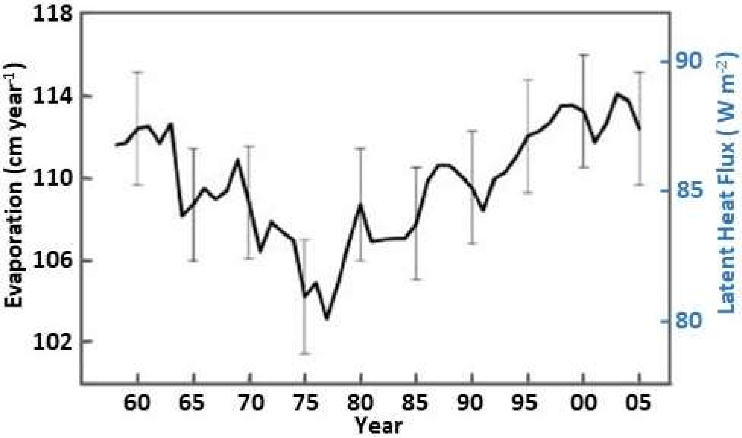

Figure 31: Average change in the global evaporation rate from 1958 to 2005. The corresponding changes in the average latent heat flux are also indicated.

The IPCC assumes that the surface responds to greenhouse gas radiative forcing with an increase in surface temperature that is amplified by a water vapor feedback, Knutti and Hegerl (2008). However, the quantitative details of the ocean surface energy transfer related to this process have not been considered. As shown above in Fig. 18b, the observed increase in the atmospheric CO_2 concentration of 140 ppm since 1800 has produced an increase in the downward LWIR flux to the surface of approximately 2 W m^{-2}. This is coupled to the surface thermal reservoir where it reduces the net LWIR cooling flux. However, the increase of 2 W m^{-2} has occurred gradually over time. At present, the average annual increase in downward LWIR flux is approximately 0.034 W m^{-2} or 34 milliwatts m^{-2} per year.

The net LWIR cooling flux, Q_{irnet}, can be simplified for discussion purposes by using Stefan's Law modified with a variable atmospheric spectral window:

$$Q_{irnet} = \sigma(\varepsilon T_s^4 - T_a^4) + Q_{winRH} - Q_{wincld} \tag{2}$$

Here, σ is Stefan's constant, ε is the surface emissivity, T_s is the surface temperature, T_a is the surface air temperature (both in Kelvin), ΔQ_{winRH} is the humidity dependent LWIR cooling flux and Q_{wincld} is the downward LWIR flux from clouds (see Fig. 23b).

The latent heat flux, Q_{lh}, is given by:

$$Q_{lh} = k_{lat}(P_{Tws} - R_h P_{Twa})U \tag{3}$$

Here, k_{lat} is an empirical constant, P_{Tws} is the saturated water vapor concentration at the surface temperature T_s, P_{Twa} is the saturated water vapor concentration at the surface air temperature T_a, R_h is the relative humidity and U is the wind speed, Clark and Rörsch (2023).

The increase in surface temperature needed to produce an increase in cooling flux of 2 W m^{-2} may be evaluated by combining equations (2) and (3). Setting $\varepsilon = 0.95$, $Q_{winRH} = 45$ W m^{-2}, $Q_{wincld} = 0$, $k_{lat} = 3$, RH = 80%, U = 6 m s^{-1}, with $T_a = T_s - 1$, gives:

$$Q_{irnet} + Q_{lh} = \sigma(0.95{*}T_s^4 - (T_s-1)^4) + 45 + k_{lat}(P_{Tws} - 0.8{*}P_{Twa}){*}6 \tag{4}$$

The water vapor pressure is calculated using a polynomial fit to the temperature. The increase in T_s is calculated using the 'goal seek' algorithm in Excel. The air temperature is not changed and only T_s is increased in the calculation. At 30 °C, (4) gives a value of 108 W m^{-2} for the latent heat flux. This is similar to the values of the latent heat flux at ±10° latitude in Fig. 25c.

Fig. 32a shows the increase in temperature needed to increase the cooling flux by 2 W m^{-2} for ocean surface temperatures from 0 to 34 °C. The blue line shows the temperature rise needed to increase just the LWIR surface emission by 2 W m^{-2} without any coupling to the latent heat flux. The orange line shows the temperature rise needed for the combined LWIR and latent heat flux. At a surface temperature of 0 °C, the increase is 0.45 °C for the LWIR flux and 0.19 °C for the combined flux. These values decrease to 0.33 °C and 0.06 °C at a surface temperature of 30 °C. Fig 32b shows the separate contributions of the LWIR and the latent heat fluxes to the 2 W m^{-2} increase in cooling flux vs. ocean surface temperature. As the temperature increases from 0 to 30 °C the latent heat fraction increases from 58% to 83%.

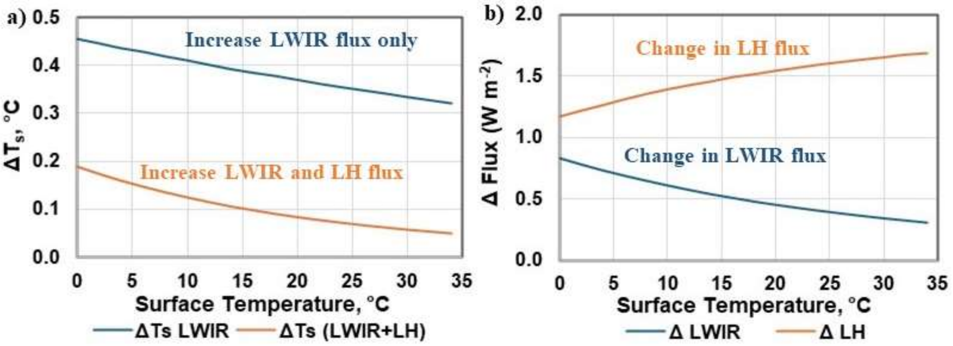

Figure 32: a) The increase in surface temperature needed to increase the LWIR flux (blue line) and the LWIR + latent heat flux (orange line) by 2 W m^{-2} as the surface temperature is increased from 0 to 34 °C. b) The separate contributions of the latent heat flux and LWIR flux to the 2 W m^{-2} total cooling flux increase vs. increase in ocean surface temperature.

This simple analysis indicates that the inclusion of the latent heat flux in the surface energy transfer produces a negative feedback. This was discussed by Harde (2017; 2014) as evaporation feedback. Part of the increase in downward LWIR flux to the surface is converted to latent heat. The additional evaporation increases the surface humidity gradient. The water molecules removed from the surface are entrained in the air flow and removed as moist convection. There is no amplification of the surface temperature by an increase in water vapor concentration in the air layer above the surface. These effects are also small compared to both the short term and longer term variations in the surface cooling flux. The IPCC assumptions that a greenhouse gas radiative forcing increases the surface temperature and that this is then amplified by a water vapor feedback require further evaluation.

4.4 The Effect of an Increase in Atmospheric CO_2 Concentration on Land Surface Temperatures

Over land, all of the flux terms are absorbed by a thin surface layer. The surface temperature initially increases after sunrise as the solar flux is absorbed. This establishes a thermal gradient with both the cooler air above and the subsurface ground layers below. The surface-air gradient drives the evapotranspiration (moist convection) and the subsurface gradient conducts heat below the surface during the first part of the day after sunrise. Later in the day, as the surface cools, the subsurface gradient reverses and the stored heat is returned to the surface. As the land and air temperatures equalize in the evening, the convection stops and the surface cools more slowly by net LWIR emission. This convection transition temperature is reset each day by the local weather system passing through. Almost all of the absorbed solar heat is dissipated within the same diurnal cycle. The heat transfer is localized. The diurnal temperature change is limited to a shallow depth, typically 0.5 to 2 m, and the seasonal temperature variations may extend to 5 m below the surface, Clark and Rörsch (2023). There are also characteristic phase shifts or time delays between the peak solar flux and the temperature response. This is not a recent discovery. The subsurface seasonal phase shift was described by Fourier (1824). Further details are given by Clark (2023). The soil temperatures at depths from 0.5 to 80 cm and the 2 m air temperature recorded at a monitoring site at O'Neill, Neb., August 13, 1953 are shown in Fig. 33, Letteau and Davidson (1957). The surface temperature phase shift, δt, and the convection transition temperature are indicated. Below the surface, the temperature rise decreases and the phase shift increases with the depth. At the surface, the temperature rise is 22 °C. The surface air temperature increase at 1.5 m above the surface is 15 °C. There is almost no measurable diurnal phase shift below 50 cm depth.

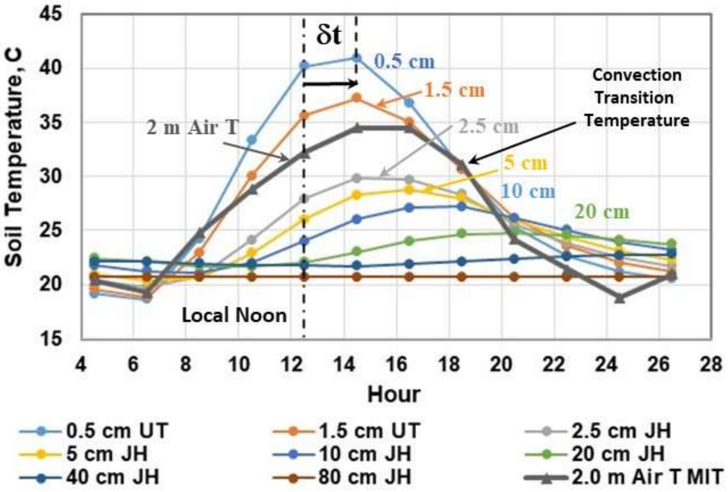

Figure 33: 2 m air temperature and subsurface temperatures recorded at O'Neill, Nebraska, August 13-14, 1953.

As shown above in Fig. 19c, almost all of the downward LWIR flux to the surface is emitted within the first 2 km layer of the troposphere and approximately half of this comes from within the first 100 m layer. Near the surface, both the relative and absolute humidity can change during the diurnal cycle. Figs. 34a and 34b show the relative and absolute humidity changes recorded at the O'Neill, Nebraska test site during the second observational period, August 13 to 14, 1953 related to the temperature changes shown in Fig. 33. The RH decreased from approximately 65% at 06:30 to 35% at 16:30 and then increased to approximately 70% by 02:30 the following morning. The absolute humidity increased from about 14 mbar at 02:30 to 20 mbar at 12:30 and decreased back to near 15 mbar by 00:30 the following morning. This is caused by evaporation from the warm surface during the day.

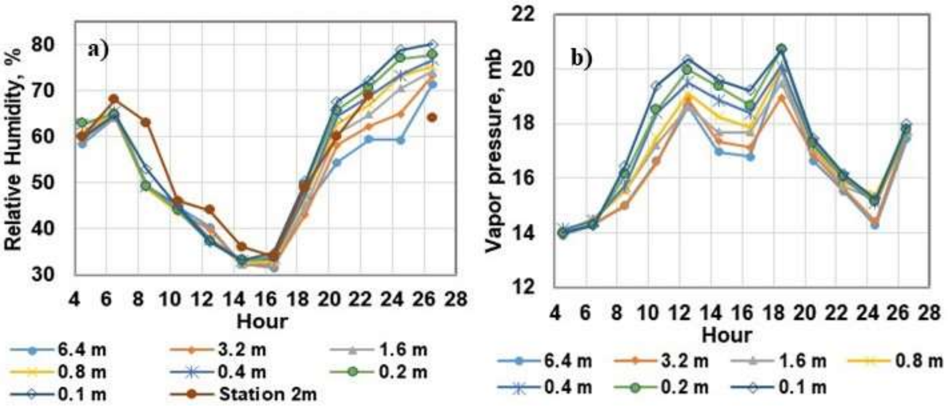

Figure 34: a) Relative humidity, % and b) absolute humidity, mbar recorded at O'Neill, Nebraska, August 13 - 14, 1953.

The fixed RH assumption also ignores the interactive coupling of the solar flux to the latent heat flux. Fig. 35 shows the total daytime and night time latent heat fluxes (MJ m^{-2} day^{-1}) recorded during the year 2008 at the Grasslands Ameriflux monitoring site located in Limestone Regional Park near Irvine, S. California. Almost all of the latent heat flux is produced during the day as the sun warms the vegetation and the surface. The peak latent heat flux occurs in March as the vegetation dries out after the winter rains. A total daytime flux of 6 MJ m^{-2} day^{-1} corresponds to an evaporation rate of approximately 140 W m^{-2}. In this region there is also a well-known transition from onshore to offshore flow. The onshore flow from the ocean brings lower temperatures and higher humidity. The offshore flow from the desert plateau produces higher temperatures and lower humidity. Fig. 36a shows the RH (%) and Fig. 36b shows the air temperature recorded over the year at half hour intervals. Some of the temperature spikes and low humidity related to the offshore flow are indicared by the dotted lines. Further details are provided by Clark and Rörsch (2023).

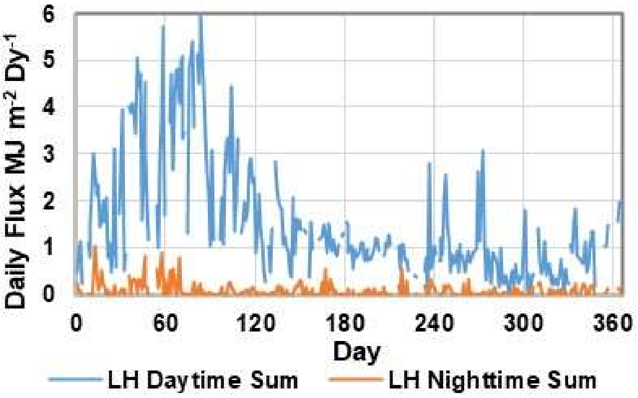

Figure 35: Total daytime and nighttime latent heat fluxes recorded at the Grasslands Ameriflux monitoring site near Irvine, CA during 2008.

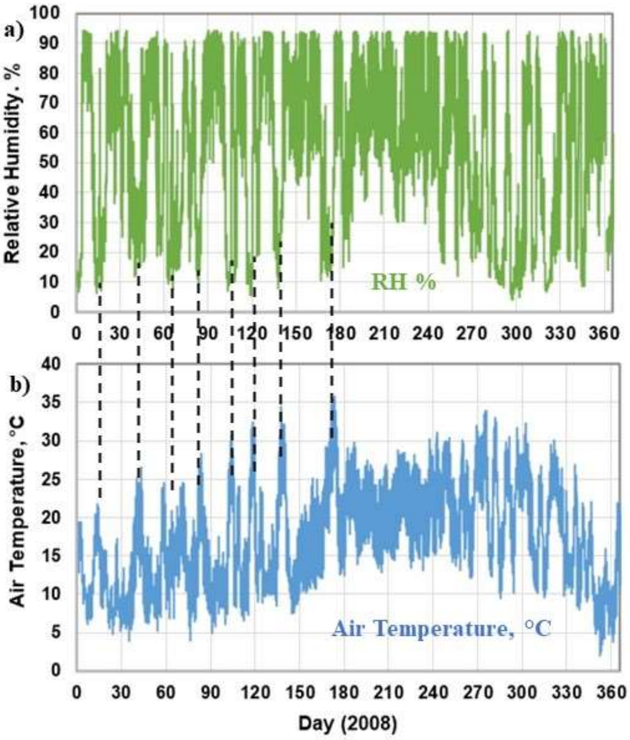

Figure 36: a) Half hour RH (%) and b) air temperature (°C) data recorded at the Grasslands site during 2008. Some of the temperature spikes and low himidity periods related to offshore flow are indicated with the dotted lines.

As discussed above in relation to Fig. 18, the average annual increase in the downward LWIR CO_2 flux from the lower troposphere to the surface is presently near 0.034 W m^{-2} yr^{-1}. This can have no measurable effect on the humidity in the surface boundary layer. The assumption of a fixed RH distribution used by M&W is not valid near the surface. Part of the absorbed solar flux can also be converted into latent heat flux. The diurnal and seasonal variations in the latent heat flux near the surface have been ignored. This contradicts the fixed RH distribution assumption used in MW67 that created the water vapor feedback.

The various flux terms interact with the surface and change the temperature at the land-air interface. However, the weather station temperature is the meteorological surface air temperature (MSAT) measured in a ventilated enclosure located at eye level, 1.5 to 2 m above the ground, Oke (2006). In general, the minimum MSAT and the minimum surface temperature are similar, but the maximum surface temperature is larger than the maximum MSAT, Clark and Rörsch (2023). The minimum and maximum temperatures are determined by different energy transfer processes. The minimum temperature is reset each day by the bulk surface air temperature of the local weather system passing through. The maximum surface temperature is set by the balance between the solar heating, the combined net LWIR flux and evapotranspiration (moist convection) and the subsurface thermal transport. The maximum MSAT is determined by the mixing of the warm air rising from the surface with the cooler air at the level of the MSAT thermometer. The important physical variables in the weather station temperature data are therefore the minimum MSAT and the delta T or difference between the maximum and minimum MSAT. The average MSAT, $(T_{max} + T_{min})/2$, has little useful meaning.

Starting in the early 1980s, the traditional white painted wooden Stevenson screen weather station enclosure fitted with Six's min/max thermometer was replaced by a smaller 'beehive' structure with an electronic thermometer, Quayle et al (1991). Since this has a faster response time, it is susceptible to short temperature transients that may bias the readings if the electronic signal is not averaged to simulate the thermal response time of six's thermometer, Hansen (2024). This may contribute to an observed warming in the weather station record.

To illustrate the normal variation in the MSAT record, the 1981 to 2010 thirty year daily climate averages for the O'Neill, Neb. weather station #256290 are shown in Fig. 37, WRCC (2022). The 1σ standard deviations and the ΔT $(T_{max} - T_{min})$ values are also shown. There is a phase shift of approximately 30 days between the peak solar flux at summer solstice, day 172 and the peak seasonal temperature response. In addition, the ΔT values remain within the approximate range 13.4 ±2 °C for the entire year while the temperature variation is ±10 °C. The 1σ temperature standard deviations increase from approximately 4 °C in summer to 8 °C in winter.

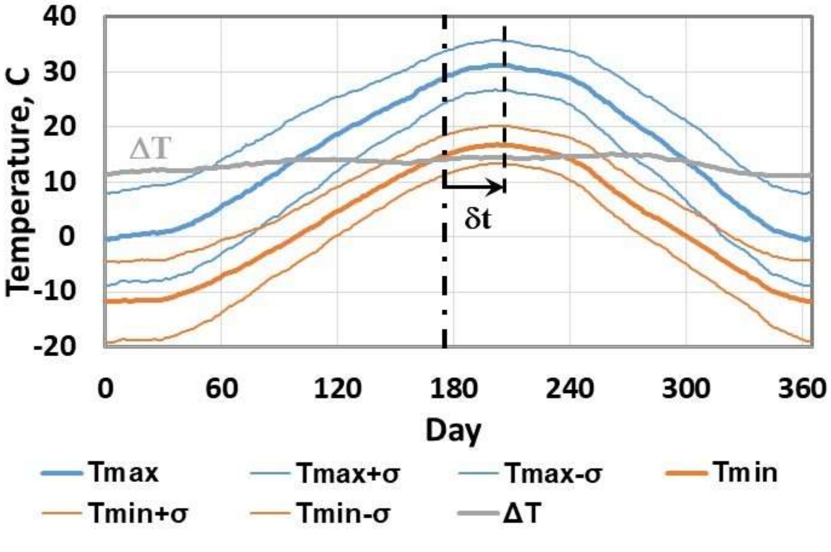

Figure 37: *1981-2010 daily climate averages for O'Neill, Neb., Station #256290. The 1σ standard deviations and the* ΔT $(T_{max} - T_{min})$ *are also shown. The seasonal phase shift, δt is indicated.*

A simple thermal engineering model of the surface and air temperatures recorded in 2008 at the Grasslands site was used to evaluate the effect of an increase in CO_2 concentration on land temperatures (Clark and Rörsch 2023; Clark, 2013a; 2013b). In this case, for a doubling of the CO_2

concentration from 280 to 560 ppm, the increase in MSAT was approximately 0.1 °C. This is too small to measure in the normal day to day variations in the convection transition temperature. In addition, the diurnal and seasonal phase shifts demonstrate that the surface thermal reservoir is not in thermal equilibrium, Clark (2023).

4.5 The Coupling of Ocean Surface Temperatures to the Weather Station Record.

Akasofu (2010) explained the global temperature record as a linear recovery from the LIA with multidecadal temperature oscillations superimposed as shown in Fig. 38. He used a wide range of proxy data in his analysis including ice core data, river freeze/breakup dates, sea level changes, sea ice changes, glacier changes, tree ring data and cosmic ray intensity data. He also proposed that the IPCC projections of climate warming attributed to greenhouse gas radiative forcings are an extrapolation of the latest warming phase of the multidecadal oscillation.

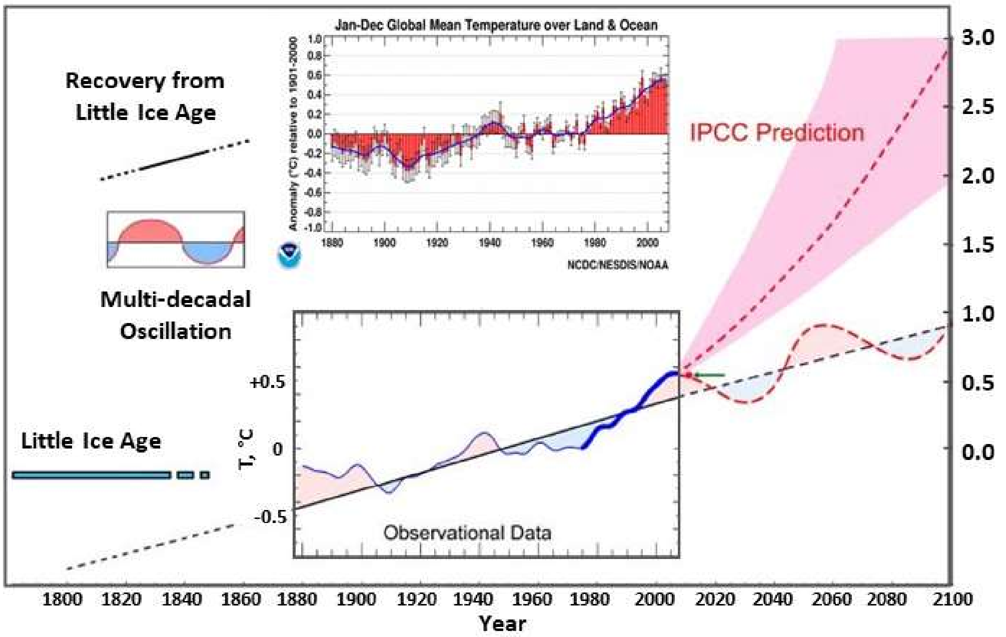

Figure 9. The figure shows that the linear trend between 1880 and 2000 is a continuation of the recovery from the LIA, together with the superimposed multi-decadal oscillation. It also shows the predicted temperature rise by the IPCC after 2000. It is assumed that the recovery from the LIA would continue to 2100, together with the superimposed multi-decadal oscillation. This view could explain the halting of the warming after 2000. The observed temperature in 2008 is shown by a red dot with a green arrow. It has been suggested by the IPCC that the thick blue lime portion was caused mostly by the greenhouse effect, so their future projection is a sort of extension of the blue line.

Figure 38: *The linear temperature recovery from the LIA with multi-decadal oscillations superimposed. Adapted from Akasofu (2010).*

When the climate temperature anomaly record, such as the HadCRUT4 data set is evaluated, the dominant term is found to be the AMO (HadCrut4, 2022; Morice et al, 2012). This is illustrated in Fig. 39a. The AMO is a long term quasi-periodic oscillation in the surface temperature of the N. Atlantic Ocean from 0° to 60° N, AMO (2022). Superimposed on the oscillation is a linear increase in temperature. This is the recovery from the LIA described by Akasofu (2010). The linear equation for the slope and the least squares fit to the oscillation are shown in Fig. 39a. Before 1970, the AMO and HadCRUT4 track quite closely. This includes both the long period oscillation and the short term fluctuations. There is an offset that starts near 1970 with HadCRUT4 approximately 0.3 °C higher than the AMO. The short term fluctuations are still similar. The correlation coefficient between the two data sets is 0.8. The influence of the AMO extends over large areas of N. America, Western Europe and parts of Africa. The weather systems that form over the oceans and move overland couple the ocean surface temperature to the weather station data through the diurnal convection transition temperature, Clark and Rorsch (2023). The contributions of the other ocean oscillations to the global temperature anomaly are smaller. The IOD and the PDO are dipoles that tend to cancel and the ENSO is limited to a relatively small area of the tropical Pacific Ocean. However, small surface temperature variations in the tropical oceans have a major impact on ocean evaporation and rainfall. Fig. 39b shows a tree ring construction of the AMO from 1567 (Gray et al, 2004a; 2004b). The modern instrument record is also indicated in green.

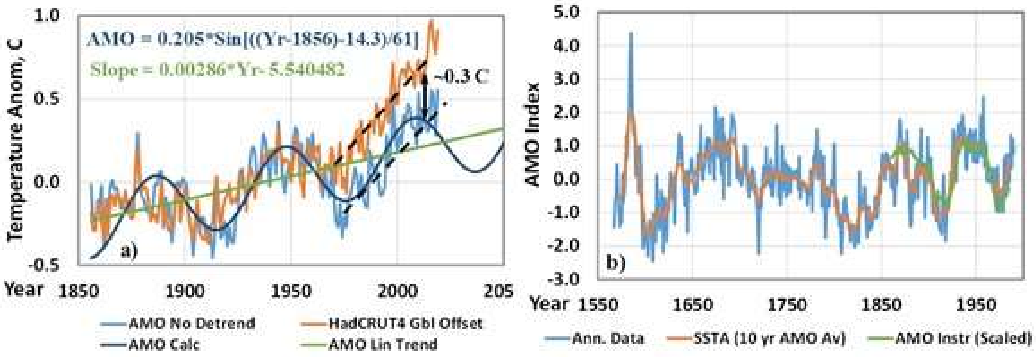

Figure 39: a) Plots of the HadCRUT4 and AMO temperature anomalies overlapped to show the similarities. Both the long term 60 year oscillation and the shorter term 'fingerprint' details can be seen in both plots. The role of 'adjustments' in the 0.3 °C offset since 1970 requires further investigation. b) Tree ring reconstruction of the AMO from 1567.

There is still an additional part of the recent HadCRUT4 warming that is not included in the AMO signal. This may be explained as a combination of three factors. First there are urban heat islands related to population growth that were not part of the earlier record. Second, the mix of urban and rural weather stations used to create the global record has changed. Third, there are so called 'homogenization' adjustments that have been made to the raw temperature data. These include the 'infilling' of missing data and adjustments to correct for 'bias' related to changes in weather station location and instrumentation. It has been estimated that half of the warming in the global record has been created by such adjustments. This has been considered in more detail for example by Andrews (2001a; 2017b; and 2017c), D'Aleo and Watts (2010), Berger and Sherrington (2022) and O'Neill et al (2022). The effect of the changes to the urban/rural weather station mix, adapted from D'Aleo and Watts (2010) is shown in Fig. 40.

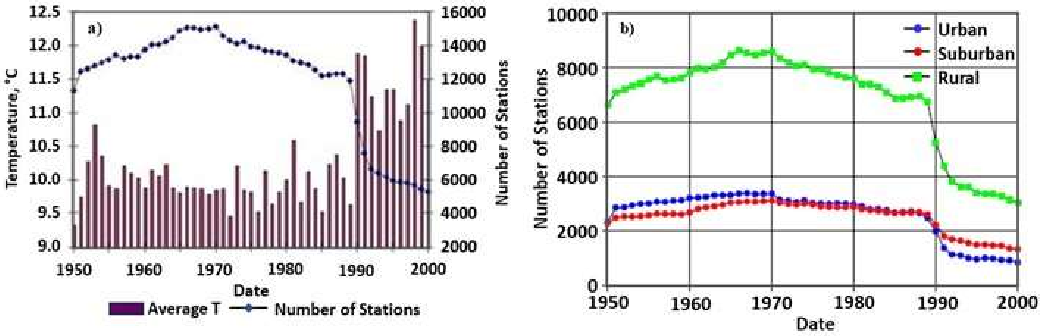

Figure 40: a) Changes in the number of stations used in the global average from 1950 to 2000 and the average temperatures. b) Changes in the number of stations by category from 1950 to 2000.

The role of the AMO in setting the surface air temperature has been misunderstood or ignored for a long time. The first person to claim a measurable warming from an increase in CO_2 concentration was Callendar (1938). The warming that he observed was from the 1910 to 1940 warming phase of the AMO and not from CO_2. During the 1970s there was a global cooling scare that was based on the cooling phase of the AMO from 1940 to 1970 (McFarlane, 2018; Peterson et al, 2008; Bryson and Dittberner, 1976). In H81, Hansen et al overlooked the 1940 AMO peak in their analysis of the effects of CO_2 on the weather station record (see Fig. 10e). Similarly, Jones et al overlooked the 1940 AMO peak when they started to ramp up the modern global warming claims (Jones et al, 1986; 1988). The IPCC also ignored the AMO peak in its First Assessment Report (FAR WG1 fig. 11 SPM p. 29, IPCC 1990) and it has continued to ignore it as shown in the recent Sixth Assessment Report (AR6 WG1 TS CS Box 1 fig. 1c p. 61, IPCC 2021). This is illustrated in Fig. 41. The AMO and the periods of record used are shown in Figure 41a. The temperature records used by Callendar, Douglas, Jones et al, Hansen et al and IPCC 1990 and 2021 are shown in Figs. 41b through 41g. The increase in atmospheric CO_2 concentration is also shown in Figs. 41d through 41g (Keeling, 2023).

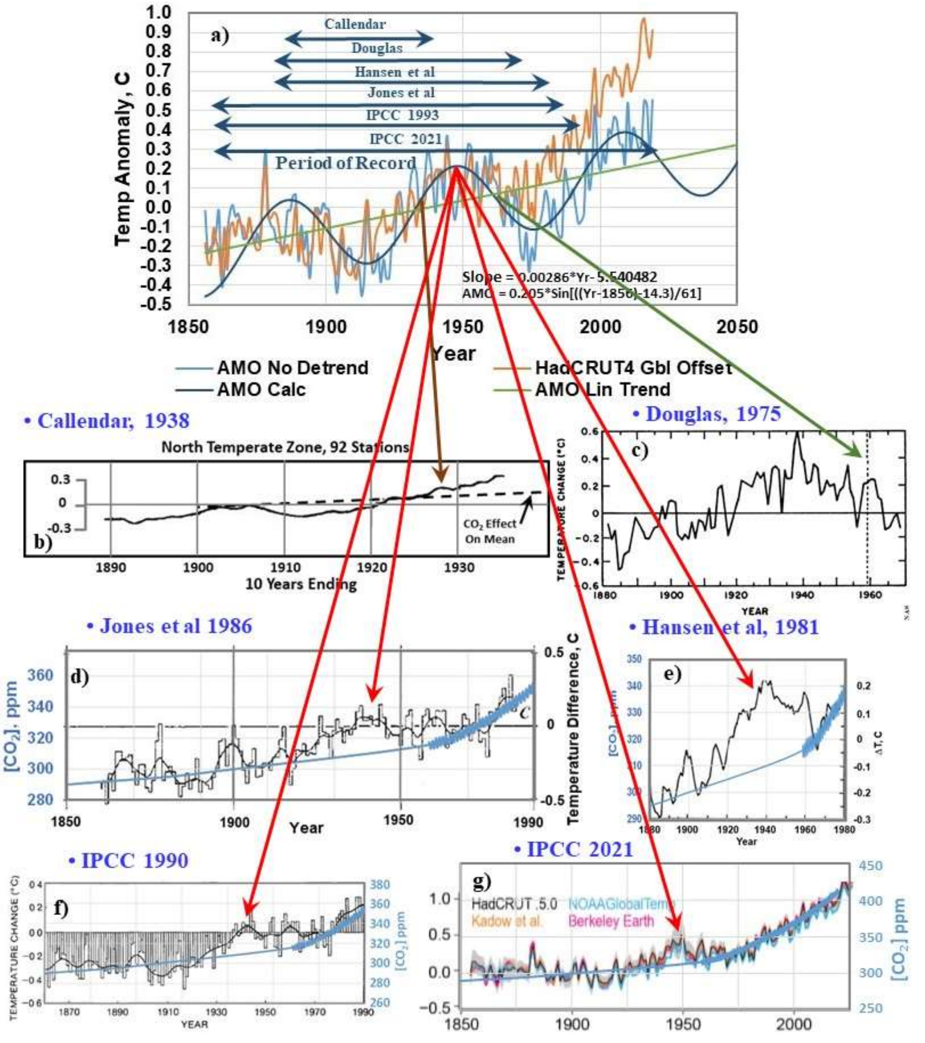

Figure 41: *a) AMO anomaly and HadCRUT4 global temperature anomaly, aligned from 1860 to 1970, b) temperature anomaly for N. temperate stations from Callendar (1938), c) global cooling from Douglas (1975), d) global temperature anomaly from Jones et al, (1986) e) global temperature anomaly from Hansen et al, (1981), f) and g) global temperature anomalies from IPCC (1990) and IPCC (2021). The changes in CO_2 concentration (Keeling curve) are also shown in d) through g). The periods of record for the weather station data are also indicated in a).*

The large scale climate models are simply tuned to match the global mean temperature anomaly. There are two different ways that the climate sensitivity is determined. First, the CO_2 concentration is simply doubled and the model is run to equilibrium or steady state. This is called the equilibrium climate sensitivity (ECS). Second, the CO_2 concentration is increased gradually, usually by 1% per year. The temperature change at the CO_2 doubling point is called the transient climate response (TCR).

In order to validate the climate models, a similar exercise is applied in reverse to the measured global mean temperature record. This may be illustrated by considering the work of Otto et al, (2013). They defined the climate sensitivities as:

$$\mathrm{ECS} = F_{2x}\Delta T/(\Delta F - \Delta Q) \qquad (5a)$$

$$\mathrm{TCR} = F_{2x}\Delta T/\Delta F \qquad (5b)$$

Here, F_{2x} is the radiative forcing produced a doubling of the atmospheric CO_2 concentration, set in this case to 3.44 W m^{-2} for a doubling from 'preindustrial levels', 280 to 560 ppm, ΔF is the change in radiative forcing (W m^{-2}), ΔT (°C) is the change in global mean temperature and ΔQ is the change in the earth system heat content, also given in W m^{-2}. The change in temperature is taken from the HadCRUT4 global temperature anomaly and the radiative forcings are taken from the CMIP5/RCP4.5 model ensemble. The change in heat content is dominated by ocean heat uptake. The decadal temperature and forcing estimates from data given by Otto et al are shown in Figs. 42a and 42b. The 1910 AMO cycle minimum and the 1940 maximum are indicated. As discussed above in Section 4.3, the increase in the downward LWIR flux related to the radiative forcing shown in Fig. 42b is coupled to the ocean surface layer and does not have any measurable effect on the bulk ocean temperature below. Using the data from Figs. 34a and 34b combined with estimates of ΔQ from various sources, Otto et al assume that their net radiative forcing estimates are responsible for the observed heating effects and that the temperature response to the change in LWIR flux is linear. Plots of ΔT vs (ΔF-ΔQ) and ΔT vs ΔF are therefore presumed to be linear with a slope that changes with the value of ECS or TCR. The results generated by Otto et al are shown in Figs. 42c and 42d. Using the data for 2000 to 2010, they create an ECS of 2.0 °C with a 5-95% confidence interval of 1.2 to 3.9 °C and a TCS of 1.3 °C with a confidence level of 0.9 to 2.0 °C.

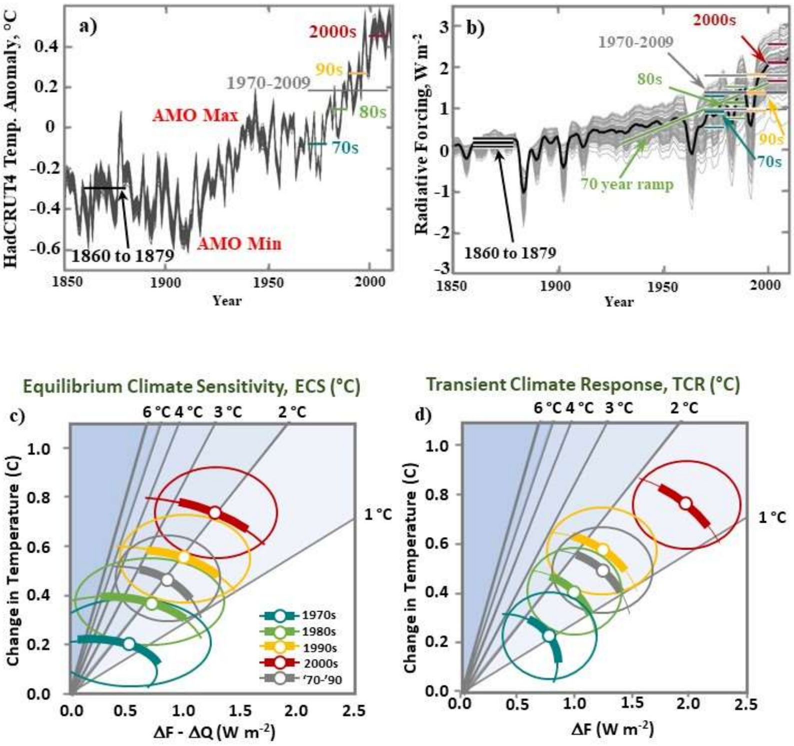

Figure 42: a) Decadal mean temperature estimates derived from the HadCRUT4 global mean temperature series. b) Decadal mean forcing with standard errors from the CMIP5 /RCP4.5 ensemble. c) Estimates of ECS and d) estimates of TCR. Data from Otto et al (2013).

4.6 Air Compression: The Neglected Heat Source

One of the more egregious applications of the equilibrium climate models has been the 'attribution' of 'extreme' natural weather events to increased CO_2 levels in the atmosphere. This is discussed above in Section 3.5. At present, the annual average increase in the atmospheric concentration of CO_2 is near 2.4 ppm per year. The corresponding annual increase in downward LWIR flux from the lower troposphere to the surface is 0.034 W m^{-2}. This can have no effect on such 'extreme' weather events. One of the main climate modeling errors has been the neglect of the heating produced by air compression. As dry air descends to lower altitudes, the lapse rate is +9.8 K km^{-1}. There are two different energy transfer processes that have to be considered. The first is heating by downslope winds and the second is the heating produced by the downward flow of air circulating within a high pressure system. These processes can produce temperature changes of 10 °C or more over a few days or less.

Downslope winds are well known in many regions of the world and there are many different names for the same effect. In S. California they are Santa Ana Winds. In N. California they are diablo winds. In the Rocky Mountains they are chinook ('snow eating') winds. In the Alps they are Föhn winds. A good example of the effect of downslope winds on temperature was recorded at Havre, Montana, December 16 to 18, 1933, Math (1934). At this time the CO_2 concentration was near 310 ppm. The thermograph trace is shown in Fig. 43a, adapted from Math (1934), fig.2. The temperature first rose by 27 °F (15 °C) in five minutes and increased by a total of 53 °F (29 °C) in less than 2 days. The temperature then cooled by 41 °F (23 °C) in two hours. There is no connection between these downslope wind events and any increase in atmospheric CO_2 concentration. Once the necessary weather pattern is established, the hot, dry winds will dry out the vegetation very quickly and any ignition source will start the fire. In S. California, a high pressure system over the Great Basin produces an offshore flow that descends from the desert plateau. The winds may be increased by an adjacent low pressure region. Fig. 43b is a Terra Satellite image taken on Dec. 5, 2017, showing the fires in S. California, NASA (2017). The smoke is blown out to sea by the offshore winds. The Marshall fire in Boulder Colorado, December 30, 2021, that destroyed about 1000 houses was caused by strong downslope winds and an ignition source related to human activity. The fuel was dry grass and any residual moisture would have been removed very quickly by the dry 100 mph winds, Mass (2022).

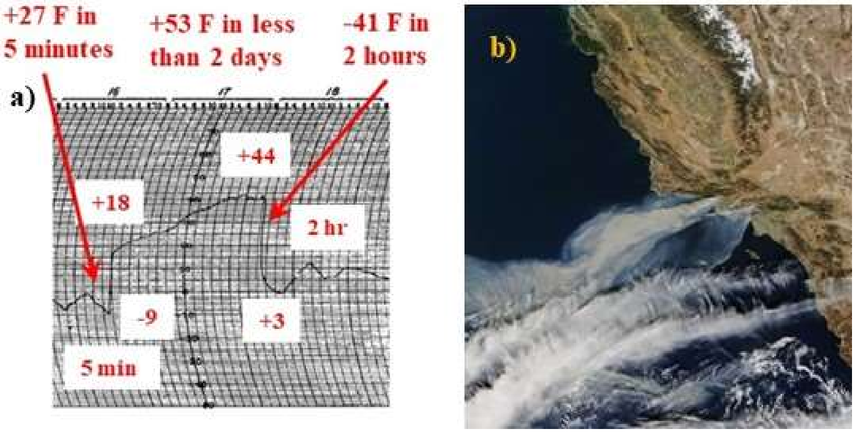

Figure 43: a) Thermograph trace of a downslope wind (Chinook) event, Havre Montana, December 1933, and b) Terra satellite image of the fires in S. California, taken Dec. 5, 2017.

A stationary or blocking high pressure system can produce significant warming over a period of several days, Clark and Rörsch (2023). None of this has any relationship to CO_2. A high pressure dome formed over the Pacific Northwest in late June 2021. This produced record high temperatures as shown in Fig. 44. As the high pressure system moved east, the temperature in Portland, Oregon dropped from 116 to 64 °F (47 to 18 °C) over the night of June 28 to 29, Watts (2021). Once a 'blocking' high pressure system pattern is established, it can persist for weeks or even months. Since these systems also block rainfall and remove soil moisture, additional heating is produced by the reduced latent heat flux at the surface. For example, there was nothing unusual about the 2003 European heat wave, Black et al (2004). Brush fires produced by ‘blocking’ high pressure systems are a normal part of the Australian climate, Foley (1947). Similarly, a high pressure system regularly forms over the area near Verkhoyansk, Siberia. This produces very high summer temperatures and very low winter temperatures (Autio, 2020; Watts, 2020).

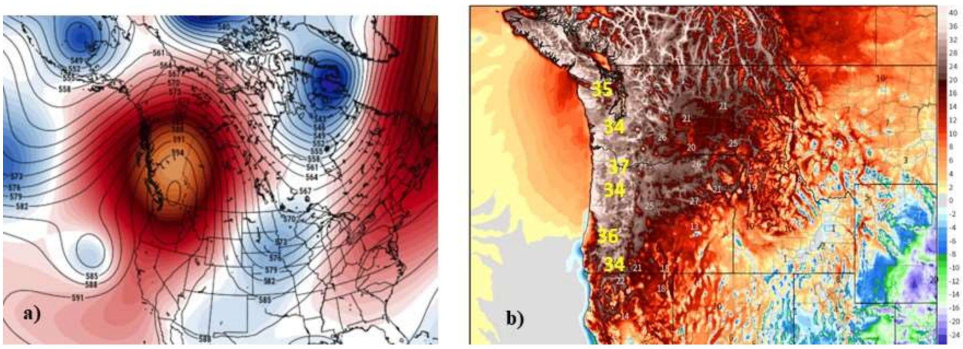

Figure 44: Blocking high pressure system over the Pacific NW, late June 2021. As the high pressure system moved east, the temperature in Portland Oregon dropped by 29 °C from 47 to 18 °C overnight, June 28 to 29.

4.7 The Dependence of the Atmospheric CO_2 Concentration on Ocean and Surface Temperatures

The analysis of the time dependent energy transfer processes that determine the surface temperature presented above in Sections 4.1 to 4.6 shows that the observed increase in CO_2 concentration of 140 ppm has not produced any measurable increase in surface temperature. Additional evidence that variations in the atmospheric concentration of CO_2 cannot cause climate change can be derived from the relationship between atmospheric CO_2 concentration and surface and ocean temperatures and from isotope studies. First, the time delays between the temperature changes and the CO_2 concentration response show that the temperature changes first and the CO_2 concentration then follows. Second, a large body of measurements contradict the ice core derived CO_2 concentrations. Third, a detailed analysis of the absorption and emission of CO_2 indicates that only a small fraction of the observed increase in CO_2 concentration can be attributed to anthropogenic causes. These areas will now be considered in turn.

Fig. 45 shows the relationship between the annual temperature changes in the HadCRUT4 and HadCRUT5 temperature series and the annual change in the CO_2 concentration measured at Mauna Loa from 1960 to 2004. The CO_2 response (green) lags the temperature response (red and blue) by 9 months to a year (Humlum, 2024; Humlum et al, 2012). Fig. 46 shows the temperature and CO_2 concentration data derived from the Vostok ice core. During the inception period (initial cooling) for each major glaciation, the decrease in CO_2 concentration lags the temperature by several thousand years, data from Mearns (2017). This is interpreted as a delay in the absorption of the CO_2 by the oceans as they cool.

The CO_2 concentration has been monitored at Mauna Loa using a non-dispersive IR technique since 1958, Keeling (2023). While this is now the preferred CO_2 monitoring method, a large number of CO_2 concentration measurements were made using conventional chemical analysis, some dating back to the early nineteenth century. A data set of these results has been compiled by Beck (2022). Fig. 47 shows the CO_2 concentration recorded for the marine boundary layer from 1870 to 1960 (adapted from Beck, fig. 25). The CO_2 concentration generally stays between 300 and 320 ppm from 1870 to 1930. There is a prominent CO_2 peak between 1935 and 1945 that reaches 380 ppm. The CO_2 concentration then decreases to values near 320 ppm for 1960 in agreement with the early CO_2 concentrations recorded at Mauna Loa. The blue crosses are the CO_2 concentrations derived from the Law Dome ice core. They are consistently lower than the Beck data and do not show the 1940 peak. The green stars are proxy CO_2 concentrations derived from leaf stomata data. Stomata are leaf pores used for gas exchange. The density of these pores is inversely proportional to the CO_2 concentration. These stomata results agree with the Beck data.

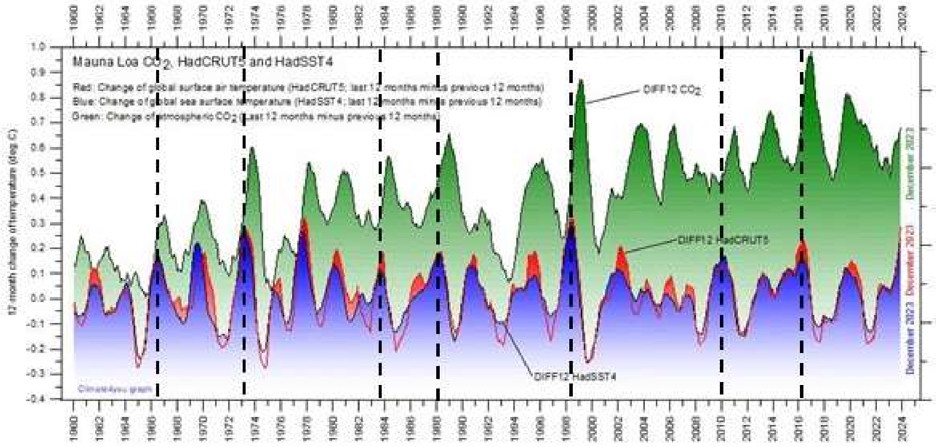

Figure 45: Annual changes in the HadCRUT4 and HadCRUT5 temperature series compared to the annual change in the CO_2 concentration measured at Mauna Loa. The increase in CO_2 concentration follows the temperature increase with a delay of 9 months to a year (Humlum, 2024).

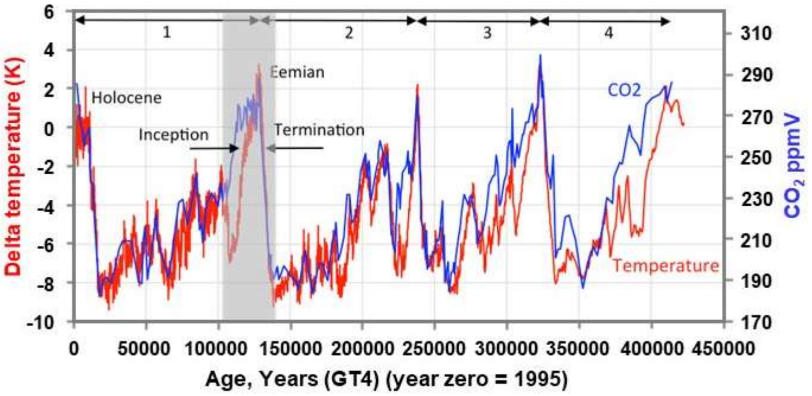

Figure 46: Temperature and CO_2 concentration data from the Vostok ice core. During the inception periods there is a major time delay between the temperature decrease and the CO_2 concentration response.

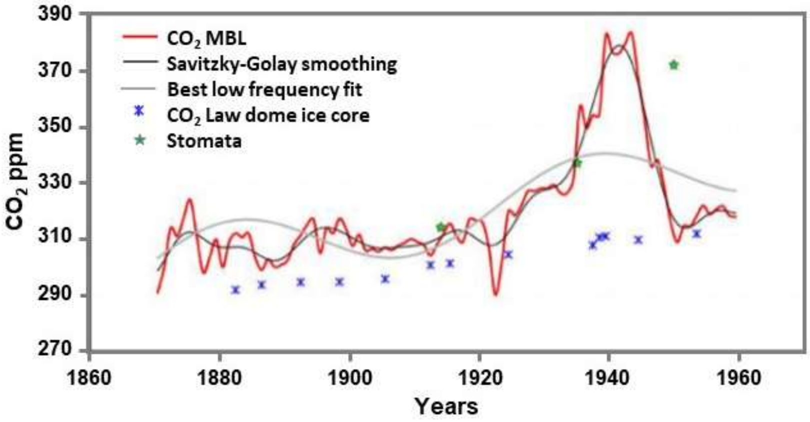

Figure 47: CO_2 concentration data measured in the marine boundary layer, 1870 to 1960 (red line), Law dome ice core data (blue crosses) and leaf stomata estimates (green stars), data from Beck (2022), figure 25.

Fig. 48 shows CO_2 concentrations derived from leaf stomata data obtained from lake sediment analysis for the time interval between 8,700 and 6800 years BP compared to Taylor Dome ice core data, from Wagner et al (2002). The leaf stomata results show a larger and more variable CO_2 concentration compared to the ice core data. The ice core data stays between 260 and 270 ppm. The leaf stomata data varies between 270 and 325 ppm. These results show that the CO_2 concentrations derived from ice core measurements are lower than those from other measurements. In addition, the time resolution is much coarser. In order for air bubbles to be trapped in the ice core, the snow deposited at the surface has to be compressed and converted to ice. The compressed snow is known as firn before it is fully converted to ice. During this compression process, physical and chemical changes occur that alter the CO_2 concentration. The drilling process may also alter the properties of the ice core. Measured ice core concentrations may be 30 to 50% lower than the real values. This is discussed by Jaworowski (2007).

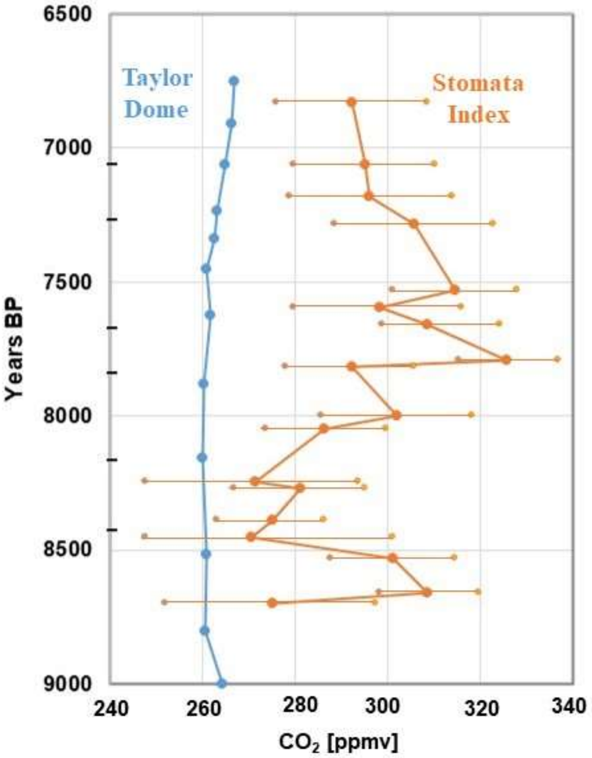

Figure 48: CO_2 concentration data from the Taylor Dome ice core compared to lake sediment leaf stomata index proxies for the period 8700 to 6800 BP.

The atmospheric concentration of CO_2 as recorded for example by the Mauna Loa Observatory, is determined by the dynamic balance between the emission and absorption of CO_2 at the earth's surface, Salby and Harde (2022a). The decline in $^{14}CO_2$ related to nuclear device testing that followed the 1963 nuclear test ban has provided a means for investigating the absorption of CO_2, Salby and Harde (2021a). The increase in atmospheric CO_2 concentration related to increases in tropical surface temperatures was then investigated, Salby and Harde (2021b). This study showed that the increase in tropical temperature over land was a major source of the observed increase in atmospheric CO_2 concentration. Further analysis was provided by Salby and Harde (2022b). This work demonstrated that the anthropogenic contribution to the observed increase in atmospheric CO_2 concentration was small. This is shown in Fig. 49 (Salby and Harde, 2022a, fig. 1).

A similar result was obtained by Koutsoyiannis (2024) using $\delta^{13}C$ analysis of the atmospheric CO_2 concentration from 1978, Keeling (2023) and the proxy record from 1520 to 1997, Böhm et al (2002). An anthropogenic CO_2 signal was not discernable in the ^{13}C isotope record.

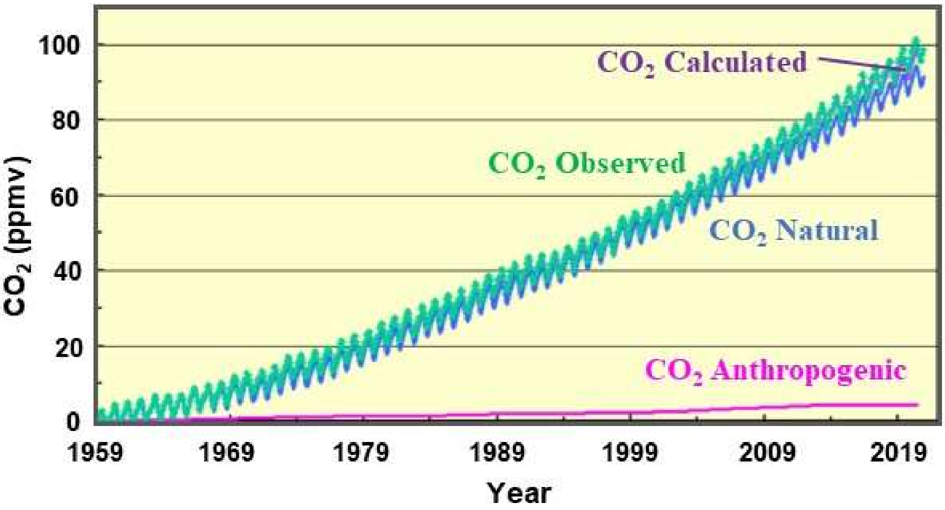

Figure 49: Measured (green) and calculated (purple) increase in CO_2 concentration from 1959. The contributions from thermally induced CO_2 emission (blue) and anthropogenic emission (magenta) are also shown. The calculated (purple) increase is almost hidden under the measured (green) line.

5. Climate Change Over Time

The earth's climate has been sufficiently stable over a period of several billion years (1 bn = 10^9) to allow for the evolution of life into its present forms. However, the climate has always changed over a wide range of time scales. Stellar evolution has produced a 20% increase in the solar flux over the last 2.5 billion years. The current composition of the atmosphere was established by photosynthesis and reached today's levels of approximately 78% nitrogen and 21% oxygen about 500,000 years ago. The atmospheric concentration of CO_2 has also varied from approximately 7000 ppm to 200 ppm. Plate tectonics has altered the distribution of the continents and caused major changes in ocean circulation. The present continental boundaries were formed by the breakup of the supercontinent Pangaea that started approximately 175 million years ago. Major ocean changes since then include the formation of the Southern Ocean and the separation of the Pacific and Atlantic Oceans by the Isthmus of Panama, Zachos et al (2001). In the more recent geological past, planetary perturbations of the earth's orbit known as Milankovitch cycles (2022) have produced a series of Ice Ages, each lasting approximately 100,000 years. Small changes in the solar energy reaching the earth related to the sunspot cycle that vary over periods of 100 to 1000 years have produced the Minoan, Roman and Medieval warming periods and the Maunder Minimum or Little Ice Age, Clark and Rörsch, (2023).

Approximately 71% of the earth's surface is ocean. The ocean-air interface involves the interaction of two fluids, air and water. The detailed description of these fluid interactions is complex and there is no simple mathematical solution, Lorenz (1963; 1973). There is no requirement for an exact flux balance between the solar heating and the surface cooling of the oceans. There are characteristic, quasi-periodic short and long term oscillations in ocean surface temperature with periods near 3 to 7 years and in the 15 to 25 year and 60 to 70 year ranges that have significant impacts on the earth's climate. Short term oscillations include the ENSO and the IOD. Longer term oscillations include the PDO and the AMO. These provide a natural noise floor for climate temperatures. Changes in land use related to agriculture and the growth of urban areas have also changed local climates. These effects include irrigation and urban heat islands.

A convenient description of the earth's climate is the Köppen or similar zonal classification scheme which starts with five basic climate types that are further subdivided into zones based on precipitation and temperature. Such a classification using 31 zones updated from Kottek et al, (2006) is shown in Fig. 50, NOAA (2023).

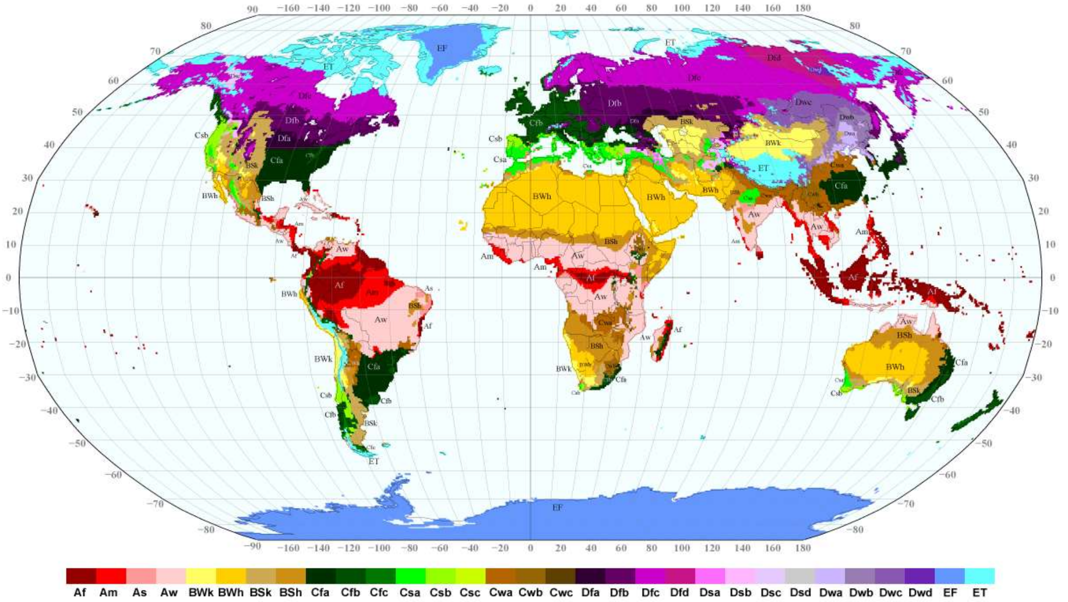

Figure 50: A world map of the Koppen-Geiger climate classification

Our understanding of climate change over different time scales is relatively recent. The first evidence for major climate change was the discovery of an Ice Age by Agassiz (1840) through observations of the glaciers in the Alps. The evidence for the Milankovitch cycles was established using deep drilled ocean sediment cores by Hays et al (1976). A more detailed history is provided by Imbrie and Imbrie (1979). The influence of ocean oscillations and ocean gyre circulation on climate was not established until the 1980s, Folland et al (1986). Any discussion of climate change requires careful consideration of all of the factors that influence temperature and precipitation over different time scales within a framework of climate zones. Climate is often defined quite narrowly as the long term trend in weather patterns. An averaging period of 30 years, updated at 10 year intervals, is commonly used. However, short term climate changes such as those related to ocean oscillations cannot be explained using 30-year averages.

5.1 The Transition from Weather to Climate

The quasi-periodic ocean oscillations provide a natural noise floor for climate studies. As weather systems that form over the oceans move over land, information about the ocean surface temperatures including seasonal phase shifts and ocean oscillations is coupled to the land based weather station data through changes to the convection transition temperature. The time scales associated with these oscillations therefore have to be included in climate analysis. The ocean gyre circulation and the main ocean oscillations are shown in Fig. 51 (Clark and Rörsch, 2023).

The ENSO and IOD vary over time scales in the 3 to 7 year range. While the temperature changes are relatively small, the related changes in evaporation and rainfall patterns are large because of the high tropical ocean temperatures. In addition, the maximum ocean surface temperature stays near 30 °C. It is the size and location of the Pacific equatorial warm pool that varies during the ENSO oscillations. The changes in area of the equatorial Pacific Ocean warm pool are illustrated in Figs. 52a and 52c for the ENSO peak in November 2015 and the minimum in December 2017, NRL (2021). The monthly ENSO index from 1979 to 2019 and the UAH global lower tropospheric (tlt) temperature anomalies are shown in Fig. 52b, UAH (2022). The lower troposphere temperatures follow the ENSO with a delay of several months.

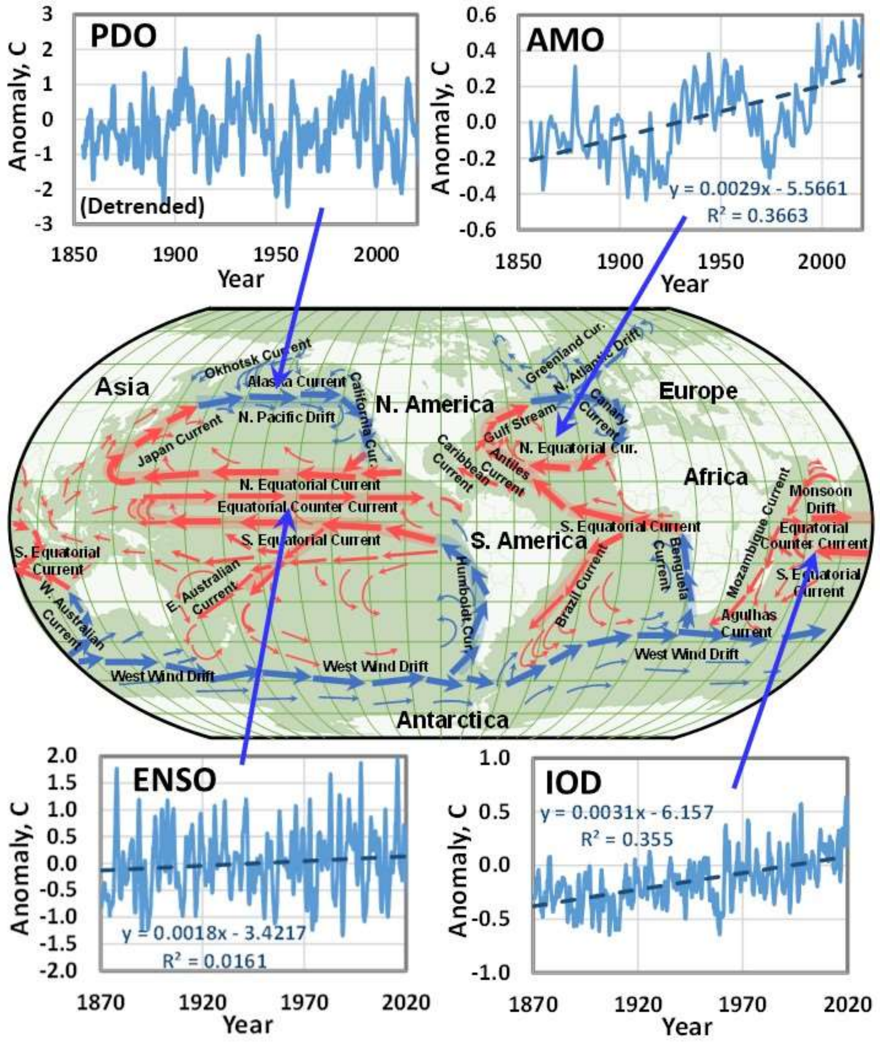

Figure 51: *The ocean gyre circulation and the four main ocean oscillations (schematic).*

The immediate cause of the ENSO is a change in the energy balance at the ocean surface between the solar heating and wind driven evaporation produced by a change in wind speed. However, the changes in ocean temperature are not limited to the surface and may reach 50 to 100 m in depth. There is a well-established inverse relationship between the Southern Oscillation Index (SOI) and the ENSO. The SOI is a measure of the wind speed derived from the surface pressure difference between Tahiti and Darwin, Australia, SOI (2022). As shown above in Fig. 29, the sensitivity of the latent heat flux to the wind speed within the ±30° latitude bands is near 15 W m^{-2}/m s^{-1}. As the wind speed decreases, the latent heat flux decreases and the ocean water warms. In addition, the ENSO region is part of the Pacific equatorial current. As the wind speed decreases, the ocean current velocity also decreases. This increases the transit time across the Pacific Ocean so more solar heat is absorbed by a cell of ocean water as it moves with the equatorial current. The ESNO index and the SOI, scaled and inverted to match the ENSO are shown in Fig. 53. The 2016 ENSO peak was produced by a decrease in wind speed near 2 m s^{-1}. The decrease in latent heat flux was approximately 30 W m^{-2} and the temperature change was 2.5 °C to a depth of at least 75 m. The change in ocean heat content to 75 m depth was approximately 800 MJ m^{-2}. Over the 6 month period of the ENSO peak, the cumulative increase in downward LWIR flux from CO_2 was 0.26 MJ m^{-2}. This is approximately 3000 times less than the change in heat content to 75 m depth produced by the ENSO peak, Clark and Rörsch, (2023). The detailed interactions that produce the ENSO oscillations are complex and include changes to the Walker circulation, Madden-Julian Oscillations and Rossby Waves, Schwendike et al (2021). Changes to the Walker circulation in the Pacific Ocean may also impact the Hadley/Walker circulation in the Atlantic and Indian Oceans.

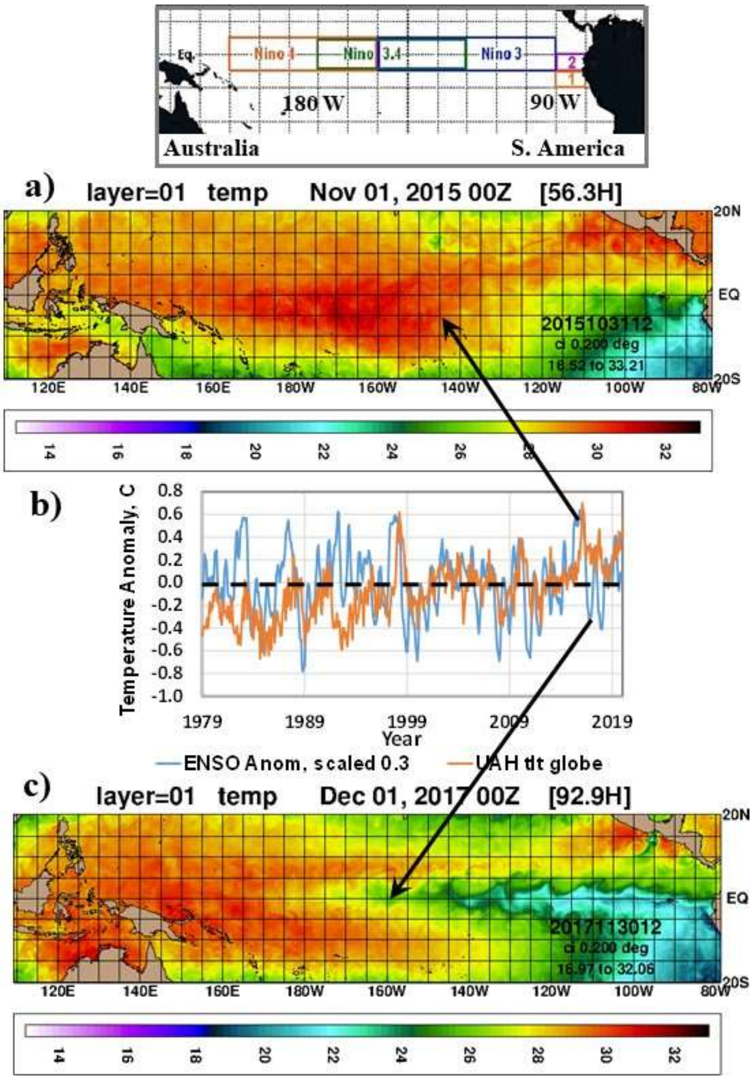

Figure 52: Surface temperatures in the equatorial Pacific Ocean for November 1, 2015 and December 1, 2017 corresponding to a) high and c) low values of the ENSO index. The map inset indicates the Nino 3.4 region used to determine the ENSO index. The monthly ENSO index (scaled) and the UAH global lower tropospheric temperature anomaly (tlt) from satellite microwave measurements are shown in b).

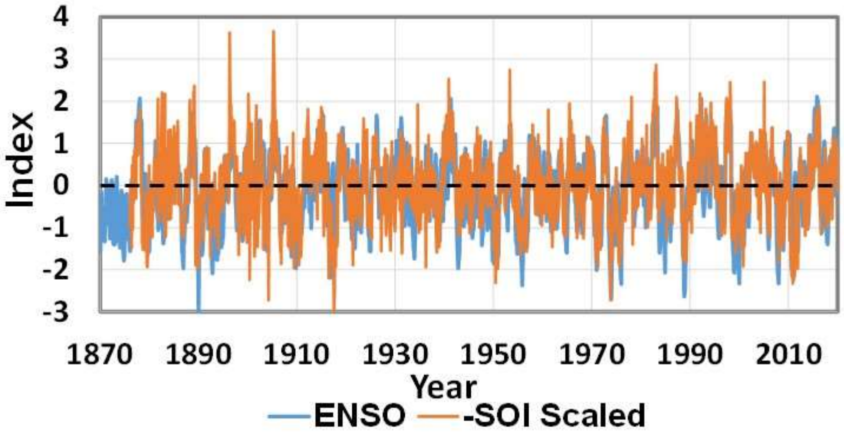

Figure 53: *Monthly ENSO data series from 1870 plotted with the scaled SOI index from 1876. The SOI is multiplied by 0.086 and the sign is reversed to match the ENSO response.*

The AMO and the PDO vary over longer time scales in the 60 to 70 year range (AMO, 2022; PDO, 2022). The AMO is discussed above in Section 4.5. The 1940 AMO peak is a prominent feature in the global mean temperature record that has been ignored in climate modeling studies (see Figures 14, 17e, 39 and 41). The PDO signal can be found in the weather station records for California and the AMO signal can be found in the UK weather station records. This is discussed in more detail by Clark and Rörsch (2023). The effect of wind speed on the ocean gyre circulation at high latitudes is the opposite of that near the equator. As the wind speed increases, the transit time decreases. There is less time for the ocean water to cool. An increase in wind speed therefore produces a warming or more accurately, a decrease in the rate of cooling along the polar leg of the N. Atlantic and N. Pacific Gyres. Most of this cooling occurs in winter as wind speeds increase and Arctic temperatures decrease (see Fig. 25). The influence of changes in solar activity on winter cooling has been discussed by Vinos (2022) as the winter gatekeeper hypothesis.

5.2 Climate Numbers and Number Series

Starting with H81, the 1-D RC model with a slab ocean was tuned to generate a time series of temperatures that approximately matched the number series obtained by averaging the weather station data. This is illustrated above in Fig. 10f. This process was later extended to the larger climate GCMs and used in all of the IPCC Climate Assessment Reports as illustrated in Figs. 13 and 14, Ramaswamy et al (2019). The weather station averages are now called global mean temperatures or temperature anomalies. These are just number series. This averaging process has been discussed in detail by Essex et al (2007). Temperature is a measure of the thermal motion of the molecules in a thermal reservoir. In thermodynamic terms it is an intensive property of the system. The corresponding extensive property is the heat content or enthalpy of the system. The average temperature of two independent systems, such as the temperatures recorded at weather stations in New York and Los Angeles, has no physical meaning. The first step in the averaging process, the sum of the temperatures is not a temperature, it is simply a number. When the sum of the temperatures is divided by the number of data points, the average is still just a number. When the mean is subtracted to create a global mean temperature anomaly, this is still just a number.

> *an average of temperature data sampled from a non-equilibrium field is not a temperature. Moreover, it hardly needs stating that the Earth does not have just one temperature. It is not in global thermodynamic equilibrium — neither within itself nor with its surroundings. It is not even approximately so for the climatological questions asked of the temperature field. Even when viewed from space at such a distance that the Earth appears as a point source, the radiation from it deviates from a black body distribution and so has no one temperature. There is also no unique "temperature at the top of the atmosphere". The temperature field of the Earth as a whole is not thermodynamically representable by a single temperature.*

Essex et al, page 2, 2007

The global mean temperature anomaly is an area weighted average of the temperature anomalies derived from individual weather station measurements that have already been adjusted (homogenized). The data points used to generate the global mean are not usually displayed and there is no discussion of the variance of the anomalies. The individual data points used to generate the global anomaly are shown in Fig. 54, adapted from Lindzen, (2024).

Similarly, a simple conservation of energy argument is used to determine a planetary average LWIR cooling flux near 239 W m^{-2} emitted at TOA. This is then converted to an effective emission temperature near 255 K using the Stefan Boltzmann Law, Möller (1964). Neither the intensity variation of the LWIR flux nor the spectral distribution are considered. Fig. 55a shows an IR image of the earth recorded March 18, 2011, using the CERES instrument on the NASA aqua satellite, CERES (2011). The intensity of the LWIR emission varies from approximately 150 to 350 W m^{-2}. The low intensity white areas near the center of the image are the LWIR emission from cloud tops. Climate stability only requires an approximate long term planetary energy balance between the absorbed solar flux and the outgoing longwave radiation (OLR). There is no exact local energy balance. Almost all of any imbalance is accounted for by changes in ocean thermal storage. Fig. 55b shows the spectral distribution of the LWIR flux at TOA for three locations recorded using the Michelson interferometer (FTIR spectrometer) on the Nimbus 4 satellite. These demonstrate that the LWIR flux emitted at TOA does not have the spectral distribution of a blackbody radiator near 255 K, data from Hanel et al (1971). These spectra were available 10 years before the publication H81.

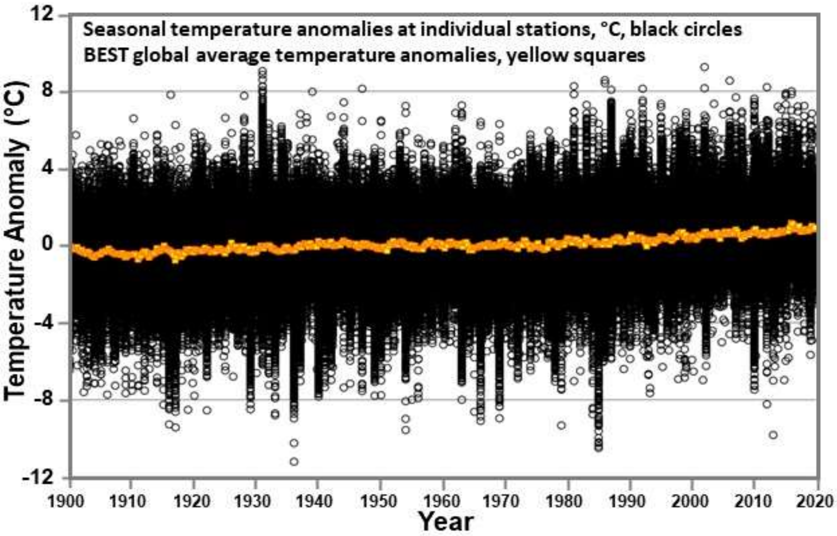

Figure 54: The seasonal temperature anomalies of the individual weather stations used to generate the BEST global average temperature anomalies. (BEST breakpoint adjusted data, minimum 100 years per station, ~ 3000 stations).

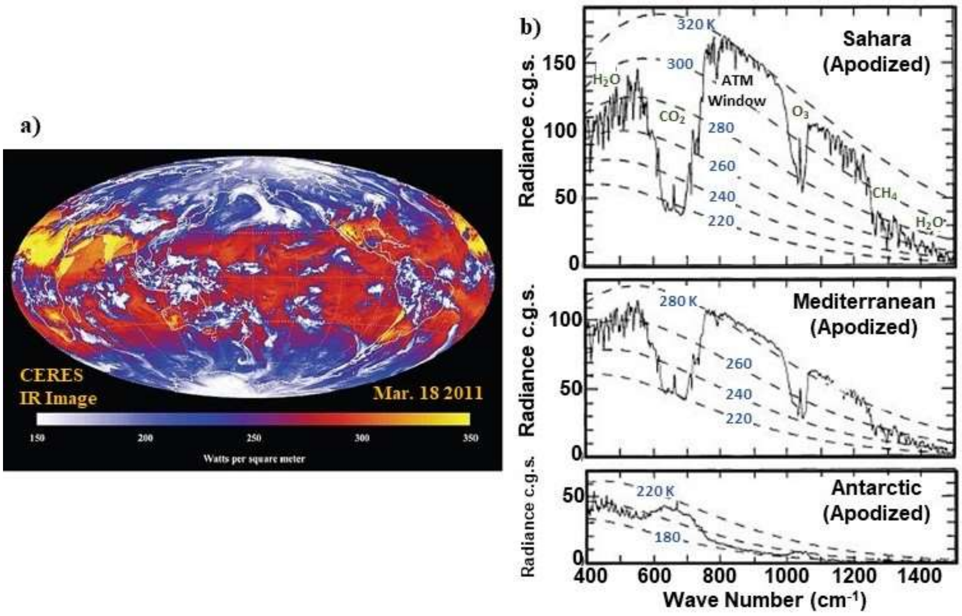

Figure 55: *a) CERES image of the LWIR emission to space from the earth, recorded March 18, 2011. b) The LWIR flux emitted at the top of the atmosphere (TOA) for selected geographic regions measured by the Michelson interferometer (FTIR spectrometer) on the Nimbus 4 satellite. A set of refence blackbody emission curves is included with the LWIR emission plots. The spectral distributions are clearly not that of a blackbody radiator at a temperature near 255 K.*

It is assumed that the fictitious effective emission temperature of 255 K would be the average temperature of a hypothetical earth without a 'greenhouse effect'. This is compared to an equally fictitious average global temperature of 288 K. The temperature difference of 33 K is then called the greenhouse effect temperature. It is assumed that the 33 K temperature increase is produced by greenhouse gas absorption and emission in the atmosphere. This is based on the equilibrium climate assumption that a global average surface temperature is determined by the solar and LWIR flux balance.

Instead of defining the greenhouse effect, G, as a temperature difference, Ramanathan and coworkers used the difference in LWIR flux between the blackbody radiation emitted by the surface, E, and the outgoing longwave radiation (OLR) emitted at TOA, F, at the same location (Raval and Ramanathan, 1989, RR89; Ramanathan and Collins,1991).

$$G = E - F \tag{6}$$

To minimize the changes in E related to the diurnal cycle, they only considered ocean temperatures. Using ERBE satellite and ocean surface temperature data they found a global average for G of 179 W m^{-2}. This was based on a surface emission, E of 421 W m^{-2} and an OLR of 242 W m^{-2}. They further divided G into a greenhouse gas 'trapping' of 146 W m^{-2} and a cloud 'trapping' of 33 W m^{-2}. The increase in G with temperature was approximately linear from 273 to 295 K with a rate of 3.3 W m^{-2} K^{-1}. They assumed that G was the result of an 'effective absorption' along the vertical path between the surface and TOA. This oversimplifies the atmospheric energy transfer processes that determine the upward LWIR flux. In order to understand the simplifications introduced by Ramanathan and coworkers it is necessary to consider atmospheric energy transfer in more detail.

Three atmospheric profiles will now be considered based on MODTRAN calculations:

1. Surface and surface air temperatures of 300 K, tropical atmosphere model, clear sky.
2. Surface and surface air temperatures of 280 K, mid latitude summer atmosphere model, clear sky.
3. Surface and surface air temperatures of 300 K, tropical atmosphere model, altostratus cloud layer, 2.6 km base, 3 km top.

The spectral range is from 0 to 2200 cm^{-1} with a resolution of 2 cm^{-1}. The molecular line structure is not resolved, MODTRAN (2024). The CO_2 concentration is 420 ppm and the default water vapor profiles (water vapor scale =1) are used, adjusted for temperature offset using fixed relative humidity. The temperature, pressure, and water vapor concentration profiles at 300 and 280 K are shown in Figs. 56a, 56b and 56c.

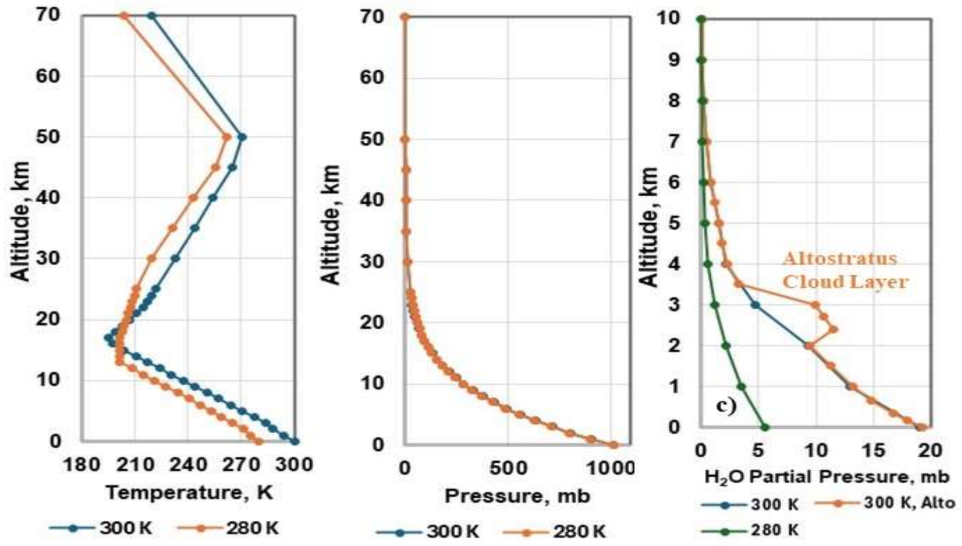

Figure 56: *a) temperature, b) pressure and c) water vapor pressure vs. altitude for the three atmospheric profiles used in the MODTRAN analysis.*

The data are from the MODTRAN output files. These examples are intended to illustrate the changes in the spectral distribution of the upward and downward LWIR flux with altitude. They are 'snapshots' of the atmospheric LWIR flux profile for the conditions specified. Both the temperature and the humidity profiles can change significantly during the diurnal cycle, especially near the surface (see Figs. 33 and 34). Radiative transfer calculations at higher spectral and spatial resolutions or with different water vapor profiles will give different quantitative results.

The spectral distribution of the total upward LWIR flux and the separate upward surface and atmospheric fluxes at selected altitudes through the atmosphere are shown in Fig. 57.

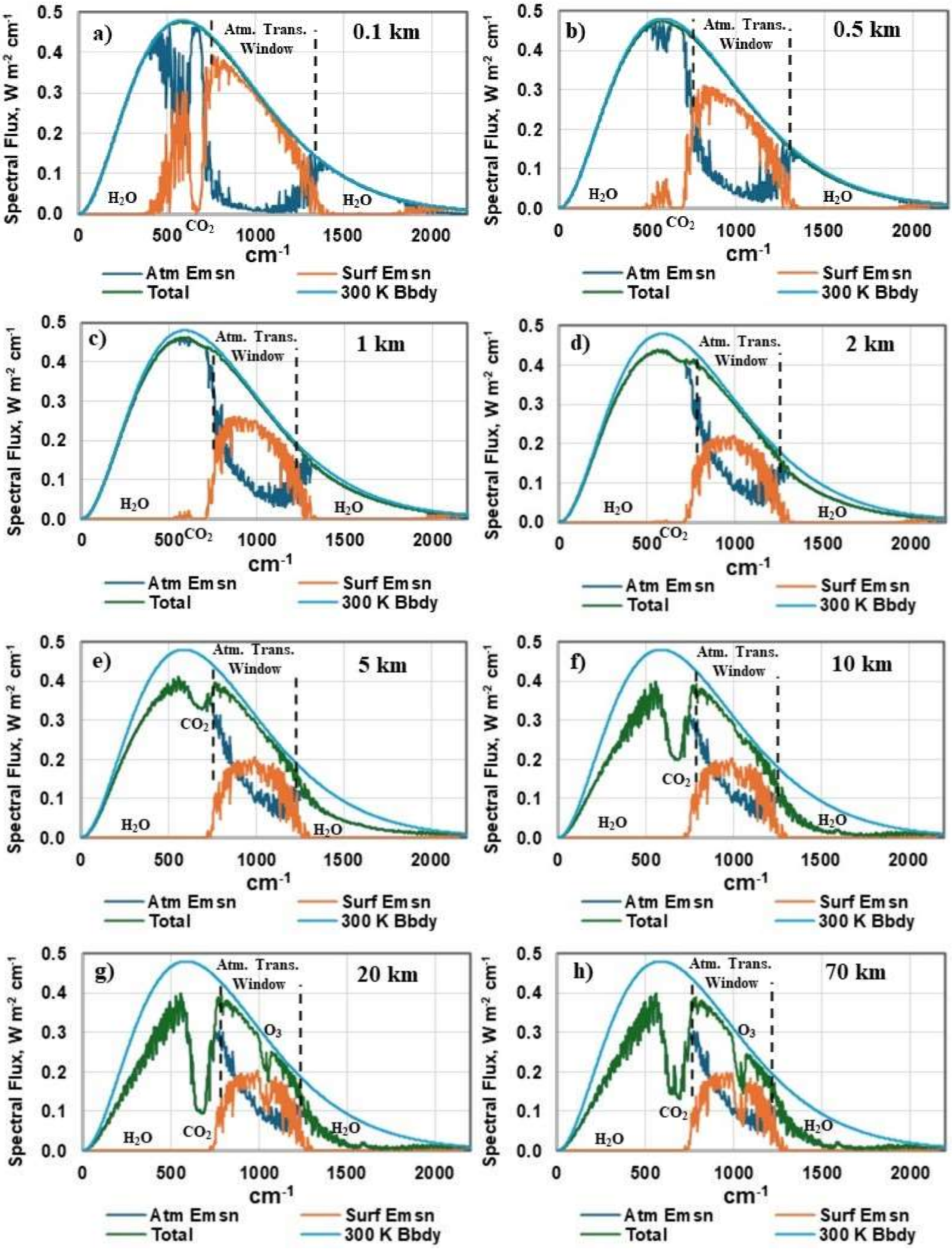

Figure 57: *The spectral distribution of the total upward LWIR flux and the separate upward surface and atmospheric fluxes at selected altitudes through the atmosphere. The main H_2O and CO_2 absorption-emission bands, the atmospheric transmission window and the stratospheric ozone absorption-emission are indicated. MODTRAN calculations, atmospheric profile 1, tropical model atmosphere, 300 K surface temperature, 0 to 2200 cm^{-1} at 2 cm^{-1} resolution (MODTRAN, 2024).*

The spectral distributions of the total upward and downward fluxes at selected altitudes are shown in Fig. 58. These are for atmospheric profile 1. Fig. 57a shows the upward LWIR flux terms at 100 meters (0.1 km) above the surface. Below 400 cm^{-1} and between 1400 and 1800 cm^{-1}, all of the upward LWIR flux emitted by the surface has already been absorbed by water vapor (orange line). In addition, the CO_2 band has absorbed at least 95% of the surface flux between 650 and 690 cm^{-1}. However, almost all the absorbed surface flux has been replaced by upward LWIR flux emitted from within the first 100 m air layer. The intensity of the total upward flux at 100 m is close to that of the surface emission. There is also a similar downward LWIR flux that is emitted from this layer to the surface. This process of absorption and emission continues through the troposphere. The total upward flux decreases with altitude. At 2 km, as shown in Fig. 57d, almost all of the surface flux below 700 cm^{-1} and between 1300 and 2200 cm^{-1} has been absorbed and replaced by atmospheric emission. Part of the upward atmospheric LWIR flux from below is also absorbed and replaced by local atmospheric LWIR emission at a lower temperature. Above 2 km, the change in the surface flux through the LWIR transmission window is small. As the temperature and water vapor pressure decrease with altitude, the absorption decreases and there is a gradual transition from absorption-emission to a free photon flux. There is little change in the water band emission above 10 km. The upward LWIR flux emitted by CO_2 continues to decrease up to an altitude of approximately 20 km. In the stratosphere, there is also an ozone absorption-emission feature near 1050 cm^{-1}.

Fig. 58a shows the upward surface emission, E, and the downward LWIR flux to the surface. These interact to establish the LWIR exchange energy (see Section 4.2 and Fig. 23). Within the spectral regions below 400 cm^{-1} and between 1400 and 1800 cm^{-1}, the downward LWIR flux is emitted from within the first 100 m layer above the surface. As the temperature and water vapor concentration decrease with increasing altitude, the downward LWIR flux decreases and the spectral profile changes. Because of increased molecular line broadening in the lower troposphere, almost all of the downward LWIR flux that reaches the surface originates from within the first 2 km layer above the surface (see Fig. 19).

When the surface temperature decreases, both the upward LWIR flux emitted by the surface and the atmospheric absorption-emission decrease. However, the net LWIR surface flux emitted into the LWIR transmission window increases. This is illustrated in Fig.59 that compares atmospheric profiles 1 and 2. Figs. 59a and 59b show the upward flux emitted by the surface and the downward LWIR flux to the surface emitted from the lower troposphere for surface temperatures of 300 and 280 K. The LWIR transmission window flux increases from 81 to 105 W m^{-2}. Figs. 59c and 59d show the upward fluxes emitted at the 100 m (0.1 km) level.

At 300 K, the surface emission is 453.4 W m^{-2} in the 0 to 2200 cm^{-1} spectral region. The first 100 m layer absorbs 255.8 W m^{-2} of this flux. It is replaced by 253.4 W m^{-2} of upward atmospheric emission from the air layer. The total upward emission at 100 m is 451 W m^{-2}. The spectral distribution of the upward flux terms at 100 m is shown in Fig. 59c. At 280 K, the surface emission is 344.9 W m^{-2}. Of this, 156.3 W m^{-2} is absorbed and replaced by 154.2 W m^{-2} of upward emission from the air layer. The total upward emission at 100 m is 342.8 W m^{-2}. The spectral distribution of the upward flux at 100 m is shown in Fig. 59d.

The absorption-emission process continues as the altitude increases and the spectral distributions change. For the 300 K surface temperature at 20 km, the total upward emission is 298.8 W m^{-2}. The downward emission from above 20 km has decreased to 9.3 W m^{-2}. For the 280 K surface temperature at 20 km, the total upward emission is 250 W m^{-2} and the downward emission is 7.6 W m^{-2}. The spectral distributions are shown in Figs. 59e and 59f.

For the 300 K profile at 70 km, 386.1 W m^{-2} of the surface emission has been absorbed and replaced by a cumulative upward atmospheric emission of 232 W m^{-2}. The total upward flux is 299.3 W m^{-2}. For the 280 K profile at 70 km, 277.7 W m^{-2} of the surface emission has been absorbed and replaced by a cumulative upward atmospheric emission of 157 W m^{-2}. The total upward flux is 250.4 W m^{-2}. The fraction of the surface flux removed by the absorption emission process is the normalized greenhouse effect, g, as defined by RR89. In the examples considered here it is 0.34 for the 300 K atmospheric profile 1 and 0.27 for the 280 K atmospheric profile 2.

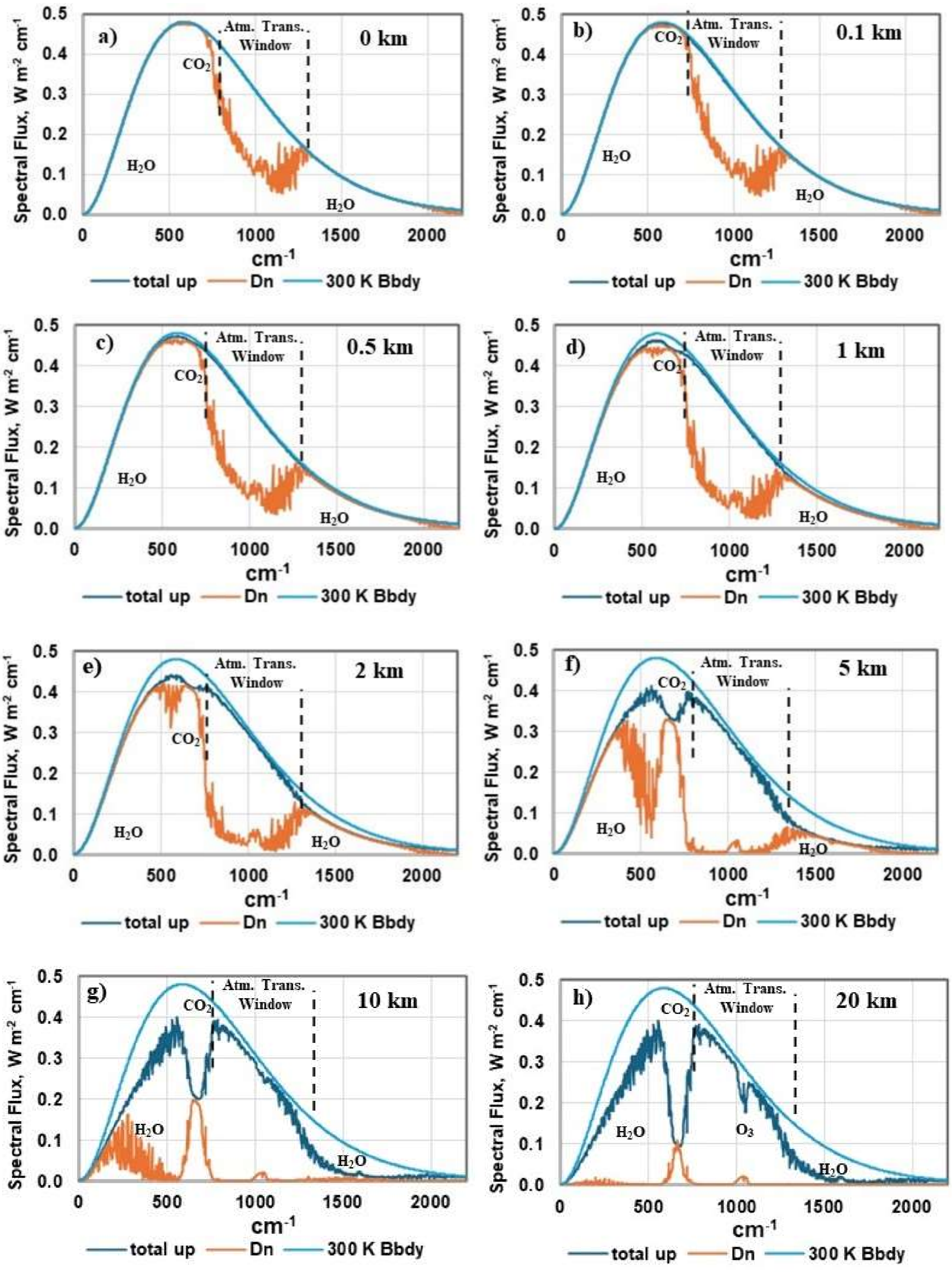

Figure 58: *The spectral distribution of the total upward and downward fluxes at selected altitudes. The main H_2O and CO_2 absorption-emission bands, the atmospheric LWIR transmission window and the stratospheric ozone absorption peak are indicated. MODTRAN calculations, atmospheric profile 1, tropical atmosphere, 300 K surface temperature, 0 to 2200 cm^{-1} at 2 cm^{-1} resolution (MODTRAN, 2024).*

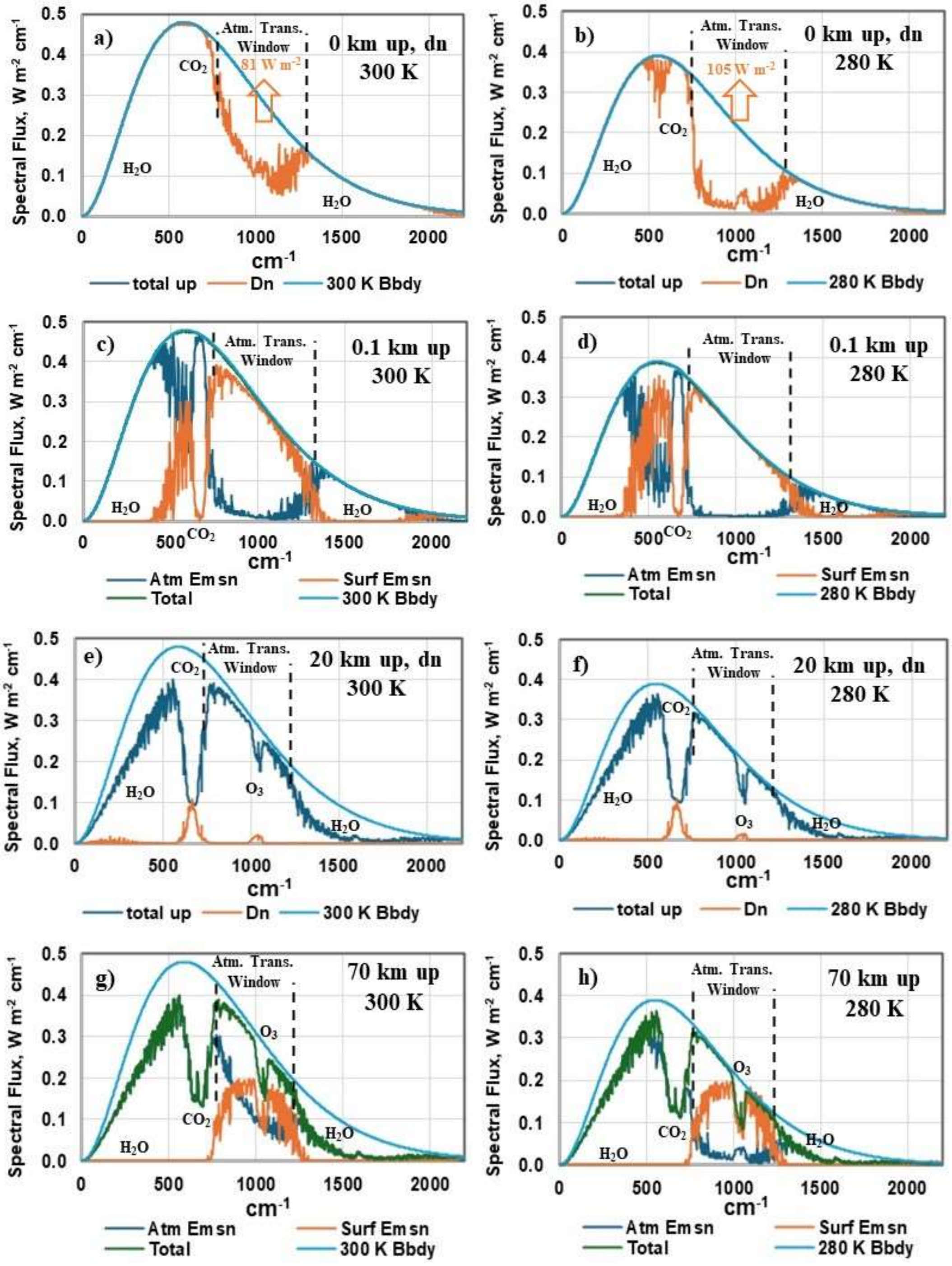

Figure 59: *Comparison of the atmospheric profiles 1 and 2 at 300 and 280 K for the upward and downward flux at the surface (a and b), the upward fluxes at 0.1 k (c and d), the upward and downward fluxes at 20 km (e and f) and the upward fluxes at 70 km (g and h). MODTRAN calculations, 300 K, 0 to 2200 cm^{-1}, 2 cm^{-1} resolution (MODTRAN, 2024).*

The total LWIR fluxes from 0 to 2200 cm^{-1} for the upward atmospheric, surface and total LWIR emission at selected altitudes for surface temperatures of 300 and 280 K are shown in Fig. 60a. The total upward and downward LWIR fluxes at selected altitudes are shown in Fig. 60b. The differences between the surface emission at 300 and 280 K and the total upward fluxes at selected altitudes are shown in Fig. 60c. This shows the change in G with increasing altitude. At 70 km, G_{300} = 151 W m^{-2} and G_{280} = 94.5 W m^{-2}, are the greenhouse effect fluxes as defined by RR89.

This is a mathematical construct that only considers the upward LWIR flux. Such an approach creates a net heat gain (‘trapping’) in the troposphere. However, when the downward flux is included, there is usually a net LWIR cooling at each level (see Fig. 21). This does not include NIR solar heating, latent heat release or local vertical motion of the air parcel.

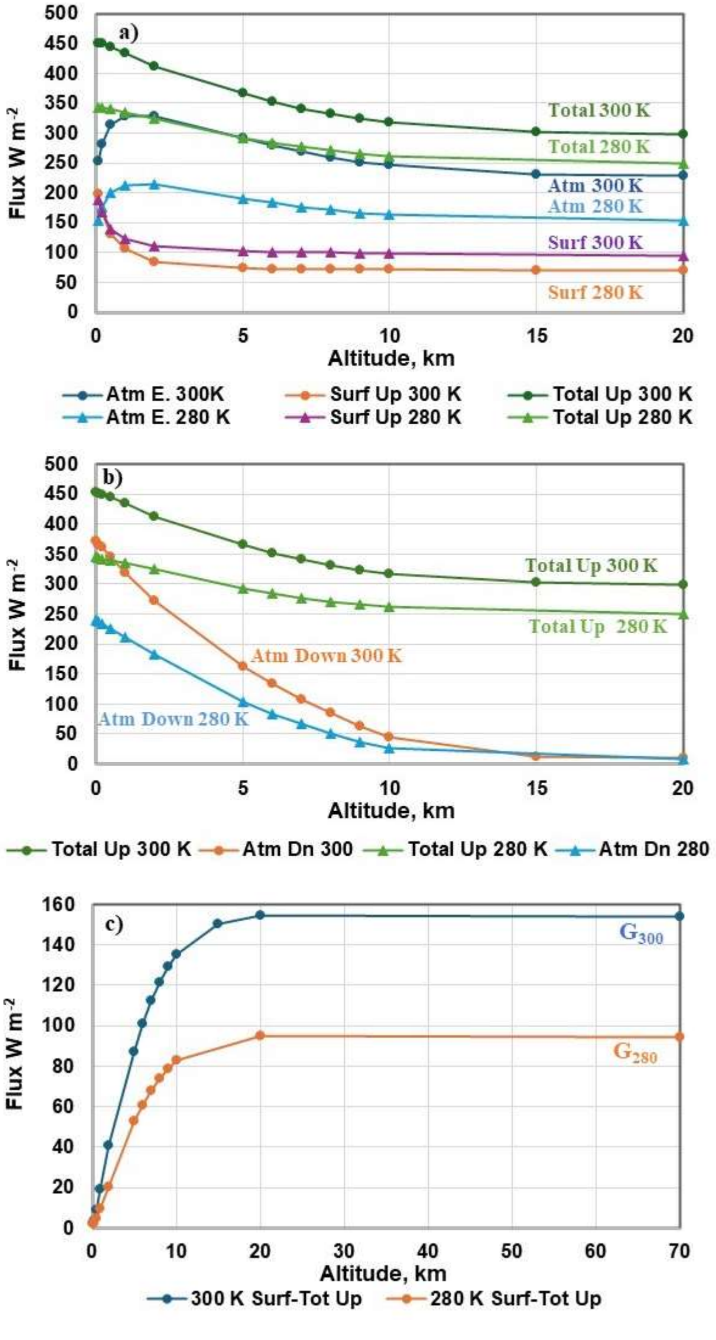

Figure 60: Comparison of atmospheric profiles 1 and 2. a) Upward LWIR atmospheric, surface and total fluxes at selected altitudes for surface temperatures of 300 and 280 K. b) Total upward and downward fluxes for selected altitudes and surface temperatures of 300 and 280 K. c) Difference between the surface flux and total upward flux for selected altitudes and surface temperatures of 300 and 280 K. The values at 70 km (TOA), G_{300} and G_{280} are the greenhouse fluxes defined by Raval and Ramanathan (1989).

Fig. 61a shows the spectral distributions of the surface emission, E, and the OLR, F, at 300 and 280 K. The surface emission increases by approximately 30% from 344.9 to 453.4 W m^{-2} as the temperature increases from 280 to 300 K. The contributions to the OLR at 300 and 280 K from the four spectral regions corresponding approximately to the H_2O and CO_2 bands and the transmission window are summarized in Fig. 61c. The main change in the OLR is the increase in emission through the atmospheric transmission window. The OLR related to water band emission below 500 cm^{-1} and above 1500 cm^{-1} is insensitive to the surface temperature, Koll and Cronin, (2018). As the temperature increases from 280 to 300 K, the water band emission to space shifts to a higher altitude, Clark (2013a). This is because the emission is determined by the local water vapor concentration. Above the saturation level, this in turn is determined by the local air temperature. There is a broad emission band with a peak near 260 K (13 °C). In this MODTRAN example, the 260 K level increases in altitude from 4 to 6.5 km as the surface temperature increases from 280 to 300 K.

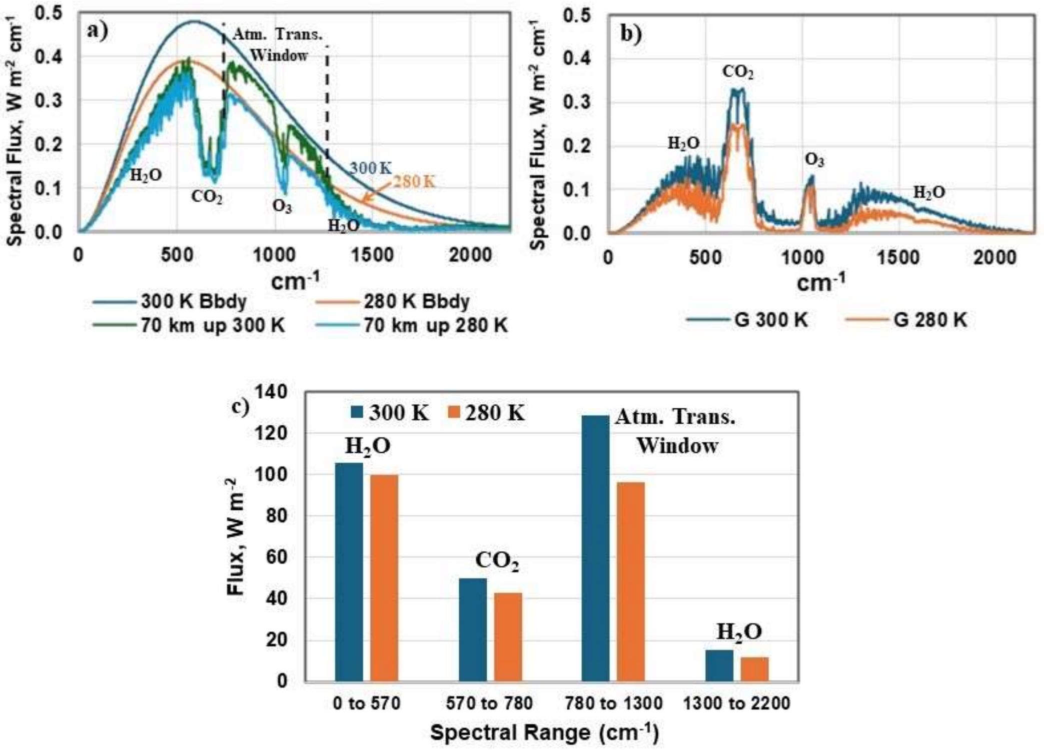

Figure 61: a) Spectral profiles of the surface and OLR emission at 300 and 280 K, b) spectral profiles of the greenhouse fluxes (surface-OLR) as defined in RR89 and c) approximate contributions of the H_2O and CO_2 bands and the transmission window to the OLR flux for the spectral regions indicated.

The spectral profiles of the greenhouse fluxes, G_{300} and G_{280}, are shown in Fig. 61b. Here, the OLR spectra shown in Fig. 61a have been subtracted from surface emission. There is an increase in absorbed flux as the temperature increases. However, it is the downward LWIR flux to the surface that determines the surface exchange energy (see Section 4.2). Most of this downward flux is emitted by the air layer close to the surface (see Fig. 19). The greenhouse effect, G, as defined in RR89 is not a useful measure of the atmospheric energy transfer processes that determine the surface temperature.

So far, this analysis has only considered clear sky conditions. A cloud layer contains water droplets or ice crystals that are good blackbody absorbers and emitters in the LWIR spectral region. Such a layer absorbs all of the upward LWIR flux from below and emits blackbody radiation downward at the cloud base temperature. It also absorbs all of the downward LWIR flux from above and emits blackbody radiation upwards at the cloud top temperature. RR89 only considered the change in the upward LWIR flux. On average, clouds reduced the OLR by approximately 30 W m^{-2}. This was called a ‘cloud trapping’. The increase in downward LWIR flux to the surface through the atmospheric LWIR transmission window was ignored. Fig. 62 shows the effect adding a cloud layer on the flux terms shown in Fig. 60 for atmospheric profile 3, the MODRAN tropical atmosphere model with a 300 K surface temperature. In this illustration, the MODTRAN altostratus cloud option with a base at 2.6 km and a top at 3 km is used. Fig. 62a shows the effect of this cloud layer on the upward flux terms. The altostratus layer is indicated by the gray bar. The upward surface flux is absorbed and is zero above the cloud layer. This is indicated by the lower red circle. The upward flux emitted by the atmosphere is also absorbed, but is replaced by blackbody emission at the cloud top temperature of 284 K. This is indicated by the upper red circle. Above the cloud layer the atmospheric emission and total emission have the same values. Fig. 62b shows the effect of the altostratus layer on the total upward and downward flux terms. The total upward flux terms are the same as in Fig. 62a. The downward flux is absorbed by the cloud layer and replaced by downward LWIR emission from the cloud base at a temperature of 286.4 K. In this MODTRAN example, the downward LWIR flux to the surface increases from 372 to 434 W m^{-2}, and the net LWIR emission into the LWIR transmission window decreases from 81 to 19.5 W m^{-2}. The increase in downward flux from the cloud base may also mask at least part of any increase in downward flux produced by an increase in atmospheric CO_2 concentration. Clouds may therefore change any possible water vapor feedback effects. Over the oceans, sea mist and water spray from breaking waves also contribute to the LWIR flux.

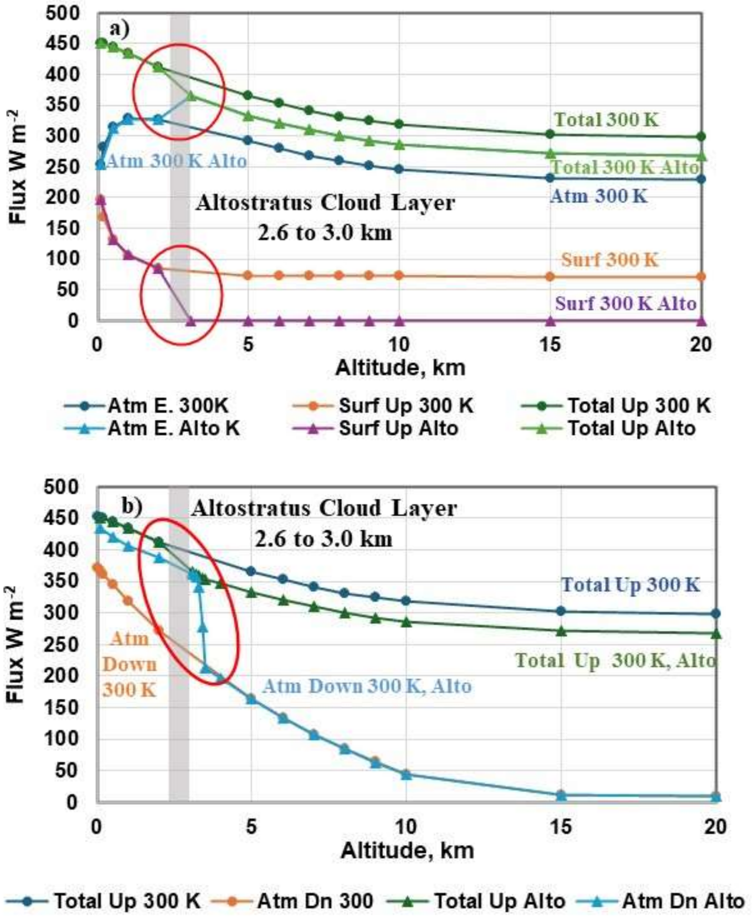

Figure 62: Atmospheric profile 3, the effect of a cloud layer on a) the upward flux terms and b) the total upward and downward flux terms. The cloud absorbs the upward and downward incident fluxes and replaces them with blackbody emission at the cloud base and cloud top temperatures.

The discussion of a greenhouse effect based on the temperature difference between an average surface temperature and an effective emission temperature at TOA (Hansen et al, 1981) or in terms of the related flux difference between the local surface emission and the OLR (Raval and Ramanathan, 1989) does not include all of the interactive energy transfer processes that determine the surface temperature. Radiative transfer through the atmosphere involves the absorption and emission of both the upward and downward LWIR fluxes by the local air parcel. In addition, the role of water in the energy transfer has been underestimated. The water related processes include ocean solar absorption, evaporation, the release of latent during cloud formation, solar attenuation by clouds, upward and downward LWIR emission by clouds and NIR solar absorption by the water vapor overtone bands. Further details are given above in Section 4 and by Clark and Rörsch (2023).

In addition to global averages of the earth's temperature field, highly detailed satellite radiometer data are often averaged to give three climate numbers, an average absorbed solar flux, an average reflected flux or albedo and the average outgoing LWIR flux. The integrated and averaged flux terms are adjusted to give the desired imbalance required by the radiative forcings used in the climate models. Fig. 63 shows the zonal averages of the net flux (absorbed solar flux minus LWIR flux) for March, June, September and December, adapted from Kandel and Voilier, (2010). Near equinox, in March and September, the net flux within the ±30° latitude bands is positive with a net energy flow into the earth of up to 100 W m^{-2}. There is net cooling at higher latitudes. In June, near summer solstice in the N. Hemisphere, the heating occurs in the N. Hemisphere and this reverses in December for the S. Hemisphere summer. The starting point for any realistic analysis of these flux terms is that the earth consists of two weakly coupled hemispheres with heating and cooling cycles that are out of phase with each other. There is no requirement for an exact flux balance. The dominant term in any imbalance is a change in ocean thermal storage.

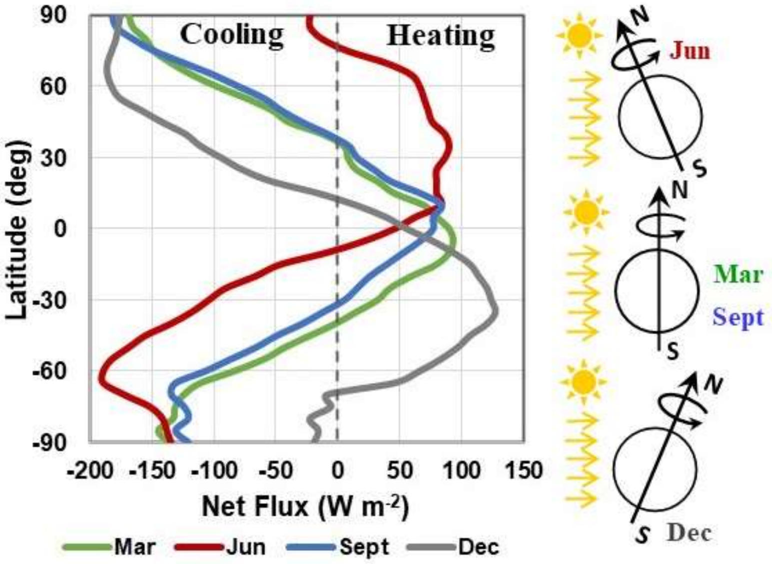

Figure 63: Zonal averages of the net flux (absorbed solar minus emitted LWIR flux), for March, June, September and December, five-year average CERES values.

Conclusions

Starting in the nineteenth century, the energy transfer processes that determine the surface temperature were oversimplified using the equilibrium climate assumption. The time dependent flux terms were replaced by average values. Physical reality was abandoned in favor of mathematical simplicity. When the atmospheric CO_2 concentration is increased, radiative transfer calculations show that there is a small decrease in the LWIR flux returned to space within the spectral emission bands of CO_2. It is assumed that this perturbs the equilibrium climate and that the surface temperature increases until the flux balance is restored. This approach was used by Arrhenius in 1896. It created surface warming as a mathematical simplification in his calculations. The idea that an increase in the atmospheric CO_2 concentration could warm the earth became accepted scientific dogma. The concept was originally proposed as the cause of an Ice Age. Gradually this was transformed to concern over warming effects from fossil fuel combustion.

In 1967, Manabe and Wetherald used the Arrhenius model as the foundation for their 1-D RC model. They added a 9 or 18 layer radiative transfer calculation with a fixed relative humidity

(RH) distribution. This added a water vapor feedback that amplified the initial CO_2 warming created by the equilibrium assumption. When the CO_2 concentration was increased from 300 to 600 ppm in the MW67 model, the total warming was 2.9 °C for clear sky conditions. They went on to incorporate their MW67 modeling assumptions into every unit cell of the 'highly simplified' GCM described in MW75. This provided an invalid benchmark for the warming created in later GCMs. Manabe's group never considered the errors associated with the equilibrium assumption and ignored the daily and seasonal variations in both temperature and RH found in the surface boundary layer. For a CO_2 doubling, the small temperature increases calculated at each step in their time integration procedure does not accumulate in the real atmosphere.

As funding was reduced at NASA after the end of the Apollo (moon landing) program, the group modeling planetary atmospheres shifted to climate studies. In H76 they simply copied the MW67 model and used it to create warming artifacts for 10 minor species including CH_4 and N_2O. The basic equilibrium climate model was completed with H81. This added a slab ocean to MW67 and introduced the CO_2 step doubling. The model was then tuned so that the calculated warming resembled the global mean temperature record derived from the measured temperature record. This established the pseudoscientific concepts of radiative forcing, feedbacks and climate sensitivity that have been used by the IPCC since it was established in 1988.

As computer technology improved, the climate models became more complex. Coupled atmosphere-ocean GCMs replaced the 1-D RC model, but the underlying equilibrium assumption was still there. Water vapor feedback still amplified the CO_2 warming artifact created by Arrhenius. Starting with the Third IPCC Climate Assessment Report (TAR), 2001, the time series of radiative forcings used to simulate the global mean temperature record was split into 'natural' and 'anthropogenic' forcings. The climate models were then rerun to create a separate 'natural baseline' and an 'anthropogenic contribution'. A vague statistical argument using changes to the normal distribution ('bell' or Gaussian curve) of temperature was then used to claim that the increase in temperature caused by 'anthropogenic' forcings would cause an increase in the frequency and intensity of 'extreme weather events'. This provided the pseudoscientific justification for the political control of fossil fuel combustion that has led to the 1.5 or 2 °C limit in the Paris Climate Accord and the disastrous net zero policy of today.

The scientific method is an interactive process of hypothesis based on available scientific evidence. This was never used in mainstream climate science. The equilibrium climate assumption became accepted scientific dogma in the nineteenth century. Climate modeling has now degenerated past dogma into a quasi-religious cult. Irrational belief in climate model results has replaced logic and reason. Instead of changing the hypothesis to explain the data, the opposite has occurred. Climate data has been made to fit the pseudoscience of radiative forcing, feedbacks and climate sensitivity. The weather station data has been 'adjusted' using 'homogenization'. Satellite radiometer data has been reduced to the three numbers used to create the illusion of an equilibrium climate. The spectral distribution of the LWIR flux returned to space has been removed from the discussion of the effective emission temperature and the greenhouse effect temperature. The Charney Report ignored the Milankovitch cycles that are the real cause of the Ice Age cycle. The role of ocean oscillations in climate change has been neglected. The paleoclimate record has been distorted to fit the climate model results. Tree ring data was unilaterally selected to reduce the temperature increase related to the medieval warming period and create the well-known hockey stick plot used in the Third IPCC Climate Assessment Report. The contribution of fossil fuel combustion to the observed 140 ppm increase in CO_2 concentration has been greatly exaggerated. Electronic controls theory has been used incorrectly to describe climate feedback effects. However other concepts in electronics such as the phase shift and the signal to noise ratio have been conveniently overlooked.

The basic requirement of a climate model is that it should accurately predict the climate observations it was configured to simulate. When climate models are examined in more detail and model outputs are compared to observations, it is found that that they have very poor predictive capabilities. The limitations of the climate models associated with the CMIP3 and CMIP5 ensembles have been discussed in detail in *Climate Change Reconsidered II: Physical Science*, Idso et al

(2013). Since short term climate change is strongly influenced by ocean oscillations, this provides a good model test. Section 1.4.1 El Niño/Southern Oscillation concludes:

> *Clearly there remain multiple problems in the ability of models to reliably simulate various aspects of climate associated with ENSO events, casting further doubt on the overall ability of models to simulate the future climate of the planet in general.*

When the pseudoscience of radiative forcing, feedbacks and climate sensitivity is removed from the climate models, what is left? Are the underlying GCMs capable of predicting natural climate changes such as those related to ocean oscillations? Model performance so far indicates that another approach is needed.

The 2.9 °C clear sky increase in surface temperature produced by a doubling of the CO_2 concentration reported in Table 5 of MW67 was produced by two mathematical artifacts created using an oversimplified 1-D RC model. These errors were never corrected and provided the foundation for the massive climate modeling fraud we have today. The part of the 2021 Nobel Prize in Physics awarded to Manabe was for climate modeling simplifications or errors that created spurious warming when the atmospheric CO_2 concentration was increased.

Instead of an extended discussion over the magnitude of the climate sensitivity, there is a simple question that climate science should address:

At present the average annual increase in atmospheric CO_2 concentration is near 2.4 ppm per year. This produces an increase in the downward LWIR flux from the lower troposphere to the surface of approximately 0.034 W m^{-2} per year. How does this change the surface temperature of the earth?

The correct answer is that any temperature changes are too small to measure. Nor can there be any effect on extreme weather events.

Guest-Editor: Jan-Erik Solheim; Reviewers: anonymous.

Acknowledgements

This work was performed as independent research by the author. It was not supported by any grant awards and none of the work was conducted as a part of employment duties for any employer. The views expressed are those of the author.

The author also thanks the SCC editor, Herman Harde, for many helpful comments that have improved the manuscript.

References

Ackerman, T. P., 1979: *On the effect of CO_2 on the atmospheric heating rates*, Tellus v. 31, pp 115-123. https://a.tellusjournals.se/articles/10.3402/tellusa.v31i2.10416

Agassiz, L., 1840: *Etudes sur les Glaciers*, Neuchatel.

Akasofu, S.-I., 2010: *On the recovery from the Little Ice Age*, Natural Science, v. 2, no. 11, pp. 1211-1224. http://dx.doi.org/10.4236/ns.2010.211149

AMO, 2022: *Atlantic Multidecadal Oscillation*. https://www.esrl.noaa.gov/psd/data/correlation/amon.us.long.mean.data

Andrews, R., 2017a: *Adjusting Measurements to Match the Models – Part 3: Lower Troposphere Satellite Temperatures*, Energy Matters, Sept 14. http://euanmearns.com/adjusting-measurements-to-match-the-models-part-3-lower-troposphere-satellite-temperatures/#more-19464

Andrews, R., 2017b: *Making the Measurements Match the Models – Part 2: Sea Surface Temperatures*, Energy Matters, Aug 2. http://euanmearns.com/making-the-measurements-match-the-models-part-2-sea-surface-temperatures/

Andrews, R., 2017c: *Adjusting Measurements to Match the Models – Part 1: Surface Air*

Temperatures, Energy Matters, July 27. http://euanmearns.com/adjusting-measurements-to-match-the-models-part-1-surface-air-temperatures/

Argo Marine Atlas, 2021: https://argo.ucsd.edu/data/data-visualizations/marine-atlas/

Arrhenius, S., 1896: *On the influence of carbonic acid in the air upon the temperature of the ground*, The London, Edinburgh, and Dublin Philosophical Magazine and Journal of Science, v. 41, pp. 237-276. https://doi.org/10.1080/14786449608620846

Autio, P., 2020: *Siberia on fire – every summer*, Watts Up with That, July 14. https://wattsupwiththat.com/2020/07/14/siberia-on-fire-every-summer/

Beck, E-G., 2022: *Reconstruction of atmospheric CO_2 background levels since 1826 from direct measurements near ground*, Science of Climate Change, v. 2, no. 2, pp.148-211. https://scienceofclimatechange.org/ernst-georg-beck-reconstruction-of-atmospheric-co2-background-levels-since-1826-from-direct-measurements-near-ground-inclusive-supplements-3-5/

Berger, T. and G. Sherrington, 2022: *Uncertainty of Measurement of Routine Temperatures–Part Three*, Watt Up with That, Oct 14. https://wattsupwiththat.com/2022/10/14/uncertainty-of-measurement-of-routine-temperatures-part-iii/

Black, E., M. Blackburn, G. Harrison, B. Hoskins and J. Methven, 2004: *Factors contributing to the summer 2003 European heatwave*, Weather, v. 59, no. 8, pp. 217-223.https://doi.org/10.1256/wea.74.04

Böhm, F., A. Haase-Schramm, A. Eisenhauer, W.-C. Dullo, M. M. Joachimski, H. Lehnert and J. Reitner, 2002: Geochemistry, *Evidence for preindustrial variations in the marine surface water carbonate system from coralline sponges*, Geophysics, Geosystems v. 3, no. 3, 10.1029/2001GC000264, pp 1-13. https://doi.org/10.1029/2001GC000264

Bolin, B., 1960: *On the Exchange of Carbon Dioxide between the Atmosphere and the Sea*, Tellus, v. 12, pp. 274-281. https://doi.org/10.3402/tellusa.v12i3.9402

Bolin, B., and Eriksson, E., 1959: *Changes in the carbon dioxide content of the atmosphere and sea due to fossil fuel combustion*, in B. Bolin, (Ed.), *The atmosphere and the sea in motion,* pp. 130-142. New York: The Rockefeller Institute and Oxford University Press. http://climatepositions.com/wp-content/uploads/2014/03/n8._Bolin___Eriksson__1958corrected.pdf

Bryson, R. A. and G. J. Dittberner, 1976: *A non-equilibrium model of hemispheric mean surface temperature*, J. Atmos. Sci., v. 33, no. 11, pp. 2094-2106. https://journals.ametsoc.org/view/journals/atsc/33/11/1520-0469_1976_033_2094_anemoh_2_0_co_2.xml

Budyko, M. I., 1969: *The effect of solar radiation variations on the climate of the Earth*, Tellus, v. 21, no. 5, pp. 611-619. https://doi.org/10.3402/tellusa.v21i5.10109

Callendar, G. S., 1938: *The artificial production of carbon dioxide and its influence on temperature*, J. Roy. Met. Soc., v. 64, pp. 223-240. https://doi.org/10.1002/qj.49706427503 Available at: http://www.met.reading.ac.uk/~ed/callendar_1938.pdf

CERES Team, 2011: NASA Langley, Press Release, OLR Image, March 18. https://ceres.larc.nasa.gov/resources/images/#public-release-satellite-images

Cess, R. D. and S. D. Goldenberg, 1981: *The effect of ocean heat capacity upon global warming due to increasing atmospheric carbon dioxide*, J. Geophysical Res. v. 86. pp. 498-502. https://doi.org/10.1029/JC086iC01p00498

Charney, J. G.; A. Arakawa, D. J. Baker, B. Bolin, R. E. Dickinson, R. M. Goody, C. E. Leith, H. M. Stommel and C. I. Wunsch, 1979: *Carbon Dioxide and Climate: A Scientific Assessment*, Report of an ad hoc study group on carbon dioxide and climate, Woods Hole, MA July 23-27. https://geosci.uchicago.edu/~archer/warming_papers/charney.1979.report.pdf

Clark, R., 2023: *Time dependent energy transfer: The forgotten legacy of Joseph Fourier*, Science of Climate Change v. 3, no. 4, pp. 1-24. https://scienceofclimatechange.org/roy-clark-time-dependent-energy-transfer/

Clark, R., 2013a: *A dynamic, coupled thermal reservoir approach to atmospheric energy transfer Part I: Concepts,* Energy and Environment, v. 24, nos. 3-4, pp. 319-340. https://doi.org/10.1260/0958-305X.24.3-4.319

Clark, R., 2013b: *A dynamic, coupled thermal reservoir approach to atmospheric energy transfer Part II: Applications*, Energy and Environment, v. 24, nos. 3-4 pp. 341-359. https://doi.org/10.1260/0958-305X.24.3-4.341

Clark, R. and A. Rörsch, 2023: *Finding Simplicity in a Complex World - The Role of the Diurnal Temperature Cycle in Climate Energy Transfer and Climate Change*, Clark Rörsch Publications, Thousand Oaks, CA. Further details and supplementary material are available at: https://clarkrorschpublication.com/index.html

D'Aleo J. and A. Watts, 2010: *Surface temperature records: policy driven deception?* Aug. 27, http://scienceandpublicpolicy.org/images/stories/papers/originals/surface_temp.pdf (Link not working) Available at: https://venturaphotonics.com/files/6.0_D'Aaleo.Watts.Surface_temp.SPPC%202010.pdf

Donlon, C. J., P. J. Minnet, C. Gentemann, T. J. Nightingale, I. J. Barton, B. Ward and M. J. Murray, 2004: *Towards improved validation of satellite sea surface skin temperature measurements for climate research*, J. Climate v. 15, no. 4, pp. 353-369. https://doi.org/10.1175/1520-0442(2002)015<0353:TIVOSS>2.0.CO;2

Douglas, J. H., 1975: *Climate change: chilling possibilities*, Science News, March 1, v. 107, pp. 138-140. https://www.sciencenews.org/wp-content/uploads/2008/10/8983.pdf

Essex, C.; R. McKitrick and B. Andresen, 2007: *Does a global temperature exist?* J. Non-Equilibrium Thermodynamics, v. 32, no. 1, pp. 1-27. https://doi.org/10.1515/JNETDY.2007.001

Also available at: http://www.rossmckitrick.com/uploads/4/8/0/8/4808045/globtemp.jnet.pdf

Feldman D.R., K. N. Liou, R. L. Shia and Y. L. Yung, 2008: *On the information content of the thermal IR cooling rate profile from satellite instrument measurements*, J. Geophys. Res., v. 113, D1118, pp. 1-14. https://doi.org/10.1029/2007JD009041

Foley, J. C., 1947: *A study of meteorological conditions associated with bush and grass fires and fire protection strategy in Australia,* BOM Bulletin 38, 238 pp. https://nla.gov.au/nla.obj-257165724/view?partId=nla.obj-257176204#page/n4/mode/1up

Folland, C. K.; T. N. Palmer and D. E. Parker, 1986: *Sahel rainfall and worldwide sea temperatures*, Nature, v. 320, pp. 602-606. https://doi.org/10.1038/320602a0

Fourier, J.-B. J., 1824: *Remarques générales sur les températures du globe terrestre et des espaces planétaires*, Annales de Chimie et de Physique, v. 27, pp. 136–167. https://gallica.bnf.fr/ark:/12148/bpt6k65708960/f142.image# English translation: http://fourier1824.geologist-1011.mobi/

Gates, W. L., 1992: AMIP: *The Atmospheric Model Intercomparison Project,* Bull. Amer. Met Soc. v. 73, no. 12, pp. 1962-1970. https://doi.org/10.1175/1520-0477(1992)073<1962:ATAMIP>2.0.CO;2

Gentemann, C. L. F. J. Wentz, C. A. Mears and D. K. Smith, 2004: *In situ validation of Tropical Rainfall Measuring Mission microwave sea surface temperatures*, J. Geophysical Research v. 109, no. C04021, pp. 1-9. https://doi.org/10.1029/2003JC002092

Gibert, F.; J. Cuesta, J.-I. Yano, N. Arnault and P. H. Flamant, 2007: *On the Correlation between Convective Plume Updrafts and Downdrafts, Lidar Reflectivity and Depolarization Ratio*, Boundary Layer Meteorology, v. 5, pp. 553-573. https://doi.org/10.1007/s10546-007-9205-6

Gray, S. T., L. J. Graumlich, J. L. Betancourt and G. T. Pederson, 2004a: *A tree-ring based reconstruction of the Atlantic Multi-decadal Oscillation since 1567 A.D.*, Geophys. Res. Letts., v.

31, L12205, pp. 1-4. https://doi.org/10.1029/2004GL019932

Gray, S. T., L. J. Graumlich, J. L. Betancourt and G. T. Pederson, 2004b: *Atlantic Multi-decadal Oscillation (AMO) Index Reconstruction,* IGBP PAGES/World Data, Center for Paleoclimatology, Data Contribution Series #2004-062, NOAA/NGDC Paleoclimatology Program, Boulder CO, USA. https://www.ncei.noaa.gov/pub/data/paleo/treering/reconstructions/amo-gray2004.txt

HadCRUT4, 2022: *HadCRUT4 Data Series*, https://www.metoffice.gov.uk/hadobs/hadcrut4/data/current/time_series/HadCRUT.4.6.0.0.annual_ns_avg.txt

Hale, G. M. and M. R. Querry, 1973: *Optical constants of water in the 200 nm to 200 µm wavelength region*, Applied Optics, v. 12, no. 3, pp. 555-563. https://doi.org/10.1364/AO.12.000555

Hanel, R. A., B. Schlachman, D. Rogers and D. Vanous, 1971: *Nimbus 4 Michelson Interferometer*, Applied Optics v. 10, no. 6, pp. 1376-1382. https://doi.org/10.1364/AO.10.001376

Hansen, J. et al., (45 authors), 2005: *Efficacy of climate forcings*, J. Geophys. Research, v. 110, D18104, pp.1-45. https://pubs.giss.nasa.gov/docs/2005/2005_Hansen_ha01110v.pdf

Hansen, J., D. Johnson, A. Lacis, S. Lebedeff, P. Lee, D. Rind and G. Russell, 1981: *Climate impact of increasing carbon dioxide*, Science, v. 213, pp. 957-956. https://pubs.giss.nasa.gov/docs/1981/1981_Hansen_ha04600x.pdf

Hansen, J.; A. Lacis, D. Rind, G. Russell, P. Stone, I. Fung, R. Ruedy and J. Lerner, 1984: *Climate sensitivity: analysis of feedback mechanisms*, in *Climate Processes and Climate Sensitivity*, Geophysical Monograph 29, Maurice Ewing Volume 5, pp. 130-163, American Geophysical Union. https://doi.org/10.1029/GM029p0130

Hansen, J. R. Ruedy, A. Lacis, M. Sato, L. Nazarenko, N. Tausnev, I. Tegen and D. Koch, 2000: *Climate modeling in the global warming debate*, in Randall, D. A. (Ed.), *General Circulation Model Development*, International Geophysics Series, v. 70, Chapter 4, Academic Press, San Diego. https://vdoc.pub/documents/general-circulation-model-development-past-present-and-future-5ki27rscn990 Available at: https://venturaphotonics.com/files/7.0_Randall_Hansen.Chap.4.GISS1.pdf

Hansen, K., 2024: *Rising Maximum Temperatures*, Watts Up with That, Jan. 5. https://wattsupwiththat.com/2024/01/05/rising-maximum-temperatures/

Harde, H., 2017: *Radiation Transfer Calculations and Assessment of Global Warming by* CO_2, Int. J. Atmos. Sci., 9251034, pp. 1-30. https://doi.org/10.1155/2017/9251034

Harde, H., 2014: *Advanced two-layer climate model for the assessment of global warming by* CO_2, Open J. Atmos. and Climate Change, v. 1, no. 3, pp 1-50. http://hharde.de/index_htm_files/Harde-ACC-V1N3-001.pdf

Harper, K. C., 2004: *The Scandinavian tag team: Providers of atmospheric reality to numerical weather prediction efforts in the U. S. (1948-1955)*, Proc. Int. Commission on History of Meteorology, v. 1, no. 1, pp. 84-91. https://journal.meteohistory.org/index.php/hom/issue/view/2

Hausfather, Z., 2019: *CMIP6: The next generation of climate models explained*, Carbon Brief, Dec. 2. https://www.carbonbrief.org/cmip6-the-next-generation-of-climate-models-explained

Hays, J. D., J. Imbrie, and N. J. Shackleton, 1976: *Variations in the Earth's Orbit: Pacemaker of the Ice Ages*, Science, v. 194, pp 1121-1132. https://www.science.org/doi/10.1126/science.194.4270.1121

Herring, S. C., N. Christidis, A. Hoell and P. A. Stott, 2022: *Explaining Extreme Events of 2020 from a Climate Perspective* Bull. Amer. Meteor. Soc., v. 101, no. 1, pp. S1–S128. https://doi.org/10.1175/BAMS-ExplainingExtremeEvents2020.1 (and prior years in this series)

Humlum, O., 2024: *Greenhouse Gases, Atmospheric carbon dioxide* (CO_2), Climate4you. http://www.climate4you.com/

Humlum, O.; K. Stordahl and J-E Solheim, 2013: *The phase relation between atmospheric* CO_2

and global temperature, Global and Planetary Change, v. 100, pp. 51-69. http://dx.doi.org/10.1016/j.gloplacha.2012.08.008

Iacono, M. J., J. S. Delamere, E. J. Mlawer, M. W. Shephard, S. A. Clough, and W. D. Collins, 2008: *Radiative forcing by long-lived greenhouse gases: Calculations with the AER radiative transfer models*, J. Geophys. Res., v. 113, D13103 pp. 1-8. https://doi.org/10.1029/2008JD009944

Idso, C. D., R. M. Carter and S. F. Singer (Eds), 2013: *Climate Change Reconsidered II: Physical Science*, Chicago Il. The Heartland Institute http://climatechangereconsidered.org/climate-change-reconsidered-ii-physical-science/

Imbrie, J. and K. P. Imbrie, 1979: *Ice Ages: Solving the Mystery*, Harvard University Press, Cambridge, Mass.

IPCC AR6, 2021: Masson-Delmotte, V., P. Zhai, A. Pirani, S.L. Connors, C. Péan, S. Berger, N. Caud, Y. Chen, L. Goldfarb, M.I. Gomis, M. Huang, K. Leitzell, E. Lonnoy, J.B.R. Matthews, T.K. Maycock, T. Waterfield, O. Yelekçi, R. Yu, and B. Zhou (eds.), *Climate Change 2021: The Physical Science Basis. Contribution of Working Group I to the Sixth Assessment Report of the Intergovernmental Panel on Climate Change*. Cambridge University Press, Cambridge, United Kingdom and New York, NY, USA. Chapter 7, pp. 923-1054. doi: 10.1017/9781009157896.009, https://www.ipcc.ch/report/ar6/wg1/

IPCC, AR5*, 2013:* Stocker, T.F., D. Qin, G.-K. Plattner, M. Tignor, S.K. Allen, J. Boschung, A. Nauels, Y. Xia, V. Bex and P.M. Midgley (eds.). *Climate Change 2013: The Physical Science Basis. Contribution of Working Group I to the Fifth Assessment Report of the Intergovernmental Panel on Climate Change,* Cambridge University Press, Cambridge, United Kingdom and New York, NY, USA, (2014)1535 pp. ISBN 9781107661820. https://www.ipcc.ch/report/ar5/wg1/

IPCC, AR4, 2007: Solomon, S., D. Qin, M. Manning, Z. Chen, M. Marquis, K. B. Averyt, M. Tignor and H. L. Miller (eds.), *Climate Change 2007: The Physical Science Basis. Contribution of Working Group I to the Fourth Assessment Report of the Intergovernmental Panel on Climate Change,* Cambridge University Press, Cambridge, United Kingdom and New York, NY, USA. https://www.ipcc.ch/report/ar4/wg1/

IPCC, TAR, 2001: Houghton, J.T., Y. Ding, D.J. Griggs, M. Noguer, P.J. van der Linden, X. Dai, K. Maskell, and C.A. Johnson (eds.), *Climate Change 2001: The Scientific Basis. Contribution of Working Group I to the Third Assessment Report of the Intergovernmental Panel on Climate Change*, Cambridge University Press, Cambridge, United Kingdom and New York, NY, USA, 881 pp. https://www.ipcc.ch/site/assets/uploads/2018/03/WGI_TAR_full_report.pdf

IPCC, SAR, 1995: Houghton, J. T.; L.G. Meira Filho, B.A. Callander, N. Harris, A. Kattenberg and K. Maskell (Eds), *Climate Change 1995, The Science of Climate Change*, Cambridge University Press, Cambridge, 1996. https://www.ipcc.ch/site/assets/uploads/2018/02/ipcc_sar_wg_I_full_report.pdf

IPCC FAR, 1990: Houghton, J. T., G. J. Jenkins and J. J. Ephraums (Eds.), *Climate Change, The IPCC Scientific Assessment*, Cambridge University Press, New York. https://www.ipcc.ch/site/assets/uploads/2018/03/ipcc_far_wg_I_full_report.pdf

Jaworowski, Z., 2007: *CO_2: The greatest scientific scandal of our time*, Executive Intelligence Review (EIR) Science, v. 34, no. 11, March 16. https://www.larouchepub.com/eiw/public/2007/eirv34n11-20070316/38_711_science.pdf

Jones, P. D., T. M. L. Wigley, C. K. Foland, D. E. Parker, J. K. Angell, S. Lebedeff and J. E. Hansen, 1988: *Evidence for global warming in the past decade*, Nature, v. 332, p. 790. https://doi.org/10.1038/332790b0

Jones, P. D., T. M. Wigley and P. B Wright, 1986: *Global temperature variations between 1861 and 1984*, Nature, v. 323, no.31, pp. 430-434. https://www.nature.com/articles/322430a0

Kandel, R. and M. Viollier, (2010): *Observation of the Earth's radiation budget from space,* Comptes Rendus Geoscience, v. 342, no. 4-5, pp. 286-300. https://doi.org/10.1016/j.crte.2010.01.005

Keeling, 2023: *The Keeling Curve*. https://scripps.ucsd.edu/programs/keelingcurve/

Knutti, R. and G. C. Hegerl, 2008: *The equilibrium sensitivity of the Earth's temperature to radiation changes*, Nature Geoscience, v. 1, pp. 735-743. https://www.nature.com/articles/ngeo337

Koll, D. D. B and T. W. Cronin, 2018: *Earth's outgoing longwave radiation linear due to* H_2O *greenhouse effect*, *PNAS*, v. 115, no. 41, pp. 10293-10298. https://www.pnas.org/doi/10.1073/pnas.1809868115

Kottek, M., J. Grieser, C. Beck, B. Rudolf and F. Rubel, June 2006: *World Map of the Köppen-Geiger climate classification updated*, Meteorologische Zeitschrift, v. 15, no. 3, pp. 259-263. https://w2.weather.gov/media/jetstream/global/Koppen-Geiger.pdf

Koutsoyiannis, D., 2024: *Net Isotopic Signature of Atmospheric* CO_2 *Sources and Sinks: No Change since the Little Ice Age*, Sci V. 6, 17 pp. 1-27. https://doi.org/10.3390/sci6010017

Lettau, H. H. and B. Davidson, 1957: *Exploring the Atmosphere's First Mile. Proceedings of the Great Plains Turbulence Field Program, 1 August to 8 September 1953* Volume II, Site Description and Data Tabulation, Oxford, Pergamon Press. Available at: https://books.google.com/books?hl=en&lr=&id=5bcJAQAAI-AAJ&oi=fnd&pg=PA377&dq=Lettau,+H.H.+and+B.+Davidson,+Exploring+the+atmosphere%E2%80%99s+first+mile.+Oxford:+Pergamon+Press,+1957.&ots=N0vbpjURx3&sig=sSTz9EMWpwi0XysXHTcWcLNxWv0#v=onepage&q&f=false

Lewis, N. and J. Curry, 2018: *The Impact of Recent Forcing and Ocean Heat Uptake Data on Estimates of Climate Sensitivity*, J. Climate, v. 31, pp. 6051-6070. https://journals.ametsoc.org/view/journals/clim/31/15/jcli-d-17-0667.1.xml

Lindzen, R., 2024: *What is Climate?* Watts Up with That, Jan. 20. https://wattsupwiththat.com/2024/01/20/what-is-climate-richard-lindzen/

Lorenz, E. N., 1973: *On the Existence of Extended Range Predictability* J. Applied Meteorology and Climatology, v. 12, no. 3, pp. 543-546. https://journals.ametsoc.org/view/journals/apme/12/3/1520-0450_1973_012_0543_oteoer_2_0_co_2.xml?tab_body=fulltext-display

Lorenz, E.N., 1963: *Deterministic nonperiodic flow*, Journal of the Atmospheric Sciences, v. 20, no. 2, pp. 130-141. https://journals.ametsoc.org/view/journals/atsc/20/2/1520-0469_1963_020_0130_dnf_2_0_co_2.xml

MacCracken, M. C. and F. M. Luther (Eds.), 1985: *Detecting the climatic effects of increasing carbon dioxide*, US Department of Energy Report DOE/ER-0235. https://doi.org/10.2172/6264945

MacCracken, M. C. and F. M. Luther (Eds.), 1985: *Projecting the climatic effects of increasing carbon dioxide* US Department of Energy Report DOE/ER-0237. https://doi.org/10.2172/5885458

Manabe, S. and F. Möller, 1961: *On the radiative equilibrium and heat balance of the atmosphere*, Monthly Weather Review, v. 89, no. 12, pp. 503-532. https://doi.org/10.1175/1520-0493(1961)089<0503:OTREAH>2.0.CO;2

Manabe, S. and R. J. Stouffer, 1980: *Sensitivity of a global climate model to an increase of* CO_2 *concentration in the atmosphere*, J. Geophys Res., v. 85, no. C10, pp. 5529-5554. https://doi.org/10.1029/JC085iC10p05529]

Manabe, S. and R. J. Stouffer, 1979: *A* CO_2*-climate sensitivity study with a mathematical model of the global climate*, Nature, v. 282, pp. 491-493.

https://www.nature.com/articles/282491a0.pdf

Manabe, S. and R. F. Strickler, 1964: *Thermal Equilibrium of the Atmosphere with a Convective Adjustment*, J. Atmospheric Sciences, v. 21, pp. 361-385. https://climate-dynamics.org/wp-content/uploads/2016/06/manabe64a.pdf

Manabe, S. and R. T. Wetherald, 1975: *The effects of doubling the CO_2 concentration in the climate of a general circulation model*, J. Atmos. Sci., v. 32, no. 1, pp. 3-15. https://journals.ametsoc.org/view/journals/atsc/32/1/1520-0469_1975_032_0003_teodtc_2_0_co_2.xml?tab_body=pdf

Manabe, S. and R. T. Wetherald, 1967: *Thermal equilibrium of the atmosphere with a given distribution of relative humidity*, J. Atmos. Sci., v. 24, pp. 241-249. http://www.gfdl.noaa.gov/bibliography/related_files/sm6701.pdf

Mass, C., 2022: *The Colorado Wildfire and Global Warming: Is there a Connection?* Watts Up with That, Jan. 6. https://wattsupwiththat.com/2022/01/06/the-colorado-wildfire-and-global-warming-is-there-a-connection/

Math, F. A., Feb. 1934: *Battle of the chinook wind at Havre, Mont.*, Monthly Weather Review, pp 54-57. https://doi.org/10.1175/1520-0493(1934)62<54:BOTCWA>2.0.CO;2

McFarlane, F., 2018: *The 1970s Global Cooling Consensus was not a Myth*, Watts Up With That, Nov. 19. https://wattsupwiththat.com/2018/11/19/the-1970s-global-cooling-consensus-was-not-a-myth/

Mearns, E., 2017: *The Vostok Ice Core and the 14,000 Year CO_2 Time Lag*, Energy Matters, June 14. http://euanmearns.com/the-vostok-ice-core-and-the-14000-year-co2-time-lag/

Meehl, G. A., G. J. Boer, C. Covey, M. Latif and R. J. Stouffer, 1997: *Intercomparison Makes for a Better Climate Model*, Eos, v. 78, no. 41, pp. 445-451 October 14. https://doi.org/10.1029/97EO00276

Meehl, G. A.; C. Covey, T. Delworth, M. Latif, B. McAvaney, J. F. B. Mitchell, R. J. Stouffer and K. E. Taylor, 2007: *The WCRP CMIP3 Multimodel Dataset: A New Era in Climate Change Research*, Bull. Amer. Met. Soc., v. 88, no. 9, pp. 1383-1394. https://doi.org/10.1175/BAMS-88-9-1383

Messiah, A., 1999: *Quantum Mechanics*, Chapter IV, Dover Publications Inc., Mineola, NY.

Milankovitch Cycles, 2022: Wikipedia. https://en.wikipedia.org/wiki/Milankovitch_cycles

MODTRAN, 2024: *Infrared Atmospheric Radiation Code*. https://climatemodels.uchicago.edu/modtran/

Monckton, C, July 2008: *Climate Sensitivity Reconsidered*, Physics and Society, v. 37, no.3, pp. 5-19. https://engage.aps.org/fps/resources/newsletters/newsletter-archives/july-2008

Morice, C. P., J. J. Kennedy,N. A. Rayner and P. D. Jones, 2012: *Quantifying uncertainties in global and regional temperature change using an ensemble of observational estimates: The HadCRUT4 data set*, J. Geophysical Res. Atmospheres, v. 117, D08101, pp. 1-22. https://doi.org/10.1029/2011JD017187

NASA, 2017: *Smoke and fire in S. California*, Earth Oservatory, Terra-MODIS Satellite Image, Dec. 5, 2017. https://earthobservatory.nasa.gov/images/91379/smoke-and-fire-in-southern-california

NOAA, 2023: *Koppen-Geiger climate classifiation map*. https://www.noaa.gov/jetstream/global/climate-zones/jetstream-max-addition-k-ppen-geiger-climate-subdivisions

NRL, 2021: Naval Research Laboratory, HYCOM consortium for Data-Assimilative Ocean Modeling. https://www7320.nrlssc.navy.mil/GLBhycomcice1-12/

O'Neill, P., R. Connolly, M. Connolly, Willie Soon, B. Chimani, M. Crok, R. de Vos, H. Harde,

P. Kajaba, P. Nojarov, R. Przybylak, D. Rasol, O. Skrynyk, O. SkrynykP. Štěpánek, A. Wypych and P. Zahradníček, 2022: *Evaluation of the Homogenization Adjustments Applied to European Temperature Records in the Global Historical Climatology Network Dataset*, Atmosphere, v. 13, no. 2, 285, pp. 1-21. https://doi.org/10.3390/atmos13020285

Oke T. R., 2006: *Initial guidance to obtain representative meteorological observations at urban sites*, Instruments and Observing Methods, Report No. 81, WMO/TD-No. 1250, World Meteorological Association, pp. 47. https://www.researchgate.net/publication/265347633_Initial_guidance_to_obtain_representative_meteorological_observations_at_urban_sites

Otto, A., F. E. L. Otto, O. Boucher, J. Church, G. Hegerl, P. M. Forster, N. P. Gillett, J. Gregory, G. C. Johnson, R Knutti, N. Lewis, U. Lohmann, J. Marotzke, G. Myhre, D. Shindell, B. Stevens and M. R. Allen, 2013: *Energy budget constraints on climate response*, Nature Geoscience, v. 6 no. 6, pp. 415-416. ISSN 1752-0894. http://eprints.whiterose.ac.uk/76064/7/ngeo1836(1)_with_coversheet.pdf

Otto Ibid, Supplementary Material. https://static-content.springer.com/esm/art%3A10.1038%2Fngeo1836/MediaObjects/41561_2013_BFngeo1836_MOESM299_ESM.pdf

PDO, 2022: *Pacific Decadal Oscillation*. https://www.ncdc.noaa.gov/teleconnections/pdo/

Peterson, T. C., W. M. Connolley and J. Fleck, 2008: *The myth of the 1970's global cooling consensus*, Bull. Amer. Meteor. Soc., v. 86, pp. 1325-1337. https://doi.org/10.1175/2008BAMS2370.1

Plass, G. N., 1956a: *The influence of the 15-micron carbon dioxide band on the atmospheric infrared cooling rate*, Quarterly Journal of the Royal Meteorological Society, v. 82, pp. 310-324. https://doi.org/10.1002/qj.49708235307 Available at: http://www.rescuethatfrog.com/wp-content/uploads/2017/02/Plass-1956c.pdf

Plass, G.N., 1956b: *The Carbon Dioxide Theory of Climatic Change*, Tellus, v. 8, no. 2, pp. 140-154. https://onlinelibrary.wiley.com/doi/abs/10.1111/j.2153-3490.1956.tb01206.x

Pouillet, M., 1837: *Memoir on the solar heat, on the radiating and absorbing powers of the atmospheric air and on the temperature of space.* In: Scientific Memoirs selected from the Transactions of Foreign Academies of Science and Learned Societies, edited by Richard Taylor, v. 4, pp. 44-90. http://nsdl.library.cornell.edu/websites/wiki/index.php/PALE_ClassicArticles/archives/classic_articles/issue1_global_warming/n2-Poulliet_1837corrected.pdf

Original publication, 1836: *Mémoire sur la chaleur solaire: sur les pouvoirs rayonnants et absorbants de l'air atmosphérique et sur la température de l'espace,* Comptes Rendus des Séances de l'Académie des Sciences, Paris. v. 7, pp. 24-65.

Quayle, R. G.; D. R. Easterling, T. R. Karl and P. Y. Hughes, 1991: *Effects of recent thermometer changes in the cooperative station network*, Bull Amer Met Soc., v. 72, no.11, pp. 1718-1723. https://doi.org/10.1175/1520-0477(1991)072<1718:EORTCI>2.0.CO;2

Ramanathan, V. 1975: *Greenhouse effect due to chlorofluorocarbons: Climatic implications*, Science, v. 190, pp. 50-52. https://www.science.org/doi/abs/10.1126/science.190.4209.50

Ramanathan, V. and W. Collins, 1991: *Thermodynamic regulation of ocean warming by cirrus clouds deduced from observations of the 1987 El Niño*, Nature, v. 351, pp. 27–32. https://doi.org/10.1038/351027a0

Ramaswamy, V., W. Collins, J. Haywood, J. Lean, N. Mahowald, G. Myhre, V. Naik, K. P. Shine, B. Soden, G. Stenchikov and T. Storelvmo, 2019: *Radiative Forcing of Climate: The Historical Evolution of the Radiative Forcing Concept, the Forcing Agents and their Quantification, and Applications* Meteorological Monographs v. 59, Chapter 14. https://doi.org/10.1175/AMSMONOGRAPHS-D-19-0001.1

Rasool, S. I. and S. H. Schneider, 1971: *Atmospheric carbon dioxide and aerosols: Effects of large increases on global climate*, Science, v. 173, pp 138-141. https://www.science.org/doi/10.1126/science.173.3992.138

Raval, A. and V. Ramanathan, 1989: *Observational determination of the greenhouse effect*, Nature, v. 342 pp. 758-761. https://doi.org/10.1038/342758a0

Revelle, R. and H. E. Suess, 1957: *Carbon dioxide exchange between atmosphere and ocean and the question of an increase of atmospheric CO_2 during the past decades*, Tellus v. 9, pp. 18-27. https://doi.org/10.3402/tellusa.v9i1.9075

Riches, M. R. and F. A. Koomanoff, 1985: *Overview of the Department of Energy Carbon Dioxide Research Program*, Bull. Amer. Met. Soc., v. 66, no. 2, pp. 152-158. https://doi.org/10.1175/1520-0477(1985)066<0152:OOTDOE>2.0.CO;2

Salby, M. and H. Harde, 2022a: *What causes increasing greenhouse gases? Summary of a Trilogy*, Science of Climate Change, v. 2, no. 3 pp. 297-301. https://doi.org/10.53234/scc202212/16

Salby, M. and H. Harde, 2022b: *Theory of increasing greenhouse gases*, Science of ClimateChange, Vol. 2, No. 3, pp. 212-238, https://doi.org/10.53234/scc202212/17.

Salby, M. and H. Harde, 2021a: *Control of atmospheric CO2 - Part I: Relation of carbon 14 to the removal of CO_2*, Science Climate Change, v. 1, no. 2, pp. 177-195. https://doi.org/10.53234/scc202112/30.

Salby, M. and H. Harde, 2021b: *Control of Atmospheric CO_2 - Part II: Influence of Tropical Warming*, Science of Climate Change, v. 1, no.2, pp. 196-212. https://doi.org/10.53234/scc202112/12.

Schwendike, J., G. J. Berry, K. Fodor, M. J. Reeder, 2021: *On the Relationship Between the Madden-Julian Oscillation and the Hadley and Walker Circulations*, JGR Atmospheres, v. 126, no. 4, 10.1029/2019JD032117, pp. 1-28. https://doi.org/10.1029/2019JD032117

Shaman, J., R. M. Samelson and E. Skyllingstad, 2010: *Air–Sea Fluxes over the Gulf Stream Region: Atmospheric Controls and Trends*, J. Climate v. 23, no. 10, pp. 2651-2670. https://doi.org/10.1175/2010JCLI3269.1

Soden, B. J. and I. M. Held, 2006: *An assessment of climate feedbacks in coupled ocean-atmosphere models*, J. Climate, v. 19, pp. 3354-3360. https://doi.org/10.1175/JCLI3799.1

SOI, 2022: *Southern Oscillation Index* http://www.bom.gov.au/climate/enso/soi/

Stone, H. M. and S. Manabe, 1968: *Comparison among various numerical models designed for computing IR cooling*, Monthly Weather Review, v. 96, no. 10, pp 735-741. https://doi.org/10.1175/1520-0493(1968)096<0735:CAVNMD>2.0.CO;2

Stott, P.A., S.F.B. Tett, G.S. Jones, M.R. Allen, J.F.B.Mitchell and G.J. Jenkins, 2000: *External control of twentieth century temperature variations by natural and anthropogenic forcings*, Science, v. 290, pp. 2133-2137. https://www.science.org/doi/abs/10.1126/science.290.5499.2133

Stouffer, R. J., V. Eyring, G. A. Meehl, S. Bony, C. Senior, B. Steven, S, and K. E. Taylor, 2017: *CMIP5 scientific gaps and recommendations for CMIP6*, Bull. Amer. Met. Soc., v. 98, no.1, pp. 95-105. https://journals.ametsoc.org/doi/pdf/10.1175/BAMS-D-15-00013.1

Taylor, K. E., R. J. Stauffer and G. A. Meehl, 2012: *An overview of the CMIP5 and the experimental design*, Bull. Amer. Met. Soc., v. 93, no. 4, pp. 485-498. https://doi.org/10.1175/BAMS-D-11-00094.1

Terando, A., D. Reidmiller, S. W. Hostetler, J. S. Littell, T. D. Beard, Jr., S. R. Weiskopf, J. Belnap and G. S. Plumlee, 2020: *Using information from global climate models to inform policymaking—The role of the U.S. Geological Survey*, U.S. Geological Survey Open-File Report 2020–1058, 25 pp. https://doi.org/10.3133/ofr20201058

Tett, S.F.B., G.S. Jones, P.A. Stott, D.C. Hill, J.F.B. Mitchell, M.R. Allen, W.J. Ingram, T.C.

Johns, C.E. Johnson, A. Jones, D.L. Roberts, D.M.H. Sexton and M.J. Woodage, 2000: *Estimation of natural and anthropogenic contributions to 20th century temperature change*, Hadley Centre Tech Note 19, pp 52, Hadley Centre for Climate Prediction and Response, Meteorological Office, RG12 2SY, UK., https://adsabs.harvard.edu/full/2000ESASP.463..201T/0000201.000.html

TRITON, 2024: *TRITON Buoy Data*. https://www.pmel.noaa.gov/tao/drupal/disdel/

Tyndall, J., 1861: *On the Absorption and Radiation of Heat by Gases and Vapours, and on the Physical Connexion of Radiation, Absorption, and Conduction*, Philosophical Transactions of the Royal Society of London, v. 151, pp. 1-36. https://royalsocietypublishing.org/doi/pdf/10.1098/rstl.1861.0001

Tyndall, J., 1863: *On radiation through the Earth's atmosphere*, Proc. Roy. Inst., Jan 23, pp. 200-206.

UAH, 2022: *tlt temperature series*, University of Alabama, Huntsville. https://www.nsstc.uah.edu/data/msu/v6.0/tlt/uahncdc_lt_6.0.txt

Vinos, J., 2022: *Climate of the past, present and future*, Critical Science Press, Madrid. https://www.researchgate.net/profile/Javier-Vinos/publication/363669186_Climate_of_the_Past_Present_and_Future_A_scientific_debate_2nd_ed/links/63296077071ea12e36487da9/Climate-of-the-Past-Present-and-Future-A-scientific-debate-2nd-ed.pdf

Wagner, F.; B. Aaby and H. Visscher, 2002: *Rapid atmospheric CO_2 changes associated with the 8,200-years-B.P. cooling event*, PNAS, v. 99, no.19, pp. 12011-12014. https://doi.org/10.1073/pnas.182420699

Wang, W. C. and G. A. Domoto, 1974: *The radiative effect of aerosols on the earth's atmosphere*, J. Appl. Meteorology, v. 13, no. 5, pp. 521-534. https://doi.org/10.1175/1520-0450(1974)013<0521:TREOAI>2.0.CO;2

Wang, W. C., Y. L. Yung, A. A. Lacis, T. Mo and J. E. Hansen, 1976: *Greenhouse effects due to man-made perturbations of trace gases*, Science, v. 194, pp. 685-690. https://pubs.giss.nasa.gov/docs/1976/1976_Wang_wa07100z.pdf

Watts, A., 2021: Media FAIL on reporting the Pacific Northwest Heatwave, Watts Up With That, June 30. https://wattsupwiththat.com/2021/06/30/major-media-fail-on-reporting-the-pacific-northwest-heatwave/

Watts, A., 2020: *Climate Change? Temperature Hits 100 Degrees above Arctic Circle, Just Like 100 Years Ago*, Watts Up with That, July 23. https://wattsupwiththat.com/2020/06/23/climate-change-temperature-hits-100-degrees-above-arctic-circle-just-like-100-years-ago/

Wijngaarden, W. A. van and W. Happer, 2022: *IR Forcing by Greenhouse Gases*, CO_2 Coalition publication, June 10. https://co2coalition.org/wp-content/uploads/2022/03/Infrared-Forcing-by-Greenhouse-Gases-2019-Revised-3-7-2022.pdf

WRCC, 2022: *Western Region Climate Center*. https://wrcc.dri.edu/sod/arch/hbF.html

Yu, L., (2007): *Global variations in oceanic evaporation (1958-2005): The role of the changing wind speed*, J. Climate v. 20, no. 21, pp. 5376-5390. https://doi.org/10.1175/2007JCLI1714.1

Yu, L., X. Jin, and R.A. Weller, Jan. 2008: *Multidecade global flux datasets from the objectively analyzed air-sea fluxes (OAFlux) project: latent and sensible heat fluxes, ocean evaporation, and related surface meteorological variables,* Woods Hole Oceanographic Institution, OAFlux project technical report OA-2008-01, 64 pp. http://apdrc.soest.hawaii.edu/doc/OAFlux_TechReport_3rd_release.pdf

Zachos, J., M. Pagani, L. Sloan, E. Thomas and K. Billups, 2001: *Trends, rhythms and aberrations in the global climate, 65 Ma to present*, Science, v. 292, pp. 86-693. https://www.science.org/doi/abs/10.1126/science.1059412

Zelinka, M. D., T. A. Myers, D. T. McCoy, S. Po-Chedley, P. M. Caldwell, P. Ceppi, S. A. Klein and K. E. Taylor, 2020: *Causes of Higher Climate Sensitivity in CMIP6 Models*, Geophysical Research Letters, v. 47, e2019GL085782, pp. 1-12. https://agupubs.onlinelibrary.wiley.com/doi/pdf/10.1029/2019GL085782

Scientific Article

The 2023 Record Temperatures:
Correlation to Absorbed Shortwave Radiation Anomaly

Antero Ollila

School of Engineering (Emer.), Aalto University, Espoo, Finland

Klimarealistene
Vollsveien 109
1358 Jar, Norway
ISSN: 2703-9072

Correspondence:
aveollila@yahoo.com

Vol. 4.1 (2024)
pp. 74-87

Abstract

According to the paradigm of the IPCC global warming is solely due to anthropogenic causes. Record-high temperatures have been measured for the summer months of 2023 and the anthropogenic climate drivers – mainly greenhouse gases - have been named as culprits. Simple analyses reveal that the temperature increase of the year 2023 cannot be explained exclusively by anthropogenic climate drivers. The hypothesis of this study is to show that the main climate driver for the high temperature of 2023 has been the Absorbed Shortwave Radiation (ASR). The approach has been to apply the CERES (Clouds and the Earth's Radiant Energy System) satellite radiation measurements, which started in March 2001. Simple climate models have been applied since General Climate Models (GCM) cannot simulate cloudiness and shortwave radiation (SW) changes properly. The ASR changes are related mainly to cloudiness and aerosol particle changes. Since 2014 the global surface temperature growth rate has accelerated but this does not apply to anthropogenic climate drivers, and therefore the ASR changes are probably related to external forcings. The total Radiative Forcing (RF) according to the AR6 was 2.70 Wm^{-2} for the period 1750-2019. This can be compared to the change in the ASR, which was 2.01 Wm^{-2} from the year 2000 to the year 2023. This finding means that natural climate drivers have altogether an important role in recent global warming.

Keywords: High temperatures; absorbed solar radiation; ASR; natural climate drivers; simple climate models; positive water feedback

Submitted 2024-03-19, Accepted 2024-04-17, https://doi.org/10.53234/scc202403/15

1. Introduction

It looks like researchers have not been willing to simulate the temperature effects of ASR increase. A notable step on this issue was the study of Rantanen and Laaksonen (2024). They have concluded that the warmest September on record globally was September of 2023 by a record margin of 0.5°C. They applied the latest generation of GCMs and showed that internal climate variability combined with the steady increase in greenhouse gas forcing would be a highly unlikely climate driver (p ~ 1%). They suggest further analysis of the impact of external forcings on the global climate in 2023. Finally, Rantanen and Laaksonen did not suppose any concrete climate driver that could have contributed to the temperature increase.

Stephens et al. (2022) studied the reasons for the reduced amount of reflected sunlight, and they concluded that there is an equal split between cloudiness reduction and aerosol particles. They applied six different GCMs for temperature simulations and found that they were rather poor in calculating the cloud and aerosol impacts. Another reason is that the present paradigm of climate change is almost totally based on Anthropogenic Global Warming (AGW) theory and that is a reason why observation-based solar input variations have not been included in the GCMs.

The objectives of mainstream research studies normally do not cover solar radiation absorption impacts on the climate since it is not in line with the AGW (Anthropogenic Global Warming) theory of the IPCC. According to the AR6 (IPCC, 2021), the only natural climate driver was solar impact with 0,7 % negative impact on warming. One of the exceptions is Pinker et al. (2005) who studied the long-term variations of solar radiation on the Earth's surface (S) before 2001 using the longest available satellite records. They found that the increase of S was 0.16 $Wm^{-2}yr^{-1}$ from 1983 to 2001.

The probable explanation is the 60- and 88-year temperature oscillations of the climate, which are usually known as the AMO (Atlantic Multidecadal Oscillation) and Gleissberg cycle (Gleissberg, 1958). Ollila and Timonen (2022) have shown that both climate oscillations are global by nature, and the impacts of these cycles have been found employing several proxy temperature indicators in different places on the Earth. The mutual positive peak of the 60- and 88-year oscillations was in 1939, the negative peak was around 1975 and the new positive phases started thereafter. The result of Pinker et al. (2005) is in line with this oscillation behaviour of the climate, and also the reason is partially the same since the Gleissberg cycle is connected to solar radiation variations (Gleissberg, 1958).

It is well-known that clouds are the main challenge to climate change science. Trenberth and Fasullo (2009) concluded that low clouds play an important role as they can reduce ASR while having relatively little impact on OLR (Outgoing Longwave Radiation). They also confirmed that clouds are the largest source of uncertainty in GCMs. The same applies to state-of-the-art GCMs used and referred to in the AR6 of the IPCC (2021). The ERF (Effective Radiative Forcing) of the aerosol-cloud in the AR6 had decreased by 50 % from the AR5 (2013) to the value of -0.22 Wm^{-2} with the great uncertainty band of 0.51 Wm^{-2} describing this problem.

The CERES satellite radiation measurements started in March 2000, and Loeb et al. (2018) recognised the increased trend of ASR according to the CERES observations starting after 2015, Figure 1.

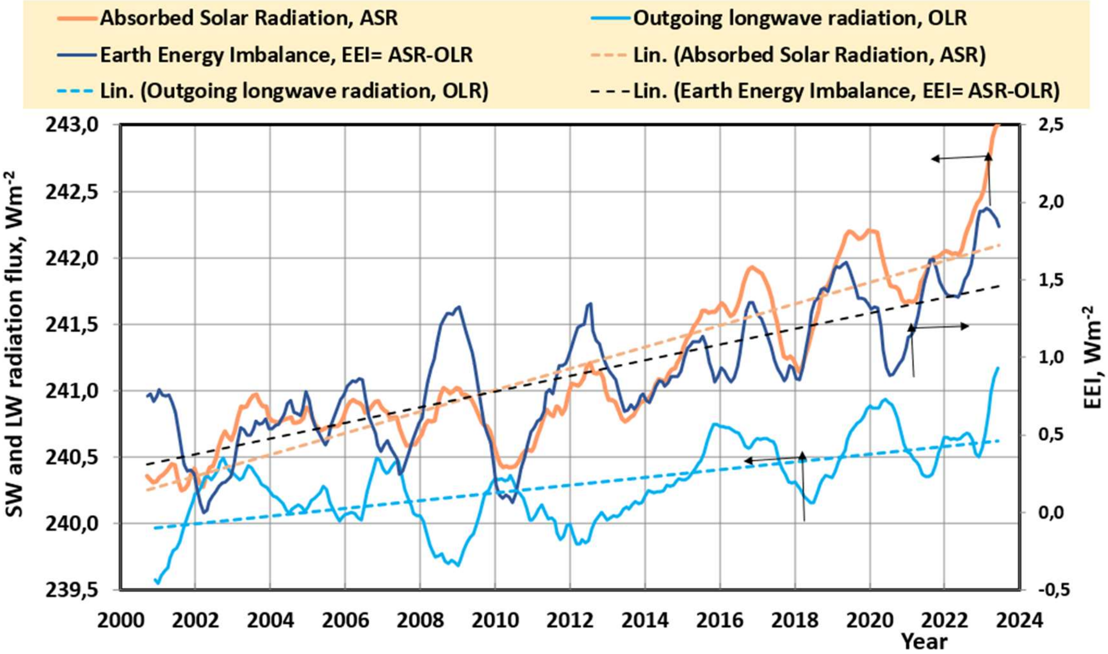

Figure 1: The ASR, OLR and EEI (Earth Energy Imbalance) trends from 2000 to 2023.

Figure 1 shows that the OLR level started to deviate from the ASR level after 2003. Loeb et al. (2021) have concluded that this increased energy input has mainly warmed the ocean, and it also has caused Earth's Energy Imbalance (EEI) since OLR has not been at the same level as the ASR since about 2003. They found that the main reason for increased ASR has been the reduction of low-level clouds.

Kato and Rose (2024) analyzed the EEI and found also a significant SW radiation absorptivity rate of 0.68 $Wm^{-2}dec^{-1}$. In the discussion section, they calculated how much temperature increase and precipitation this would cause.

CERES instruments (Priestley et al., 2011) were designed to provide 2-4 improvements in accuracy and stability over the previous satellite observation system ERBE (Earth Radiation Budget Experiment). There are four instruments on two satellites named *Terra* and *Aqua*, which cover three filtered radiance measurement bands: the shortwave band (0.3 – 5 μm), the total (0.3 – 100 μm), and the atmospheric window (8-12 μm). There is an Internal Calibration Module (ICM), which carries out automatic in-flight calibrations for each instrument. According to Priestley et al. (2011), the long-term ICM calibration stability has been better than 0.2 %, and the calibration traceability from ground to flight is 0.25 %.

Matthews has carried out research studies called the Moon and Earth Radiation Budget Experiment (MERBE) applying the albedo measurements of the Moon, whose reflectivity is very constant. According to Matthews (2021), the MERBE calibration system has revealed instrument telescope degradations, which are undetectable by the CERES calibration system. He has concluded that the Earth's albedo has been constant during his research period from 2001 to 2015, which would mean that the ASR variations by CERES instruments have been artifacts.

The author has not found any comments from NASA for the critics raised by the MERBE results. The research study Matthews was conducted in 2020 but it did not cover the period from 2015 onward, when the ASR variations started to increase significantly, and also the gap between the ASR and OLR increased at the same time. If the constant albedo of the Earth would have continued also during 2015-2020, it would have meant a major failure in the CERES calibration system.

Since mainstream climate scientists have continued to apply the published CERES radiation observations as noticed in the AR6 (IPCC, 2021), the author thinks that it is still justified to use CERES data. On the other hand, the gap between the OLR and the ASR radiation trends can be estimated at least partially to originate from the accuracy problems between these measurements. It should be noticed that the OLR instrument has a significantly broader measurement span than the ASR measuring instruments, which decreases the absolute accuracy of OLR measurements. This issue will be also addressed in the Discussion and Conclusion section.

The purpose and the scope of this study are to carry out analyses on the impact of ASR forcings on the temperature since 2000 except in a couple of studies giving perspective. The present GCMs do not apply to the analyses, since they do not utilise direct CERES radiation observations (Ollila, 2021) and are poor at simulating ASR variations (Trenberth and Fasullo, 2005; Stephens et al., 2022). The later analyses below reveal that GCMs do not consider indirect aerosols and cloud observations or estimates either according to the AR5 and the AR6 (IPCC, 2013; IPCC 2021). Therefore, simple climate models have been applied in this study.

2. Methods

2.1 Data

The temperature data are from GISS (2024) and UAH (2024), radiation data are from ERBE/ ERBS (Wong et al., 2005) and CERES (2024) satellite observations, and the Oceanic Niño Index (ONI, 2024) from NOAA. Greenhouse (GH) gas concentrations are from NOAA (2024) as well as the GH index values (AGGI, 2024).

2.2 Simple climate models

The main method is to analyze the impacts of anthropogenic and natural climate drivers by applying simple climate models and comparing the results to real temperature observations. The surface temperature values can be calculated using Eq. (1), as defined by the IPCC (2013) on page 664

$$dTs = \lambda \cdot RF \ [°C] \quad (1)$$

where dTs is the global mean surface temperature change, and λ is the climate sensitivity parameter. The temperature impact of effective radiative forcings (ERF) can be analyzed by this simple climate model which gives practically the same results as complicated GCMs on the global scale.

A mathematical expression for the climate sensitivity parameter λ can be derived from the Earth's energy balance

$$SC \cdot (1-\alpha) \cdot (\pi r^2) = \varepsilon \cdot \sigma \cdot T_e^4 \cdot (4\pi r^2) \; [Wm^{-2}] \qquad (2)$$

where SC is the solar constant, α is the albedo of the Earth, ε is emissivity, σ is the Stefan–Boltzmann constant, and T_e is the average emission temperature of OLR. The emissivity of the Earth's surface can be approximated to be 1, and therefore it can be omitted. From eq. (2) $T_e = (SC(1-\alpha)/(4\sigma))^{0.25} = 255.29$ K = -17.87°C.

The term SC(1-α) is the net radiative forcing RF_{net} of the Earth and eq. (1) can be written as $RF_{net} = \sigma T_e^4$. When this equation is derived, it will be $d(RF_{net})/dT_e = 4\sigma T_e^3 = 4RF_{net}/T_e$. By inverting this equation, λ will be

$$\lambda = dTe/d(RF_{net}) = T_e/(4RF_{net}) = T_e/(SC(1-\alpha)) \; [K/(Wm^{-2})] \qquad (3)$$

Using the average CERES (2021) values for the period 2008–2014 (Ollila, 2023), $\lambda = 255.29$ K/ $(1360.04*(1-0.2916)$ $Wm^{-2}) = 0.265$ $K/(Wm^{-2})$. This λ value means no water feedback mechanism and it has been applied in the counterfactual simple climate model called the "Ollila model" in this article utilising the varying radiation flux observations for SC and α calculations.

There might be doubts that the IPCC does not use any more so simple climate model as eq. (1). The IPCC has reported in chapter 7.4.2.1 of AR6 (IPCC, 2021) the latest results in calculating Planck response α_P, called also Planck feedback; α_P is called Planck feedback parameter. Planck feedback plays a fundamental stabilizing role in Earth's climate, and it is strongly negative: a warmer planet's surface radiates more energy to space. The AR6 (IPCC, 2021) defines that the equilibrium temperature change ΔTP is calculated in response to a radiative forcing ΔF like this:

$$\Delta TP = -\Delta F / \alpha_P \; [°C] \qquad (4)$$

Eq. (4) is in fact the same as eq. (1), if we notice that ΔTP = dTs, ΔF is the same as RF with the negative sign (RF reduces outgoing OLR), and $\alpha_P = -1/\lambda$.

An interesting analysis can be carried out on the greenhouse (GH) effect G, the magnitude of α_P, and the TCR of the IPCC. The normalized GH effect G_{av} (IPCC, 2021) has been defined as the ratio between G and the upwelling longwave (LW) flux at the surface LW_{up}. Applying the current flux estimates of the IPCC, the magnitude of $G_{av} = 159$ Wm^{-2} / 359 $Wm^{-2} = 0.4$, and this value can be assumed to be fairly constant (IPCC, 2021). LW_{up} can be calculated by the Planck radiation law $LW_{up} = \varepsilon \cdot \sigma \cdot T_s^4$. Planck feedback parameter α_P, which is an angle coefficient of a linearized Planck equation, can be calculated from equation $\alpha_P = -1/\lambda$ by applying the surface temperature T_s temperature 288 K (15 °)

$$\alpha_P = -1/\lambda = SC(1-\alpha)/T_s = (1360.04*(1-0.2916)/288 = -3.345 \quad [Wm^{-2}K^{-1}] \qquad (5)$$

The latest α_P value of the IPCC (2021) is -3.22 $Wm^{-2}K^{-1}$ based on the multi-kernel and multi-model average.

The Transient Climate Response (TCR) value of the AR6 (IPCC, 2021) is 1.8 °C caused by the RF value of 3.9 Wm^{-2}. The temperature increase of 1.8 °C increases the LW_{up} value by 10 Wm^{-2}. It means that the GH effect increase must be 10 Wm^{-2} – 3.9 Wm^{-2} = 6.1 Wm^{-2}. The G_{av} is now 0.61, which is 52.5 % more than $G_{av} = 0.40$ calculated using the flux and temperature values of the present climate. The reason can be easily identified. By applying the Planck feedback parameter -3.33 $Wm^{-2}K^{-1}$ (or λ value of 0.3 $K/(Wm^{-2})$, the temperature impact of 3.9 Wm^{-2} would be only 1.17 °C. This is close to 1.2°C as reported in chapter 8.6.2.3 of the AR4 (IPCC, 2007) without water feedback. The LW_{up} value corresponding to the T_s value of 16.3°C + 1.17°C = 17.48° is 404.6 Wm^{-2}, and the GHE effect is 404.6 - 239 = 165.5 Wm^{-2}. It means that the $G_{av} = 165.5$ Wm^{-2} / 404.6 Wm^{-2} = 0.409. It is close to the G_{av} value in the present climate of 0.40 but using the positive water feedback, the G_{av} value of 0.61 deviates significantly from 0.40, which should not happen according to the AR6 (IPCC, 2021).

The earlier λ values of the IPCC were taken from the study of Ramanathan et al. (1985), based on eight research papers giving an average value of 0.5 K/(Wm^{-2}), varying from 0.47 K/(Wm^{-2}) to 0.53 K/(Wm^{-2}). When Syuruko Manabe was awarded the Nobel Prize for Physics in 2021, one of Manabe's main credits was that Manabe and Wetherald (1967) were the first to introduce positive water feedback. They proposed that water feedback doubles the original RF of CO_2, and their λ value was 0.53 K/(Wm^{-2}). This quality became one of the essential features of GCMs as early as the 1980s.

The λ value of 0.5 K/(Wm^{-2}) was also specified in assessment reports 3 and 4 of the IPCC (2001, 2007). The AR5 of the IPCC (2013) did not specify the exact λ value but it can be calculated. The RF value of CO_2 concentration was 3.70 Wm^{-2} and the average TCR (Transient Climate Response) value was 1.8°C (5% to 95% range 1.2°C to 2.4°C) in the AR5 (IPCC 2013) giving λ value of 0.49 K/(Wm^{-2}).

The IPCC (2021) did not report a λ value for ERF in AR6, but it can be calculated from the data in Fig. 7.6 and Fig. 7.7 of the AR6, which are based on the GCM calculations. The λ value is 1.27 K / 2.70 Wm^{-2} = 0.47 K/(Wm^{-2}), which is applicable for a temperature change calculation according to eq. (1).

Even though eq. (1) looks so simple, it can be applied with astonishing accuracy to the temperature calculations from 1750 onward for monthly, annual, and decadal temperature changes and even to scenario calculations till 2100. Applying eq. (1) gives the TCR value of 1.85°C (= 0.47 °C/(Wm^{-2}) *3.93 Wm^{-2}), while the best estimate of the AR6 (IPCC 2021) is 1.8°C. The dTs for the worst-case Shared Socio-economic Pathway scenario SSP5-8.5 would be according to eq. (1), dTs = 0.47 K/(Wm^{-2}) * 8.5 Wm^{-2} = 4.0°C (IPCC 2021). The average warming value according to the AR6 (IPCC, 2021) is the same. These examples show that the average warming values calculated with the complicated GCMs can be calculated using eq. (1). The explanation is that the temperature changes caused by ERF alternations less than 10 Wm^{-2} depend almost linearly on ERFs (Ollila, 2023). Both the TCR and SSP scenario calculations, reported and approved by the IPCC, assume that positive water feedback duplicates the warming impacts of CO_2.

2.3 ASR trend and impact on temperatures

According to the AR5, the total ERF in 2011 was 2.34 Wm^{-2}, which caused a warming of 1.15°C per eq. (1). This is 0.3°C more than the observed 0.85°C (IPCC, 2013) meaning a 35% error.

The IPCC (2021) writes in the AR6 (Figures 7.6, and 7.7) that the global warming calculated by GCMs by 2019 was 1.27°C and this was caused by the ERF of 2.7 Wm^{-2}. The ERF was a sum of anthropogenic ERF values of 2.72 Wm^{-2} and an insignificant change in solar activity of -0.02 Wm^{-2}. This is an almost perfect result considering IPCC climate models, as the corresponding observed temperature increase in 2020 was 1.26°C according to Figure 1.12 of AR6 (IPCC, 2021). Even though this is looking good, a closer analysis reveals discrepancies.

The observed temperature increased by 0.44°C from 2011 to 2019, and at the same time, the ERF increased from 2.34 Wm^{-2} to 2.70 Wm^{-2} (IPCC, 2013; IPCC, 2021) meaning an increase of 0.36 Wm^{-2}. The ERF change of 0.36 Wm^{-2} from 2011 to 2019 causes a temperature change dTs = 0.47 K/(Wm^{-2}) * 0.36 Wm^{-2} = 0.17°C. Since the observed dTs change of this period was 0.44°C, the non-anthropogenic (natural) climate drivers have caused the rest of the change of 0.27°C. This result is in conflict that the anthropogenic ERF of 2.72 Wm^{-2} alone can cause global warming of 1.27°C. It also raises questions about the role of natural climate drivers in global warming during the longer period from 1750 to 2100.

The same analysis can be carried out for the year 2023. The NOAA Greenhouse Index (AGGI, 2023) collects the annual RF values of GH gases. The annual growth rate has been about 1.8% during recent years, and it means that the annual RF increase for the year 2023 has been about 0.042 Wm^{-2}. The CO_2 forcing according to the IPCC has been 0.032 Wm^{-2} meaning the portion of 79%. The annual temperature increase of 2023 has been 0.28°C (GISS, 2023). Applying eq. (1) the RF of 0.042 Wm^{-2} would mean the temperature impact of 0.47°C/(Wm^{-2}) * 0.042 Wm^{-2} = 0.019°C, which is only 6.8% from the observed temperature increase of 0.28°C. This finding is in line with the conclusion of Rantanen and Laaksonen (2024) that nonanthropogenic forcings must have a significant impact on the September temperatures of 2023.

ASR is the difference between the total solar irradiance (TSI) and the reflected shortwave radiation upward (SWup) from the Earth. The ASR trend of the 2000s cannot be explained by changes in incoming solar radiation, as the TSI trend is negligible (−0.053 Wm^{-2} per decade). Loeb et al. (2021) have concluded that the increase in EEI from 2005 to 2019 is primarily due to an increase in ASR and a decrease in OLR. They also conclude that the increased energy input of the Earth has warmed the ocean, and the land, and melted ice, and therefore the surface temperature has not increased in direct proportion to this energy increase.

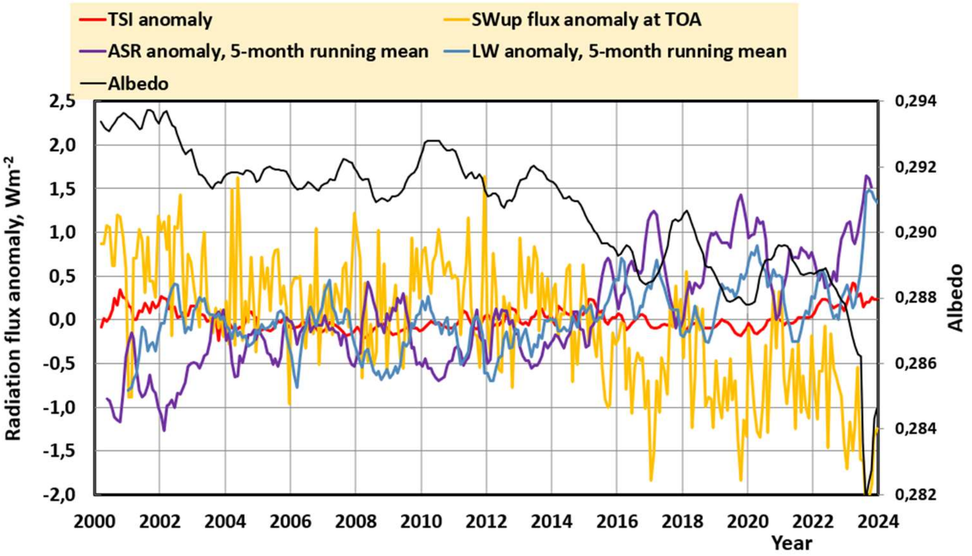

Figure 2: The anomaly trends of TSI, SW flux, LW flux, and ASR at the TOA as well as the albedo trend of the Earth. The numerical values of the radiation flux trends have been excerpted from the CERES (2024) data.

Figure 2 shows the well-known oscillatory behaviour of the solar cycle, which is now closing its maximum peak, which will probably happen in 2024 - 2025. The ASR anomaly (ASRa) trend shows that it has increased from 2015 onward but the TSI anomaly marked as TSIa has had only a small impact on this increase. It means that the ASRa increase is mainly due to the decrease of the Earth's albedo. The maximum difference in monthly ASRa values from March 2000 to October 2023 is 3.5 Wm^{-2}. The annual increase from the first year 2000 to 2023 is 2.01 Wm^{-2}, and the total RF from 1750 to 2019 has been 2.70 Wm^{-2}. By comparing the magnitude of the ASRa signal to the RF value of CO_2 forcing, it is easy to notice that it is a very significant climate driver. The average value of the LW anomaly for 2001-2023 is 0.00 Wm^{-2}, and the same ASR anomaly is +0.05 Wm^{-2}, which is not an essential difference. The problem between the ASR and LW fluxes seems to be in absolute radiation flux observations.

The main objective of this study is to find out the roles of ASR and ENSO (El Niño Southern oscillation) in explaining the high temperatures of the period 2015-2023 and to show that natural climate drivers have a significant role in the temperature increase in the recent years.

3. Results

3.1 Temperature trend correlation to ASR in the 2000s

Before analysing these figures more closely, the surface temperature trends and ASRa trends are useful to depict together.

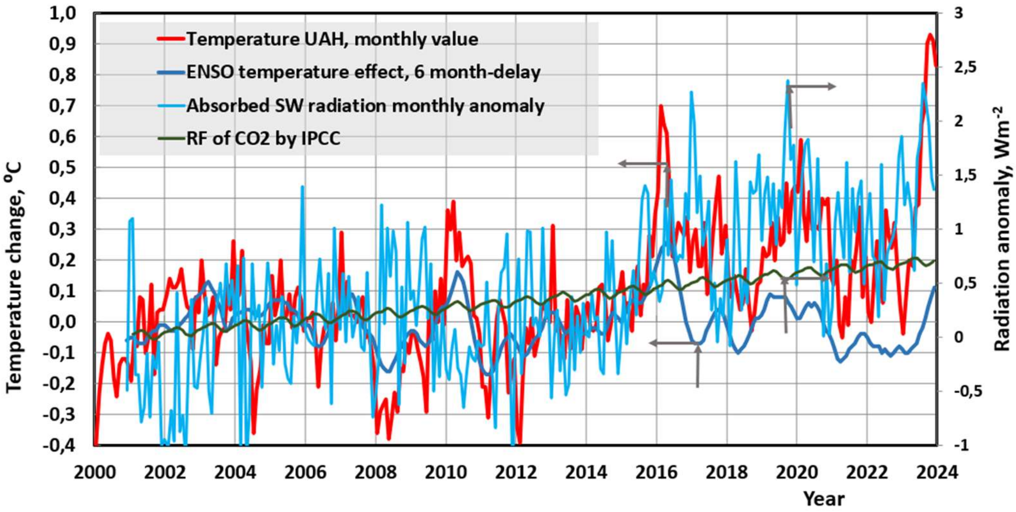

Figure 3: The trend in UAH (2023) temperature anomaly, ASRa trend, change in radiative forcing (RF) of carbon dioxide (NOAA 2023) calculated from 2010 onwards according to the IPCC (2023), and the temperature effect of ENSO.

The growth rates of the temperature trend (GISS 2023) and the ASRa trend (CERES 2023) in Figure 3 show a strong correlation after the temperature pause of 2000-2014. During the period 2011-2019, the ERF value of the IPCC (2021) increased in eight years by 0.36 Wm^{-2} meaning a yearly RF value of 0.045 Wm^{-2} (= 0.36 Wm^{-2} / 8), which causes an insignificant average yearly temperature growth of 0.021°C (=0.47 K/Wm^{-2} * 0.045 Wm^{-2}) according to eq. (1). Figure 3 depicts the ERF impact of CO_2 (IPCC, 2021), which does not correlate to monthly temperature changes, since its monthly RF impacts are exceedingly small: about 0.027 Wm^{-2}.

The ASRa increase from 2011 to 2019 was 1.29 Wm^{-2} having a global temperature impact of 0.34°C (= 0.265 K/(Wm^{-2}) * 1.29 Wm^{-2}). Adding this impact to the observed temperature of 0.85°C in 2011 would give a warming value of 1.19°C leaving only 0.10°C for other climate drivers. There is no ASR climate driver among the RF agents in Figures 7.6 and 7.7 of the AR6 (IPCC, 2021). The ASR impacts should be identified in the RF agent “Aerosols-cloud” and/or “Aerosols-radiation”. The sum of the “Aerosols-clouds” has decreased from -0.82 Wm^{-2} in 2011 to -1,00 Wm^{-2} in 2019 per the AR5 and AR6. It means that according to the IPCC science, the ASR, aerosols, and clouds have decreased the radiative forcing and they have decreased temperature by -0.085°C. This is not in line with the CERES observations, which show the opposite change.

Record-high temperatures have been measured for the summer months of 2023, Figure 4. The temperature increase from January 2023 to October 2023 was 1.02°C (UAH, 2024). According to AR6 of the IPCC (2021), global warming is solely due to anthropogenic causes but this rapid warming rate is not in line with this theory considering the warming impacts of anthropogenic climate drivers as analyzed in the Introduction section.

The warming impact of the ENSO effect emerged after April 2023 (ONI, 2023), when La Niña started to fade, and the present El Niño emerged in May. The positive impact of ENSO on surface temperatures started in August-September 2023 since there is a 6-month delay in the temperature impact of the ONI index (Trenberth and Fasullo, 2015; Ollila, 2021). The conclusion is that the increase in recent temperatures in 2023 has mainly been due to non-anthropogenic causes.

The ASR signal trend shows a decrease after August 2023, when at the same time the ONI index starts to increase. This may be connected to the increased cloudiness in the Niña regions. The study of Ollila (2020) found that the cloudiness of Niña regions 3, 4 and 5 increased as the ONI index increased. The ASR forcing increase is very probably related to the decrease of low clouds in the ocean areas (Loeb et al., 2021).

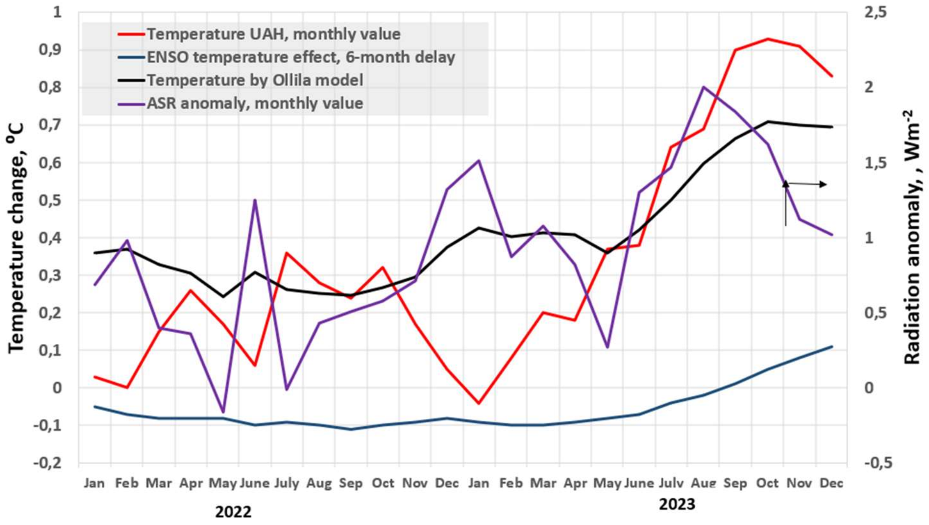

Figure 4: The UAH temperature, ASR, ENSO temperature trends and the Ollilla-model calculated temperature from January 2022 to December 2023.

The trends in Figures 2 and 3 originate from NASA's measurements by CERES satellites, which are also shown in Figure 7.11 of AR6. This issue has been reported or analyzed only in a few publications (Loeb et al., 2018; Stephens et al., 2022; Loeb et al., 2021; IPCC, 2021; Ollila, 2022; Kato and Rose, 2024) and has not been reported in the media. According to the IPCC, anthropogenic radiative forcings for the period 1750 to 2019 were a total of 2.70 Wm^{-2}. The change in ASR in August 2023 was about 3.1 Wm^{-2} more than in 2000 (Figure 2), i.e. more than all anthropogenic factors together from 1750 to 2019 (IPCC, 2021).

The problem is that the IPCC calculation shows no increase in the ASR of 1.29 Wm^{-2} from 2011 to 2019, for which there are direct CERES measurements. It can be estimated that the increase of 1.29 Wm^{-2} according to IPCC science corresponds to a temperature increase of about 0.61°C (= 0.47 K/Wm^{-2} * 1.29 Wm^{-2}). This temperature effect cannot be found in Figures 7.6 and 7.7 of the AR6 (IPCC 2021). A possible explanation is that because climate models cannot reliably calculate changes in cloud cover, the IPCC has completely excluded the ASR impact from warming calculations.

3.2 Connection between ASR and super El Niños

Ollila (2020) noticed that during the two very strong El Niños 1997-1998 and 2015-2016 – also called super El Niños - the ASR temperature effect was slightly more than the El Niño temperature effect. The same phenomenon can be found also during the ongoing El Niño 2023-2024, Fig. 5.

A closer analysis reveals that in these three cases, the ASR anomaly maximum happens in September-October, which is 2-3 months before the El Niño maximum in December. This is a rather strong piece of evidence that the ASR maximum peak may trigger and contribute to El Niño becoming a super El Niño.

An opposite event happened during the strong El Niño 2009-2010. It can be theorized that this El Niño did not develop into a super El Niño, since the ASR anomaly was negative, and also its peak value did not happen 2-3 months before December.

It can be noticed in Figure 5 that the GISS temperature started to deviate from the UAH (the University of Alabama in Huntsville) satellite observations after 2003. It looks like the UAH temperature is more sensitive to El Niño spikes.

It can be also noticed in Figure 5 that during the ongoing El Niño, the ASR temperature effect is about 100% more than the El Niño effect itself. This seems to be related to a higher overall ASR anomaly level after El Niño 2015-2016. It means that there has been an enduring change in the atmospheric conditions – probably in the reduced amount of low-level clouds.

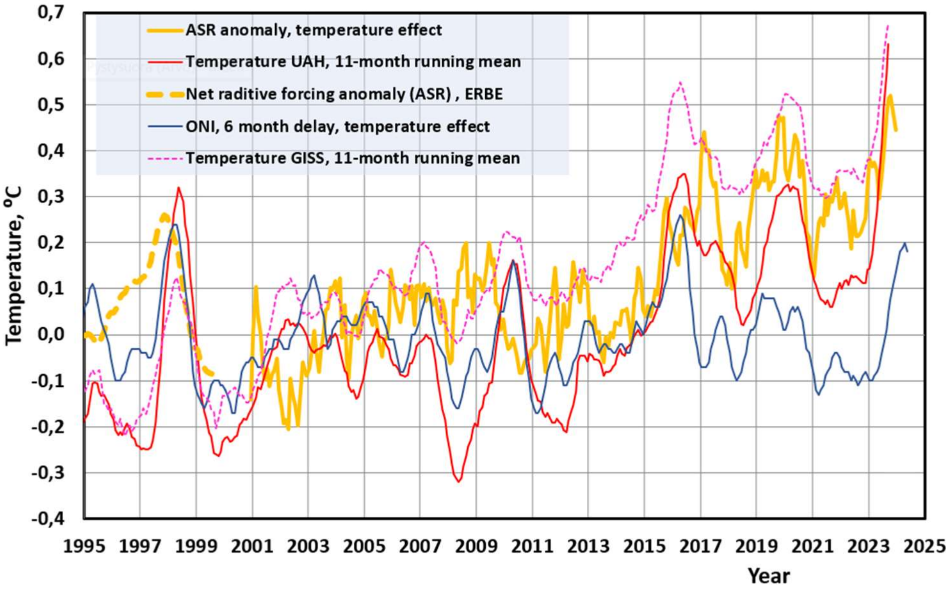

Figure 5: The UAH and GISS temperature trends, ENSO temperature effects and ASR simulated temperature effects according to ERBE and CERES observations.

3.3 Simple climate model simulations

The temperature effects from 2001 to September 2023 can be simulated using both the IPCC's simple climate model and the simple climate model of Ollila (2023) by starting temperature changes from zero in 2001, Figure 6. In the IPCC model, a λ value of 0.47 Wm^{-2} was applied, and the CO_2 impact was calculated using eq. (1), but the other GHG effects were omitted due to their insignificant temperature impact of about 0.02°C in the 21-year simulation period. ERF equation of Ollila (2023) was applied for CO_2 ($ERF = 3.83 * \ln(CO_2/280)$), which gives the ERF value of 2.65 Wm^{-2} for 560 ppm. The ASR value was calculated according to CERES observations as a difference between TSI and SWup anomalies. The λ value was calculated according to the actual CERES observation variations (SWup / TSI). In both models, the temperature impact dTs of the ENSO effect has been calculated from the ONI index by applying an equation $dTs = 0.1 * ONI$ with a 6-month delay in temperature impact (Trenberth and Fasullo, 2013; Ollila 2021). The dynamical time constants for the ocean were 2.74 months and for land 1.04 months (Stine et al., 2009).

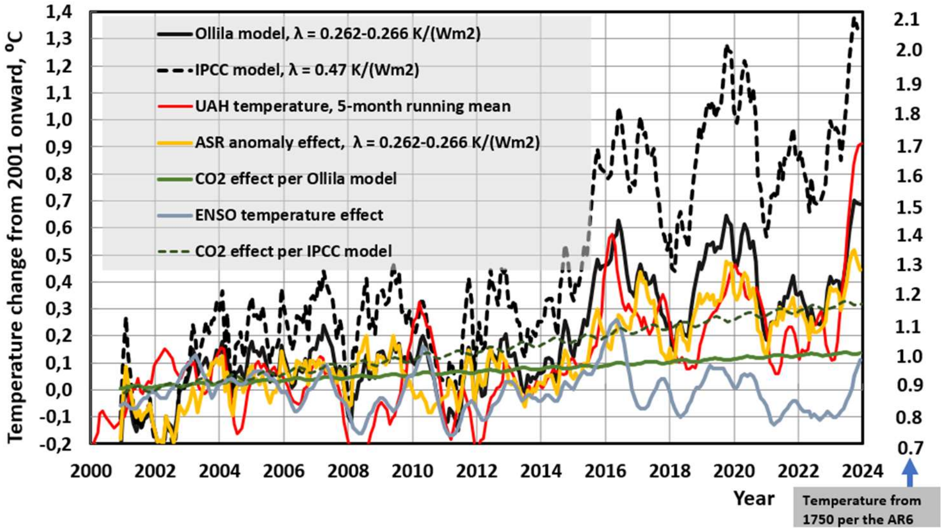

Figure 6: The results of two simple climate models, considering the increase in absorbed solar radiation (ASR) from 2001 onwards.

The temperature increase from the reference period 2001-2014 to 2023 was 0.52°C (UAH, 2024). The corresponding temperature change according to the IPCC's simple model is the sum of the ASR change of 0.68°C, CO_2 forcing 0.22°C, and the ENSO effect, -0.01°C, to give a total of +0.89°C, meaning an error of +0.37°C. The Ollila model is the sum of an ASR change of 0.39°C, CO_2 forcing of 0.09°C, and ENSO effect of -0.01°C, for a total of 0.47°C, meaning an error of +0.05°C in respect of UAH temperature.

The major ASRa increase occurred after the end of the pause of 2014. The average UAH temperature of 2015-2023 is 0.28°C, the Ollila model calculated temperature is 0.39°C and the IPCC-model calculated average value is 0.85°C. Both models follow the dynamic changes of the temperature very well confirming that the time constants of dynamics are correct. The difference between the two models is mainly due to the water feedback mechanism and of course the missing ASRa impact in the IPCC model.

During the simulation period from 2001 to 2024, the albedo value varied from 0.2937 to 0.2819 (Figure 2). The climate feedback parameter λ varied from 0.262 to 0.266 K/(Wm^{-2}). It means that the average λ value 0.265 K/(Wm^{-2}) is applicable in simulations.

There are justified questions about the homogenisation practises applied in the updating GISS temperature data sets, which have decreased the historical temperatures and increased the temperatures of the recent decades. Another problem with global data sets is the UHI (Urban Heat Island) phenomenon which has increased the modern time temperatures due to changes in measurement sites from nonurban areas to urban areas. To avoid these problems, the UAH temperature data set was applied as a reference.

Figure 6 shows that changes in global temperature, especially after 2014, are due to the ASR and the ENSO effect. Carbon dioxide has an insignificant impact on annual and monthly temperature changes. El Niño (ONI, 2023), which has been developing during the summer of 2023, has started to have a temperature impact after August 2023, since its global temperature effects will come with a delay of about six months. The high temperatures of the recent months of 2023 are almost solely due to the increased ASR values, the values of which are currently known only until December 2023.

4. Discussion and conclusion

Some special reasons have been suggested in public discussions as explanations for the high temperatures of 2023, which can be shortly analyzed. The impact of El Niño has been the most popular explanation but as analyzed in the text, its impact in 2023 has not been significant.

A positive anthropogenic effect on the ASR anomaly can be expected from the new regulations of the International Maritime Organization (IMO 2019) limiting sulphur emissions from the shipping industry since a reduction in sulphur aerosols reduces cloudiness. Diamond (2023) has studied the quantitative impacts of sulphur emissions and the result was that the instantaneous radiative forcing on a global scale was at a maximum of 0.1 Wm^{-2} up to date. Rantanen and Laaksonen (2024) have estimated this impact to be from 0.02 to 0.06 Wm^{-2}, and the effects of Hunga Tonga volcano eruption to be from 0.02 to 0.07 Wm^{-2}. These impacts are insignificant in relationship to ASR forcing changes. Stephens et al. (2022) estimated that aerosol reductions have a greater impact.

Hodnebrog et al. (2024) have also concluded that aerosol emission reductions have increased the ASR but during the last two decades according to GCM simulations, the major impact has increased EEI. They estimated that accelerated surface warming may be expected in this decade. The GCMs could not explain about 40 % of the extra ASR indicating the well-known problems of GCMs in aerosol and cloud simulations. The CERES data shows that reflectivity has been falling in both hemispheres whereas pollution has fallen mainly in the north.

Gavin Schmidt, who is the director of the NASA Goddard Institute for Space Studies (GISS), has written in the World View article (Nature, 2024) that the anthropogenic drivers have increased the temperature since 2022 by only about 0.02 °C, and even taking all plausible explanations into account, the gap between the expected and observed annual mean temperatures in 2023 remains about 0.2 °C. This opinion is noteworthy since it may be the first time that an acknowledged climate scientist admits that they are confounded since it looks like they are on unchartered territory.

Marsh and Svensmark (2000) have found a likely reason for cloudiness changes as they identified a relationship between the solar-modulated cosmic rays on global cloud cover (≤ 3 km). The Sun itself is also a secondary source of cosmic rays in the form of charged energetic particles known as the solar wind. So far there is no generally accepted evidence about the reasons for the changes in the Earth's albedo causing the changes in the ASR. The ASR trends during the last ten years urge further research on this subject.

The analyses of this study show that natural climate drivers have had a significant role in global warming after the temperature pause ended in 2014. In September 2023, the radiative forcing of ASR anomaly has been greater than the sum of the anthropogenic climate drivers from 1750 to 2019 according to the IPCC science. The IPCC has omitted the ASR anomaly impacts in the summary of the climate radiative forcings in Figure 7.6 and Figure 7.7 of the AR6 (IPCC, 2021) even though they have referred to this anomaly in Figure 7.3, which is consistent with the CERES observation data and the graphs of Loeb et al. (2018) and Ollila (2021).

The analysis revealed that the positive water feedback in TCR values - GCM-calculated or by a simple climate model - conflicts with the normalized G effect values (G_{av}) calculated by applying the IPCC's method and numerical values. The temperature simulations by simple climate models show that the positive water feedback results in significant errors during the period from 2000 to 2024.

Ten researchers of Hadley Center have proposed in their comment article (Betts et al., 2023) a new procedure to define the temperature calculation method, which could be used for recognising overriding the 1.5°C threshold. They got an incentive since they thought that there was no definition for the reference period nor the actual temperature measurement period in the Paris Agreement in 2015 (IPCC, 2015).

Indeed, these definitions cannot be found in the Paris Agreement (COP21, 2015) but they were defined later in the document of the IPCC (2018). In this document, the reference period is calculated from 1850 to 1900 representing the preindustrial time. Warming will be calculated for any given time as a 30-year average for smoothing out natural variability, which means a period starting 30 years before the calculation point. Betts et al. (2023) propose a 20-year period, which is a combination of ten historical yearly values concerning the last observation year and ten years of forecast values based on estimated emissions used as input in GCMs. This procedure would react faster to temperature changes than the IPCC definition giving thus more time for cutting emissions. This proposal is based on the IPCC science that global warming is almost solely due to anthropogenic causes, and ASR rapid and strong anomalies have no impacts.

Two observations can be made. CO_2 emissions reached the present rate of about 10 GtC (gigatons of carbon) during the COVID-19 pandemic. Still, the CO_2 concentration has been increasing at almost a constant rate. On the other hand, the climate community have closed their eyes to the fact that the ASR has increased at a significant rate varying from -1.52 Wm^{-2} to +1.84 Wm^{-2} from 2001 to December 2023. The RF value of the ASR has increased from 2001 to 2023 with the value of 2.01 Wm^{-2}, which is 74 % of the total RF value of 2.70 Wm^{-2} reported by the IPCC from 1750 to 2019. The ASR variations together with the ENSO effects explain quite well the global temperature variations.

There are scientific groundings to question the accuracy and calibration capabilities of the CERES measurements. The analyses and the results of this study show that the ASR based on the CERES observations can explain the temperature variations of the 2000s exceptionally well. It is a good reason to use the CERES measurements until more evidence can be gathered against the CERES calibration deficiencies.

Anyway, the temperature simulations by a simple climate model show that the observed and model-calculated temperatures have good equivalence. Since the surface temperature is closely related to the longwave radiation of the surface and further to the OLR, it raises a justified question that EEI may be an artifact based on the accuracy problems between the SW and LW measurements by the CERES instruments.

It looks like at least one natural climate driver - which has a name and measurable radiative forcing value - has a significant role in the recent high temperatures. Media and politicians are not aware of this fact. This also means that the planned and agreed actions on CO_2 emissions are not based on the real impacts of the anthropogenic climate drivers.

Statements and Declarations

This work has not received any funding. The author declares that he has no conflict of interest.

Chief-Editor: H. Harde; Reviewers: anonymous.

References

AGGI, 2024: *The NOAA annual Greenhouse Index (AGGI).* https://gml.noaa.gov/aggi/aggi.html

Betts RA, Belcher SE, Hermanson L, Klein Tank A, Lowe JA, Jones CD, Morice CP, Rayner NA, Scaife AA, Stott PA, 2023: *Approaching 1.5°C: how will we know we've reached this crucial warming mark?* Nature 624, 33-35. https://doi.org/10.1038/d41586-023-03775-z

CERES, 2024: *CERES EBAF-TOA Data.* The National Oceanic and Atmospheric Administration (NOAA). https://ceres-tool.larc.nasa.gov/ord-tool/jsp/EBAFTOA42Selection.jsp

COP21, 2015: *Adoption of the Paris Agreement framework convention on climate change*. UNFCCC, Paris, 1-32, https://unfccc.int/sites/default/files/english_paris_agreement.pdf

Diamond MS, 2023: *Detection of large-scale cloud microphysical changes within a major shipping corridor after implementation of the International Maritime Organization 2020 fuel sulfur regulations.* Atmos. Chem. Phys. 23, 8259–8269. https://acp.copernicus.org/articles/23/8259/2023/

GISS, 2024: *Land-ocean temperature index of NASA*. https://data.giss.nasa.gov/gistemp/tabledata_v4/GLB.Ts+dSST.txt

Gleissberg W, 1958: *The eighty-year sunspot Cycle.* J. Br. Astron. 68, 148-152.

Hodnebrog Ø, Myhre G, Jouan C, Andrews T, Forster PM, Jia H, Loeb NG, Olivié DJL, Paynter D, Quaas J, Raghuraman SP, Schulz M, 2024: *Recent reductions in aerosol emissions have increased Earth's energy imbalance.* Commun Earth Environ. 5, 166. https://www.nature.com/articles/s43247-024-01324-8

IMO, 2019: *Resolution mepc.320(74) 2019 guidelines for consistent implementation of the 0.50 % sulphur limit under marpol annex v*. London, UK. https://www.imo.org/en/OurWork/Environment/Pages/Index-of-MEPC-Resolutions-and-Guidelines-related-to-MARPOL-Annex-VI.aspx

IPCC, TAR, 2001: *Climate Change 2001, The Physical Science Basis. Contribution of Working Group I to the Third Assessment Report of the Intergovernmental Panel on Climate Change.* Cambridge Univ. Press, Cambridge, U.K., and New York, https://www.ipcc.ch/site/assets/uploads/2018/03/WGI_TAR_full_report.pdf

IPCC, AR4, 2007: *Climate Change 2007, The Physical Science Basis. Contribution of Working Group I to the Fourth Assessment Report of the Intergovernmental Panel on Climate Change.* Cambridge Univ. Press, Cambridge, U.K., and New York, https://www.ipcc.ch/site/assets/uploads/2018/02/ar4-wg1-frontmatter-1.pdf

IPCC, AR5, 2013: *Climate Change 2013, The Physical Science Basis. Contribution of Working Group I to the Fifth Assessment Report of the Intergovernmental Panel on Climate Change*. Cambridge Univ. Press, Cambridge, U.K., and New York, https://www.ipcc.ch/site/assets/uploads/2017/09/WG1AR5_Frontmatter_FINAL.pdf

IPCC, 2018: *Summary for Policymakers, Global Warming of 1.5 °C*. World Meteorological Organization*.*, Geneva, Switzerland, https://www.ipcc.ch/sr15/

IPCC, AR6, 2021: *Climate Change 2021, The Physical Science Basis. Contribution of Working Group I to the Sixth Assessment Report of the Intergovernmental Panel on Climate Change*. Cambridge Univ. Press, Cambridge U.K., https://www.ipcc.ch/report/ar6/wg1/

Kato S, Rose FG, 2024: *Global and regional entropy production by radiation estimated from satellite observations.* AIP Conf. Proc. 2988, 050007. https://pubs.aip.org/aip/acp/article/2988/1/050007/3022156/Global-and-regional-entropy-production-by

Loeb NG, Thorsen TJ, Norris JR, Wang H, Su W, 2018: *Changes in Earth's energy budget during and after the "pause" in global warming: An observational perspective.* Climate 6, 62, https://www.mdpi.com/2225-1154/6/3/62

Loeb NG, Johnson GC, Thorsen TJ, Lyman JM, Rose FG, Kato S, 2021: *Satellite and ocean data reveal marked increase in Earth's heating rate*. Geophys. Res. Lett. 48, e2021GL093047. https://doi.org/10.1029/2021GL093047

Manabe S, Wetherald RT, 1967: *Thermal equilibrium of the atmosphere with the given distribution of relative humidity.* J. Atm. Sci. 24(3), 241-259. https://climate-dynamics.org/wp-content/uploads/2016/06/manabe67.pdf

Marsh ND, Svensmark H, 2000: *Low cloud properties influenced by cosmic rays*. Phys. Rev. Lett. 85(23), 5004–5007, https://journals.aps.org/prl/abstract/10.1103/PhysRevLett.85.5004

Matthews G, 2021: *NASA CERES spurious calibration drifts corrected by lunar scans to show the Sun is not increasing global warming and allow immediate CRF detection.* Geophys. R. ch Lett. 48, e2021GL092994. https://doi.org/10.1029/2021GL092994

NOAA, 2024: *Carbon dioxide, methane and nitrogen oxide concentrations.* Global Monitoring Laboratory (GML) of the National Oceanic and Atmospheric Administration (NOAA). https://gml.noaa.gov/ccgg/trends/

Ollila A, 2020: *The pause end and major temperature impacts during super El Niños are due to shortwave radiation anomalies.* PSIJ 24(2), 1-20, https://doi.org/10.9734/psij/2020/v24i230174

Ollila A, 2021: *Global Circulation Models (GCMs) simulate the current temperatures only if the shortwave radiation anomaly of the 2000s has been omitted*. Curr. J. App. Sci. Techn. 42(46), 111-183, https://doi.org/10.9734/cjast/2021/v40i1731433

Ollila A, 2023: *Radiative forcing and climate sensitivity of carbon dioxide (CO_2) fine-tuned with CERES data.* Curr. J. App. Sci. Techn. 40(17), 45-52, https://doi.org/10.9734/cjast/2023/v42i464300

Ollila A, Timonen M, 2023*: Two main temperature periodicities related to planetary and solar activity oscillations.* https://hal.science/hal-04160543

ONI, 2024: *Oceanic Niño Index (ONI),* NOAA, https://ggweather.com/enso/oni.htm

Pinker RT, 2005: *Do Satellites Detect Trends in Surface Solar Radiation?* Science, 308(5723). 850–854. https://doi.org/10.1126/science.1103159

Priestley KJ, Smith GL, Thomas S, Cooper D, Lee III RB, Walikainen D, Hess P, Szewczyk ZP, Wilson R, 2011: *Radiometric Performance of the CERES Earth Radiation Budget Climate Record Sensors on the EOS Aqua and Terra Spacecraft through April 2007*. J. Tech. 28(1), 3–21. https://doi.org/10.1175/2010JTECHA1521.1

Ramanathan V, Cicerone RJ, Singh HB, Kiehl TJ, 1985: *Trace gas trends and their potential role in climate change*. J. Geophys. Res. 90, 5547-5566, https://doi.org/10.1029/JD090iD03p05547

Rantanen M, Laaksonen A, 2024: *The jump in global temperatures in September 2023 is extremely unlikely due to internal climate variability alone*. npj. Clim. Atmos. Sci. 7, 34, https://www.nature.com/articles/s41612-024-00582-9

Schmidt G, 2024: *Climate models can't explain 2023's huge heat anomaly — we could be in uncharted territory*. Nature 627*,* 467, https://www.nature.com/articles/d41586-024-00816-z

Stephens GL, Hakuba MZ, Kato S, Gettelman A, Dufresne J-L, Andrews T, Cole JNS, Willen U, Mauritsen T, 2022: *The changing nature of Earth's reflected sunlight*. Proc. R. Soc. A 478, 20220053, https://doi.org/10.1098/rspa.2022.0053

Stine AR, Huybers P, Fung IY, 2009: *Changes in the phase of annual cycle of surface temperature.* Nature 457, 435-441, https://www.nature.com/articles/nature07675

Trenberth KE, Fassullo JT, 2009: *Global warming due to increasing absorbed solar radiation*. Geophys. Res. Lett. 36, L07706. https://doi.org/10.1029/2009GL037527

Trenberth KE, Fasullo JT, 2013: *An apparent hiatus in global warming*? Earth's Future, 1(1), 19-32. https://doi.org/10.1002/2013EF000165

UAH, 2024: *UAH global temperature data set*. The University of Alabama Huntsville. https://www.nsstc.uah.edu/data/msu/v6.0/tlt/uahncdc_lt_6.0.txt

Wong T, Wielicki BA, Lee III RB, Smith LS, Bush KA, Willis JK, 2005: *Reexamination of the observed decadal variability of the Earth radiation budget using altitude-corrected ERBE/ERBS nonscanner WFOV data.* J, Climate 19, 4028-4040. https://ntrs.nasa.gov/api/citations/20080014856/downloads/20080014856.pdf

Klimarealistene
Vollsveien 109
1358 Jar, Norway
ISSN: 2703-9072

Correspondence:
ilkmcnaughton@hotmail.com

Vol. 4.1 (2024)
pp. 88-106

Temperature Measurements Versus Carbon Dioxide Concentrations & Population Growth

Ian L K McNaughton

Sydney, Australia

Abstract

For many years, the scientific debate about the threat of rising global temperatures caused by rising atmospheric carbon dioxide concentration has depended on estimation, homogenization, the use of anomalies rather than actuals, and complex computer modelling of key variables. This estimation process with its complexity leaves their broad conclusions open to challenge. This paper attempts a simpler approach using temperature data from the seven Australian Capital Cities, seven Australian towns and five global cities/regions, and only basic computations, mainly graphical, to test the relationship between the key variables in the debate.

None of the graphs showed any visible correlation between exponentially increasing concentrations of CO_2 and increasing temperatures. Admittedly, both these variables are rising but that does not mean there is a connection between the two in the manner claimed by some climate scientists: namely, that the rise in carbon dioxide concentration is causing the global temperatures to rise. Indeed, there is an increasing body of opinion that claim the opposite is true: namely, in addition to the many other sources of carbon dioxide emissions, the naturally occurring rise in temperature causes the release of carbon dioxide from the oceans thus contributing to increasing its concentration in the atmosphere. This paper supports that view.

It is accepted by all scientists that global temperatures are rising. This paper concludes that this is due to cosmic, global and local influences and not to the rising concentration of carbon dioxide.

It was not the purpose of this paper to discuss how changes in complex local, global, and cosmic processes over extended periods of geological time influence the weather except to agree that they do, noting that the rise in global temperature can be linked directly to the inter glacial cycles that have occurred during the past thousands of years and will continue to occur indefinitely.

Instead, this paper focusses on the outcome of their combined effects in terms of surface temperature levels and atmospheric CO_2 concentrations, presented in graphical form and extrapolated to provide an indication of what values they are likely to take in the future.

Keywords: Population; CO_2; temperature

Submitted 2024-03-20, Accepted 2024-06-20. https://doi.org/10.53234/SCC202406/18

1. Introduction

Controversy around climate change continues to be widespread throughout the world. Although there is wide agreement that the world's climate is changing – always has, always will – the controversy centres on whether CO_2 generated by human activity is the cause of what is claimed to be a more rapid increase in temperature that would otherwise ***not*** have occurred without the presence of humans, especially during the period of the Industrial Revolution (1760 – 1840) and beyond.

The bulk of one side of this debate has centred on complex calculations of the trend in average global temperatures over the last century and a half, expressed as temperature "anomalies" [1]. The complexity of these calculations and reliability of the result are seen by some as problematic. When set against rising carbon dioxide concentration in the atmosphere, the temperatures resulting from these calculations are stated by some Climate Scientists to have a strong positive correlation. Extrapolation of this relationship into the future by complex computer modelling has led to widespread concern about life-threatening "global warming" caused by the presence of humans, now and into the future. Not unexpectedly, this has created a demand throughout the world for urgent action to reduce the concentration of atmospheric CO_2 at the global level.

This paper challenges the results of the above modelling [2] by adopting the simpler approach of graphing actual temperatures for the chosen surface sites (measured since 1672 in one case and since the late 1800s in most other cases) against accepted data for global CO_2 concentration, and a basic extrapolation of that data into the future. To do this, use was made of the wide range of data now available on the web for the various target sites: Sydney, other Australian cities and some Australian towns [3], Central England [4] and later to include Autauga County Alabama USA [5], Bangkok [6], Boston [7], and Sacramento [8]. In total, data from nineteen local and global sites was obtained and graphed, all of which are shown in Sections 11, 12 and 13.

Figure 2 shows the variation of CO_2 globally for the period 1650 to 2022. The raw data shown has been enhanced using an EXCEL tool that provides a "best-fit" curve (Trend Line) [9] – in this case, a polynomial of the 4th degree extrapolated to the year 2100. Figure 3 shows both the variation of CO_2 and the population growth in Sydney enhanced with a "best-fit" curve – a polynomial of the 2nd degree, also extrapolated to the year 2100. Other mathematical options available in EXCEL for Trend Line generation were polynomial, logarithmic, power, and moving-average. The "moving-average" Trend line closely resembled the graph of the raw data but could not be extrapolated in either direction. Extrapolation of the temperature Trend line using a polynomial of the 2nd degree produced results close to the linear solution for the first few years, but 3rd, 4th, 5th or 6th degrees produced significantly unreal increases or decreases or both in the predicted future temperatures at Observatory Hill and Central England, so were not used.

Trend Lines are seen to be an excellent representation of the change over time for each of the variables, and closely follow the actual recorded values of temperature and CO_2 concentration data from the various sources.

Figure 3 shows that the increase in CO_2 concentrations correlates well with increases in population represented by Sydney data [10] – this is to be expected - but increases in temperature (Figure 2) continue independently of these two factors, being influenced mostly, if not entirely, by the ever-present local, global, and cosmic forces that have affected temperatures throughout geological time. This suggests that, regardless of what action the world takes to reduce or eliminate future increases in CO_2 concentrations, global temperatures will continue to increase independently from the concentration of CO_2 in the atmosphere. We are currently in an inter-glacial period at a point where it is accepted that there are general temperature rises (and falls) due to cosmic influences.

The year 1740 was chosen as closest to the lower limits of useful data; the year 2100 was chosen as common for current discussions of climate change in the literature. In the final set of graphs for the seven Australian cities, the date range, 1740 to 2100, was used since this range clearly shows the variation of CO_2 concentrations for over 200 years.

In some graphs, the year 2050 was also chosen as a date commonly used in discussions. It is favoured by Global Warming activists and by the many governments who are encouraging and implementing solutions (all involving a reduction in the concentration of CO_2 in the atmosphere) to ensure the increase in temperature by 2050 is kept to less than 2.0 °C above the average global temperature as measured in 2023. The predictions for 2050 in this paper are only a third of that amount: ~0.47 °C (see Table 1).

The rates of change for temperatures at all sites were calculated from measurements taken at any two points on their linear Trend Lines. Options available in EXCEL were used to ensure that the measurements from graphs were as accurate as possible.

2. Central England Temperatures

The UK Met Office maintains a detailed national and regional temperature database extending back to 1672 for the Central England region (CE). According to the literature, there were:

> *".....too few reliable long-term temperature records to extend the series to the whole of the UK prior to 1884, and before that, scientists relied upon a composite regional database known as the Central England Temperature series, or CET. The CET series draws on records from a roughly triangular area bounded by Lancashire, London, and Bristol.*
>
> *This temperature series starts in 1659 and was originally compiled by Cambridge climatologist Gordon Manley in 1953. It is the longest instrumental temperature record in the world, and is updated monthly by the Met Office Hadley Centre in Exeter....."*

The temperatures recorded for Central England were average temperatures for the region.

Data for Central England temperatures was only available in graphical form (Figure 1) from the website, so a technique was devised to simplify extraction of data from the graph into the digital format used in Figure 2.

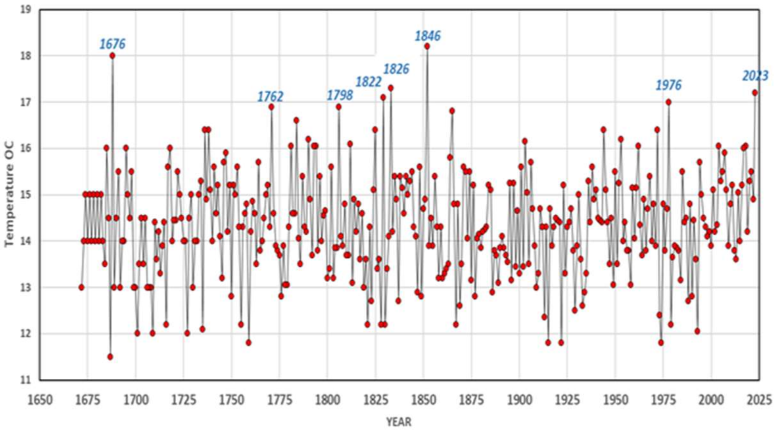

Figure 1: June mean temperatures in Central England, 1659 to 2023.

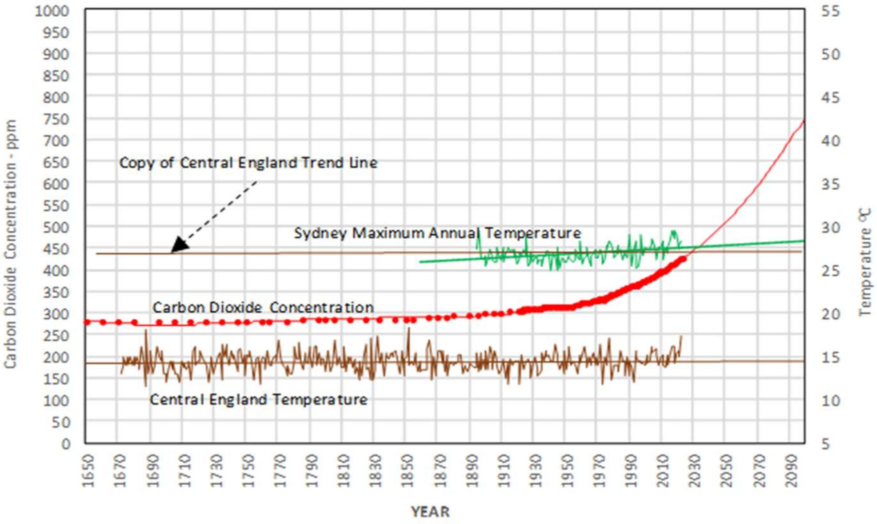

Figure 2: Sydney & Central England Temperatures versus CO_2 Concentrations for the overall period, 1650 to 2100.

Note the huge annual variability in the original temperature graph (Figure 1) which is a challenge to any analysis based on averages calculated for small periods within the full date range.

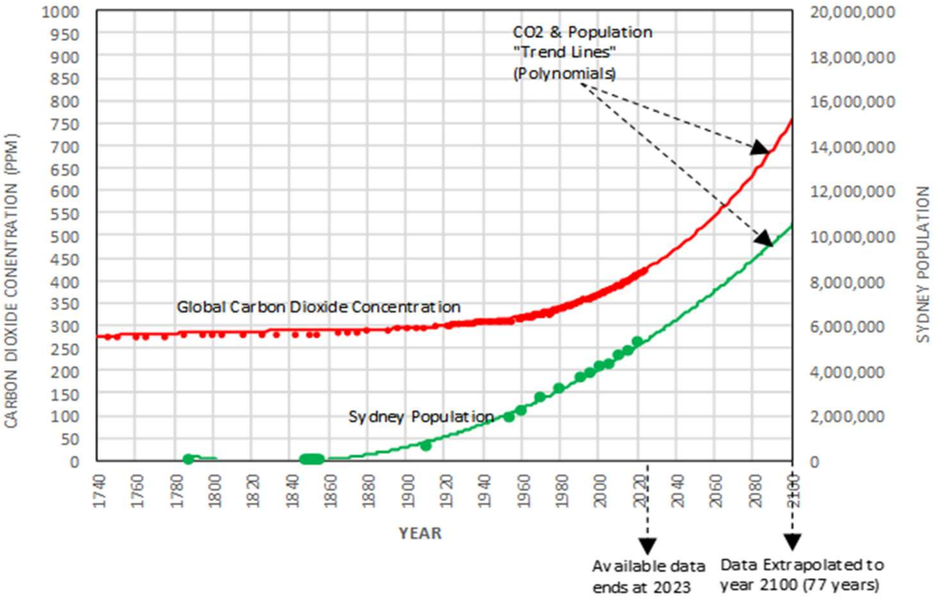

Figure 3: Carbon Dioxide Concentration versus Population Growth in Sydney for the periods 1740 (CO_2) and 1788 to 2023 (population).

3. Urban Effect on Temperature

Using the increasing population of Sydney to represent the increasing population of the world, Figure 3 indicates a degree of correlation between population and the increasing global concentration of CO_2 caused by the increasing number of people, vehicles and other machinery that emit an increasing volume of CO_2 over the years in an urban environment.

There is a phenomenon known as the urban heat island (UHI) [11] that, it is claimed, affects temperatures recorded in cities such as Sydney. Considering all the sources of heat that exist in a city compared to the countryside, it is not surprising that the UHI exists. For example, the population of ~5 million people in Sydney generates an average of 100 Watts per person which totals 500 MW, although admittedly, this heat is spread very thinly over an area of approximately 12,367 square kilometres. Add to this the heat being generated by all the (heat-emitting) machinery that exist in a large city and it is not surprising that when combined, these factors have an impact on the temperatures being recorded in cities.

In the book, "The Urban Physical Environment: Temperature and Urban Heat Islands", by Gordon M. Heisler, Anthony J. Brazel [14] and published in 2010, is written:

> *".....The UHI effect is strongest with skies free of clouds and with low wind speeds. In moist temperate climates, the UHI effect causes cities to be slightly warmer in midday than rural areas, whereas in dry climates, irrigation of vegetation in cities may cause slight midday cooling compared to rural areas. In most climates, maximum UHIs occur a few hours after sunset; maximum intensities increase with city size and may commonly reach 10°C, depending on the nature of the rural reference. Since the recognition of London's UHI by Luke Howard in the early 1800s, UHIs of cities around the world have been studied to quantify the intensity of UHIs, to understand the physical processes that cause UHIs, to estimate the impacts of UHIs, to moderate UHI effects, and to separate UHI effects from general warming of Earth caused by accumulation of greenhouse gases in the upper atmosphere....."*

Also written:

> *"……Despite considerable research, many questions about UHI effects remain unanswered. For example, it is still not clear what portion of the long-term trends of increasing temperatures at standard weather stations is caused by UHI effects and how much is contributed by greenhouse gas effects. Also not well quantified is the effect of increasing tree cover in residential areas on temperatures….."*

Regardless of the above and other related phenomena, this paper only considers the ***outcome*** of the combined effect of all the meteorological processes in terms of the temperatures measured at specific city and regional sites.

4. Types of Temperatures Measured

In the case of the Sydney temperature data, two sets are used in this paper corresponding to a compilation of the highest temperature recorded in each year in one set, and the lowest temperature recorded in each year in the other. Figure 4 shows the two sets of temperature data covering the ranges, 1860 to 2023 for minimum temperatures and 1895 to 2023 for the maximum temperatures for each year along with CO_2 concentrations. The graph includes boundary lines parallel to the Trend Lines and enclosing the extremes of each of the temperature data sets.

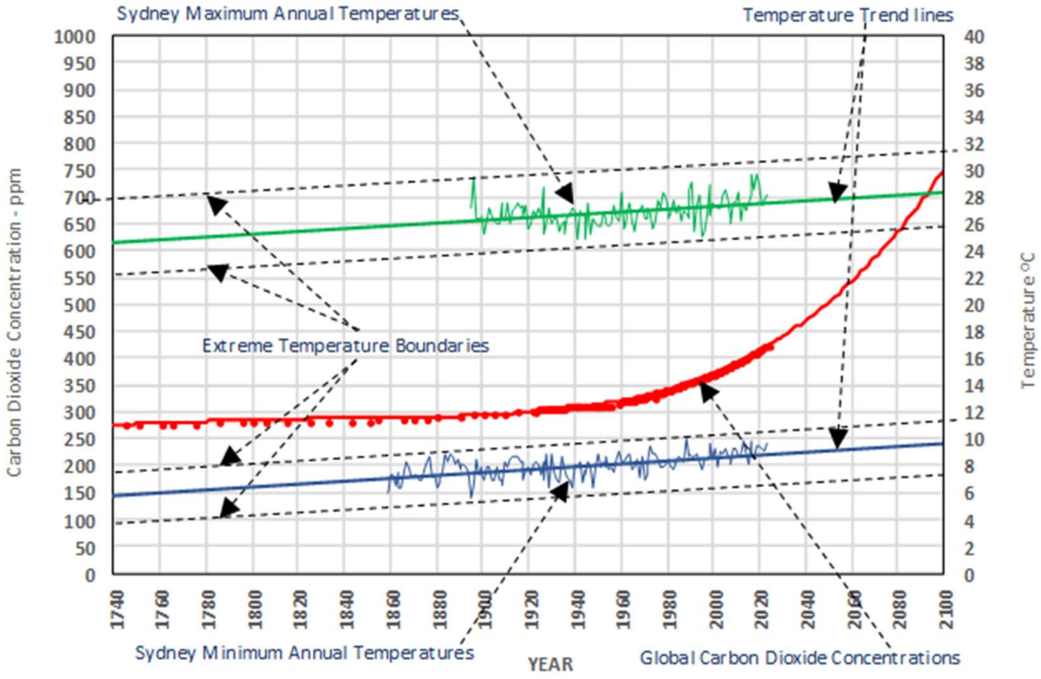

Figure 4: Carbon Dioxide Concentration versus Highest & Lowest Annual Temperatures in Sydney for the period 1859 to 2023.

An unexpected outcome when comparing the Sydney and Central England temperatures, was that their rates of increase were similar despite the two locations being in opposite hemispheres of the world and separated by over 17,000 kms – the similarity is demonstrated in Figure 2 where the Trend line for Central England has been copied and pasted next to the Trend line for Sydney. Part of the difference could be due to different "adjustments" made by each of the Met Bureaus to the raw temperature data.

5. Interpretation of the Graphs and Resulting Predictions

The graphs allow the levels of temperatures for the next few decades to be predicted with reasonable accuracy since the observable variations of temperature in many of the chosen sites as measured from the Trend lines, have been consistent for well over a century, even during the later years (1980s and beyond) when the concentration of CO_2 began to increase exponentially beyond its previous levels for the earlier period, 1740 to 1940. The consistency of the data is discussed further in Section 7 where a distinct discontinuity at or near the year 1950 in the anomaly data sourced from the Australian Bureau of Meteorology was discussed (highlighted with Trend lines) in Figure 9. It was assumed that the anomaly data was derived from the temperature data and as expected, a similar discontinuity was detected in the temperature data for the combined Australian cities around about the date, 1950 (Figure 11).

The graphs appearing in this paper show there is little (if any) correlation between the rate of change of the concentration of CO_2 and that of the temperatures measured at any of the sites examined. If there were, with carbon dioxide as the "driver", there would be a noticeable exponential increase in temperatures when the concentration level of CO_2 began to increase exponentially during the 1940s and beyond. Despite the discontinuity mentioned above, overall, the temperatures in Sydney and the other sites were seen to continue to rise at approximately the same linear rate as for the previous centuries regardless of changes in the concentration of atmospheric CO_2.

The extreme temperature boundary lines in Figure 4 indicate that in all the years leading up to 2100, higher annual (ie extreme) temperatures could be recorded at Observatory Hill in Sydney. Temperatures in regions, inland from Sydney, will be different, depending upon their locations; example - the outer regions of Sydney such as Penrith (~50 kms west) will always record higher averaged annual temperatures than those recorded at Observatory Hill which was the source of temperature data for Sydney in this paper. Analysis of the available data showed that Penrith maximum annual temperatures were an average of 4 ^{O}C warmer than Sydney with a possible extreme high temperature of 6 ^{O}C warmer than Sydney. Sydney, being located next to the ocean, has the benefit of cool sea-breezes that lower its temperatures, a benefit not shared by inland cities.

6. CO_2 Concentrations and Health

It is worth noting that if the concentration of CO_2 continues to increase in line with a 4th degree polynomial, the predicted concentration of CO_2 by 2240 will be about 2,600 ppm compared to the current concentration of ~420 ppm. This is not alarming for human activity based on the safety parameters for CO_2 concentrations set by OSHA, the Occupational Safety and Health Administration of the USA. They set a permissible exposure limit (PEL) for CO_2 in the workplace at 5,000 parts per million (ppm) over an 8-hour workday. However, they also warned that exposure to concentrations higher than 5,000 ppm could cause adverse symptoms such as headache, dizziness, increased heart rate, confusion, and in extreme cases, unconsciousness, or death.

Based on the above information for CO_2 concentrations, today's humanity should not be concerned about the possibility of adverse health effects from even 2,600 ppm concentration of CO_2, as predicted for 2240, 216 years into the future.

However, the future levels of CO_2 concentration remain uncertain because of the multiple factors that affect its concentration.

Current attempts by governments to reduce global CO_2 emissions from coal powered power stations have been hampered by China as well as the reliance of developing countries on coal for electricity generation and the slow growth of reliable capacity from alternative sources. The likely outcome of all these factors is a continuation of the rise in CO_2 concentration as shown by the graphs. Disregarding the various mechanisms that could affect the concentration of CO_2 in the atmosphere of which there are many, for simplicity it was assumed that the concentration of CO_2 in the atmosphere would continue to rise in a manner similar to the rises already experienced during the past few decades. Although there are certainly other factors that influence the concentration of CO_2, it is not the intention of this paper to investigate those factors or their effects – only to look at the ***outcome*** of those factors to date, and to extrapolate from that data into the future

Finally, in considering the increasing concentration of CO_2 in the atmosphere, there was no other choice but to accept the data published on various websites; in this case, the website [12] which contained an ***interactive*** graph from which the CO_2 data was extracted and graphed as shown in Figure 5.

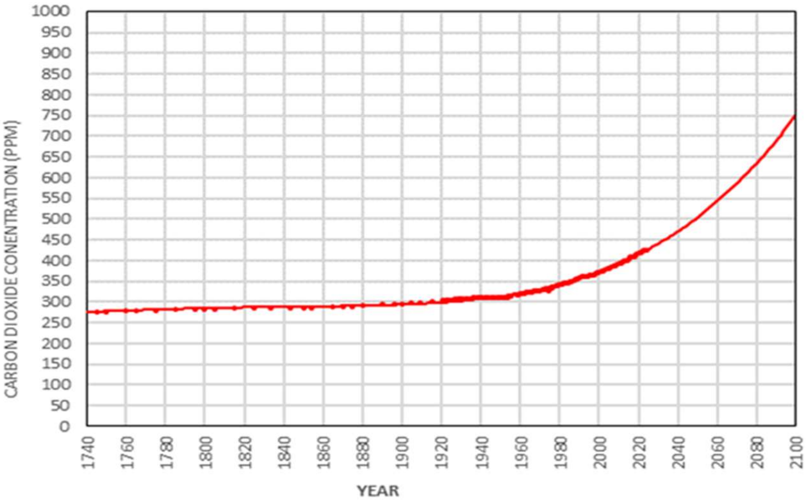

Figure 5: Concentrations of carbon dioxide using data from 1740 to 2023 and extrapolated to the year 2100.

7. Integrity of the Temperature Data Used

It has been said that it is very difficult to acquire actual raw temperature data. In the 1990's one could see real raw data from any US monitoring station, but since about the year 2000, that access has been shut off. What is available now is adjusted data. The same can be said for the temperature data for Australian cities and towns used in this paper, sourced from the Australian CSIRO Bureau of Meteorology website, and for global cities, sourced from weather bureau websites in their countries. Just how that data had been adjusted before being published is unknown – at least, unknown to this author. Although it is highly likely that the temperatures have indeed been adjusted, this author had no other choice but to accept them since there were no other reliable sources of temperature data available.

“Adjustments” to temperature records may not always provide results that are consistent with reality as observed in a detailed discussion by experts about the homogenization of temperature records. It is accepted that providing consistent and accurate temperature records from several diverse reporting stations over a large number of years is not an easy task.

In their joint paper, “Evaluation of the Homogenization Adjustments Applied to European Temperature Records in the Global Historical Climatology Network Dataset”, the following comments were made by the authors:

> *“.......after comparing the different homogenization adjustments applied by the National Oceanic and Atmospheric Administration (NOAA) to their widely used Global Historical Climatology Network (GHCN) monthly temperature dataset, we found a disconcerting inconsistency between the updates to the dataset from day to day...... “*
>
> *and:*
>
> *“........this remarkable inconsistency in the results from NOAA’s application of the Pairwise*

> *Homogenization Algorithm (PHA) to the GHCN since 2011 is quite surprising since the PHA has performed quite well over the years against various benchmarking tests. However, we note that those earlier assessments of the PHA were generally "one-off" assessments, i.e., they did not evaluate the consistency of the breakpoints and adjustments applied with repeated runs of the algorithm. Therefore this inconsistency of the PHA adjustments between consecutive runs would have been inadvertently overlooked by those earlier tests....“*
>
> *and:*
>
> *"...we believe these findings should be used as motivation for improving our approaches to homogenizing the available temperature records. Meanwhile, the results raise serious concerns over the reliability of the homogenized versions of the GHCN dataset, and more broadly over the PHA techniques, which do not appear to have been appreciated until now.....“*

However, the prediction of temperature rises made in this paper should hold true providing (a) the Australian Met Bureau (and the other bureaus) continue to "adjust" their temperature data in the same manner they have used during the past few decades, and (b) whatever biases they might have embedded in their "adjustment" processes do not have an increasingly unreal impact on the consistency of temperatures being reported. The impact of such "biases", if they have been incorrectly constructed, may not be evident for ten or twenty years by which time it will be too late to halt the expenditure of trillions of dollars to combat what will have turned out to be a non-existent problem. Should that happen, the temperatures being reported will be higher than the raw temperatures being recorded although this discrepancy may not be noticed by the public for a few more years.

This author has made intensive use of temperature data available from the Australian Bureau of Meteorology, an example of which is Figure 6.

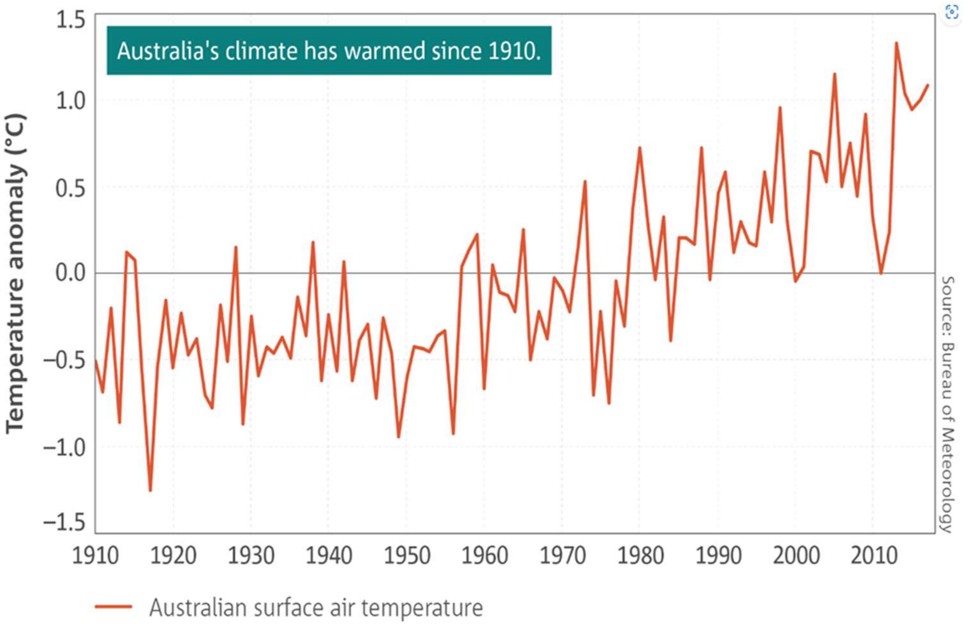

Figure 6: Australian Surface Temperature Anomalies only available in graphical form – digitalized in Figure 7 to allow later comparison with other temperature data already in digital format.*

** A temperature anomaly refers to a deviation from the long-term average temperature for a specific location or region over a set period of time. It's a measure used in climate science to assess how much warmer or cooler the temperature is compared to the expected norm for that time and place. Anomalies can be positive (warmer than average), negative (cooler than average), or near zero (close to the long-term average).*

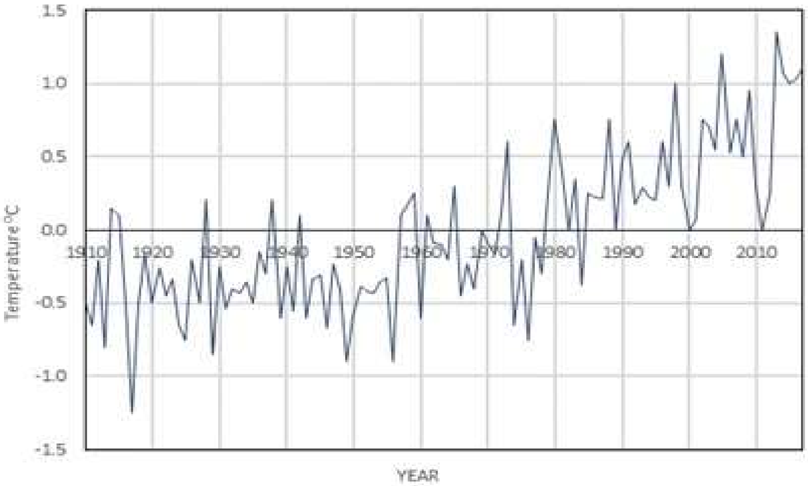

Figure 7: *Result of digitalizing the Australian data (shown in Figure 6).*

To allow the anomalies data to be compared graphically with temperature, it was further modified by adding 33 ^{O}C to each of the data points. This process did ***not*** alter the important factor discussed in this paper – the ***rate of change*** of temperatures.

Later, during the analysis, it was noticed that the Trend line for the Bureau's Anomalies data had a similar rate of change as that for the temperatures averaged over six of the seven Australian cities (temperature data for Perth did not cover a sufficient range of dates to be included). Furthermore, by adding a specific 28.9 ^{O}C to each of the anomaly temperature points shown in Figure 7, the trend lines for the anomalies and temperatures graph almost coincided as from 1950, as shown in Figure 10.

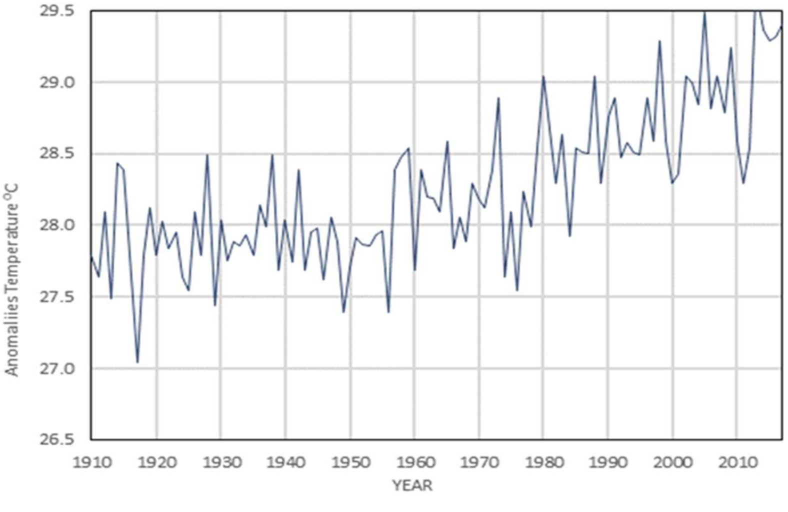

Figure 8: Anomalies plus 28.29 ^{O}C

The first trend line (brown) for the anomalies data in Figure 9 for the period ending in 1950 indicated a moderately consistent, but very small rise in temperature of 0.001 ^{O}C per year.

The second Trend line (*blue*) for the Anomalies data from 1950 to 2017 shows a much larger and consistent rise of 0.019 ^{O}C per year.

The cause of such a discontinuity occurring over two years or less, cannot be explained easily as being the influence of either CO_2 concentrations or natural processes since changes caused by Cosmic and Global influences occur over much longer periods, so the discontinuity was assumed to be caused by a change in the method used by the Bureau to "adjust" their temperature records.

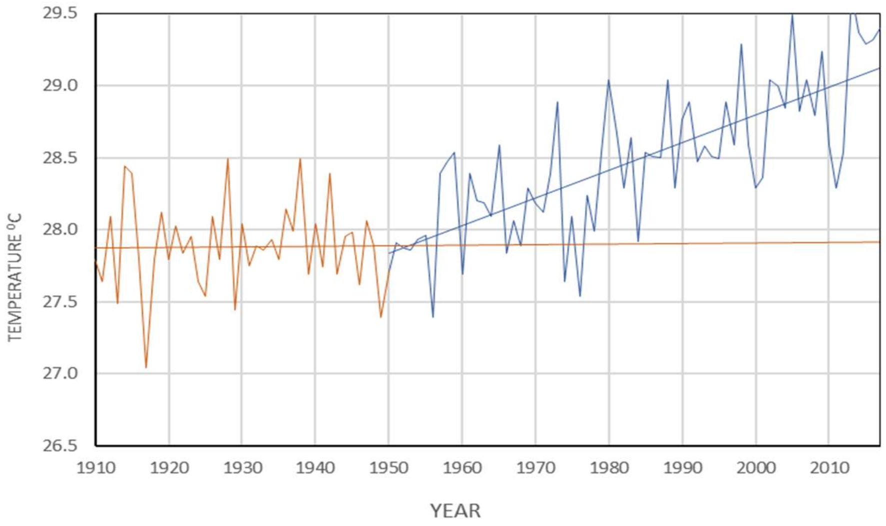

Figure 9: The first Trend line (brown) is that for anomalies data from Australian Bureau of Meteorology, for the period, 1910 to 1950. The second Trend line (blue) is anomalies data for the period 1950 to 2023.

Trend lines for Anomalies (red) and Averaged Australian Cities data (black) are compared in Figure 10 and show close correlation between the two variables for the period 1950 to 2022 as seen from the set of (almost) overlapping black and red Trend lines.

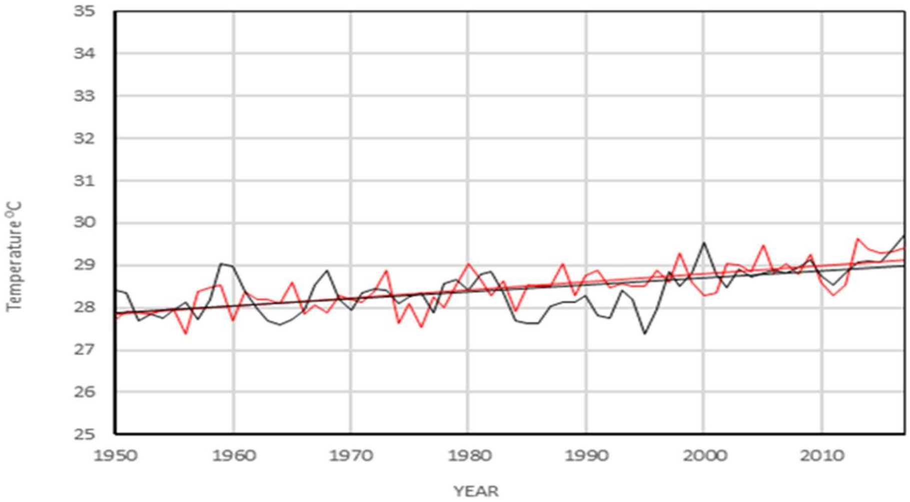

Figure 10: A comparison - combined Australian Cities Averaged High-Temperatures (black) versus Anomalies (red) - 1950 to 2017.

The discontinuity at the end of the period 1949-1950 shown in the Anomalies graph (Figure 7) also appears in the combined Australian cities temperature graph (Figure 11). This is not surprising since the data for both variables is from the same source, the Australian Bureau of Meteorology, and most likely subject to the same "adjustment", albeit, as from 1950.

It was not the purpose of this paper to investigate the reasons behind the apparent erratic temperature measurements prior to 1950 or the complex method of "adjustments" applied to the post 1950 raw data and so for simplicity, has focused on measuring the temperature trends post 1950 for the three categories examined: namely, (a) all Australian cities (averaged high temperatures), (b) a selection of Australian towns (averaged high temperatures), and (c) a selection of Global cities and regions (averaged temperatures).

Measurements of the rates of change of temperatures from those studies are summarised in Table 1.

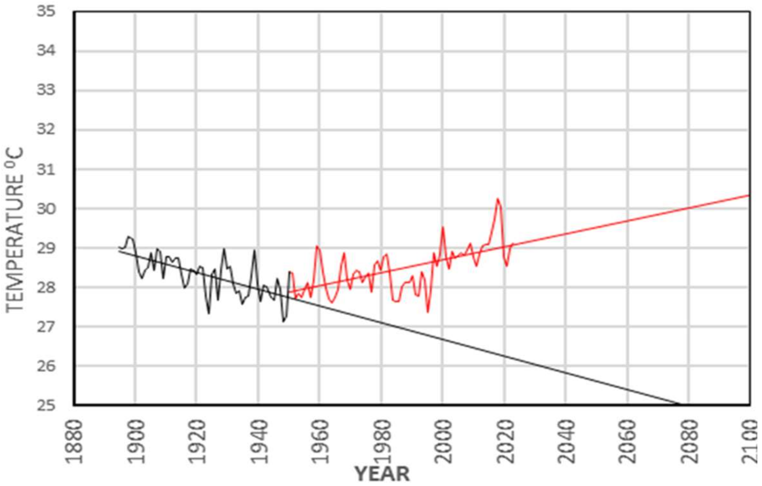

Figure 11: Averaged Pre and post 1950 Australian City temperatures.

Some cities and towns were omitted from the calculations due to insufficient temperature data being available. They were:

Australian Cities:	Perth
Australian towns:	Albany, Oodnadata, Cloncurry, Burrinjuck Dam
Global Cities / Regions:	Bangkok

Table 1: Predictions for the year 2050 compared to 2024 levels (calculated from post-1950 temperature data).

LOCATION	TEMPERATURE		
	Rate of Change °C per Year	Increase by 2050 (°C)	Increase by Year 2100 (°C)
Australian Cities	0.017	0.44	1.29
Australian Towns	0.017	0.44	1.29
Global Cities	0.020	0.52	1.52
Average - All Cities & Towns	0.018	0.47	1.37
Anomalies	0.019	0.49	1.44

The predictions for the year 2050 (compared to 2024 levels) are:

- rate of temperature change averaged over all cities and towns studied:	0.018 °C/year,
- rise in temperature averaged over all cities and towns studied:	0.47 °C,
- maximum temperature at Observatory Hill, Sydney:	30.0 °C,
- extreme temperatures that might occur at Observatory Hill, Sydney:	32.0 °C,
- extreme temperatures that might occur at Penrith (NSW):	38.0 °C,
- concentration of CO_2 in the atmosphere:	500 ppm.

Should temperatures as measured by the Australian Bureau of Meteorology and other global climate bureaus, continue to be adjusted as they have since 1950, Table 1 shows that the expected rise in temperature averaged over all the cities and towns examined, will be 1.37 °C by the year 2100.

Another observation of the Global city temperatures was the absence of any discontinuity during the period 1949-1950. Figure 12 shows the Trend lines generated for (a) a subset (black) of Global City temperatures covering the period 1910 to 1949, (b) a second subset (green) 1950 to 2023 and a third full set (brown - hidden) 1910 to 2023.

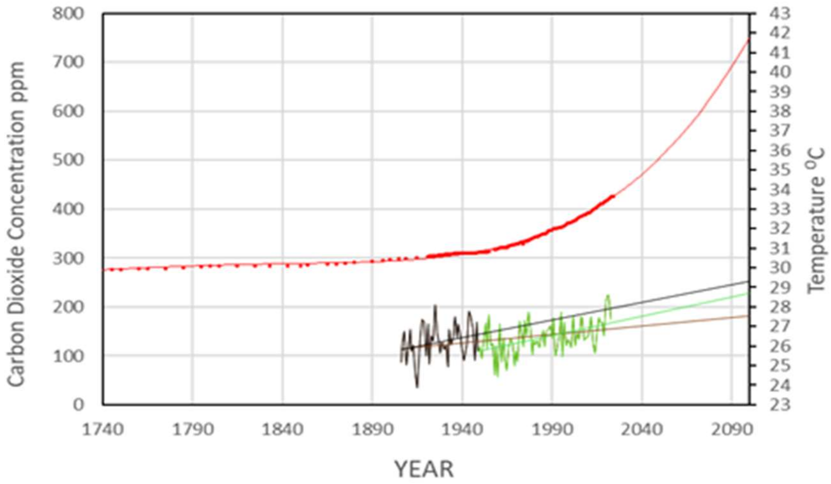

Figure 12: Global City Temperatures - three Sets: 1906 - 1950, 1950 - 2100 & 1906 - 2100.

In Figure 12, the average Global City temperatures at 2100 calculated from the linear Trend Lines for pre and post 1950 data, differ by only ~0.7 ^{O}C thus supporting the assertion that if any adjustments had been made to the Global Cities data, then they were applied to the data sets corresponding to the full date-range.

Neither of these two sets of temperatures show any visible correlation with the exponentially increasing concentrations of CO$_2$.

8. Interglacial Cycles over the Past 450,000 Years

This paper supports the assertion that it is local, global, and cosmic forces and not atmospheric CO$_2$ concentrations that are driving the massive changes in climate experienced by the earth during the past 400,000+ years as shown by the five major cycles in Figure 13 [13]. It therefore depends upon where we are in the glacial cycles as to whether the current increases in temperature will continue.

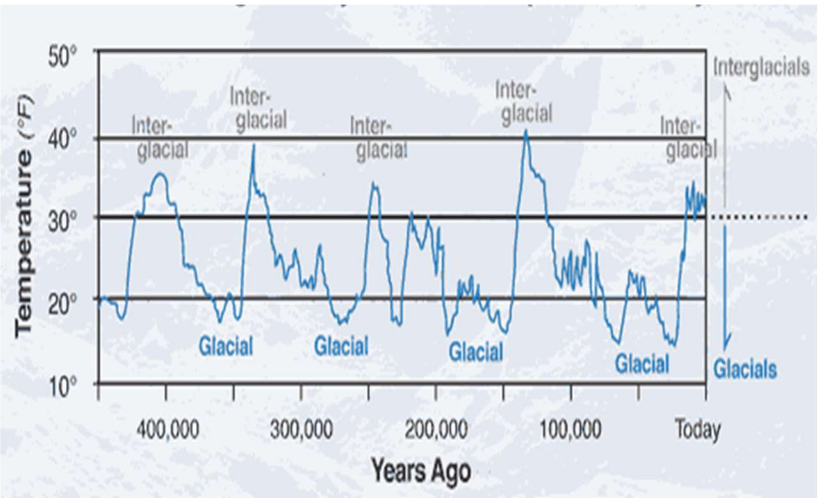

Figure 13: Temperatures obtained from glacial records for a period of 450,000 years.

Although the overall ***rate***s of temperature changes either up or down during the ***major*** glacial cycles are small, within the sub-cycles of major glacial changes, temperature changes can be in either direction and at much higher rate, and it is assumed that the earth is in such a sub-cycle.

The range of years important in this paper, 2023 to 2100, is within a glacial sub-cycle and very small compared to Interglacial time periods. Figure 13 provides an indication of just how small that timeframe is; nevertheless, it is the timespan that concerns humanity.

Measurements from glacial sub-cycles show that the rate of change of temperature can vary from 0.014 to 0.025 ^{O}C per year. The average of measurements from current temperature records summarised in Table 1 (0.018 ^{O}C per year) lie within that range.

If the current rate of change of measured temperatures continues, the temperatures that would be recorded at Observatory Hill, 10,000 years from now, might be considered by some as being moderately uncomfortable but still bearable. However, this paper concludes there is little humanity can do to avoid these rises, since they would ***not*** be caused by the higher CO_2 concentrations in the atmosphere expected then.

Unless the world destroys itself in the meantime, within those 10,000 years, advances in technology might finally find a solution to address the problem – if there is a problem. The world may also be at a different stage of the inter-glacial cycle when the global temperature might even be reducing, and no such solution would be required.

9. Carbon Cycle

When the author was attending secondary school, the carbon cycle [15] was part of the curriculum. In those days, the concept was simple with no concerns about the concentration of carbon dioxide in the atmosphere. The Carbon Cycle in Figure 14 shows carbon dioxide being both absorbed and released by trees, vegetation, lakes, seas, oceans and animals. During the hundreds of millions of years of the earth's history when plant and animal life flourished, a portion of that carbon dioxide was being locked up in deposits of coal, oil, gas and some minerals.

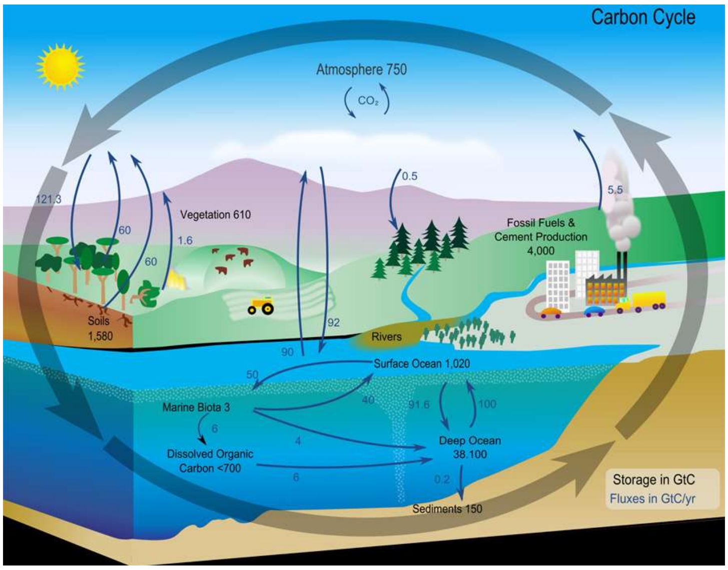

Figure 14: The Carbon Cycle.

The carbon cycle was strongly impacted by the industrial revolution and beyond through the increasing use of machinery that utilised gas, coal and oil to provide energy. Burning that coal, oil or gas returned CO_2 back to the atmosphere. Suddenly, carbon dioxide that had been stored for hundreds of millions of years was being released back into the atmosphere at a much faster rate – a rate that has been increasing exponentially since the 1940s to 1950s.

It was exceedingly easy for alarmists to link increasing global temperatures with the increasing concentrations of CO_2 in the atmosphere and for those looking for a cause, that concept was like a gift from heaven.

For governments, it provided reasons to appear to be competent, knowledgeable and caring – and to spend trillions of dollars supported by those who declared that "the science is in" thus stifling further debate.

For the private sector, the opportunities for massive profits were too tempting to ignore.

For activists looking for a cause, the (apparent) CO_2 issue satisfied all their desires.

This paper shows that the science is "not in" and concludes that CO_2 is not a pollutant! Quite the opposite - CO_2 is an essential part of life.

10. Seven Australian Cities

Since the Australian government is very concerned about Australia's contribution to what they regard as the cause of global warming, CO_2, it was thought appropriate to finish the paper with a presentation of the temperature variations over the past centuries for each Australian city and compare them with the increasing concentrations of CO_2.

The graphs in Sections 11, 12 and 13 show the variation of the highest temperature (or in some cases, the average temperature) recorded for each of the cities, towns and regions for each year.

Although both global temperatures and CO_2 concentrations are increasing, there is no visible evidence in the graphs for the 19 cities, towns or regions included in this study, that correlates temperature increases with the ***exponentially*** increasing CO_2 concentrations.

It is useful to note that the data used for this paper is freely available on the internet for anyone to use, and the URLs used to source that data are provided in the Reference Section should an independent check be considered as necessary.

Realistically, the man-in-the-street is ***not*** interested in temperature anomalies – they are only interested in and affected by the actual temperature they are experiencing – surface temperatures that are recorded by their local meteorological stations. Those temperatures are used in this paper and shown in the graphs although there are strong signs they may no longer be "raw" measurements and that "adjustments" to them have probably been made by the Australian Bureau of Meteorology.

Ideally, unadulterated raw temperatures would have been far preferable for this paper, but they were not available.

The graphs for Australian city temperatures discussed in this paper show the highest temperatures recorded each year for each city. A few Australian media outlets delight in describing some current weather events/temperatures as "extreme", and that such weather events have never been experienced before.

The Australian Bureau of Meteorology provides support for these claims by the media outlets by stating on its website:

> *"……Australia's weather and climate continues to change in response to a warming global climate..........with most warming since 1950. This warming has seen an increase in the frequency of extreme heat events.....eight of Australia's top ten warmest years on record have occurred since 2005........increases in temperatures are observed across Australia in all seasons with both day and night temperatures showing warming. The shift to a warmer climate in Australia is accompanied by more extreme daily events…."*.

Figure 4, which shows the rise in high temperature measured in Sydney from 1880 to 2023, includes a boundary for the most extreme temperature experienced during that period. As the years pass by, the boundary of the most extreme temperature also rises, and so it is logical that future extreme temperatures will be the highest ever recorded.

The average annual increase in temperature for the seven Australian cities and towns was calculated to be 0.017 ^{O}C per year so the increase in temperature by the year 2050 (26 years into the future) was calculated to be 0.44 ^{O}C, or 1.29 ^{O}C by the year 2100 as listed in Table 1.

Some may still argue that drawing a conclusion from the analysis of data from only five global cities, seven Australian cities and some Australian towns is not sufficiently rigorous to be accepted by the scientific community. Before advancing that argument, it would be appropriate for them to obtain and graph temperature data for any city/cities in the world they might choose. It is unlikely their conclusions would differ from the conclusion in this paper.

For consistency, the following graphs were constructed with the full data sets available for each city and town. Some of those data sets such as the one for Bangkok cover only a small range of dates.

None of the graphs show any visible correlation between the rapidly rising concentrations of CO_2 and the rises in temperature. They do, however, show rising temperatures in almost all locations, as was expected.

11. Temperatures versus CO_2 Concentrations – Seven Australian Cities

HOBART

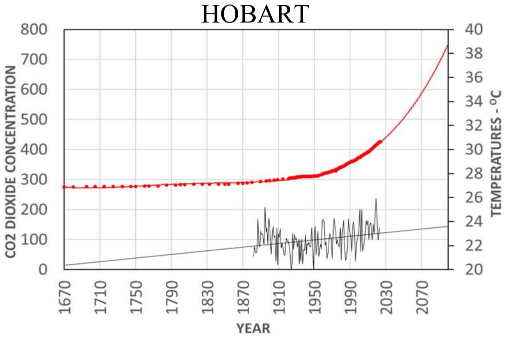

SYDNEY

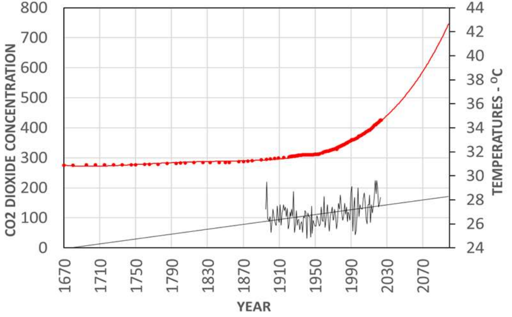

MELBOURNE

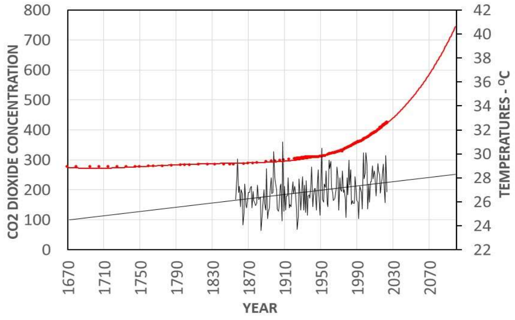

BRISBANE

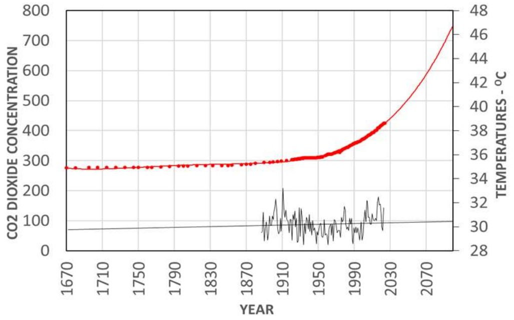

PERTH

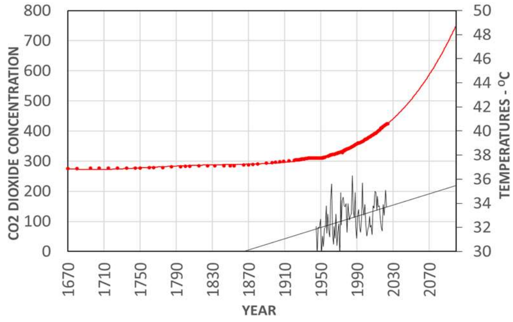

ADELAIDE

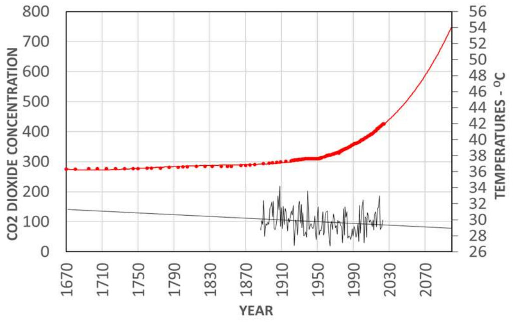

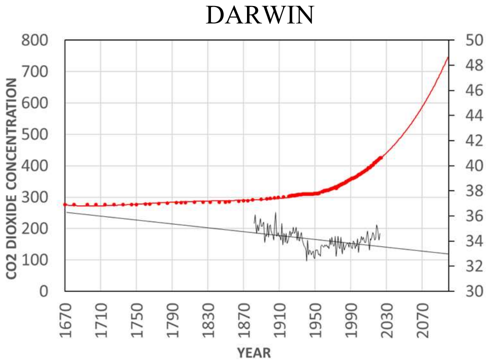

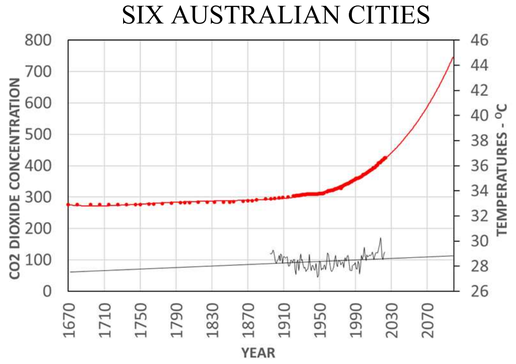

12. Temperatures versus CO_2 Concentrations – Seven Australian Towns

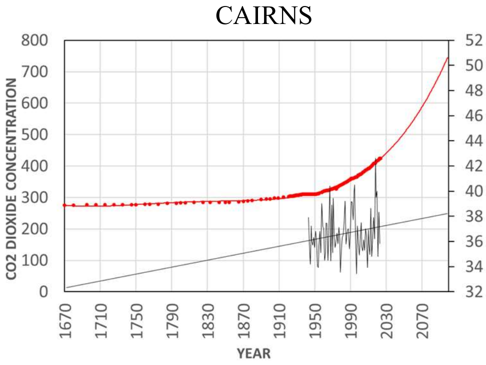

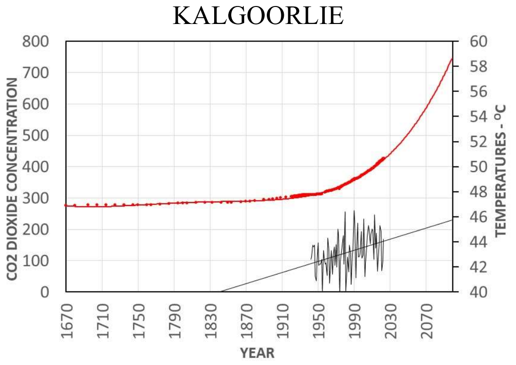

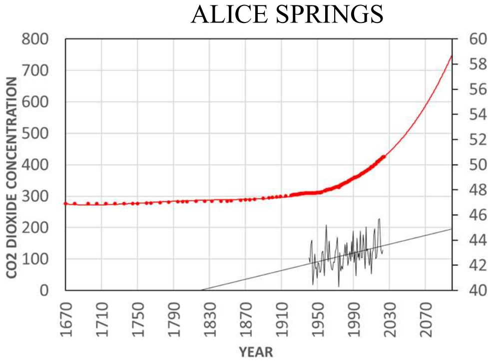

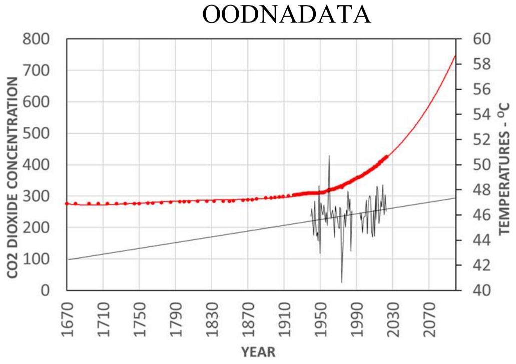

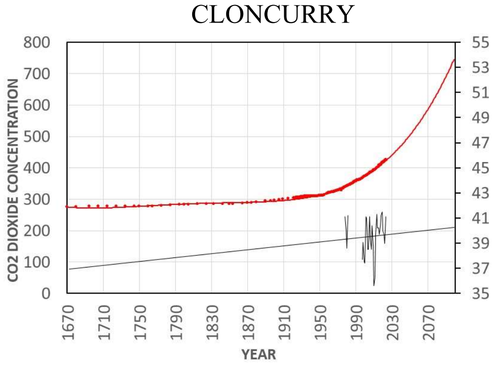

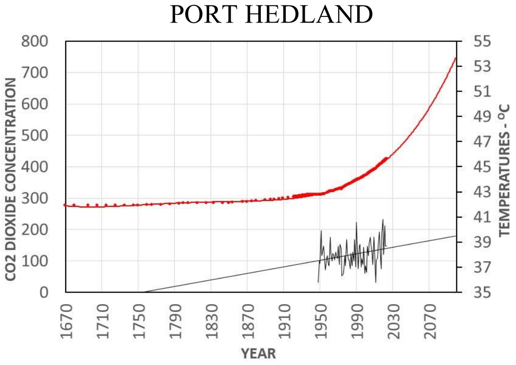

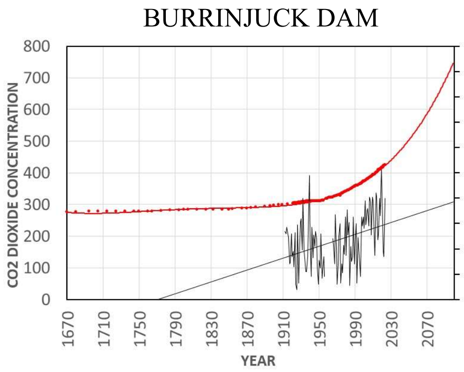
BURRINJUCK DAM

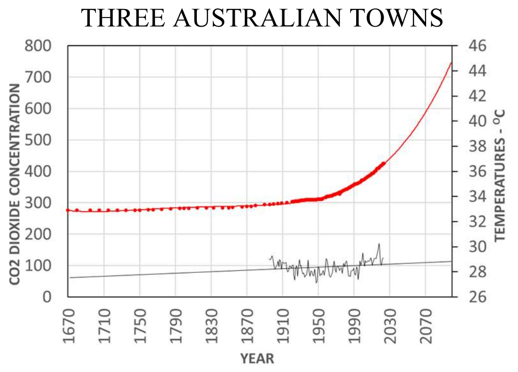
THREE AUSTRALIAN TOWNS

13. Temperatures versus CO_2 Concentrations - Five World Cities / Regions

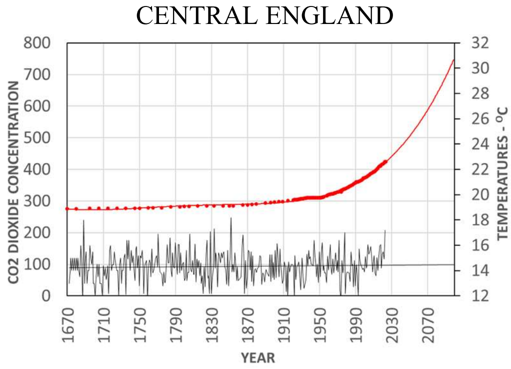
CENTRAL ENGLAND

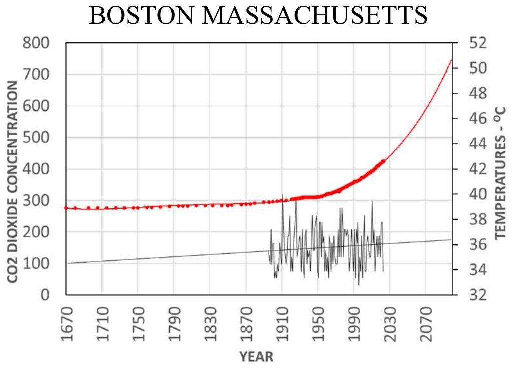
BOSTON MASSACHUSETTS

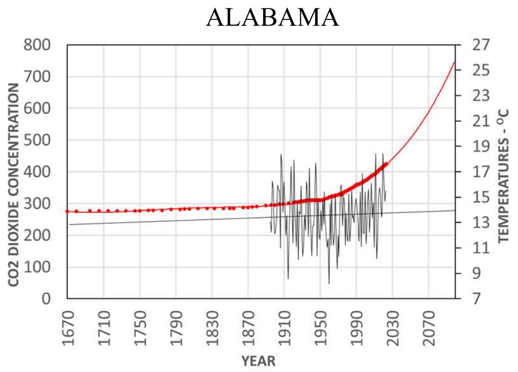
ALABAMA

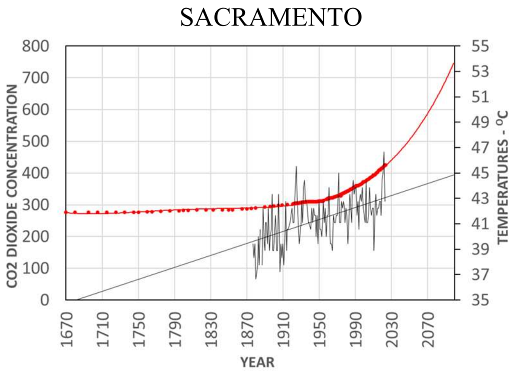
SACRAMENTO

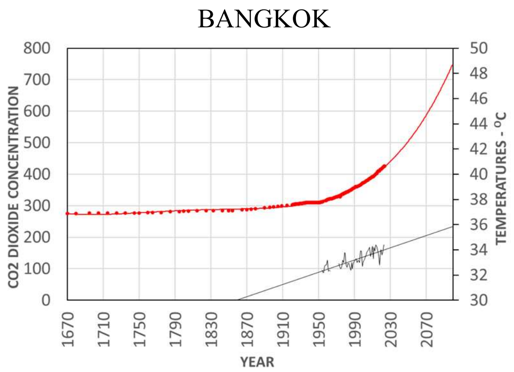
BANGKOK

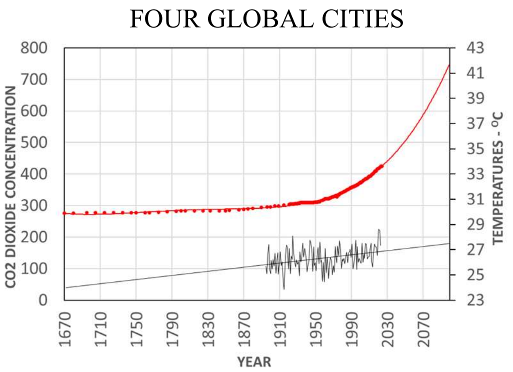
FOUR GLOBAL CITIES

AUSTRALIAN ANOMALIES

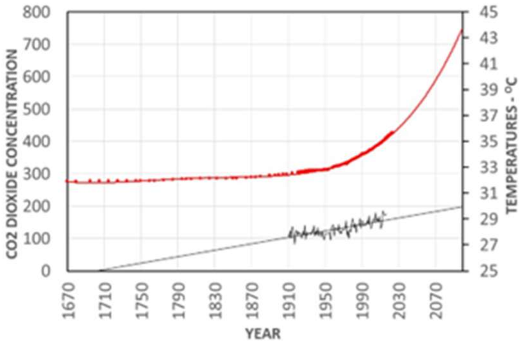

14. Conclusion

The relationship between the exponentially increasing global concentrations of CO_2 and increasing global temperatures for all the sites studied has been shown to be tenuous at least, and most likely, non-existent.

The findings in this paper strongly suggest that increases in the concentrations of global atmospheric CO_2, regardless of its sources, should no longer be of concern to humanity, both now and in the future, and that the trillions of dollars being wasted on projects to reduce or eliminate CO_2 emissions, be immediately redirected to essential work that will benefit humanity.

Increases in the concentration of CO_2 in the atmosphere are not a problem – it is quite the opposite! It can only improve the quality and abundance of plant growth that has occurred during some of the past millennia without harming the world's inhabitants.

Whether the concentration of CO_2 increases, decreases or remains steady should be of no concern to humanity – the rise in global temperature will continue at its current rate of 0.018 ^{O}C per year for the foreseeable future, independent of CO_2 concentrations.

There is, however, a clear (and expected) correlation between the increasing concentrations of CO_2 and the increasing population of the world, as represented by the population growth in Sydney. The problem here is not the CO_2 - it is the ability of governments to sustain higher levels of populations in terms of food, transport and accommodation.

Funding: John McRoberts.

Chief-Editor: H. Harde; Reviewers: anonymous.

Acknowledgements

The author would like to thank Prof Gabriël Moens, John McRobert and Ted Mouritz for their assistance and advice.

References

1. Temperature Data Adjustments: https://www.bom.gov.au/akamai/https-redirect.html, https://www.mdpi.com/2073-4433/13/2/285
2. Climate Change Scepticism: https://www.ncbi.nlm.nih.gov/pmc/articles/PMC3002211/

3. Australian City & Town Temps: https://reg.bom.gov.au/climate/data/stations/
4. Central England Average Temps: https://theconversation.com/june-2023-was-the-hottest-in-england-since-1846-heres-why-it-was-so-unusual-208692
5. Alabama Average Temperatures: https://www.ncei.noaa.gov/access/monitoring/climate-at-a-glance/county/time-series
6. Bangkok Temperatures: https://en.tutiempo.net/climate/ws-484550.html
7. Boston Massachusetts: https://www.currentresults.com/Yearly-Weather/USA/MA/Boston/extreme-annual-boston-high-temperature.php
8. Sacramento: https://www.currentresults.com/Yearly-Weather/USA/CA/Sacramento/extreme-annual-sacramento-high-temperature.php
9. Trend (Best Fit) Lines: https://help.tableau.com/current/pro/desktop/en-us/trend-lines_add.htm
10. Sydney Population: https://en.wikipedia.org/wiki/Demographics_of_Sydney
11. Urban Heat Island: https://acsess.onlinelibrary.wiley.com/doi/abs/10.2134/agronmonogr55.c2
12. Global CO_2 Concentrations: https://www.co2levels.org/#sources
13. Glacial and Interglacial periods: https://energyeducation.ca/encyclopedia/Glacial and interglacial periods; https://skepticalscience.com/print.php?r=337
14. G. M. Heisler, A. J. Brazel, 2010: *The Urban Physical Environment: Temperature and Urban Heat Islands*, https://acsess.onlinelibrary.wiley.com/authored-by/Heisler/Gordon+M.
15. The Carbon Cycle: https://scied.ucar.edu/image/carbon-cycle-diagram-nasa

Klimarealistene
Vollsveien 109
1358 Jar, Norway
ISSN: 2703-9072

Correspondence:
ajsadar@geneva.edu

Vol. 4.1 (2024)
pp. 107-109

Will Climate Change Crush Air Quality by Boosting Temperature Inversions, or Not?

Anthony J. Sadar[1]

Geneva College, Beaver Falls, PA

Keywords: Temperature inversions; air quality; regional climatology.

Submitted 2024-04-09, Accepted 2024-04-14. https://doi.org/10.53234/scc202404/16

Commentary

Seventy-five years ago, in late 1948, 21 residents of Donora, Pennsylvania, US, and vicinity died from high concentrations of fumes emitted from the local heavy industry. This tragic event in Donora, a small town about twenty miles south of Pittsburgh, sparked the national air quality laws and regulations in the US.

The notorious incident was triggered by several days of stagnant air caused by persistent temperature inversions.

Temperature inversions have been a key component of some of the worst air pollution generated disasters in history, including in Europe in the 1950s. And interest in the impact of climate change on pollution-inducing temperature inversions is gaining traction.

What is a temperature inversion and why is it a challenge to good air quality?

A temperature inversion is an atmospheric condition where warm upper-level air rests above cool lower-level air. This is a stable situation because light air is floating above heavy air, keeping the air from circulating. When a temperature inversion exists at the earth's surface, the air becomes stagnant and air pollution levels can increase dramatically.

Notably, the number and strength of surface inversions can be altered depending on how climate changes, just like severe weather conditions such as tornadoes and hurricanes.

In 2022, I had a first-of-its-kind surface-inversion climatology report published in an environmental science journal (Sadar, 2022). The peer-reviewed research paper presented results from my assessment of 30 years (January 1991 through December 2020) of morning and evening upper-air measurements collected by the Pittsburgh National Weather Service.

Review and analysis of more than 21,000 observations revealed the amount and strength of surface inversions and their trends over the decades.

During the 30-year period, people in the Pittsburgh area awoke to significant surface inversions on nearly half of all mornings. Evening inversions occurred with a frequency of about 20 percent.

Interestingly, there was a discernable decline in both morning and evening inversion frequencies over the three-decade duration. However, while surface inversion strength in the morning was

---

[1] Anthony J. Sadar is an adjunct associate professor of science at Geneva College, Beaver Falls, PA, and coauthor of Environmental Risk Communication: Principles and Practices for Industry (CRC Press).

also generally on the decline, the evening inversion strength was increasing.

Consequently, like so much research, the hard data suggest some good and some bad outcomes from a warming climate during the 30-year record.

Comparison of my results with another recent 30-year investigation of surface inversion data from nearly 500 measurement stations throughout the world shows good agreement with such research results (Zeng et al., 2022). The trends in that recent work for the northeast US matched up well with the findings in my study.

Of course, as with all meticulous scientific studies, further investigation is needed to understand and corroborate these findings with observed atmospheric conditions, climate trends, and the climate system.

Investigation of the atmosphere just above the earth's surface relates directly to the understanding of climate change mechanics because changes to the trends in near-surface atmospheric temperature along with moisture content (both measured at least twice a day across the globe by launching weather balloons) have a profound effect on the earth's hydrologic (water) cycle.

In a just-released book, Climate and Energy: The Case for Realism edited by historian E. Calvin Beisner and climatologist David R. Legates (2024), the role of water in climate change is addressed in lucid detail. For instance, it's noted in a chapter by climatologist Roy Spencer that water vapor is "the strongest of Earth's greenhouse gases. Together with the clouds we see, water vapor accounts for about 75% of the greenhouse effect." In addition, "the processes that limit how much water vapor accumulates in the atmosphere - precipitation - are not known in enough detail to predict how the weak direct-warming effect of [carbon dioxide] will be either amplified or reduced by precipitation limits on water vapor" (pp. 157-159).

It is well known that the presence, strength, and duration of surface inversions affects the transport and transformation of atmospheric moisture, and vice versa, as water in the air impacts inversions. And as a direct link to air quality, more precipitation can help cleanse polluted air. In fact, rainfall helped to end the pollution episode in Donora, Pennsylvania.

So, surface inversions have a marked connection to complex climate change, clean air, and the water cycle.

Further evaluation of surface inversion conditions and trends is necessary to better understand a phenomenon that has such a critical influence on air quality and moisture. The discovery of additional correlations between changing surface inversion conditions and air quality levels and tendencies will help to expand understanding and subsequent mitigation of serious air pollution episodes in ever-changing climate conditions.

Nuanced science must advance regardless of political narratives that claim simplicity to the complexity of atmospheric dynamics. Research on temperature inversions, which focuses on the literal depth of atmospheric changes, is critical to further interpreting climate change and to fend off unhelpful politicking.

References

1. Sadar, A.J., 2022: *Climatology and trends of morning and evening temperature inversions in southwestern Pennsylvania with air quality implications*, Environ. Sci. Pollut. Res. 2022, 29, 49411-49421,
   https://doi.org/10.1007/s11356-022-20504-7.
   Note: Ref. 1 provides further details on surface-inversion conditions and the data set prepared from the University of Wyoming Department of Atmospheric Science website
   http://weather.uwyo.edu/upperair/sounding.html
   and for missing data when available, from the Plymouth State University website https://www.plymouth.edu/.

Ref. 1 also includes analysis of surface-inversion break times and monthly conditions. Contact the author for inquiries regarding the full dataset.

2. Zeng, H.; Tian, P.; Zhang, M.; Cao, X.; Liang, J.; Zhang, L., 2022: *Rapid change in surface-based temperature inversions across the world during the last three decades*, J. Appl. Meteor. Climatol. 2022, 66, 75-184, https://doi.org/10.1175/jamc-d-21-0093.1.
3. Beisner, E.C.; Legates, D.R., Editors, 2024, *Climate and Energy: The Case for Realism*, Washington, D.C.: Regnery Publishing.